Time-Resolved Spectroscopic Investigations into Reactions of Transition Metal Complexes

Genevieve Garwood MSci

School of Chemistry

University of Nottingham

Thesis submitted to the University of Nottingham for the degree of Doctor of Philosophy

September 2022

For dad,

I know you would be proud

Declaration

I hereby declare that this Thesis and the work contained in it are my own, unless acknowledged otherwise.

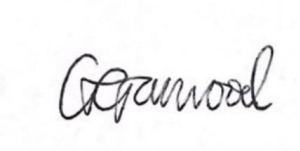

Genevieve Garwood

September 2022

Abstract

Chapter 1

An introduction to the photochemistry of organometallic complexes and the history of transition metal alkane and noble gas complexes, which have been studied throughout this thesis, is given. The main technique used in this thesis, i.e., time-resolved infrared spectroscopy, is described here.

Chapter 2

In this Chapter, the photochemical reactions of polypyrazolylborate rhodium complexes, Tp*Rh(CO)$_2$ and Bp*Rh(CO)$_2$, in perfluorinated solvents have been probed by pico- and nano-second time-resolved infrared spectroscopy. The photochemical reactions of Tp*Rh(CO)$_2$ were probed in a mixture of cyclopentane and perfluoromethylcyclohexane (PFMCH) due to its insolubility in the latter. Tp*Rh(CO)$_2$ was observed to activate the C–H bonds of cyclopentane and there was some evidence for the activation of the C–F bonds of PFMCH, as indicated by the presence of previously unseen peaks in the ns-TRIR and an extension to the lifetime of the κ^3 intermediate in the ps-TRIR.

The solubility of Bp*Rh(CO)$_2$ in PFMCH allowed for the characterisation of Bp*Rh(CO)X, where X = PFMCH, *c*-pentane, *n*-heptane, C_2H_6 and Xe. These complexes have not been observed before in the literature under ambient conditions, if at all. The photoproduct lifetimes were determined and found to be on the microsecond timescale, with the exception of Bp*Rh(CO)(PFMCH), which lived for nanoseconds. The lifetimes increased in the order Bp*Rh(CO)(PFMCH) $\ll$ Bp*Rh(CO)(Xe) < Bp*Rh(CO)(C_2H_6) < Bp*Rh(CO)(C_5H_{10}) < Bp*Rh(CO)(C_7H_{16}), following known trends in lifetimes of alkane complexes, with the exception of Bp*Rh(CO)(C_5H_{10}) < Bp*Rh(CO)(C_7H_{16}). The measured lifetimes were all exceptionally long compared to typical rhodium complexes,

as normally further reaction occurs in the form of C–H activation, hence decreasing the typical lifetimes of rhodium alkane complexes. However, this alternative pathway is not available for $Bp^*Rh(CO)_2$, as it is unable to activate the C–H bonds in alkanes. We also postulate that a second factor resulting in these remarkable lifetimes is the complexes sixteen electron nature, or in other words its electron deficiency.

The lifetimes of $Bp^*Rh(CO)(X)$ (X = C_2H_6, *c*-pentane, *n*-heptane and Xe) were measured at varying temperatures to deduce the activation parameters of these complexes. The determined activation energies, E_a, and Gibbs free energies, $\Delta G^{\ddagger}$, were compared to DFT calculated bond dissociation energies, and found to be in good agreement. Calculated $\Delta S^{\ddagger}$ values remained relatively constant across all reactions, and the large, negative values indicated that all reactions proceeded via an associative mechanism, agreeing with previous work on other rhodium complexes. Values for $\Delta H^{\ddagger}$ varied across all reactions, showing that this was the most important factor in controlling the reactions.

Chapter 3

In this Chapter, density functional theory has been used to calculate a number of bond dissociation energies for a range of non-conventional transition metal alkane and noble gas complexes. Due to the results in Chapter 2, which found a sixteen electron complex to be an excellent precursor for remarkably long lived alkane and noble gas complexes, other non-conventional complexes were explored. The alkane complex derivatives of seventeen electron $M(CO)_6$ (M = V, Nb or Ta) were compared and contrasted against standard eighteen electron complexes $M(CO)_6$ (M = Cr, Mo or W) and $M(CO)_5(NO)$ (M = V, Nb or Ta). Indeed, the seventeen electron complexes were found to bind more strongly to the alkane than their eighteen electron counterparts.

The bond dissociation energies of other electron deficient cationic alkane complexes of group VI, VII and VIII metals were explored. Complexes with the structure $[Tpm'M(CO)(NO)(X)]^+$ (Tpm' = Tpm or Tpm*, M = Cr, Mo or W and X = CH_4 or C_7H_{16}) were studied and the bond dissociation energies were found to be significantly

increased in comparison to their neutral analogues, and are among the highest known for group VI complexes. Bond dissociation energies of $[Tp'M(CO)(NO)(X)]^+$ and $[Tpm'M(CO)_2(X)]^+$ (Tp' = Tp or Tp*, Tpm' = Tpm or Tpm*, M = Mn or Re and X = CH_4 or C_7H_{16}) were calculated. The BDE values were again significantly increased in comparison to those of their neutral counterparts; however, they were not as high as those calculated for other cationic group VII complexes.

The last group of complexes to be calculated were the cationic relatives of the bispyrazolylborate rhodium complex studied in Chapter 2 and their iridium analogues, $[Bpm'M(CO)(X)]^+$ (Bpm' = Bpm or Bpm*, M = Rh or Ir, X = CH_4 or C_7H_{16}). These complexes were calculated to have exceptionally high bond dissociation energies—the highest calculated in this Chapter—and present a promising new area for experimental research.

Overall, trends in bond dissociation energies were that the energies increased on moving from group V to group VII, and that methane complexes were always more weakly bound than heptane complexes. For all complexes, the bond lengths were also analysed to look for trends in changes in the bond lengths. All complexes exhibited a lengthening of the alkane C–H bond bonded to the metal. Larger bond dissociation energies corresponded to an increased lengthening of this C–H bond. Energies of the lowest occupied molecular orbital (LUMO) were also analysed, as previous research has shown that a lower LUMO may result in a stronger bond. Indeed, all cationic complexes exhibited a much lower LUMO than their neutral analogues; however, the magnitude of this difference was not always a good indicator of the magnitude of the difference in overall bond dissociation energy.

Chapter 4

In this Chapter, the photochemical reactions of $CpMn(CO)_3$ and $CpRe(CO)_3$ have been studied in alkanes and silanes by time-resolved spectroscopy. We have expanded on the previously studied reaction of $CpMn(CO)_3$ in heptane doped with triethylsilane by

studying the effects of varying the concentration of triethylsilane. On photolysis at 266 nm, the intermediate $CpMn(CO)_2$(heptane) decays to form the final photoproduct: 'partially activated' $CpMn(CO)_2H(SiEt_3)$. Increasing the concentration of triethylsilane led to a shorter lifetime of the intermediate $CpMn(CO)_2$(heptane). We measured the lifetime of this intermediate at five different concentrations of triethylsilane (30–240 mM) to afford the Stern–Volmer constant. This information will be key for future time-resolved X-ray absorption experiments.

We have also studied the corresponding reaction with $CpRe(CO)_3$. Previous studies had not been able to discern whether doping triethylsilane in heptane leads to production of a $CpRe(CO)_2$(heptane) intermediate which then forms the final photoproduct $CpRe(CO)_2H(SiEt_3)$, as $CpRe(CO)_2$(heptane) was too long-lived at the studied timescale and triethylsilane concentration to see its decay on the nanosecond timescale. We have increased the concentration of triethylsilane in this reaction to 2 M, to confirm that indeed, photolysis of $CpRe(CO)_3$ in triethylsilane doped heptane results in formation of $CpRe(CO)_2$(heptane) which decays to form $CpRe(CO)_2H(SiEt_3)$. Again, we have monitored this reaction at different concentrations of triethylsilane (2–5 M), finding that increasing the concentration results in a decreased lifetime of the intermediate $CpRe(CO)_2$(heptane).

In these studies, we have observed an as yet unobserved phenomenon in the photochemical reactions of $CpRe(CO)_3$, in that the ν(CO) peaks of the intermediate $CpRe(CO)_2(X)$ (X = $SiHEt_3$ or C_7H_{16}) appear to shift by 1–2 cm^{-1}. We have investigated this further by studying the reactions of $CpRe(CO)_3$ in a series of linear and cyclic alkanes, namely *n*-heptane, *n*-hexane, *c*-hexane, *n*-hexane-d_{14} and *c*-hexane-d_{12}. In all linear alkanes we saw a $\sim$1 cm^{-1} blueshift in the ν(CO) of the photoproducts, $CpRe(CO)_2$(alkane), whilst in cyclic alkanes, we observed no such shift. In deuterated hexane, we saw no significant change in the magnitude of the shift compared to non-deuterated hexane. We tentatively assigned this shift as a change from η^1 to η^2 bonding in both the silane and alkane complexes.

Time-resolved X-ray absorption spectroscopy has been used to study the reaction of $CpRe(CO)_3$ in triethylsilane. Preliminary results show that upon photolysis, there was a redshift in the absorption edge, indicative of an increase in electron density. We also saw a redshift in the absorption edge between 1–2 μs and 4–5 μs, supporting observations of a 2 cm^{-1} blueshift in the ν(CO) of the intermediate seen in the infrared. This is further evidence to support our assignment of a shift from η^1 to η^2 bonding.

Chapter 5

In this Chapter, we have studied the effect of temperature on the photophysical and photochemical reactions of $[Re(CO)_4(bpy)][PF_6]$ in dichloromethane (dcm) and acetonitrile (acn). Beginning by repeating previous work, we found that two excited states were formed upon photolysis, 'State I' and 'State II', the latter of which decayed to form the CO loss photoproduct, $[Re(CO)_3(bpy)(X)][PF_6]$ (X = CH_2Cl_2 or CH_3CN), agreeing with previous works. We have found evidence for a difference in the reactivity between the excited states in the different solvents at room temperature.

Performing the ns-TRIR at a series of temperatures between 5 and 35 °C in dichloromethane, we have found that temperature has no effect on the lifetimes of the excited states. There was a slight increase in photoproduct formation at 30 and 35 °C; however, there was no trend at lower temperatures. In contrast, in ns-TRIR experiments performed at a series of temperatures between 15 and 55 °C in acetonitrile, we found the excited state lifetimes showed a high dependence on temperature. Remarkably, the lifetime of 'State I' *increased* with temperature. Additionally, there was a clear increase in photoproduct production coupled with a decrease in the reformation of the parent as the temperature was increased. Therefore, we have hypothesised that the CO loss state is thermally accessible from State I in acetonitrile.

High level density functional calculations have been used to elucidate the reaction in the different solvents. Calculations indicate the formation of three excited states; $^3(ILCT_1)$, $^3(MLCT_1)$ and $^3(MLCT_2)$. The $^3(ILCT_1)$ can be confidently assigned as 'State I', as seen

in ns-TRIR experiments. In dichloromethane, the calculations indicate that the CO loss photoproduct $[Re(CO)_3(bpy)(CH_2Cl_2)][PF_6]$ is formed from solely the $^3(MLCT_1)$ state, whereas in acetonitrile, $[Re(CO)_3(bpy)(CH_3CN)][PF_6]$ may be formed by both $^3(MLCT_1)$ and $^3(MLCT_2)$. The nature of $^3(MLCT_1)$ and $^3(MLCT_2)$ also appears to change between solvents.

Calculations have further revealed that the accessibility of the $^3(MLCT_1)$ state varies between the two solvents. Analysis of the Marcus parabolas calculated for both solvents show a remarkably different picture. In dichloromethane the Marcus parabola exhibits inverted character, whilst in acetonitrile, the parabola shows normal character, therefore explaining the excited state lifetime's dependence on temperature, or lack thereof. Additionally, estimations of the transition state energies of the $^3(ILCT_1)$ to $^3(MLCT_1)$ transition show that in dichloromethane, the transition state may lie at high energy, resulting in a large activation barrier. In acetonitrile, the transition state occurs at lower energy; therefore, transfer from 'State I' to the CO loss state is more favourable. This supports experimental observations of an increase in photoproduct production at higher temperatures.

Chapter 6

The experimental methods, spectroscopic apparatus and techniques used throughout this thesis are outlined in this Chapter.

Acknowledgments

First and foremost, I would like to thank my supervisor Professor Mike George. Without his insight, guidance and calming reassurance during difficult times this wouldn't have been possible. Thank you for the opportunities you have given to me and thank you for believing in me.

I owe a great deal of thanks to Drs. Surajit Kayal and Xue-Zhong Sun for their vital role in the time-resolved infrared experiments in Nottingham. Surajit's encyclopedic knowledge in particular has been invaluable. Another key person who helped me at the very start of my PhD is Dr Xue Wu, without whom this thesis would be empty, so thank you for your incredible patience and teaching me everything you know. An extra special thank you must go to Drs. Ashley Love and Katherine Reynolds, for always being there to answer any question or provide insight—a particular thanks to Katie for sharing with me all her knowledge on rhenium photophysics.

I'd like to thank Edward Bowman for all his help with X-ray absorption experiments and for his excellent company on late nights during beamtime. I also would like to extend a thank you to Professor Andrew Dent and Dr Stuart Bartlett of the Diamond Light Source for sharing their vast knowledge and experience. Additionally, thanks to Drs. Xiaoyi Zhang and Jin Yu and Mr Rick Spence of the APS for their invaluable assistance. Thanks to our collaborators Dr Stefan Kupfer and Mr Alexander Schwab at Freidrich Schiller University for their calculations and specifically for their insightful inputs and patience with my questions.

No one could have foreseen when I started this journey in 2018 how the world would change in the next four years, but there was truly no better place to be during testing times. To all past and present members of the George/Poliakoff group (there are too many to name), thank you for all the cakes in Sue's, for the jokes in the Fort, for the tea breaks on

Zoom, for the socially distanced lunches and for finally being there for the new normal.

Last but not least, a very special thank you to all my friends and family, who have kept me sane. To my friends in particular, thanks for never changing and being a constant source of laughter. Finally, Mum, you have provided unwavering support to me throughout my whole life, through the good and the bad, you are my rock.

Thank you.

Abbreviations

Abs . . . . . absorbance

acn . . . . . acetonitrile

BDE . . . . . bond dissociation energy

Bp . . . . . bis(pyrazolyl)borate

Bp* . . . . . bis(3,5-dimethyl-pyrazolyl)borate

Bpm . . . . . bis(pyrazolyl)methane

Bpm* . . . . . bis(3,5-dimethyl-pyrazolyl)methane

bpy . . . . . bipyridine

Cp . . . . . cyclopentadienyl

Cp* . . . . . pentamethylcyclopentadienyl

dcm . . . . . dichloromethane

DFT . . . . . density functional theory

E_a . . . . . activation energy

EXAFS . . . . . extended X-ray absorption fine structure

fs, ps, ns, μs, ms . . . . . femto-, pico-, nano-, micro-, millisecond

FTIR . . . . . Fourier transform infrared

FWHM . . . . . full width at half maximum

HOMO . . . . . highest occupied molecular orbital

ILCT . . . . . intra-ligand charge transfer

IR . . . . . infrared

k$_{obs}$ . . . . . observed rate constant

LMCT . . . . . ligand-to-metal charge transfer

LUMO . . . . . lowest unoccupied molecular orbital

MCT . . . . . mercury cadmium telluride

^{3}**MLCT** . . . . . triplet metal-to-ligand charge transfer

MLCT . . . . . metal-to-ligand charge transfer

NMR . . . . . nuclear magnetic resonance

PFMCH . . . . . perfluoro(methylcyclohexane)

Tp . . . . . tris(pyrazolyl)borate

Tp* . . . . . tris(3,5-dimethylpyrazolyl)borate

Tpm . . . . . tris(pyrazolyl)methane

Tpm* . . . . . tris(3,5-dimethylpyrazolyl)methane

TRIR . . . . . time-resolved infrared spectroscopy

TR-EXAFS . . . . . time-resolved extended X-ray absorption fine structure

UV/Vis . . . . . ultraviolet/visible

XANES . . . . . X-ray absorption near edge structure

XAS . . . . . X-ray absorption spectroscopy

Δ**Abs** . . . . . change in absorbance

$\Delta\mathbf{G}^{\ddagger}$ . . . . . Gibbs free energy of activation

$\Delta\mathbf{H}^{\ddagger}$ . . . . . enthalpy of activation

$\Delta\mathbf{S}^{\ddagger}$ . . . . . entropy of activation

ν**(CO)** . . . . . carbonyl stretching frequency

τ . . . . . lifetime

Contents

Chapter 1

Introduction

Understanding how a reaction proceeds is vital to designing better and more efficient processes. The observation of reaction intermediates, providing key information about their structure or lifetime, can allow for a full understanding, and ultimately control, of a particular reaction. This is particularly true for transition metal chemistry, where applications range from the development of catalysts[1] and the manufacture of pharmaceuticals[2] to utilisation of sunlight for energy production.[3,4] This work focusses on the reactions of transition metal carbonyl complexes, where a loss of a carbonyl ligand is induced upon photochemical excitation. In the presence of a solvent, the reactive sixteen electron intermediate formed after carbonyl loss will likely coordinate with a solvent molecule. Depending on the nature of the solvent, and if there are any additives present in the solution, reaction intermediates and their kinetics can be quite varied. These intermediates are short-lived, typically having lifetimes on the ns–μs timescale,[5] but longer lifetimes on the millisecond timescale have been reported.[6] Detection of species with these short lifetimes is beyond the capabilities of conventional spectrometers; therefore, specialist methods are required.

1.1 Monitoring Reactive Intermediates

Two different but often complementary techniques can be employed to detect photochemically generated short-lived species. The first technique is to extend the lifetime of an intermediate using low temperature or matrix isolation. The second is to use a spectroscopic technique that can detect species on a timescale faster than which they decay. This approach is called time-resolved spectroscopy and is the technique employed most widely in this work; however, we will also give a brief introduction to the first technique.

1.1.1 Matrix Isolation and Low Temperature Solution Spectroscopy

Matrix isolation is one of two methods used to extend the lifetime of reactive intermediates in order to study them using conventional techniques such as FTIR. It was first developed in the 1950s, particularly in work by the Pimentel group.[7] The material of interest is trapped within an inert matrix host, which for example could be a frozen hydrocarbon glass,[8] noble gas[9] or polymer.[10] The theory behind matrix isolation is that any photochemically generated intermediates are trapped within the matrix material. This isolates the intermediates from other species, making further reaction less likely. When coupled with low temperature conditions, the lifetime of these intermediates are sufficiently lengthened to be able to perform conventional spectroscopic analysis.

There are, however, some drawbacks to matrix isolation. The first is that the technique is limited to certain types of reactions, for example, reactive intermediates to be studied must often be accessible by unimolecular processes.[11] Another drawback is that due to the presence of different guest sites within the matrix, there can be additional features in the IR spectrum; this is called the 'matrix splitting' effect.[12] The intermediate of interest may also react with the matrix material itself, for example, any remaining C=C double bonds in polyethylene. However, this can often be overcome by altering the matrix material used.

Carrying out the reaction in low temperature solution allows us to significantly lower the energy of any intermediate species and prolong their lifetime enough for the intermediate

to be analysed using conventional FTIR. It also eliminates the unimolecular reaction limitation, as intermediates are still able to diffuse through the solution. Low temperature solutions also have an advantage over matrix isolation in that there is no splitting of FTIR bands and kinetic information can be gained.[12]

1.1.2 Time-resolved Spectroscopy

The method used most widely in this work is time-resolved spectroscopy. Time-resolved spectroscopy is a 'pump–probe' method, in which the sample is 'pumped' with a UV source to excite the sample and a UV or IR 'probe' is used to track the intermediates and products of a reaction, Figure 1.1. This approach was created in Nobel Prize winning work by Norrish and Porter in the 1940s.[13]

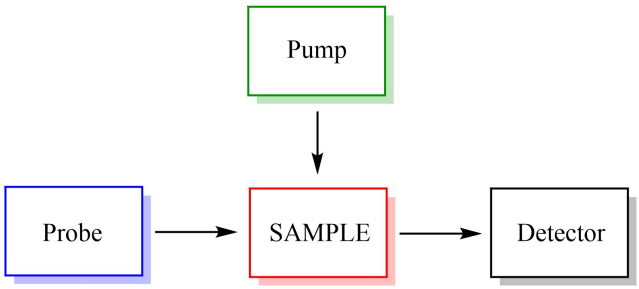

Figure 1.1: *A schematic of the basis of a pump–probe experiment used for fast and ultrafast time-resolved spectroscopy*

Norrish and Porter made use of a gas-discharge flash lamp, developed primarily for photography, to excite molecules. A second lamp, producing a much shorter flash, recorded the absorption spectrum of these excited molecules. The timings of these flashes were determined by a rotating wheel, and they were detected by photographic film, see Figure 1.2. Initial work included studies of the kinetics of HO radicals in a H_2–O_2–NO_2 system,[14] and also kinetics of ClO formation and decay in a Cl_2–O_2–N_2 system; identifying the ClOO radical intermediate.[15,16]

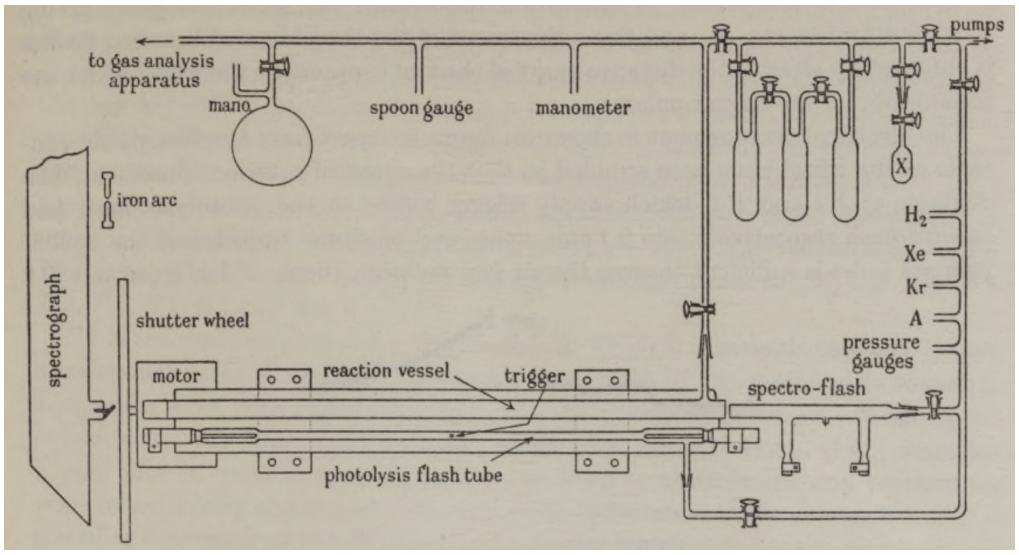

Figure 1.2: *A diagram of the original time-resolved spectroscopy experimental setup pioneered by Norrish and Porter, reproduced from reference 17*

1.1.2.1 Time-resolved Infrared Spectroscopy

Modifications of the original pump–probe experiment by Tanner and King[18] and later by Pimentel,[19] replaced the second UV flash lamp with a rapid scan infrared spectrometer. This, named rapid scan spectroscopy, is the first example of infrared spectroscopy being used to monitor transient species. For these rapid scan methods, spectroscopic information was obtained by repeatedly firing the flash lamp and taking measurements at different time delays after each flash.[20] A modified IR spectrometer allowed for the rotating detector grating to be synchronised with the flash lamp. The time resolution of these methods was effectively limited by the time it takes for one full spectrum to be collected, limiting the minimum time resolution that could be achieved to a few milliseconds. Nevertheless, some significant breakthroughs were made with this equipment, including the observation of CF_2, CH_3 and CD_3 in the gas phase.[21–23] Setups of this type are no longer in use; succeeded by the commonplace rapid scan Fourier transform infrared (FTIR) spectroscopy.

A later development, called 'point-by-point' TRIR spectroscopy, measured the change in absorption with time at a specific wavelength after excitation. Repetition at a series of different wavelengths built a spectrum 'point-by-point', thus earning its name, see Figure

1.3. The original spectrometer, developed by Seibert, was used to detect the recombination of dissociated CO from carboxymyoglobin on the millisecond timescale.[24] This technique was refined further by Schaffner and co-workers, who used it to probe the reaction of a number of metal carbonyl complexes with alkanes at room temperature with microsecond resolution.[25–27]

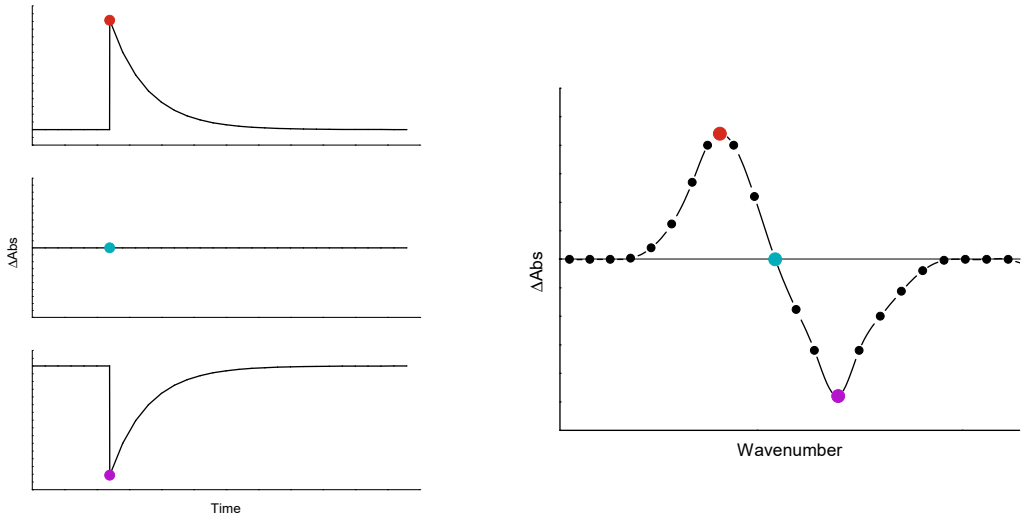

Figure 1.3: *An example of how a TRIR point-by-point spectrum is built by plotting the change in absorbance against wavenumber for any specified time delay*

Point-by-point TRIR spectroscopy is limited by the response time of the detector, and fast MCT detectors have improved the time resolution to nanosecond levels. Furthermore, with the advent of continuous wave (cw) and quantum cascade lasers (QCL) as replacements for the IR source, time resolution could be improved even further.[28] However, to realise subnanosecond, or 'ultrafast' resolution, an altogether different approach must be used.

1.1.2.2 Ultrafast Time-resolved Infrared Spectroscopy

Time-resolved spectroscopy with sub-nanosecond time resolution is referred to as ultrafast time-resolved infrared spectroscopy. In order to achieve such time resolution, ultrafast pulsed lasers must be used. An example of an ultrafast system is shown in Figure 1.4.

In this example the pump and probe beams come from difference sources; however, in many cases there may only be a single seed beam which is split, thus allowing the individual beams to be changed to the required frequency by optic parametric amplification (OPA). The probe pulse is delayed with respect to the pump pulse and a difference spectrum is recorded at this specific time delay. This process is repeated at different time delays. Generally, the delay is achieved by using a delay line for the pump beam, which alters the distance the pump beam must travel before reaching the sample, and consequently the time it takes to reach the sample (0.3 mm = 1 ps). The pump and the probe beams meet at the sample, with every second pump beam blocked by a chopper so that a difference spectrum can be obtained by subtracting the 'pump-off' signal from the 'pump-on' signal. Under continuous irradiation, the sample is likely to degrade, causing precipitation of photoproduct on the cell windows; therefore, the sample cell is rastered. In addition to this, the sample solution is continuously refreshed by circulating from a sample reservoir. At first, ultrafast TRIR experiments employed the use of narrowband IR probe pulses, in a similar fashion to the earlier 'point-by-point' approach.[29] However, it is now more common to use broadband IR probe pulses (100–500 cm^{-1} FWHM) which can probe component IR wavelengths simultaneously.

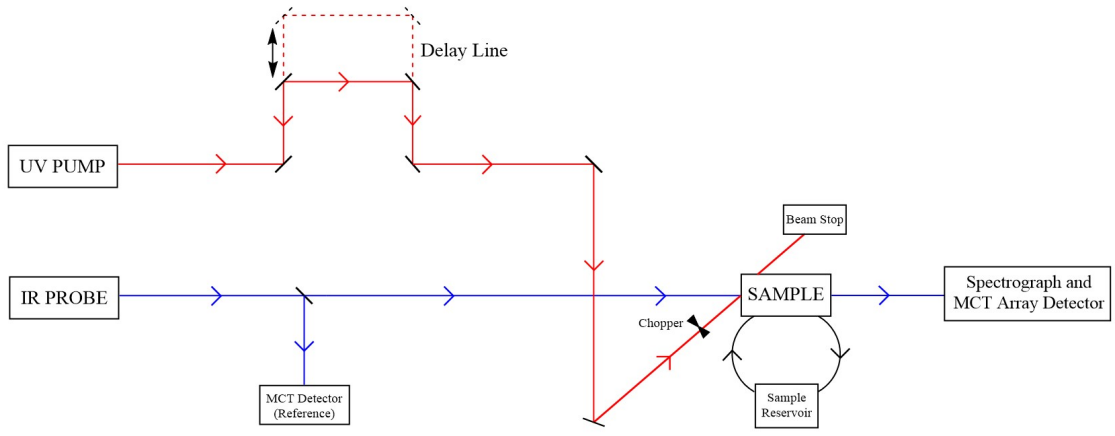

Figure 1.4: *An example of a typical ultrafast TRIR setup*

Improvement of ultrafast pulsed lasers means that modern systems, with time resolution limited only by the laser pulse width, can achieve resolution on the femtosecond

timescale.[30] Their high power also enables greater concentrations of transient species to be excited, enabling easier detection.[31] However, this technique comes with a drawback in that it is limited spatially by the length of the delay line, for example, delays of up to 3 ns require a delay line of 90 cm. Therefore, for monitoring delays on the nanosecond timescale and above, it is common to use a ns pump laser and control the time delay electronically.

A detailed description of the TRIR setup used in this thesis can be found in Chapter 6.

1.2 Photochemistry of Organometallic Complexes

1.2.1 Organometallic Alkane Complexes

Alkanes are attractive as precursors for the chemical industry because they are the main constituents of oil and natural gas.[32] Currently alkanes are predominantly used in combustion reactions to generate energy. These reactions are conducted at high temperatures (300–500 °C) and have low selectivity. This process also produces carbon dioxide and water, two economically and, in the case of carbon dioxide, environmentally undesirable products. Therefore, the lure of a new process, one that is conducted under mild conditions and can selectively turn alkanes into valuable alcohols, ketones, carboxylic acids and so on, proves considerably attractive. If this key reaction were realised, then alkanes could present a cheaper, cleaner and more abundant feedstock for the petrochemical industry. However, the high stability and inert nature of C–C and C–H bonds in hydrocarbons presents a challenge to achieving this goal. One answer to this is the process of C–H activation by transition metal complexes. Activation of a C–H bond involves the introduction of different functional groups into the molecule, i.e., substituting a C–H for a C–X, where X could be nitrogen, oxygen or a carbon from another molecule.[33]

The first example of a direct observation of C–H activation by a transition metal complex was reported separately by two groups in the early 1980s.[34,35] Both groups reported that two related complexes of iridium pentamethylcyclopentadienyl (Cp*Ir) could

activate the C–H bonds of alkanes upon irradiation with UV light. Subsequently, many examples of transition metal complexes activating alkanes by photochemical means have been reported, predominantly by group VII–X metals.

The mechanism of photochemical C–H activation by transition metal complexes has been widely discussed. UV light causes dissociation of a ligand to form a coordinatively unsaturated sixteen electron intermediate. Many postulate that the key second intermediate is a transition metal–alkane complex, a so called 'σ-complex', in which the metal centre is bound to the C–H σ-bond, as detailed in Figure 1.5. A more in-depth introduction into σ-complexes will be given in Chapter 4.

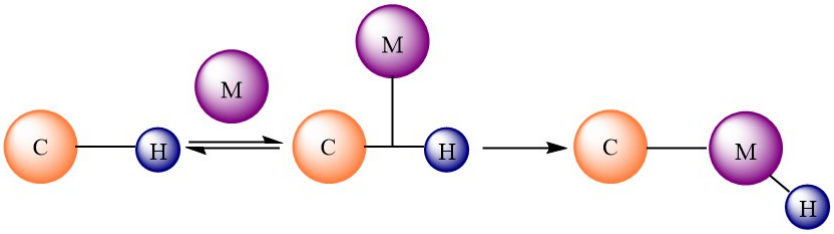

Figure 1.5: *Proposed mechanism for C–H activation, involving the key 'σ-complex' intermediate. A metal binds weakly to the C–H bond in an equilibrium process, then inserts into the bond. Adapted from reference 33*

Alkanes do not possess the qualities of a good ligand; therefore, coordination of an alkane to a metal centre as seen in σ-complexes is somewhat unexpected. The alkane's low-lying HOMO and high energy LUMO make for both a poor electron donor and acceptor.[36] Nevertheless, alkane σ-complexes have been observed, but naturally are extremely short-lived, with lifetimes typically on the ps–ns timescale at room temperature and pressure.

The first alkane complexes were characterised by Perutz and Turner when they identified the formation of $Cr(CO)_5(CH_4)$ following photolysis of $Cr(CO)_6$ in cryogenic matrices at 12 K.[37] Evidence of this coordination came from the shift in UV/Vis absorbance maximum and IR ν(CO) positions. The first alkane complex to be observed at room temperature in solution was $Cr(CO)_5$(cyclohexane) by Kelly *et al.*,[38] who showed that complexation of cyclohexane to $Cr(CO)_5$ occurred within 50 ns. Much later studies have shown, however, that this complexation actually occurs within the first picosecond after photolysis.[39,40]

Subsequently, many alkane complexes have been characterised at room temperature in solution, all with varying stabilities. There are several variables that can impact the lifetime of the alkane σ-complex, including both the nature of the metal and the alkane. On moving from Group V to Group VII metals, the reactivity of the alkane complex decreases, for example, manganese–alkane complexes typically have a lifetime of over 2 orders of magnitude larger than those of vanadium. Furthermore, metal alkane complexes become less reactive upon descending the group. Consequently, Re–alkane complexes are often the longest lived, see Figure 1.6.[41]

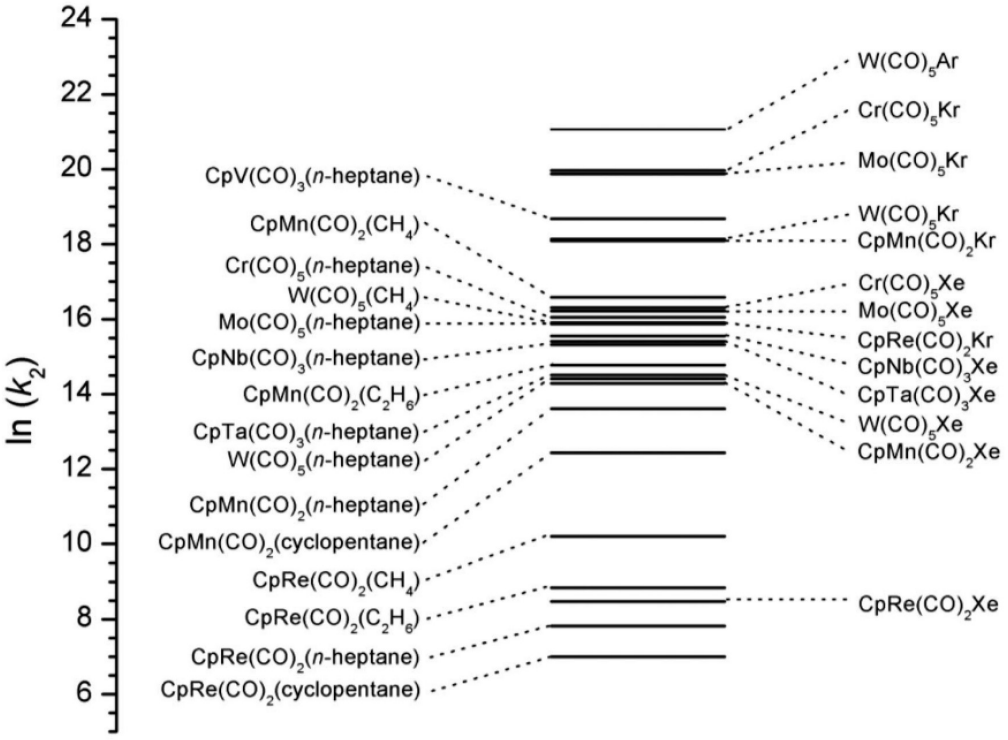

Figure 1.6: *Values of ln(k) for the reaction of a series of organometallic alkane and noble gas complexes with CO at 25 °C, reproduced from reference 41*

As for the alkane, studies have shown than cyclic alkanes form more stable complexes than their linear counterparts,[42,43] while short chain alkanes such as methane have shown a much weaker bonding to the metal compared to those with longer chains.[44,45]

The longest measured lifetime of a σ-complex at room temperature and pressure is that of $CpRe(CO)_2$(cyclopentane), which has a lifetime of 125 ms at room temperature and ~1 hour at 180 K,[42] long enough at low temperature to be characterised by NMR

spectroscopy.[46] Only a handful of metal alkane complexes have been found to be long-lived enough to be characterised by low temperature NMR, these are predominantly rhenium alkane complexes, although several manganese[47,48] and even tungsten,[49] rhodium[50,51] and iridium[51] complexes have been observed.

These NMR experiments were able to reveal in more detail the nature of the binding mode of the alkane to the metal centre. In the first reported NMR study of an organometallic alkane complex, for the above-mentioned $CpRe(CO)_2$(cyclopentane), the authors were able to observe that the alkane bound complex exists in a rapid equilibrium between η^2-C,H and η^2-C,H', Figure 1.7(a).[46] A second ^{1}H NMR study by Lawes *et al.* on the binding of linear alkanes showed that, upon photolysis, the $^{iPr}CpRe(CO)_2$ fragment was bound to all three different types of pentane C–H bonds, with a slight preference for the secondary and tertiary CH_2 units, as opposed to the terminal CH_3 units, Figure 1.7(b).[52]

This preference was deduced from integration of the resonances due to **1**, **2** and **3** (Figure 1.7) giving a ratio of 6:6.07:2.90, respectively. This, compared to the theoretical ratio of 6:4:2, demonstrated a slight favouring of the CH_2 sites. Furthermore, at any one instant, the bonding was found to be primarily through one particular C–H bond, which then rapidly exchanged between the other C–H bonds in the chain.

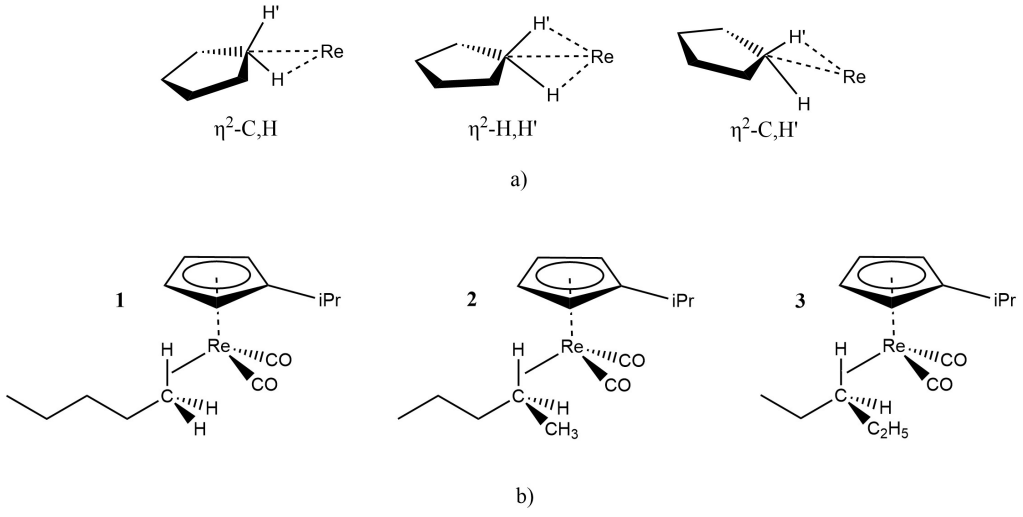

Figure 1.7: *a) Representation of the different binding modes of cyclopentane to the metal centre, in this case Re, adapted from reference 46, and b) Terminal (**1**), secondary (**2**) and tertiary (**3**) bonding of n-pentane to $CpRe(CO)_2$, adapted from reference 52*

In an NMR study of (HEB)W(CO)$_2$(pentane) (HEB = η^6-hexaethylbenzene), conducted by Young *et al.*, it was observed that only the terminal CH_3 units were bound to the metal, contrary to the study of CpRe(CO)$_2$(*n*-pentane). They found that binding through the CH_2 groups involves the pentane adopting an unfavourable gauche conformation. This is an important observation as it implies that tailoring of the metal complex can manipulate the site at which the ligand bonds, leading to the potential for regiospecific alkane functionalisation in the future.[49]

A small handful of X-ray crystallography studies have also been performed on metal σ-complexes, the structures of which are shown in Figure 1.8. The first reported structure was of coordination of heptane to an iron porphyrin: Fe(DAP)(*n*-heptane), where DAP = double A-frame porphyrin (**1**, Figure 1.8).[53] Due to structural disorder, they were unable to completely quantify the Fe–alkane interaction; however, they were able to deduce the Fe–C bond distances (2.5 and 2.8 Å), which are within the accepted range for agostic interactions. The second, reported by Castro-Rodriguez *et al.*, reported a number of cycloalkanes bonding to a U(III) metal centre (**2**, Figure 1.8).[54] For all structures, the complexes favoured an η^2-C,H bonding mode. Both of these complexes are thought to be stabilised by a host–guest interaction, though neither were stable on solvation.

In a considerable breakthrough, the crystal structure of a Rh–alkane complex was reported in Nature by Pike *et al.*, that of [Rh(^{i}Bu$_2$PCH$_2$CH$_2$P^{i}Bu$_2$)(C$_7$H$_{12}$)][BAr$_4^F$], Complex **3** in Figure 1.8.[55] By generating the Rh(I) alkane complex directly by a solid–gas reaction, they were able to avoid decomposition of the short lived alkane complexes in solution. Again, the Rh–C bond lengths (2.494 and 2.480 Å) were indicative of Rh–C agostic interactions. In this complex, the alkane was interacting with the metal centre through two C–H σ-bonds, and similar to the two previous studies, the authors hypothesised that the complex was stabilised through host–guest interactions.

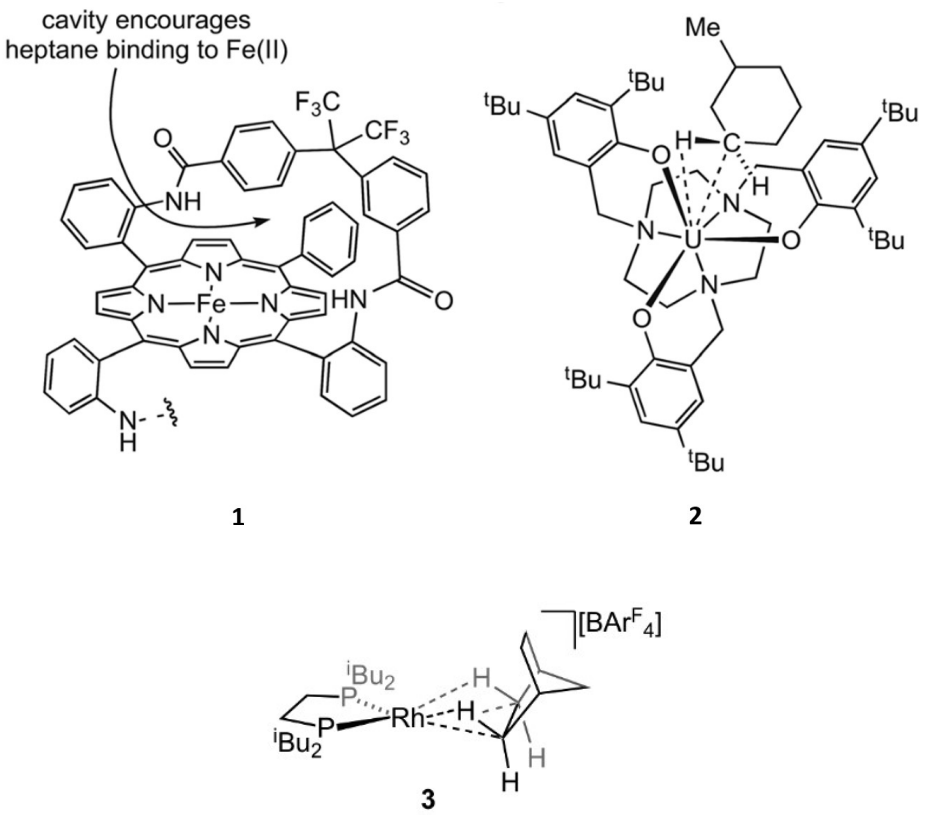

Figure 1.8: *Previously characterised σ-complexes in the solid state; 1) Fe(DAP)(n-heptane), where DAP = double A-frame porphyrin, 2)[((ArO)$_3$tacn)U(C_n)].(cy-C_n), where Ar = 3,5-di-tert-butyl-2-hydroxybenzyl, tacn = triazacyclononane and here C_n = methylcyclohexane, and 3) [Rh(^{i}Bu$_2$PCH$_2$CH$_2$P^{i}Bu$_2$)(C_7H_{12})][BAr$^F_4$]. Reproduced from reference 55*

In another exciting development in later work by the same group, the structure of an η^1 bound alkane complex, [Rh($Cy_2P(CH_2)_5PCy_2$)–COA][BAr$^F_4$] (Cy = cyclohexyl and COA = cyclooctane), see Figure 1.9, was characterised in the solid state.[56] Again, by directly synthesising the complex in a solid–gas single crystal to single crystal reaction, they were able to avoid the complex decomposing in solution. The Rh–H–C bond angle was measured to be 141°, clearly indicating an η^1 interaction. These experimental measurements were supported by DFT calculations. This is an important demonstration of how sterics can constrain the binding mode of the alkane and of how η^1 complexes can be stabilised.

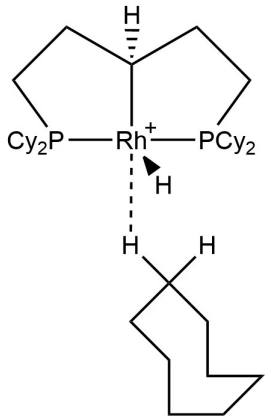

Figure 1.9: *Structure of the cation of [Rh($Cy_2P(CH_2)_5PCy_2$)–COA][BAr^F_4] (Cy = cyclohexyl and COA = cyclooctane), an η^1 bound alkane σ-complex characterised in the solid state, adapted from reference 56*

A relatively new technique in the field of studying metal σ-complexes is time-resolved X-ray absorption spectroscopy (TR-XAS). TR-XAS is an incredibly useful technique because it can be used to measure structural information in solution, in contrast to traditional X-ray crystallography measurements which require a crystalline solid sample. This is ideal for transition metal alkane complexes, which often do not exist and/or are incredibly short-lived in the solid state. As concluded by previous NMR studies, on binding to the metal centre, the alkane can rapidly switch between carbons within the chain, a process referred to as 'chain walking'. A combined TRIR and TR-XAFS study was used to analyse the reaction of $W(CO)_6$ with *n*-heptane and other weakly binding ligands.[57] The authors experimentally determined the W–C bond length as 3.07 Å, which was longer than the DFT calculated value for W–C on binding to the primary C–H (2.86 Å), but shorter than the corresponding value on binding to the secondary C–H (3.12 Å). The statistical average of all calculated W–C bond lengths (3.02 Å) was much more comparable to the experimental value of 3.07 Å, leading them to conclude that there is indeed chain walking occurring between the primary and secondary carbons of *n*-heptane in solution. A more in-depth introduction to XAFS and TR-EXAFS will be given in Chapter 4.

1.2.2 Organometallic Noble Gas Complexes

The chemistry of the noble gases is generally relatively limited; their full outer shell of electrons leads to highly stable atoms. Out of all the noble gases, only radon, krypton and xenon have been shown to form compounds with other atoms. The majority of the compounds formed by noble gases are with highly electronegative fluorine and oxygen. However, even with their high stability, noble gases have been shown to act as ligands, binding to reactive sixteen electron transition metal intermediates.

The study of organometallic noble gas complexes often goes hand in hand with those of organometallic alkane complexes, going back to when they were first studied together in early matrix isolation flash photolysis experiments.[37,58,59] The first observation of a noble gas transition metal complex was described by Perutz and Turner, when $Cr(CO)_6$ was photolysed in a range of matrices at 12 K to form $Cr(CO)_5L$ (L = Ar, Kr, Xe and CH_4).[37] Much of their early work revealed detailed information into the reactivity of group VI hexacarbonyls in inert matrices.[60,61] Many other noble gas complexes of Ar, Xe and Kr were characterised by matrix isolation, including $Fe(CO)_4Xe$,[62] (dfpe)$Cr(CO)_3X$ (dpfe = $(C_2F_5)_2PCH_2CH_2P(C_2F_5)_2$ and X = Ar or Xe),[63] $Ru(CO)_2(PMe_3)_2X$ (X = Ar or Xe)[64] and $Ru(CO)_2$(dmpe)(X) (dmpe = $Me_2PCH_2CH_2PMe_2$ and X = Ar or Xe).[65] While matrix isolation was a vital early tool in characterising these complexes, it was also important to investigate their solution phase reactivity and kinetics.

The first solution phase observation of an organometallic noble gas complex was reported by Simpson and coworkers.[59] Photolysis of $Cr(CO)_6$ in *liq*Xe gave the complex $Cr(CO)_5Xe$, which was found to be surprisingly long-lived (τ = 2 s at –98 °C). Other complexes characterised in liquid noble gas solution include $M(CO)_5L$ (M = Cr, Mo or W and L = Ar, Kr, Xe),[60] $CpM(CO)_2(L)$ (M = Mn or Re and L = Kr or Xe),[42,66] $CpM(CO)_3Xe$ (M = Nb or Ta)[67] and Cp'Rh(CO)(L) (Cp' = Cp or Cp* and L = Kr or Xe).[68] The latter complex exhibits interesting chemistry in that CpRh(CO)Xe was found to be *ca.* 20 times less reactive than Cp*Rh(CO)Xe, with similar differences in reactivity found for CpRh(CO)Kr and Cp*Rh(CO)Kr. This is in stark contrast to early

transition metal complexes, where for example $CpRe(CO)_2Xe$ and $Cp^*Re(CO)_2Xe$ have similar reactivities. Further investigations into the reaction mechanism suggested that the reaction of Cp'Rh(CO)Xe with CO proceeds via an associative mechanism, in contrast to their early transition metal counterparts.[68]

Recent advancements mean that noble gas complexes can now be seen at room temperature in supercritical fluids; TRIR has been used to characterise several complexes including $M(CO)_5L$ (M = Cr, Mo or W and L = Ar, Kr, Xe).[69] Supercritical fluids are unique in that they possess both properties of a liquid and a gas, for this purpose they are useful in that they have the liquid-like ability to dissolve the metal complex but also are completely miscible with other gases, allowing study of transition metal reactions in solution with dissolved gases.[70] Moreover, changes in temperature or pressure can 'tune' their physical properties, such as their density or viscosity.

The reactivities of transition metal noble gas complexes $Cp'M(CO)_x(L)$ and $M(CO)_5(L)$ are summarised in Figure 1.10, clearly showing $Cp'Re(CO)_2(Xe)$ (Cp' = Cp or Cp*) as the most stable organometallic noble gas complexes. The figure also demonstrates that Xe complexes are always more stable in comparison to Kr and Ar complexes. In fact, Xe complexes are far more comparable in stability to their analogous alkane complexes. However, not all complexes can be compared to their alkane counterparts. While CpRh(CO)Xe was shown to be the most stable noble gas complex following the rhenium complexes, living on the microsecond timescale, its analogous alkane complexes are much less stable as they undergo the secondary process of C–H activation. For example, $CpRh(CO)(C_6H_{12})$ lives for just nanoseconds, the C–H bond being activated to form $CpRh(CO)(C_6H_{11})(H)$.[71]

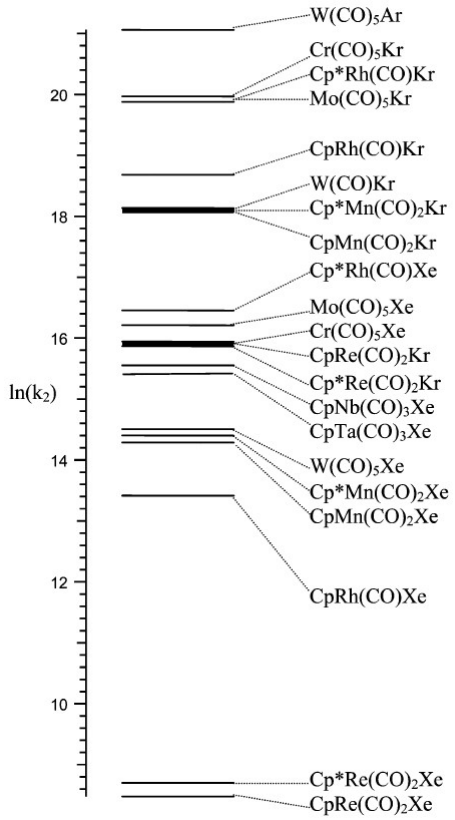

Figure 1.10: *Values of ln(k) for the reaction of a series of organometallic noble gas complexes Cp'M(CO)$_x$(L) and M(CO)$_5$(L) with CO, reproduced from reference 68*

The marked stability of $CpRe(CO)_2(Xe)$ identified the complex as an excellent candidate for NMR study. Ball *et al.* designed an altered form of $CpRe(CO)_3$ by introducing an ^{i}Pr group attached to the cyclopentadienyl ligand and replacing a CO with CF_3 to form $(^{i}PrCp)Re(CO)_2(PF_3)$.[72] In doing this, two things were achieved; the complexes' solubility in *sc*Xe was increased, and two NMR active nuclei were introduced in the form of ^{19}F and ^{31}P. Photolysis of this complex in supercritical Xe led to two photoproducts: $(^{i}PrCp)Re(CO)_2Xe$ and $(^{i}PrCp)Re(CO)(PF_3)Xe$. For the latter complex, the chemical shift of Xe (δ(Xe) = −6179 ± 3 ppm), showed a significant difference (between 719 and 1044 ppm) from free Xe. Using ^{129}Xe as the solvent caused a split in the ^{19}F and ^{31}P signals ($^{2}J_{XeP}$ = 41.8 ± 1 Hz and $^{3}J_{XeF}$ = 5.1 ± 0.8 Hz). These observations of coupling to Xe are important because they proved that the Xe ligand was not rapidly interchanging with free Xe in solution. All these observations from the NMR experiments are key indications of a metal–ligand interaction between Re and Xe. This remains the only NMR study of an

metal–xenon bond to date.

There also is only one reported X-ray crystal structure of a transition metal–noble gas complex; that of $[AuXe_4][(Sb_2F_{11})_2]$ shown in Figure 1.11.[73] Stable up to −40 °C, and even stable at room temperature in solution under a Xe pressure of 10 bar, isolation of this complex presented a major breakthrough in the study of transition metal noble gas complexes. The square planar $[AuXe_4]^{2+}$ cation contains four covalent Au–Xe bonds, with bond lengths ranging from 2.728 to 2.750 Å. A series of DFT calculations estimated the Au–Xe bond dissociation energy (BDE) to be 199 ± 49 kJmol^{-1}.

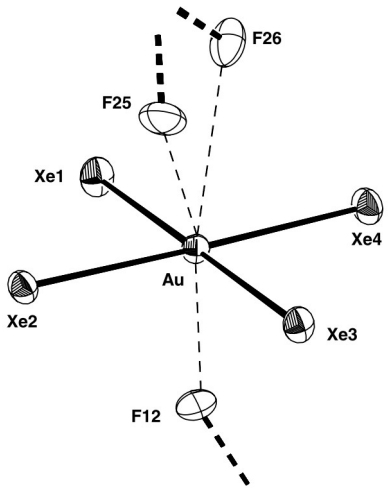

Figure 1.11: *Crystal structure of the cation $[AuXe_4]^{2+}$, reproduced from reference 73*

The study of organometallic alkane and noble gas complexes is intrinsically linked as they are both weakly bonding in nature. Xenon, in comparison with the other noble gas complexes, forms the most stable organometallic complexes and studies have found that the rate constants for a series of Xe complexes were very similar to those of their corresponding alkane complexes. For example, $CpRe(CO)_2(Xe)$ is only 2× more reactive towards CO in supercritical Xe compared to $CpRe(CO)_2$(*n*-heptane) in *n*-heptane solution.[41] In the same TR-XAFS experiments described in Section 1.2.1, the W–Xe bond length for the complex $W(CO)_5(Xe)$ was experimentally determined to be 3.10 Å, incredibly similar to the W–C bond lengths in $W(CO)_5$(*n*-heptane) (3.07 Å).[57] Moreover, for a vast range of studied complexes, Xe followed the same trends in reactivity as corresponding alkane complexes.

The comparison of the two weakly bonding ligands is important in understanding the trends of both complexes.

It is important to discover more long-lived transition metal alkane and xenon complexes so that more in-depth analyses of these complexes can be made through techniques such as NMR and X-ray crystallography. All these studies of alkane σ-complexes are imperative in understanding the C–H activation reaction. In addition to revealing information about the structure of any intermediates, they can also provide insight into the mechanism and rate of reaction, by measuring changes in absorption of reactive intermediates with time.

1.2.3 Activation Parameters

Using techniques such as time-resolved infrared spectroscopy has been incredibly useful in determining the lifetimes of reactive intermediates. One can additionally monitor the change in lifetime of a particular species with temperature, to determine important parameters such as activation energy, E_a, enthalpy of activation, $\Delta H^{\ddagger}$, and entropy of activation, $\Delta S^{\ddagger}$. These are determined by analysis of the Arrhenius and Eyring equations, see Equations 1.1 and 1.2, respectively. These values can not only give an indication of the bond strength between the transition metal and alkane or noble gas by analysis of E_a and $\Delta H^{\ddagger}$ values, but the value of $\Delta S^{\ddagger}$ can also shed light on the reaction mechanism. In general, negative $\Delta S^{\ddagger}$ values are indicative of an associative reaction mechanism and a positive $\Delta S^{\ddagger}$ implies a dissociative mechanism, whilst values that are only slightly negative/positive may reflect an interchange mechanism. However, these values must be taken with a pinch of salt, as the equation does not include contributions from other effects such as the electrostriction effect.[74] In addition, there are large errors in $\Delta S^{\ddagger}$ associated with the extrapolation of data.

$$k = Ae^{\frac{-E_a}{RT}} \tag{1.1}$$

$$k = \frac{k_B T}{h} e^{\frac{-\Delta H^{\ddagger}}{RT}} e^{\frac{\Delta S^{\ddagger}}{R}} \tag{1.2}$$

However, many valuable insights can be taken from calculations of activation parameters. Long and coworkers investigated the rate of reaction of $Cr(CO)_2(\eta^6$-arene)–(alkane) with CO and found that the value of $\Delta H^{\ddagger}$ did not change upon variation of the bonded alkane.[43] They concluded that the difference in rates of reaction of $Cr(CO)_2(\eta^6$-arene)–(alkane) with CO for different alkanes could be explained by variation in values of $\Delta S^{\ddagger}$. The Cr–alkane bond dissociation energy, 50 ± 5 kJmol^{-1},[75] previously calculated by photoacoustic calorimetry (PAC), was double the calculated value for $\Delta H^{\ddagger}$ (24 ± 2 kJmol^{-1}). Later work by this group found similar reactivity trends for the reactions of $M(CO)_5$(alkane) (M = Cr, Mo and W) and Mo(η^6-arene)$(CO)_2$(alkane) with CO, with again $\Delta H^{\ddagger}$ remaining constant and the reactivity dependent on $\Delta S^{\ddagger}$.[76]

Work in our group has also investigated the metal–Xe reaction kinetics. The activation parameters for $CpM(CO)_2(X)$, where M = Mn or Re and X = alkane or Xe, were calculated and it was shown that the alkane complexes react with CO with an associative mechanism while contrastingly, the Xe complexes showed dissociative behaviour.[42,66] However, in a study by Jina *et al.*, it was suggested that late transition metal noble gas complexes may react with a different mechanism, as the reaction of Cp'Rh(CO)(Xe) (Cp' = Cp or Cp*) with CO showed significant associative behaviour, in stark contrast to the reaction of Cp'$Re(CO)_2$(Xe) with CO.[68] They found much lower $\Delta H^{\ddagger}$ values for the reactions of Cp'Rh(CO)(Xe) ($\Delta H^{\ddagger}$ = 15.2 and 4.6 kJmol^{-1} for Cp and Cp*, respectively) compared to Cp'$Re(CO)_2$(Xe) ($\Delta H^{\ddagger}$ = 47.2 and 43.9 kJmol^{-1} for Cp and Cp*, respectively).

These studies showing the different mechanism of reaction between early and late transition metals and also between alkanes and noble gases highlight that there is still much to uncover in their reactivity.

Chapter 2

Time-resolved Infrared Investigations into Reactions of Transition Metal Scorpionate Complexes with Weakly Coordinating Ligands

2.1 Introduction

Scorpionates are a group of ligands discovered by Trofimenko in the late 1960s and compounds containing these ligands are the focus of study in this chapter. The general structure of a scorpionate ligand is shown in Figure 2.1.

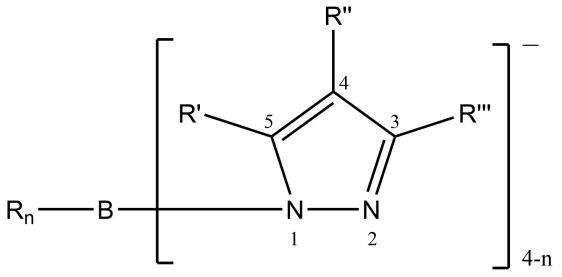

Figure 2.1: *General structure of a scorpionate ligand, $[R_nB(pz)_{4-n}]^-$, where n can be 0, 1 or 2 and R can be H, an aryl or an alkyl group, adapted from reference 77*

The ligand is chelating and can coordinate to the metal through N2 on each pyrazole group. The positions at 3, 4 and 5 can be substituted with alkyl or aryl substituents, giving rise to a vast array of structural variations, allowing for fine tuning of the compounds steric and electronic features.[77] Consequently, a vast library of works investigating these compounds has amassed, detailing the various properties and applications of scorpionates, some of which include enzyme modelling[78,79] and catalysis.[80,81] The nomenclature for these ligands generally obeys the following system; Bp/Tp$^{R',R'''}$, where Bp = bispyrazolylborate (n = 2) and Tp = trispyrazolylborate (n = 1). The most common ligands, Bp^{Me,Me} and Tp^{Me,Me}—the two that are studied in this Chapter—are often shortened to Bp* and Tp*, respectively.

The name 'scorpionate' was coined as a reference to the bonding mode of the ligand. The most common forms of scorpionate ligands, Tp$^{R',R''}$, contain three pyrazole groups. Almost always, two of these pyrazolyl groups are bound to the metal.[82] Comparatively, the nitrogen on the third pyrazolyl group is more weakly bound to the metal, and therefore can easily dechelate. This movement between tridentate (κ^3) and bidentate (κ^2) bonding is likened to the sting of a scorpion moving up and down, Figure 2.2. Different substitutions on the pyrazole rings can lead to a complex favouring either κ^3 or κ^2. The κ^2 configuration is generally favoured for late transition metals such as Rh(I) and Pd(II).

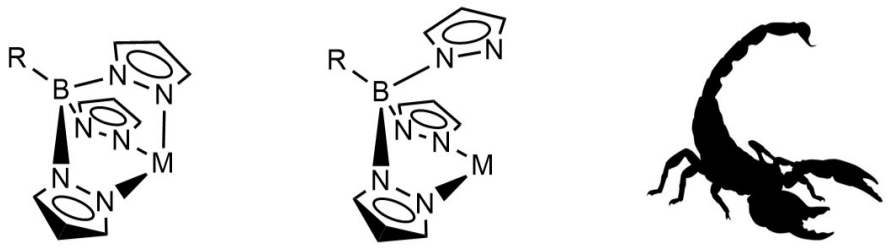

Figure 2.2: *Representation of the scorpionate 'sting'; the pyrazole group can readily interconvert between κ^3 and κ^2 coordination modes*

Transition metal complexes featuring Tp' (where Tp' indicates substituted R groups on the pyrazole) are well studied. In addition to their own raft of unique chemical properties, Tp' ligands are comparable to cyclopentadienyl (Cp) ligands; they are isoelectronic (each donating six electrons to the metal) and the pyrazole and Cp rings can be subject to substitution.[83] However, the bonding nature of the two ligands is different. Tp contains 'hard' nitrogen σ donors while Cp is a 'soft' π donor ligand. The ability of Tp' ligands to move from κ^3 to κ^2 also sets it apart from its Cp counterpart, as the Cp ring has no equivalent mechanism. Tp' ligands also offer more substitution options than Cp, with positions on the pyrazole rings and the boron open to substitution, giving ten substitutable positions compared to just five for Cp.

2.1.1 Rhodium Scorpionate Complexes

This work focusses primarily on the photochemistry of bis- and tris-pyrazolylborate complexes of rhodium. The structure of octahedral Tp*Rh(CO)$_2$ is shown in Figure 2.3. As is common with late transition metal trispyrazolylborate complexes, the third pyrazole ring is more weakly bound to the metal, and as such can move between κ^3 and κ^2 coordination, shown in Figure 2.4. For this compound, studies have shown that the κ^3–κ^2 equilibrium lies heavily in favour of κ^3, with K_{eq} = 100 in room temperature solution.[84] An in-depth computational study has proposed that the complex is in fact in a nonclassical square-pyramidal structure with a slightly longer Rh–N bond ($\kappa^{2.5}$), Figure 2.4, centre.[85]

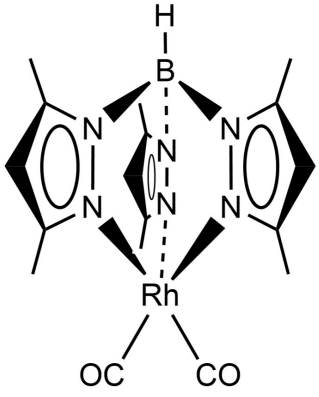

Figure 2.3: *The structure of Tp*Rh(CO)$_2$*

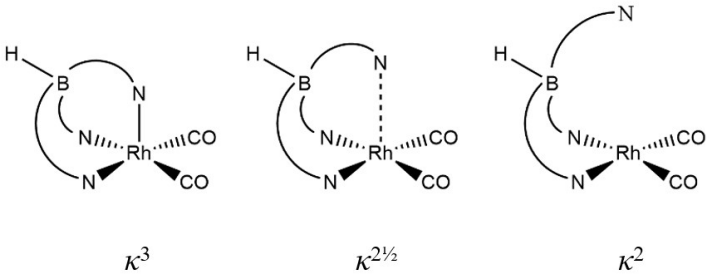

Figure 2.4: *The different bonding modes of the Tp* group*

The hapticity can also depend on the solvent environment. For Tp*Rh(CO)$_2$, infrared spectra taken in polar solvents such as dichloromethane contain four peaks in the ν(CO) region, alluding to the presence of both κ^2-Tp*Rh(CO)$_2$ and κ^3-Tp*Rh(CO)$_2$ in solution simultaneously. In non-polar solvents such as alkanes, however, there are only two peaks in the ν(CO) region. For Tp*Rh(CO)$_2$, and all transition metal carbonyl complexes, the CO region in the infrared spectrum can be an indication of the electron density of the metal. For scorpionate complexes, it can also reveal the hapticity of the complex. For pentacoordinated κ^3 complexes, there is more electron density on the metal; hence, more electron density is donated into the carbonyl antibonding orbitals. The weaker CO bond leads to a shift to lower wavenumbers. Tetracoordinated κ^2 complexes have less electron density on the metal, consequently leading to a stronger CO bond and a shift to higher wavenumbers. Thus, CO can be a very effective reporter ligand on the structure of any intermediates and products in photochemical reactions of Tp*Rh(CO)$_2$ and related complexes.

2.1.2 Rhodium Trispyrazolylborate Complexes and C–H Activation

The first example of C–H bond activation by a pyrazolylborate metal complex was reported in work by Ghosh and Graham, where Tp*Rh(CO)$_2$ was found to selectively activate aromatic and saturated C–H bonds with high selectivity and quantum efficiency,[86] which was reported to be around 30 %.[87] Graham *et al.* proposed that the reaction proceeded with such high efficiency because of the facile κ^3 to κ^2 interconversions. Further studies

were conducted into the reaction by Bloyce and coworkers in low temperature matrices, confirming that κ^3 to κ^2 interconversions are indeed observed upon photochemical excitation of Tp*Rh(CO)$_2$.[88] A study by Harris *et al.* in Science revealed the full reaction mechanism, detailed in Figure 2.5.[89,90]

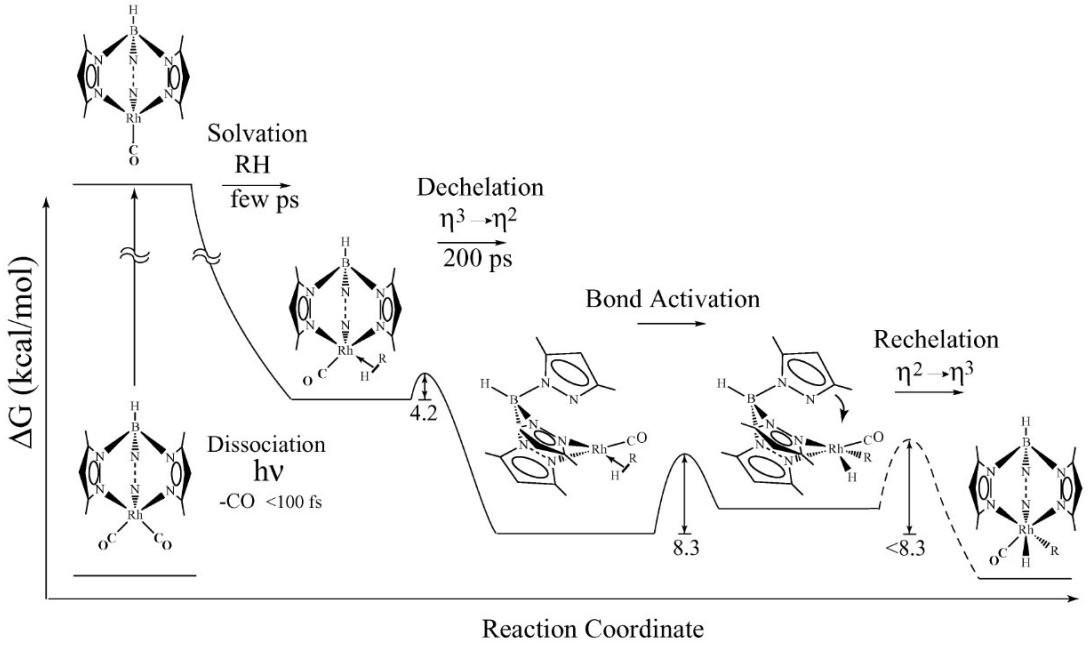

Figure 2.5: *Mechanism and energy diagram for the C–H activation reaction of Tp*Rh(CO)$_2$ in alkane solution, reproduced from reference 84*

Upon loss of a carbonyl ligand, a solvent molecule (in this case cyclohexane) coordinates to the reactive 16 electron intermediate within a few picoseconds. Following this, the Tp* ligand undergoes dechelation from κ^3 to form a κ^2-Tp*Rh(CO)(cyclohexane) complex, occurring within 200 ps. This complex then activates the cyclohexane C–H bond in 230 ns. The final step is rechelation to form the final product, κ^3-Tp*Rh(CO)(C_6H_{11})(H).

In the same work, as further evidence to prove the assignment of a κ^2 intermediate in the C–H activation process, a model complex was synthesised to compare against experimental data. This model complex, Bp*Rh(CO)$_2$, see Figure 2.6, is a known, stable 16 electron complex.

The investigation revealed that upon photolysis, the parent bands of Bp*Rh(CO)$_2$ depleted, coinciding with the growth of a new peak at 1992 cm^{-1}, matching the spectral

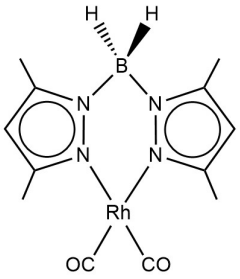

Figure 2.6: *Structure of Bp*Rh(CO)$_2$*

profile of the observed intermediate in the Tp*Rh(CO)$_2$ experiment.[84] This species at 1992 cm^{-1}, assigned as Bp*Rh(CO)(cyclohexane), confirmed the identity of the κ^2-Tp*Rh(CO)(solvent) intermediate.

Furthermore, this investigation found that the Bp*Rh(CO)$_2$ complex was unable to activate the C–H bonds of cyclohexane, unlike its Tp* relative. This was further confirmation that the key step was κ^3 to κ^2 interconversions. This inability to activate C–H bonds has been found to be because of the lack of electron density on the rhodium.[91]

Other C–H activation reactions of trispyrazolylborate rhodium dicarbonyl complexes are documented in the literature, but not to the extent of Tp*Rh(CO)$_2$, nor do they equal the efficiency reported for that of Tp*Rh(CO)$_2$. These include Tp'Rh(CO)$_2$, where Tp' = Tp^{Ph}, Tp^{iPr_2} and Tp^{CF_3,Me}.[92,93]

An in-depth computational study by Blake *et al.* sought to fully elucidate the reaction. The proposed reaction path is shown in red in Figure 2.7. Upon photolysis of TpRh(CO)$_2$, the first intermediate is a κ^3-TpRh(CO)–HR (^{3}**3**, Figure 2.7) species, where the alkane is weakly bound to the metal. This intermediate is predicted to be in the triplet state. The complex undergoes a triplet to singlet surface crossing to form the second intermediate: the singlet $\kappa^{2.5}$-TpRh(CO)–HR (**4**, Figure 2.7). This intermediate was not seen in the TRIR experiments, possibly as it is predicted to have the same ν(CO) as one of the parent bands. The pyrazole arm then completely dechelates to form the third intermediate, κ^2-TpRh(CO)–HR (**5**, Figure 2.7). The DFT calculations suggest that all three intermediates are in equilibrium with each other. The study found that of all intermediates, the $\kappa^{2.5}$

species is the one that activates the alkane. This is because the κ^2 intermediate strongly binds to the alkane but does not have enough electron density to activate it, whilst the κ^3 intermediate has more electron density, which is essential in order to activate the alkane, but does not bind strongly enough to it. The $\kappa^{2.5}$ coordination mode of Tp had also been suggested by Clot *et al.* in a DFT study of the addition of propane to TpRh(CNMe).[94,95]

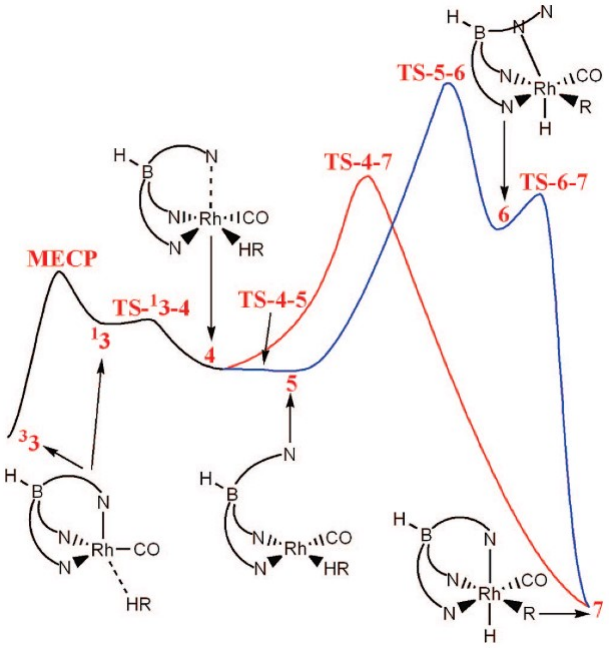

Figure 2.7: *Energy diagram summarizing the mechanistic route for C–H bond activation from density functional calculations, reproduced from reference 91*

The authors noted that a concerted mechanism was considered, i.e., a mechanism in which the third pyrazole group rechelates and the C–H bond breaks simultaneously, which would be consistent with experimental results. However, the authors were unable to find a mechanism with a single transition state in any model with multiple combinations of basis sets and functions.

Notably, the study found that in the κ^3 intermediate, the alkane is bound in an η^1 fashion. As the third pyrazole arm dissociates, this allows the alkane to convert to a stronger η^2 coordination of the alkane. This was the same for all alkanes studied. This η^1 coordination had also been calculated in a previous study of transition states in the reaction of $TpRh(CO)_2$ with CH_4.[96]

Compared to its related complex Tp*Rh(CO)$_2$, there have been relatively few studies into Bp*Rh(CO)$_2$. Much of the previous work has taken advantage of Bp*Rh(CO)$_2$'s square planar, sixteen electron configuration as a model complex for κ^2-Tp*Rh(CO)$_2$.[84] And while the complex has not been found to activate C–H bonds, it does exhibit some unique chemistry of its own, as Yeston and Bergman found that the Bp* ligand was able to undergo intramolecular B–H bond activation to form a rhodium (III) carbene hydride, Figure 2.8.[97]

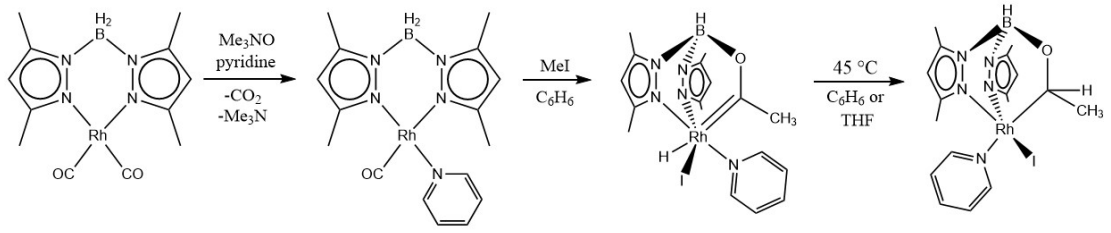

Figure 2.8: *Mechanism of reaction for the intramolecular B–H activation to form a rhodium (III) carbene hydride followed by reverse α-hydride migration to form the final product, reproduced from reference 97*

2.1.3 Rhodium Scorpionate Noble Gas Complexes

In comparison with the photochemical reactions of Tp' complexes (Tp' = Tp or Tp*) with alkanes, there have been relatively few studies into their reaction with noble gases. A study by Yeston and co-workers showed that photolysis of Tp*Rh(CO)$_2$ in liquid Xe and cyclohexane at −50 °C resulted in simultaneous formation of κ^2-Tp*Rh(CO)Xe and κ^3-Tp*Rh(CO)Xe, each decaying with the same rate constant to form the alkyl hydride activation product.[98] This is an interesting observation, as this behaviour is in contrast to the reaction observed in room temperature alkane solvent, which only produced the κ^3-Tp*Rh(CO)(cyclohexane), which then underwent quantitative isomerisation to form the κ^2 solvate. These differences highlight the dependency of the reaction mechanism and kinetics on solvent and temperature. The assignment of κ^2-Tp*Rh(CO)Xe and κ^3-Tp*Rh(CO)Xe was backed up by the spectroscopic observation of the analogous complex Bp*Rh(CO)(Xe).

2.1.4 Perfluorinated Solvents

In the case of studying alkane σ-complexes and C–H activation of longer chain alkanes (from pentane upwards), the alkanes are liquid at room temperature and pressure and therefore can be simultaneously used as a solvent and a reagent. However, for shorter chain alkanes such as methane, and also for noble gases, which are gases under ambient conditions, for this purpose it is necessary to use high temperatures and pressures to condense them into the liquid or supercritical phase. Such processes involve costly specialist equipment and complicated processes. It also means that kinetics under ambient conditions remain unknown.

Using perfluorinated solvents presents a solution to this problem. Some unique properties of perfluorinated solvents include their high stability, hydrophilicity and low surface tension, arising from the large electronegativity of fluorine and larger bond dissociation energy of a C–F bond in comparison to C–H. These unique properties have allowed perfluorinated solvents to be utilised in a wide range of applications, including as corrosion and oxidation inhibitors,[99,100] as biosensors[101] and in the polymerisation of water sensitive monomers.[102]

One notable property of fluorinated solvents which underlines their usefulness in alkane activation reactions is their remarkable gas solubility. In a paper published by Dias *et al.*, the solubility of oxygen in perfluorohexane was found to be almost twice that of its solubility in *n*-hexane.[103] These properties have been taken advantage of in medicine, where fluorinated solvents have been used for delivery of respiratory gases.[104] Hence, in the reactions of short chain alkanes or noble gases with transition metals, perfluorinated media can be immensely useful as a solvent with their ability to dissolve both the gaseous and solid reactants simultaneously, allowing for measurements of the reaction parameters under ambient conditions.

These solvents' weakly coordinating properties also lend well for such studies. While noble gases and alkanes are also known for their weakly bonding properties, making their study problematic, in a reaction conducted in a perfluorinated solvent, the alkane or noble

gas will show preferential binding over the solvent. Coupled with the increased solubility of alkane and noble gases in such solvents, perfluorinated media can present an interesting alternative to conventional solvents in photochemical reactions of organometallic complexes with alkanes and noble gases.

However, the limited solubility of metal complexes in perfluorinated solvents is an issue. One way to overcome this is to introduce perfluorinated chains into molecules of interest, increasing their solubility in perfluorinated media. A common way to do this is to introduce perfluorous 'ponytails' onto the ligand of choice. Ràbay *et al.* reported the C–H activation of methane by $Cp^fIr(CO)_2$ (where $Cp^f = C_5H_4(CH_2)_2(CF_2)_5CF_3$) in perfluoromethylcyclohexane, as detected by NMR.[105] This is an important example of C–H activation of methane at room temperature and pressure, one that could not have been achieved without the use of a perfluorinated solvent.

2.2 Aims

Whilst the reactions of Tp*Rh(CO)$_2$ and to a lesser extent, Bp*Rh(CO)$_2$, have been extensively studied, their reactions in perfluorinated media are yet unknown. Tp*Rh(CO)$_2$ is insoluble in perfluorinated solvents; however, its bipyrazole anologue, Bp*Rh(CO)$_2$, is. The solubility of Bp*Rh(CO)$_2$ in perfluorinated solvents provides a new opportunity to explore the reactivity of weakly bonding solvents to a coordinatively unsaturated complex. The aims of this chapter are therefore as follows:

(i) To synthesise a perfluorous-soluble analogue of Tp*Rh(CO)$_2$ to investigate the photochemical reactions of Tp*Rh(CO)$_2$ with short chain gaseous alkanes and xenon.

(ii) To investigate the photochemical reactions of Bp*Rh(CO)$_2$ in perfluorinated solvents to probe its reaction with weakly bonding alkanes and xenon.

(iii) Investigate these reactions with weakly bonding substrates at different temperatures, to afford the Arrhenius parameters to compare with computationally calculated values of bond dissociation energy (BDE).

2.3 Results

2.3.1 TRIR Investigations into the Reactions of Tp*Rh(CO)$_2$ in Perfluorinated Media

The insolubility of Tp*Rh(CO)$_2$ in perfluorinated solvents presents an issue in the study of their reaction with gaseous alkane and noble gas dopants. Therefore, synthesis of a pyrazole group with a perfluorous ponytail was attempted, see Figure 2.9, following an adapted literature synthesis route.[106,107] Pyrazole is known to be deprotonated at the nitrogen; therefore, it is necessary to introduce a protecting group, the most common of which is dihydropyran (DHP). Protection of the pyrazole proceeded with an 84 % yield. Deprotonation of the protected pyrazole occurs at the endocyclic CH group,[108] and successful addition reactions have been widely reported in the literature, including the addition of a series of linear iodoalkanes (iodomethane–iodohexadecane) in excellent yields.[106] However, multiple attempts at the second step involving deprotonation of the pyrazole and addition of 1-iodo-1H,1H,2H,2H-perfluorodecane (n = 7) were unsuccessful, with no product detected by NMR or mass spectroscopy.

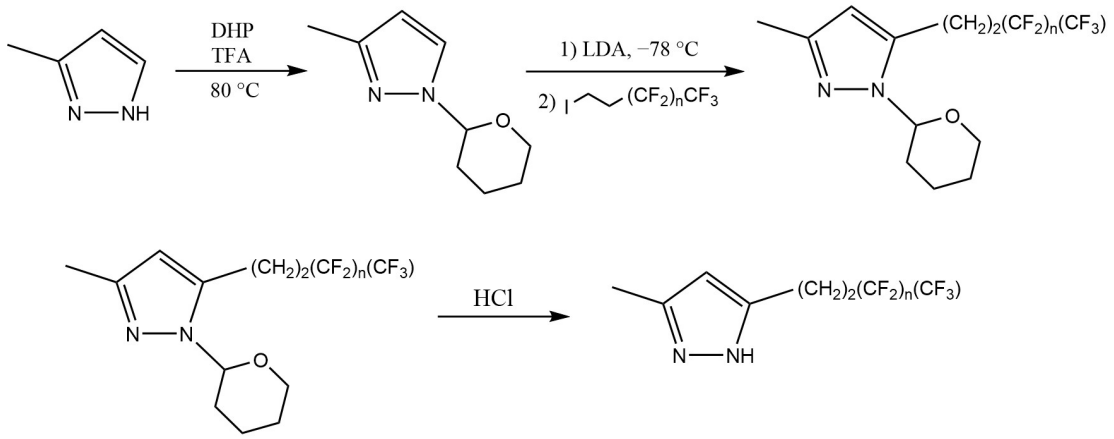

Figure 2.9: *Proposed synthesis of a perfluorous soluble pyrazole, following an adapted literature procedure from reference 106*

This length of chain was chosen to maximise the product's solubility in perfluorinated

solvents, as increasing the length of the fluorinated chain increases the resulting complexes' solubility in perfluorinated media.[100,109] Synthesis with a shorter chain, 1,1,1-trifluoro-4-iodobutane (n = 0), was also attempted, to see if this resulted in reaction; however, this was also unsuccessful. To our knowledge, addition of fluorinated chains to pyrazoles has not been previously reported in the literature. We hypothesise that sterics may be a factor in the failure of this reaction, as the approach of the bulky fluorinated chain may interact unfavourably with the DHP protecting group.

A second synthesis of $Tp^{CF_3,CF_3}Rh(CO)_2$, see Figure 2.10, which has been previously reported in the literature,[110] was then attempted. Whilst successful, the product was purified in very small yields, and whilst soluble in PFMCH, its absorbance in the infrared was negligible and unsuitable for TRIR.

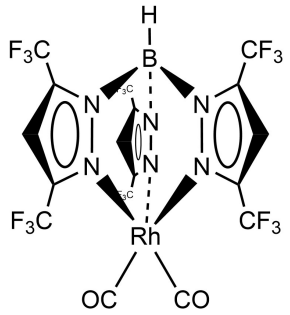

Figure 2.10: *Proposed synthesis of a perfluorous soluble analogue of Tp*Rh(CO)$_2$*

Due to these unsuccessful attempts to synthesise a perfluorous soluble analogue of $Tp^*Rh(CO)_2$, the TRIR was investigated in a mixture of perfluoromethylcyclohexane (PFMCH) and alkane, in this case cyclopentane. A solution of 30 % v:v *c*-pentane:PFMCH was chosen as it gave a suitable absorbance whilst still remaining a homogeneous solution. Solutions above 30 % v:v ratio were biphasic, whilst at below 30 %, the complexes solubility was low, again giving a low absorbance in the infrared and hence it was unsuitable for use in TRIR.

2.3.1.1 ps-TRIR of Tp*Rh(CO)$_2$ in cyclopentane

Our first experiments look to replicate previous literature experiments and to serve as a comparison for experiments carried out in a mix of alkane and PFMCH solvents. Selected ps-TRIR spectra obtained on photolysis of Tp*Rh(CO)$_2$ at 355 nm in cyclopentane are shown in Figure 2.11.

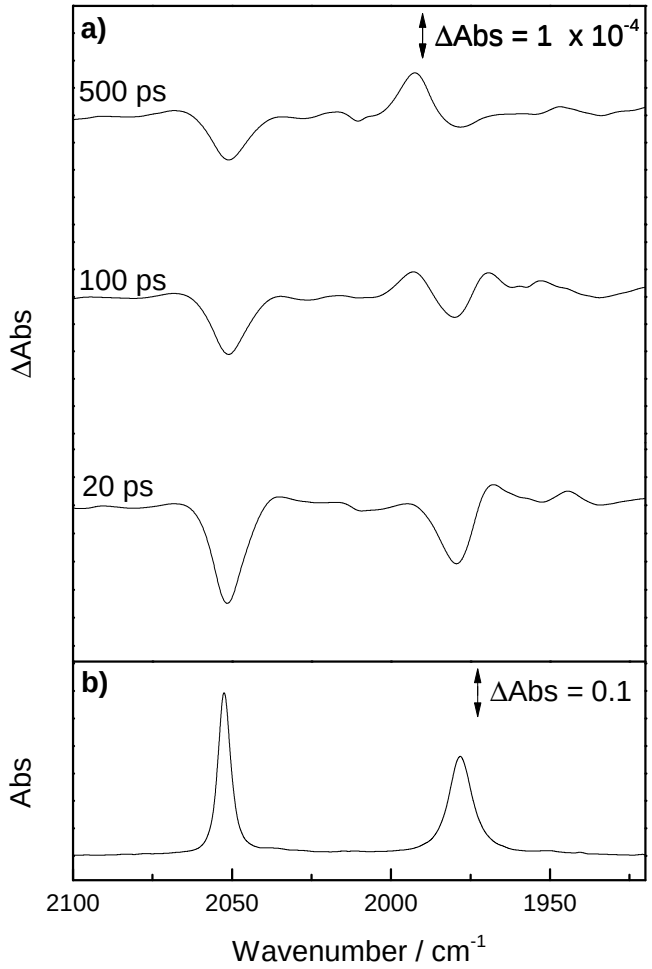

Figure 2.11: *a) ps-TRIR difference spectra at selected time delays for the 355 nm photolysis of Tp*Rh(CO)$_2$ in cyclopentane and b) Ground state FTIR spectrum of Tp*Rh(CO)$_2$ in cyclopentane*

After photolysis, we see the bleach of the parent bands at 2054 and 1979 cm^{-1} and immediately after excitation, there is a relatively strong absorption at 1969 cm^{-1} alongside some weaker features at 2035, 1959 and 1944 cm^{-1}. These weak features are attributed to 'vibrationally hot' excited states. Previous studies have shown the these vibrationally

excited electronic ground states form on photolysis and decay within the first few hundred picoseconds.[111] Kinetic analysis of the band at 1944 cm^{-1} shows a lifetime for vibrational cooling of around 35 ps which occurs alongside the partial reformation of the parent bands.

The band at 1969 cm^{-1} continues to grow in until around 50 ps. The apparent growth of this band may be due to an actual growth, i.e., it is formed form a precursor species such as an excited state, or it is formed on a much faster timescale in a vibrationally excited state and its apparent growth is due to cooling of this hot species.

After 50 ps the band at 1969 cm^{-1} then starts to decay with a lifetime of 186.3 ± 14.2 ps, corresponding with the growth of a new peak at 1992 cm^{-1} (τ = 112.9 ± 6.6 ps), shown in Figure 2.12. This final photoproduct is stable for the remainder of the experiment.

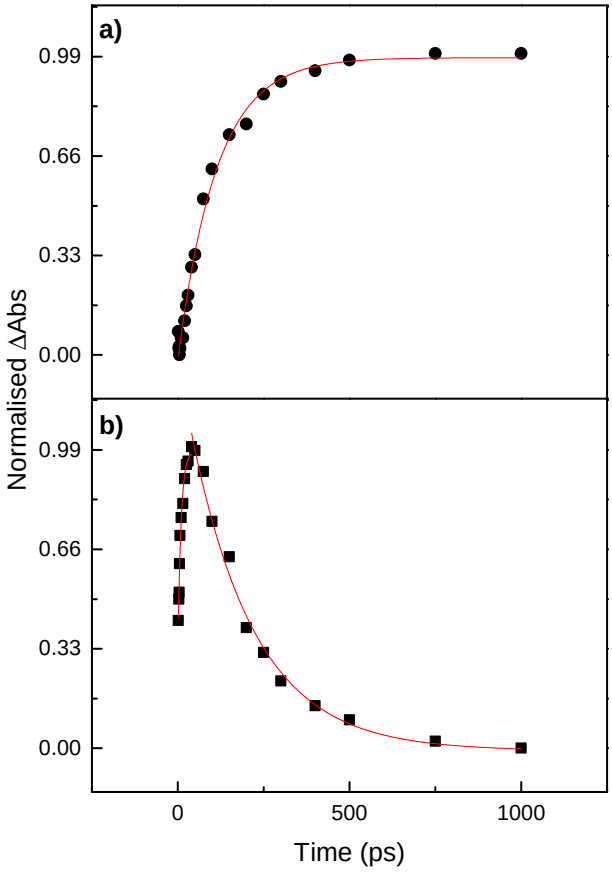

Figure 2.12: *Normalaised TRIR kinetics traces for a) the growth of κ^2-Tp*Rh(CO)(cyclopentane) (τ = 110 ± 7 ps) and b) the decay of κ^3-Tp*Rh(CO)(cyclopentane) (τ = 190 ± 15 ps) following photolysis at 355 nm in cyclopentane*

The mechanism of the photochemical reaction of Tp*Rh(CO)$_2$ in alkanes is widely accepted to proceed through κ^3–κ^2 interconversions; hence, as they closely resemble similar peaks seen in the literature, the peaks at 1969 and 1992 cm^{-1} are assigned to κ^3-Tp*Rh(CO)(cyclopentane) and κ^2-Tp*Rh(CO)(cyclopentane), respectively. Furthermore, the lifetime for the decay of the κ^3 species is comparable to that measured by Bergman and Harris, who found that κ^3-Tp*Rh(CO)(cyclohexane) decayed to the κ^2 bonded species with a lifetime of 200 ps.[89]

2.3.1.2 ps-TRIR of Tp*Rh(CO)$_2$ in cyclopentane:pfmch (30 % v:v)

The ps-TRIR was investigated to see if the κ^3 to κ^2 conversion previously seen on this timescale in cyclohexane is still present in this new solvent environment. The results are shown in Figure 2.13. At around 20 ps after excitation there are several new features in the spectra, due to 'vibrationally hot' species of Tp*Rh(CO)$_2$, most of which decay by 75 ps, alongside the partial regrowth of the parent bands. This leaves a new peak at 1969 cm^{-1}, which continues to grow until 50 ps. After 50 ps, this peak starts to decays with the growth of a peak at 1992 cm^{-1}. These two peaks at 1969 and 1992 cm^{-1} are identical to those seen in ps-TRIR of Tp*Rh(CO)$_2$ in neat cyclopentane and are hence assigned to κ^3-Tp*Rh(CO)(cyclopentane) and κ^2-Tp*Rh(CO)(cyclopentane), respectively.

The peak at 1969 cm^{-1} decays with a lifetime of 360.3 ± 60.5 ps. This lifetime is almost double that of its lifetime in neat cyclopentane (τ = 186.3 ± 14.2 ps). Lifetimes of transient species generally vary between solvents; however, such a significant extension of the lifetime is unexpected. Moreover, the decay of the peak at 1969 cm^{-1} does not match the growth of the peak at 1992 cm^{-1} (τ = 136.9 ± 7.5 ps), as shown in Figure 2.14.

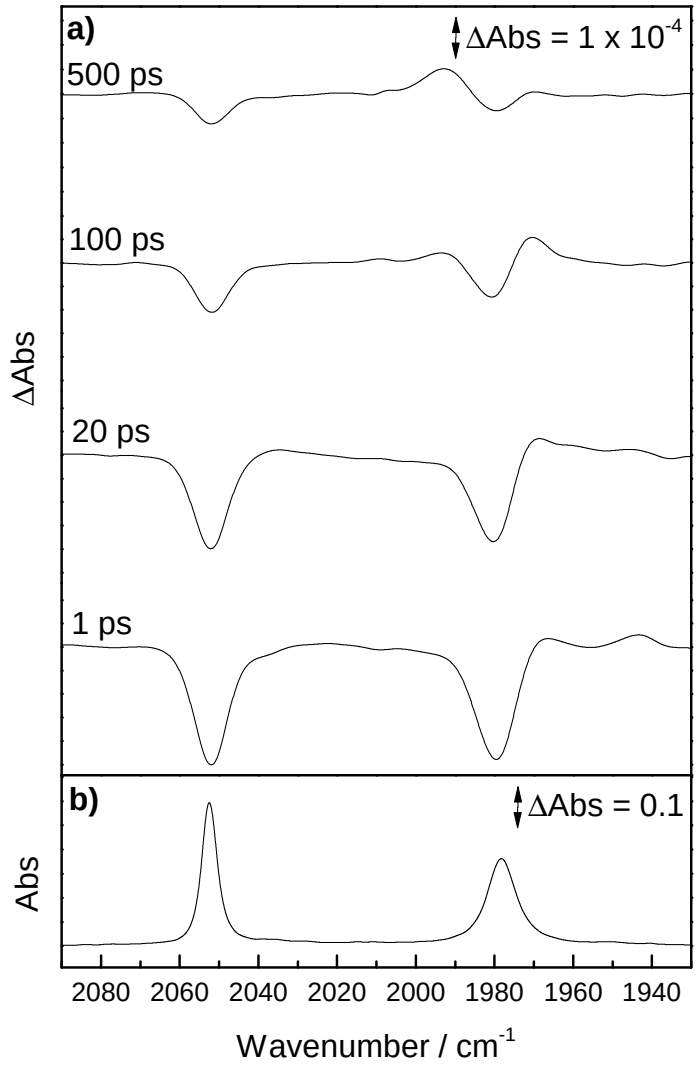

Figure 2.13: *a) ps-TRIR difference spectra at selected time delays for the 355 nm photolysis of Tp*Rh(CO)$_2$ in cyclopentane:perfluoromethylcyclohexane (30% v:v) and b) Ground state FTIR spectrum of Tp*Rh(CO)$_2$*

The κ^3–κ^2 interconversion is a widely accepted mechanism in these reactions; hence, a different reaction mechanism is unlikely and not considered. Instead the implication is that there is another species present around 1969 cm^{-1}, and the two competing decay processes are distorting the apparent lifetime.

Alkanes have been shown to preferentially bind over perfluorinated solvents; however, since there is a significant amount of PFMCH present, indeed, it makes up the majority of solution, it is suggested that there may be a equilibrium present in solution between κ^3-Tp*Rh(CO)(PFMCH) and κ^3-Tp*Rh(CO)(*c*-pentane). However, it has been shown

before that even in solutions where the ratio of alkane:PFMCH is much lower than it is here, the alkane will still preferentially bind over the PFMCH.[112] Perhaps there are some further processes that lead to PFMCH complexation being increasingly favoured. Therefore, the second species present is tentatively assigned as κ^3-Tp*Rh(CO)(PFMCH). It is also proposed that the large, bulky nature of PFMCH may be sterically hindering the conversion to κ^2-Tp*Rh(CO)(PFMCH), hence why the growth lifetime for the species at 1992 cm^{-1} is relatively unchanged compared to that in neat cyclopentane.

It is important to probe the nanosecond-TRIR to see if there are any further processes which may explain why formation of κ^3-Tp*Rh(CO)(PFMCH) is more favoured.

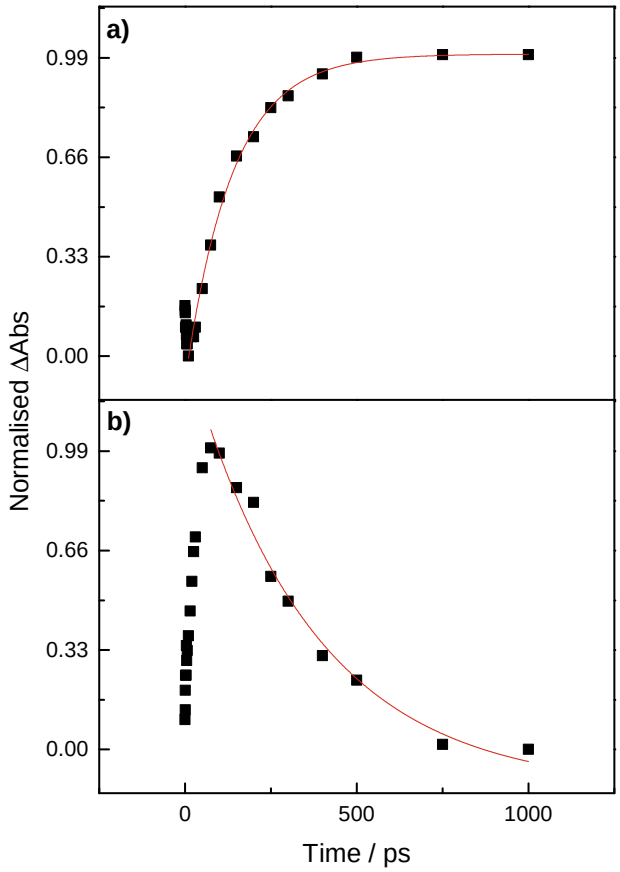

Figure 2.14: *Normalised TRIR kinetic traces for a) The growth of κ^2-Tp*Rh(CO)(cyclopentane) (τ = 140 ± 8 ps) at 1992 cm^{-1} and b) The decay of κ^3-Tp*Rh(CO)(cyclopentane) (τ = 360 ± 60 ps) at 1966 cm^{-1} following photolysis of Tp*Rh(CO)$_2$ at 355 nm in cyclopentane:perfluoromethylcyclohexane (30 % v:v)*

2.3.1.3 ns-TRIR of $Tp^*Rh(CO)_2$ in cyclopentane:PFMCH (30 % v:v)

The nanosecond TRIR was investigated to see if the presence of PFMCH further altered the reaction. The spectra show a bleach in the parent bands at 2056 and 1981 cm^{-1}, and the appearance of several new bands. One nanosecond after photolysis there are two new peaks in the spectrum at 1996 and 1963 cm^{-1}. These decay at different rates and are therefore attributed to two separate species. By 750 ns there are two other new peaks in the spectrum; a large peak at 2031 cm^{-1} and a small peak at 2048 cm^{-1}.

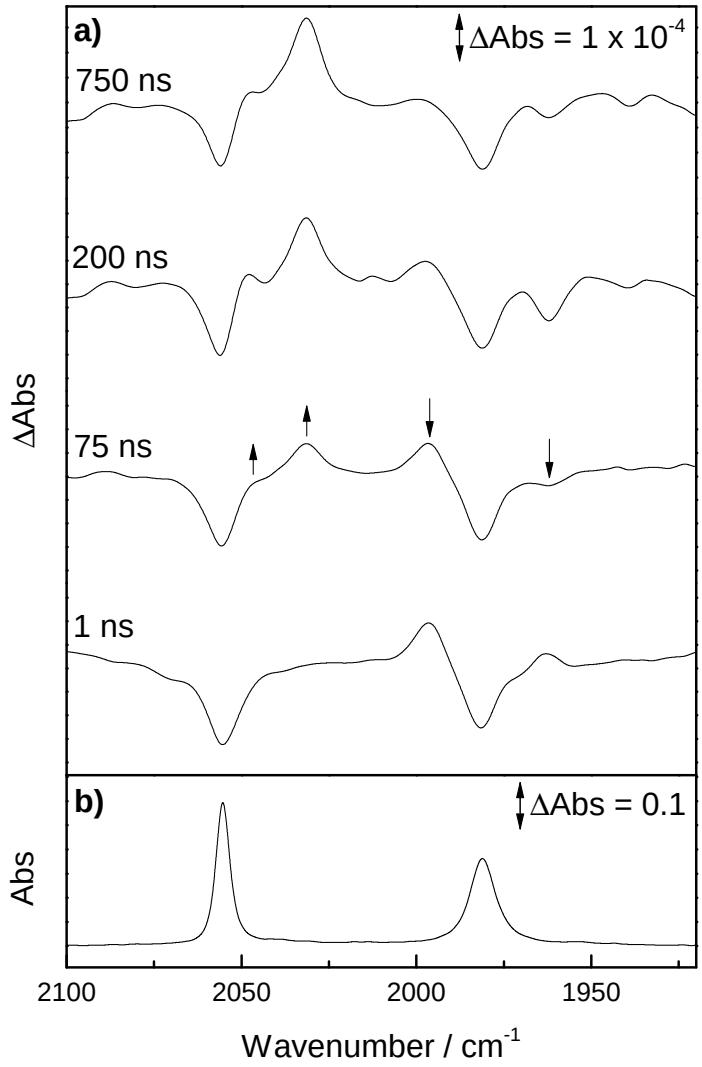

Figure 2.15: *a) ns-TRIR difference spectra at selected time delays for the 355 nm photolysis of $Tp^*Rh(CO)_2$ in cyclopentane:perfluoromethylcyclohexane (30% v:v) and b) Ground state FTIR spectrum of $Tp^*Rh(CO)_2$*

The decay of the peak at 1996 cm^{-1} (τ = 245 ± 25.7 ns) corresponds to the growth of the peak at 2031 cm^{-1} (τ = 180.7 ± 10.0 ns), shown in Figure 2.16. The two values are not within error of each other; however, this phenomena is also seen in the literature and is due to thermal effects caused by the parent bleach at 1981 cm^{-1}. Absorption of a laser pulse by a sample absorbs a high amount of energy into the system. This absorption of energy leads to a transient increase in the temperature of the sample and therefore a change in the refractive index of the sample. This appears as a time dependent change in absorption near the absorption peaks; hence, the lifetime of transient peaks near strong absorptions appear longer.[84,113] Thus, the decay of the peak at 1996 cm^{-1} appears longer.

On comparison to the literature and experiments in the previous sections, the peaks at 1996 and 2031 cm^{-1} are assigned as κ^2-Tp*Rh(CO)(cyclopentane) and the C–H activated product, Tp*Rh(CO)(C_5H_9)H, respectively.

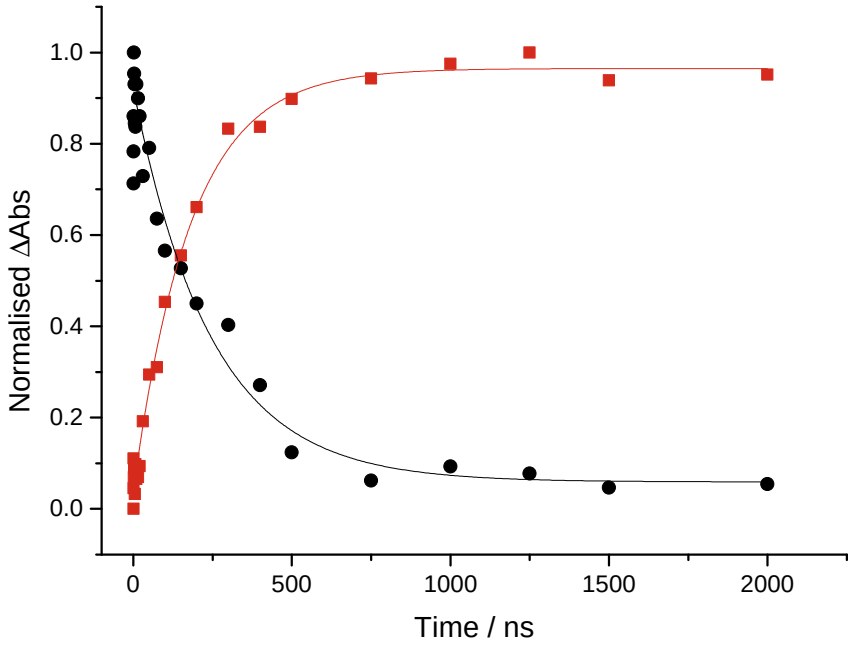

Figure 2.16: *Normalised TRIR kinetic traces for the decay of κ^2-Tp*Rh(CO)(cyclopentane) (τ = 250 ± 25 ns) at 1992 cm^{-1} and the growth of Tp*Rh(CO)(C_5H_9)(H) (τ = 180 ± 10 ns) at 2031 cm^{-1} following photolysis of Tp*Rh(CO)$_2$ at 355 nm in cyclopentane:perfluoromethylcyclohexane (30 % v:v)*

The peak assigned to κ^2-Tp*Rh(CO)(cyclopentane) (1996 cm^{-1}) is slightly shifted to that in neat cyclopentane (1992 cm^{-1}), most likely due to the change in solvent en-

vironment. The literature value for the lifetime of κ^2-Tp*Rh(CO)(cyclopentane) in neat cyclopentane (τ = 230 ± 10 ns) is also comparable to the value obtained here.

The peaks at 1961 and 2047 cm^{-1} are harder to assign as the presence of two different solvents in this experiment leads to several potential photoproducts. In addition, their kinetic profiles match, shown in Figure 2.17, indicating that one species is formed from the other.

If we assume loss of a carbonyl upon excitation, the excited monocarbonyl species, Tp*Rh(CO), is too short lived to be seen on this timescale. There are several reaction pathways that this reactive species could take that could lead to the species with an absorbance at 1961 cm^{-1}. The wavenumber is characteristic of a κ^3 bonded solvated monocarbonyl, very similar to that of κ^3-Tp*Rh(CO)(cyclopentane) and the proposed κ^3-Tp*Rh(CO)(PFMCH) seen in the ps-TRIR.

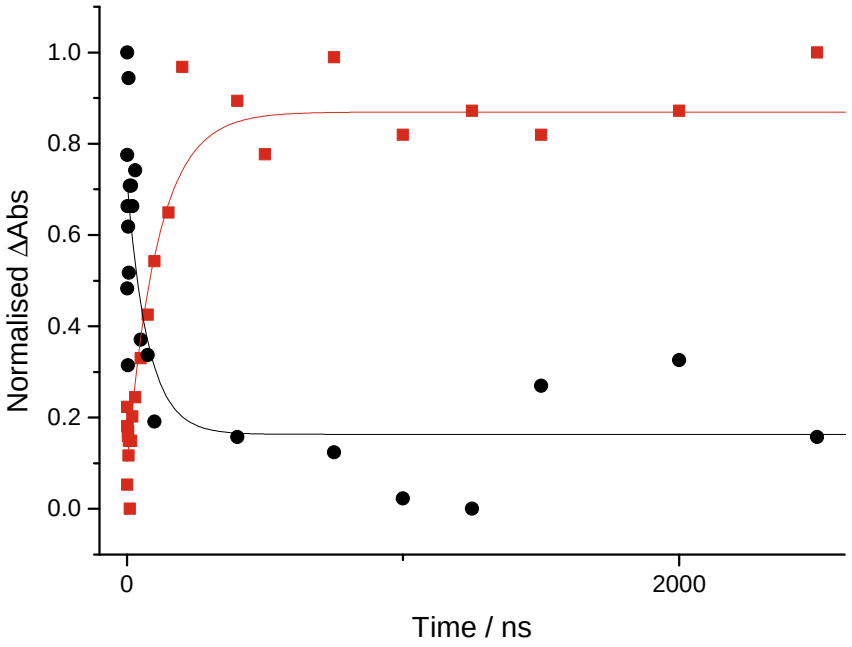

Figure 2.17: *Normalised TRIR kinetic traces for the decay of proposed κ^3-Tp*Rh(CO)(PFMCH) (τ = 80 ± 35 ns) at 1963 cm^{-1} and the growth of proposed Tp*Rh(CO)(C_7F_{13})F (τ = 110 ± 20 ns) at 2048 cm^{-1} following photolysis of Tp*Rh(CO)$_2$ at 355 nm in cyclopentane:perfluoromethylcyclohexane (30 % v:v)*

However, both of those species decayed on the picosecond timescale; therefore, it is not expected that we see this photoproduct on the ns timescale. Nevertheless, since the species

at 1961 cm^{-1} is highly suggestive of a κ^3 type monocarbonyl species, this peak is very tentatively assigned as κ^3-Tp*Rh(CO)(PFMCH). However, this would contradict trends in lifetimes of alkane and perfluorinated solvents, as perfluorinated solvent complexes are recognised to be shorter lived than their alkane solvent complex counterparts. However, if, as suggested in the ps-TRIR experiments, the complex is sterically hindered by the bulky PFMCH, the third nitrogen may not be able to dechelate. It is possible that this steric hindrance is prolonging the lifetime of the κ^3 PFMCH bonded species. Another possibility is that the peak at 1963 cm^{-1} is due to the reactive monocarbonyl bonding to an impurity present in the solution.

The nature of the peak at 1963 cm^{-1} is also interesting. At early time it appears as a growth in the spectrum but at later times, ΔAbs is negative. One explanation for this apparent bleach could be that because a background spectrum is taken before each individual photolysis, if there is any remaining absorbance from any intermediate in the background, this would appear as a bleach at later time delays. Alternatively, as cyclopentane and perfluoromethylcyclohexane are not completely miscible, this could also be affecting absorbance measurements. However, analysis of the solvents' background spectra show no peaks at 1963 cm^{-1}.

The small peak at 2048 cm^{-1} falls at a higher wavenumber relative to the solvated monocarbonyl species suggesting a decrease in electron density around the metal. A similar change in wavenumber is seen upon C–H activation. The peak at 2048 cm^{-1} occurs at *ca.* 15 cm^{-1} higher than the C–H activated species suggesting a further decrease in electron density. A C–F activated species would be expected to occur lower energy than the C–H activated species due to the electron withdrawing effect of fluorine. It has been reported in work in this group that $CpRh(CO)_2$ was able to activate C–F bonds of PFMCH and PFH.[114] As detailed in Section 2.1, Cp and Tp ligand have much in common, and their reactions tend to be similar. $Tp^*Rh(CO)_2$ has been found to be more efficient at activating C–H bonds than $Cp^*Rh(CO)_2$ so it is certainly not unreasonable to suggest that $Tp^*Rh(CO)_2$ is able to activate C–F bonds like its Cp counterpart. In addition, in a study

by Procacci *et al.*, Tp*Rh(PMe_3)H_2 was found to be able to simultaneously activate C–H and C–F bonds.[115] Therefore, it is likely that Tp*Rh(CO)$_2$ is able to activate C–F bonds, although to our knowledge there are no other reports of this in the literature.

The difference in wavenumber between the C–H activated CpRh(CO)(C_5H_9)H and the reported CpRh(CO)(C_7F_{13})F was 7 cm^{-1},[114,116] not dissimilar to the difference in wavenumber seen here (17 cm^{-1}). Therefore, it is proposed that the species present at 2048 cm^{-1} could be the C–F activation product, Tp*Rh(CO)(C_7F_{13})F. However, if the C–F activated species is directly formed from κ^3-Tp*Rh(CO)(PFMCH), then this would go against the commonly accepted reaction pathway of κ^3–κ^2 interconversions that analogous C–H activation reactions follow.

The complexes Tp*Rh(CO)(PFMCH) and Tp*Rh(CO)(CF_3)F (the latter complex was used to decrease computational time) were calculated using DFT and the results of the frequency calculations are shown in Table 2.1. Calculations of κ^3-Tp*Rh(CO)(PFMCH) converged to a κ^2-bonded complex; therefore, the unsolvated monocarbonyl κ^3-Tp*Rh(CO) was calculated instead as an comparable compound to its solvated equivalent.

Table 2.1: Calculated ν(CO) values for selected Tp*Rh(CO)$_2$ complexes

Complex	Calculated ν(CO) / cm^{-1}	Calculated ν(CO) / cm^{-1} with correction factor
Tp*Rh(CO)$_2$	2162, 2095	2053, 1990
κ^3-Tp*Rh(CO)(PFMCH)	2077*	1973*
κ^2-Tp*Rh(CO)(PFMCH)	2096	1991
Tp*Rh(CO)(CF_3)F	2184	2075

*calculated for κ^3-Tp*Rh(CO)

The calculations show that the κ^3 species absorbs in the ν(CO) at 1973 cm^{-1}, whilst κ^2-Tp*Rh(CO)(PFMCH) has an absorbance at 1991 cm^{-1}, confirming that the experimentally

observed species at 1963 cm^{-1} is more characteristic of a κ^3 bonded species. Calculations show that Tp*Rh(CO)(CF_3)F exhibits a stretch in the carbonyl region at 2075 cm^{-1}. This is markedly higher than the 2047 cm^{-1} seen in the experiment and would place this peak at even lower energy than the low energy ν(CO) of the parent. It could be that the directly bonding CF_3 unit has more of an electron withdrawing effect than the perfluorocyclohexyl group would, and more calculations need to be done to assess this effect.

It is clear that investigating this reaction in a mixture of solvents is complicating analysis of the reaction. In the future it is hoped that a perfluorous soluble analogue of Tp*Rh($CO)_2$ could be synthesised in order to probe the reaction without the need for an alkane dopant. This would confirm whether Tp*Rh($CO)_2$ is able to activate the C–F bonds of fluorinated compounds, and the mechanism with which it does this.

The carbonyl stretching frequencies and lifetimes of the photoproducts of Tp*Rh($CO)_2$ are summarised in Table 2.2.

Table 2.2: Infared ν(CO) bands and lifetimes (in ns) of κ^3/κ^2-Tp*Rh(CO)(X) (X = PFMCH, cyclopentane) and their relative C–H and proposed C–F activation products in different solvents

Compound	Solvent	ν(CO) / cm^{-1}	Lifetime / ns	Reference
κ^3-Tp*Rh(CO)(*c*-pentane)	*c*-pentane	1969	0.19 ± 0.01	This work
	PFMCH/ *c*-pentane	1969	0.36 ± 0.06	This work
κ^2-Tp*Rh(CO)(*c*-pentane)	*c*-pentane	1992	230 ± 10	116
	PFMCH/ *c*-pentane	1992	245.3 ± 25.7	This work
κ^3-Tp*Rh(CO)(PFMCH)	PFMCH/ *c*-pentane	1963	75.3 ± 34.7	This work
Tp*Rh(CO)(C_5H_9)H	PFMCH/ *c*-pentane	2031	N/A	This work
	c-pentane	2030	N/A	116
Tp*Rh(CO)(C_7F_{13})F	PFMCH/ *c*-pentane	2048	N/A	This work

2.3.2 TRIR Investigations into the Reactions of Bp*Rh(CO)$_2$ in Perfluorinated Media with Weakly Coordinating Ligands

As detailed in the introduction, investigations into Bp*Rh(CO)$_2$ have mostly been limited to study of its reactions as a model complex for κ^2-Tp*Rh(CO)$_2$. The complexes solubility in perfluorinated media presents a new area of research for the potential production of short chain alkane and noble gas complexes. The reactions of Bp*Rh(CO)$_2$ have hence been probed in perfluoromethylcyclohexane (PFMCH) with a series of dopants.

2.3.2.1 ps-TRIR of Bp*Rh(CO)$_2$ in perfluoromethylcyclohexane

Initially, the ps-TRIR of Bp*Rh(CO)$_2$ was investigated. Photolysis at 266 nm resulted in the decay of the parent bands at 2018 and 2084 cm^{-1} and the appearance of a new band at 2000 cm^{-1}, Figure 2.18. Alongside these there are some weak broad features assigned as 'vibrationally hot' species of Bp*Rh(CO)$_2$, these decay completely by 100 ps, leaving the peak at 2000 cm^{-1}. The presence of a sole band in the carbonyl region is indicative of formation of a monocarbonyl species, confirming that CO has been lost upon photolysis of Bp*Rh(CO)$_2$. This band grew with a lifetime of 6.5 ± 1.2 ps and was stable for the duration of the picosecond experiment, see Figure 2.19. This band could be assigned to one of two monocarbonyl forms; fourteen electron Bp*Rh(CO), or its solvated form, in this case Bp*Rh(CO)(PFMCH). Whilst Bp*Rh(CO) is expected to be formed immediately following photolysis, the lifetime of such species is expected to be extremely short. Indeed, it was found that following photolysis, the species Cr(CO)$_5$ was solvated within a few ps.[39,40] The species at 2000 cm^{-1} is still present at the end of the experiment (1.5 ns) and furthermore, the timescale of formation of this species is consistent with those associated with solvent complexation. Therefore, it assigned to the solvated monocarbonyl Bp*Rh(CO)(PFMCH).

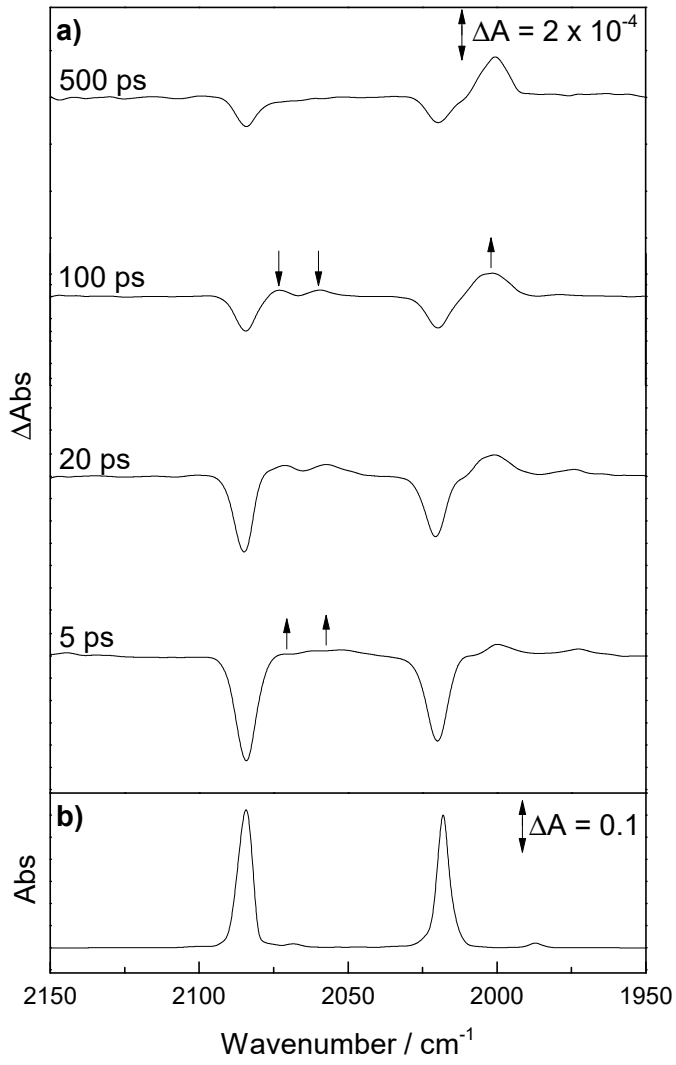

Figure 2.18: *a) ps-TRIR difference spectra at selected time delays for the 266 nm photolysis of Bp*Rh(CO)$_2$ in perfluoromethylcyclohexane and b) Ground state FTIR spectrum of Bp*Rh(CO)$_2$ in perfluoromethylcyclohexane*

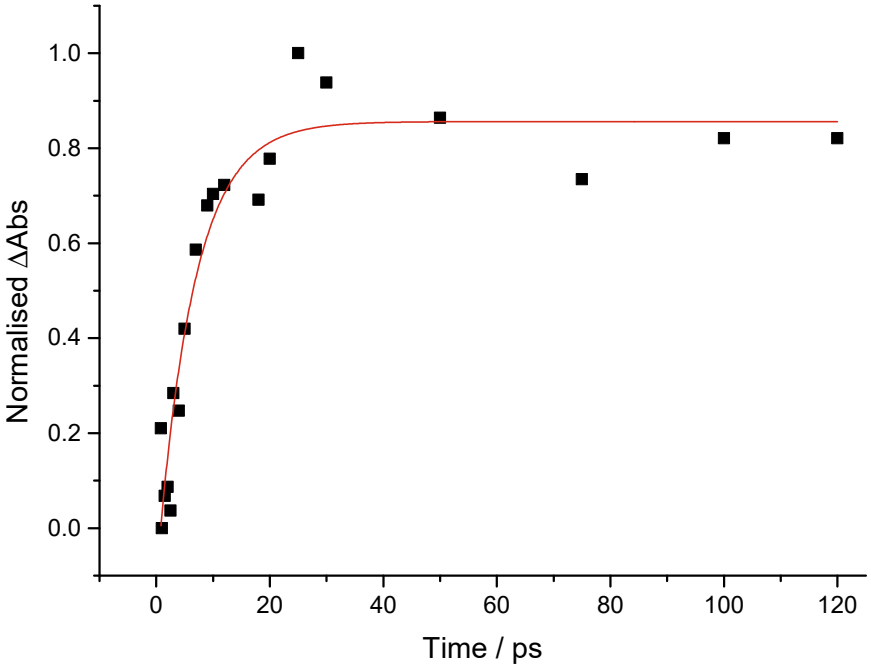

Figure 2.19: *Normalised TRIR kinetic traces for the growth of Bp*Rh(CO)(PFMCH) (τ = 6.5 ± 1.2 ps) following photolysis of Bp*Rh(CO)$_2$ at 266 nm in perfluoromethylcyclohexane*

2.3.2.2 ns-TRIR of Bp*Rh(CO)$_2$ in perfluoromethylcyclohexane

As the species Bp*Rh(CO)(PFMCH) was stable for the duration of the picosecond experiment, for this experiment and all following experiments, the nanosecond TRIR was investigated, Figure 2.20.

Again, we see the immediate bleach of the parent bands at 2018 and 2084 cm^{-1} and the appearance of a new band at 2000 cm^{-1}. This band was attributed, in comparison with the ps-TRIR, to the solvated species Bp*Rh(CO)(PFMCH). This species decays (τ = 49.1 (± 6.1) ns) with the growth of three bands at 2098, 2029 and 1986 cm^{-1}. These three bands grow in with the same rate constant (within error) and are therefore assigned to the same species.

The presence of three peaks suggests that this species is a form of dimer, possibly formed from reaction of the intermediate with another intermediate molecule, or even a

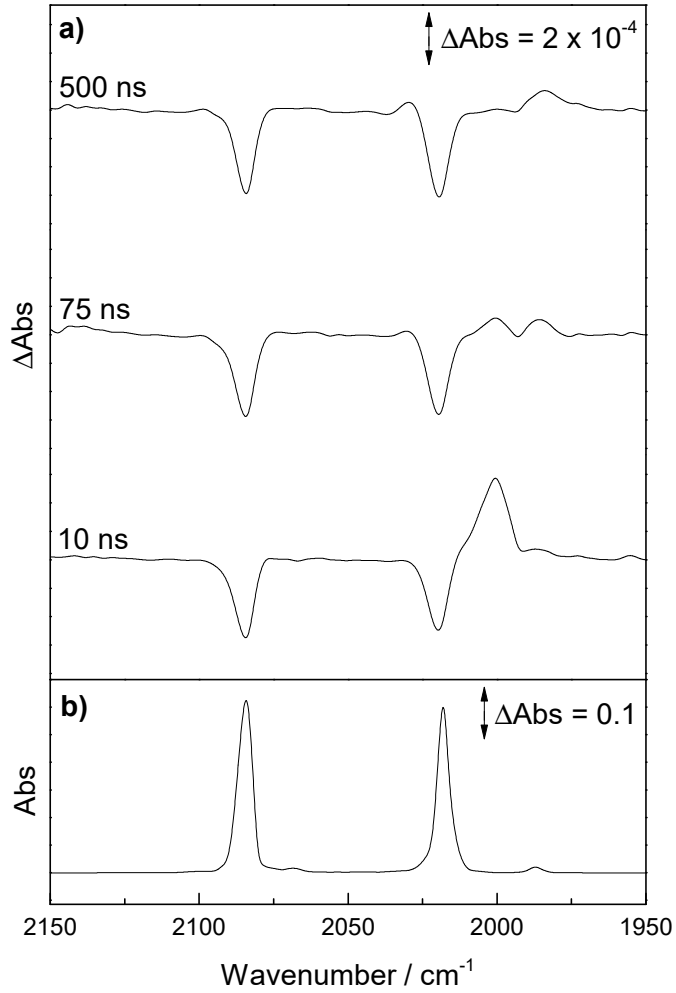

Figure 2.20: *a) ns-TRIR difference spectra at selected time delays for the 266 nm photolysis of Bp*Rh(CO)$_2$ in perfluoromethylcyclohexane and b) Ground state spectrum of Bp*Rh(CO)$_2$ in perfluoromethylcyclohexane*

reaction between the intermediate and the parent. Indeed, analysis of the parent peaks do show a decrease in intensity with time, Figure 2.21, which is an unusual observation, as usually we observe a reformation of the parent bands as the transition state can decay back to the parent. The observation here suggests that the parent Bp*Rh(CO)$_2$ is undergoing further reaction.

The kinetics of this dimer species at 2098, 2029 and 1986 cm^{-1} are also complex, partly due to the very small ΔAbs (~1–2 × 10^{-5}). This could be due to the low solubility of the proposed dimer species in PFMCH. Some kinetics however were able to be analysed at the peak at 2029 cm^{-1}. The complex grows in (τ = 51.6 (± 16.9) ns) at the same rate as

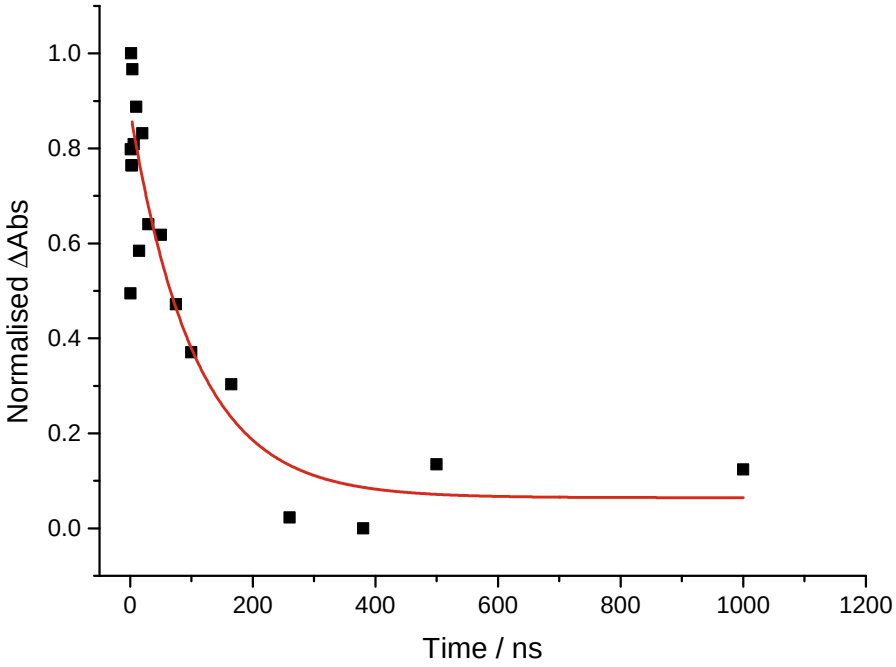

Figure 2.21: *Normalised TRIR kinetic traces for the further decay of the parent, Bp*Rh(CO)$_2$, (τ = 92.2 ± 24.0 ns) at 2018 cm^{-1} following photolysis at 266 nm in perfluoromethylcyclohexane*

the decay of the solvated monocarbonyl, shown in Figure 2.22.

Yeston *et al.* also noted that upon photolysis of Bp*Rh(CO)$_2$ in liquid Xe, decay of Bp*Rh(CO)(Xe) was linked to the formation of a species at 1984 cm^{-1} which they also attributed to a dimer species.[98] They did not however observe formation of this product in the presence of buffering CO. A dimer of this compound could take two forms; a complex with bridging carbonyl groups, or a complex with bridging pyrazole groups. The species Cp*Rh(CO)$_2$ is known to form a dimer with bridging CO units,[117] yet dimer complexes containing pyrazole groups are known to form 'exobidentate' pyrazolylborate ligands, Figure 2.23, which are generally stable under room conditions.[118] The dimer species here appears to be unstable, with no evidence of it found in the FTIR spectra after the experiment. This instability would support its assignment as a dimer with bridging CO units, and not the more stable form of 'exobidentate' dimer.

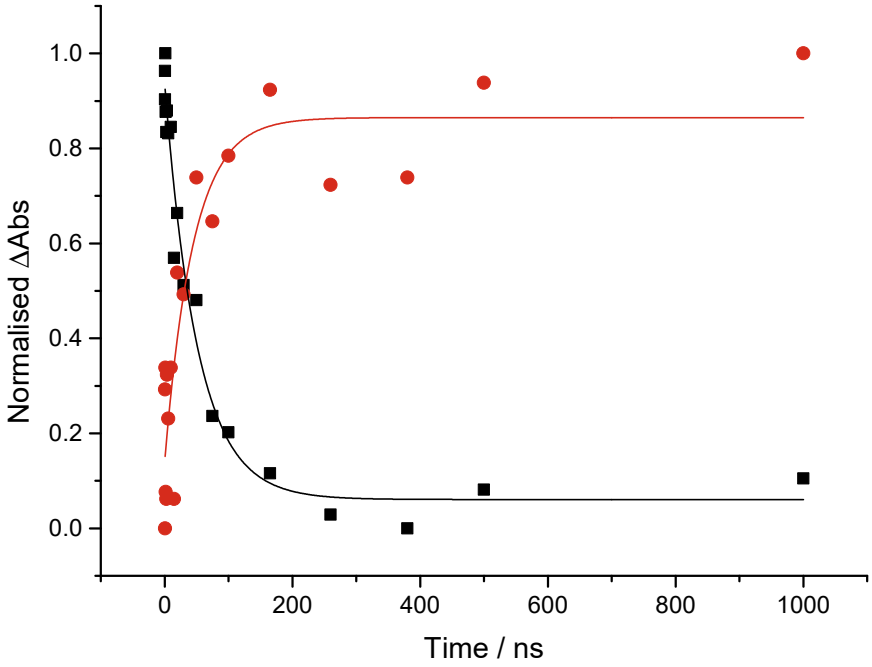

Figure 2.22: *Normalised TRIR kinetic traces for the decay of Bp*Rh(CO)(PFMCH) (τ = 51.7 ± 7.1 ns) at 2000 cm^{-1} and the growth of the proposed dimer species (τ = 51.6 ± 17 ns) at 2029 cm^{-1} following photolysis at 266 nm in perfluoromethylcyclohexane*

Furthermore, the 'exobidentate' dimer form of Bp*Rh$(CO)_2$ has been fully characterised.[119] The IR peaks in dichloromethane were reported to be at 2080, 2060 and 2005 cm^{-1}. Even accounting for the shift due to the change in solvent, the peaks do not match those reported for $(CO)_2$Rh(μ-Bp)Rh$(CO)_2$. Therefore, the species observed here is tentatively assigned as a dimer with bridging CO units. Since the bridging carbonyl region is not probed in this TRIR experiment, it is difficult to definitively characterise. The presence of a bridging band may provide additional support for the assignment.

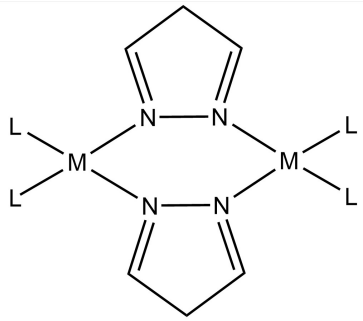

Figure 2.23: *Example of an 'exobidentate' polypyrazolyl borate metal dimer*

2.3.2.3 ns-TRIR of Bp*Rh(CO)$_2$ in cyclopentane

For a comparison between PFMCH and an alkane solvent, the reaction of Bp*Rh(CO)$_2$ in cyclopentane was investigated. Due to the long-lived nature of the solvated species in Section 3.2, the nanosecond timescale was probed. The ns-TRIR spectra of Bp*Rh(CO)$_2$ following photolysis (266 nm) in cyclopentane is shown in Figure 2.24.

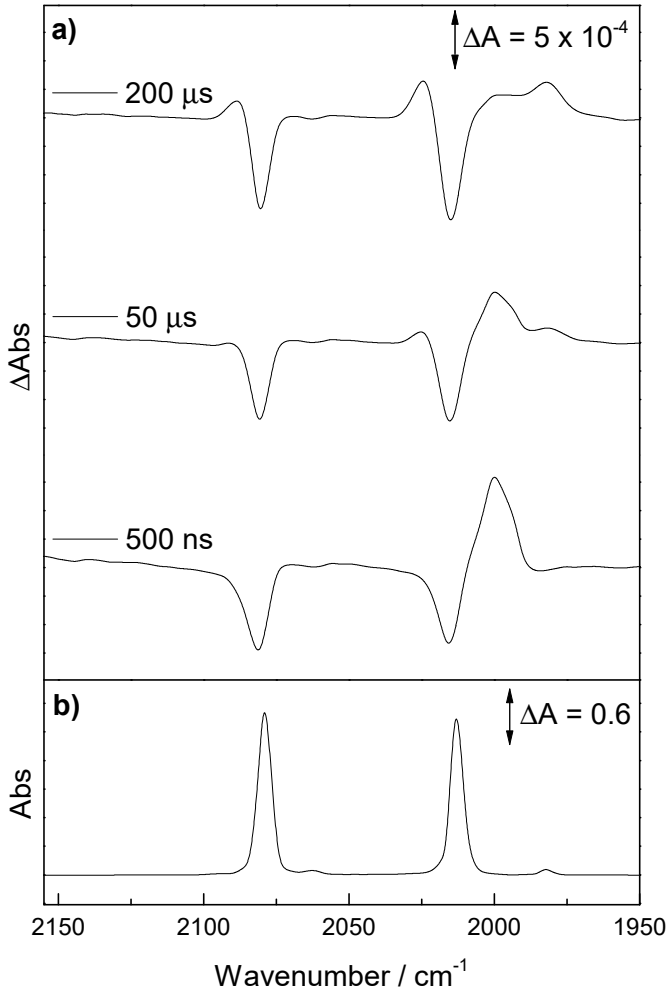

Figure 2.24: *a) ns-TRIR difference spectra at selected time delays for the 266 nm photolysis of Bp*Rh(CO)$_2$ in cyclopentane and b) Ground state FTIR spectrum of Bp*Rh(CO)$_2$ in cyclopentane*

After photolysis at 266 nm, the parent bands at 2081 and 2015 cm^{-1} were seen to bleach and there was the appearance of a new band at 1998 cm^{-1}. This band decays with a lifetime of 75.68 (± 11.68) μs and corresponds with the growth of a new species at

2089, 2024 and 1982 cm^{-1}, shown in Figure 2.25. The band at 1998 cm^{-1} is assigned to the monocarbonyl solvated product, Bp*Rh(CO)(cyclopentane), on comparison with the similar complex Bp*Rh(CO)(cyclohexane) (ν(CO) = 1992 cm^{-1}) reported by Bromberg *et al.*[84] This species is still present in very small concentrations at the end of the experiment (200 μs).

As before, the species with three peaks in the CO region at 2089, 2024 and 1982 cm^{-1} is assigned to a dimer species with bridging CO units. This product is stable for the duration of the experiment (200 μs).

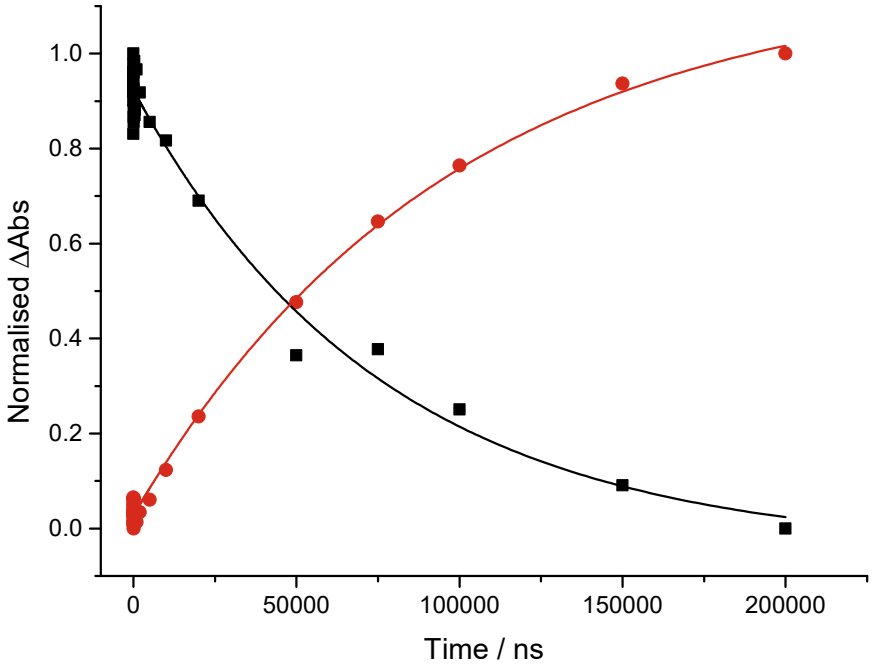

Figure 2.25: *Normalised TRIR kinetic traces for the decay of Bp*Rh(CO)(cyclopentane) (τ = 76 ± 11 μs) at 2000 cm^{-1} and the growth of the proposed dimer species (τ = 97 ± 6.6 μs) following photolysis at 266 nm in cyclopentane*

The solvated intermediate Bp*Rh(CO)(cyclopentane) (τ = 75.68 (± 11.68) μs) has a lifetime over three orders of magnitude greater than that of Bp*Rh(CO)(PFMCH) (τ = 49 (± 6) ns). This marked increase in stability of the cyclohexane complex compared to the PFMCH complex attests to the weakly bonding nature of PFMCH to the metal centre.

2.3.2.4 ns-TRIR of Bp*Rh(CO)$_2$ in *n*-heptane

Next, the ns-TRIR of Bp*Rh(CO)$_2$ in a linear alkane, *n*-heptane, was probed. Ten nanoseconds after photolysis, the parent bands are observed to bleach, with the appearance of one new band in the spectrum at 1998 cm^{-1}. This band is still present at the end of the experiment (200 μs); however, it has mostly decayed, alongside the growth of three bands at 2085, 2024 and 1981 cm^{-1}, assigned to the dimer species, Figure 2.26.

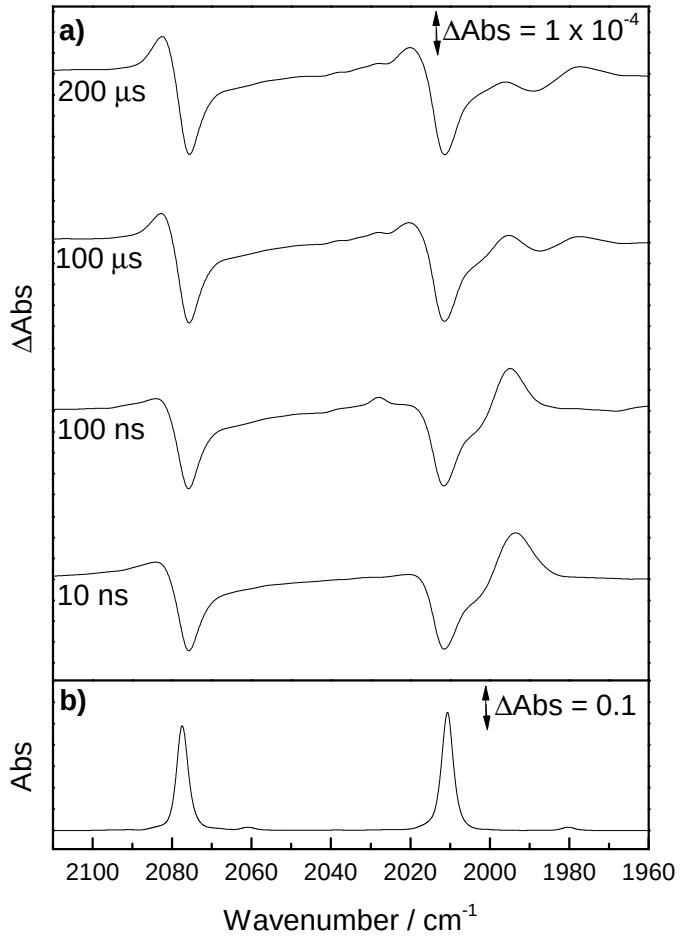

Figure 2.26: *a) ns-TRIR difference spectra at selected time delays for the 266 nm photolysis of Bp*Rh(CO)$_2$ in n-heptane and b) Ground state FTIR spectrum of Bp*Rh(CO)$_2$ in n-heptane*

The band at 1998 cm^{-1} decays with a lifetime of 114.3 ± 6.1 μs, Figure 2.27, and is assigned as Bp*Rh(CO)(*n*-heptane). This lifetime is longer than its cycloalkane counterpart Bp*Rh(CO)(*c*-pentane) by ~ 40 μs. This is an unusual observation as generally, cyclic

alkane complexes are longer lived than linear alkane complexes. We are not sure why this complex goes against expected trends, and more investigations are needed to explore this further.

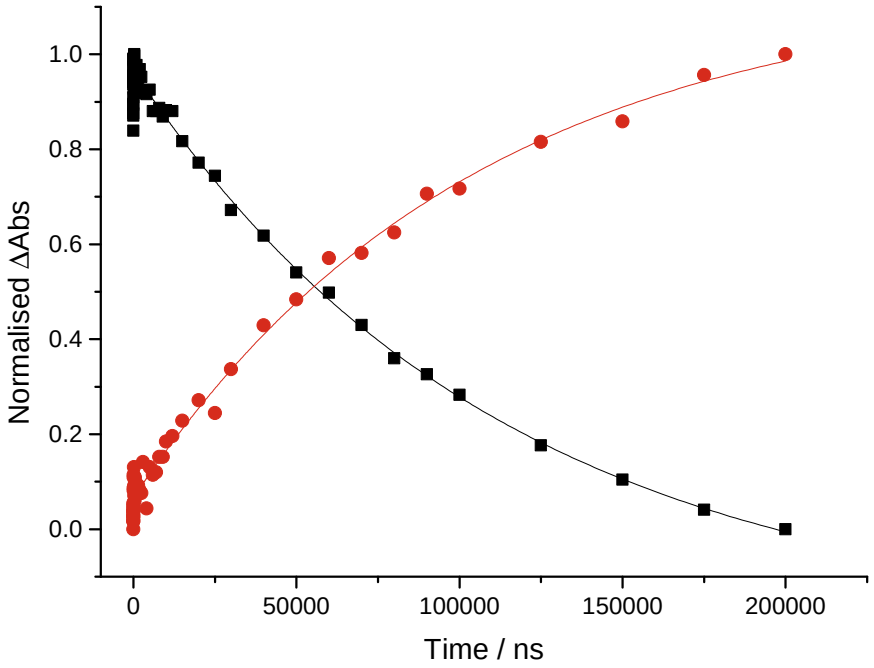

Figure 2.27: *Normalised TRIR kinetic traces for the decay of Bp*Rh(CO)(n-heptane) (τ = 114 ± 6.1 μs) at 1998 cm^{-1} and the growth of the proposed dimer species (τ = 99.8 ± 7.8 μs) at 2020 cm^{-1} following photolysis at 266 nm in n-heptane*

2.3.2.5 ns-TRIR of Bp*Rh(CO)$_2$ in cyclopentane doped perfluoromethylcyclohexane

To prove the preferential bonding of alkanes over PFMCH, the reaction was probed in cyclopentane doped PFMCH solution (5:1 PFMCH:cyclopentane). Preferential bonding af the alkane was observed by Kelly and Long, who identified cyclohexane bonding to $Cr(CO)_5$ in a solution of perfluoromethylcyclohexane doped with cyclohexane.[120]

Upon doping in the alkane, the ground state bands did not significantly shift from those in pure PFMCH; therefore, we can assume that the complex is dissolved predominantly in PFMCH. Upon photolysis at 266 nm, the parent peaks at 2086 and 2021 cm^{-1} decreased and the appearance of a new band at 2006 cm^{-1} was seen, shown in Figure 2.28.

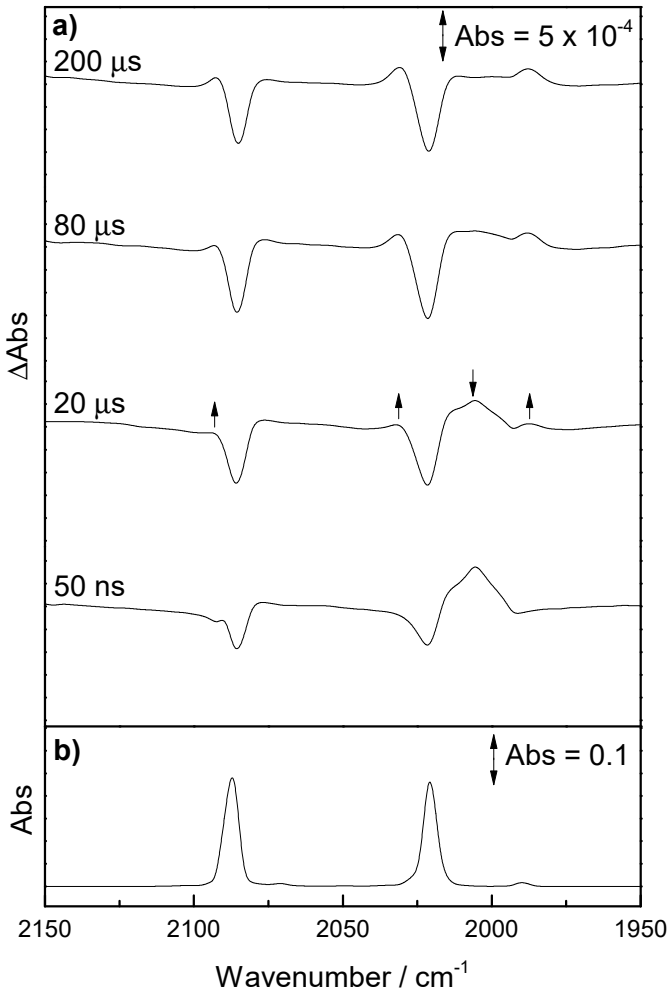

Figure 2.28: *a) ns-TRIR difference spectra at selected time delays for the 266 nm photolysis of Bp*Rh(CO)$_2$ in cyclopentane doped perfluoromethylcyclohexane and b) Ground state FTIR spectrum of Bp*Rh(CO)$_2$ in perfluoromethylcyclohexane*

This band was seen to decay (τ = 34.4 ± 4.6 μs) with the growth of a second species at 2092, 2032 and 1988 cm^{-1}, Figure 2.29, in agreement with previous experiments.

The species at 2005 cm^{-1} is expected to be a solvated monocarbonyl product, but the fourteen electron Bp*Rh(CO) could bind to either PFMCH or cyclopentane. The species Bp*Rh(CO)(PFMCH) has a peak at 2000 cm^{-1} in PFMCH, a difference of 5 cm^{-1} to what is observed here. We have already assumed that the complex is predominantly dissolved in PFMCH; therefore, we can say that if the band at 2005 cm^{-1} was due to Bp*Rh(CO)(PFMCH) the shift in wavenumber is not a solvent effect. On consideration of this, this species is assigned to the intermediate Bp*Rh(CO)(cyclopentane). Furthermore,

its lifetime is much more comparable to the alkane complex observed in the previous experiment. The complex Bp*Rh(CO)(PFMCH) had a lifetime of 49 (± 6) ns, which is 3 orders of magnitude shorter than the solvated complex in this experiment. While the ν(CO) is slightly blueshifted compared to Bp*Rh(CO)(cyclopentane) in neat cyclopentane by 5 wavenumbers, this shift is easily explained due to the change in solvent environment.

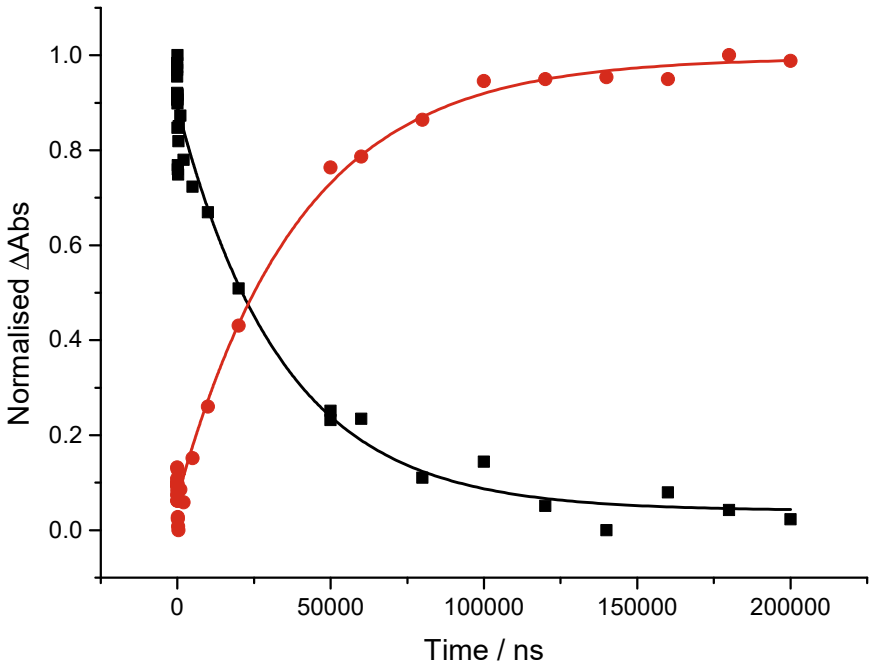

Figure 2.29: *Normalised TRIR kinetic traces for the decay of Bp*Rh(CO)(cyclopentane) ($\tau = 34 \pm 4.6$ μs) at 2005 cm^{-1} and the growth of the proposed dimer species ($\tau = 40 \pm 3.1$ μs) at 2032 cm^{-1} following photolysis at 266 nm in cyclopentane doped perfluoromethylcyclohexane*

There is the possibility that the Bp*Rh(CO) intermediate could react with both the PFMCH and cyclopentane present to form a mixture of Bp*Rh(CO)(cyclopentane) and Bp*Rh(CO)(PFMCH). Since the wavenumbers of both these complexes are very similar (indeed, they both have an identical absorption of 2000 cm^{-1} in their respective solvents), it would be extremely difficult to distinguish if there was a mixture of cyclopentane and PFMCH solvates. However, the kinetics of the decay of the peak at 2006 cm^{-1} fit to a simple single exponential decay and since the rate constants of the two cyclopentane and PFMCH solvates are different by several orders of magnitude (1.4×10^7 *vs.* 9.1×10^3

M^{-1} s^{-1}, respectively), we can assume that any equilibrium that might be present in the mixture is heavily favoured towards Bp*Rh(CO)(cyclopentane).

2.3.2.6 ns-TRIR of Bp*Rh(CO)$_2$ in Ethane Doped Perfluoromethylcyclohexane

For the following experiments, we looked to take advantage of the high gas solubility of perfluoromethylcyclohexane by doping weakly binding gaseous ligands into solution to induce preferential binding of the dopant. First was the gaseous alkane, ethane. The solution was degassed and placed under 1 bar of ethane gas. The ns-TRIR results are shown in Figure 2.30.

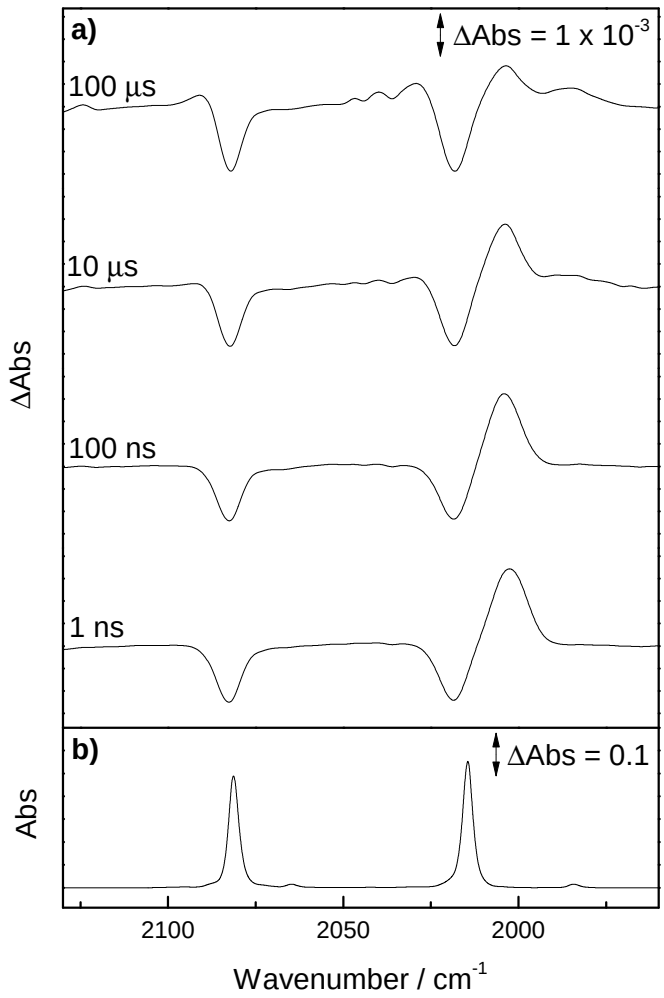

Figure 2.30: *a) ns-TRIR difference spectra at selected time delays for the 266 nm photolysis of Bp*Rh(CO)$_2$ in ethane doped perfluoromethylcyclohexane and b) Ground state FTIR spectrum of Bp*Rh(CO)$_2$ in perfluoromethylcyclohexane*

One nanosecond after excitation, there is one peak in the spectrum at 2005 cm^{-1}. By 10 μs, this peak had started to decay with the growth of several new peaks. As seen in previous experiments, there were three peaks at 2090, 2029 and 1985 cm^{-1}, assigned to a dimer. The rate of decay of the peak at 2000 cm^{-1} was seen to match the growth of the dimer peaks, Figure 2.31, with a lifetime of 20.3 ± 1.5 μs. The lifetime of this species is several orders of magnitude longer than Bp*Rh(CO)(PFMCH) and much more comparable to alkane bonded species previously assigned Bp*Rh(CO)(*c*-pentane) and Bp*Rh(CO)(*n*-heptane); therefore, it is assigned as Bp*Rh(CO)(ethane).

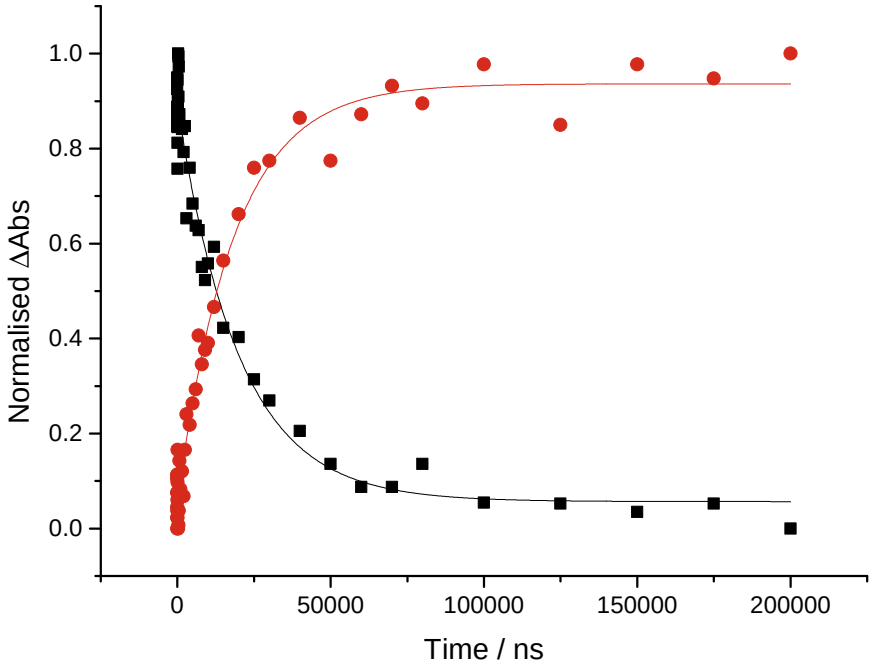

Figure 2.31: *Normalised TRIR kinetic traces for the decay of Bp*Rh(CO)(ethane) (τ = 20.3 ± 1.6 μs) at 2005 cm^{-1} and the growth of the proposed dimer species (τ = 18.5 ± 1.2 μs) at 2092 cm^{-1} following photolysis at 266 nm in ethane doped perfluoromethylcyclohexane*

There are also two other peaks at 2047 and 2040 cm^{-1}, which also grow in at the same rate as the other peaks. A second feature of this experiment is that the peak due to Bp*Rh(CO)(ethane) does not appear to fully decay. In experiments performed at higher temperatures later in this Chapter, this peak appears to have a biexponential decay, with a shorter lifetime on the order of tens of microseconds, and a second lifetime which is much

longer, only very slowly starting to decay by the end of the experiment.

Therefore, it is proposed that there are two species present at the peak at 2005 cm^{-1}; Bp*Rh(CO)(ethane) and another unknown species. Since the lifetime of the unknown species is exceptionally long, indeed it is only seen to start to decay at 50 and 60 °C, it is feasible that there is a water bound complex present, Bp*Rh(CO)(H_2O). Water complexes have been shown to be very long-lived.[121] Since both the compound and the solvent were dried thoroughly prior to the experiment (no traces of water were found in compound analysis and the PFMCH was tested and found to have a water content of < 10 ppm), it is most likely that the water has been introduced into the solution via the ethane gas.

The presence of these extra peaks at late time delays may suggest that the dimer that forms contains the weakly bonding ligand. The new peaks at 2047 and 2040 cm^{-1} in the spectra are tentatively assigned as a dimer containing a H_2O molecule.

2.3.2.7 ns-TRIR of Bp*Rh(CO)$_2$ in Xenon Doped Perfluoromethylcyclohexane

For this experiment, the aim was again to take advantage of the high gas solubility of PFMCH by doping gaseous xenon into solution. In doing this, it was hoped that the xenon would preferentially bind over the PFMCH and we would be able to create a metal-xenon bond. Upon photolysis, the parent bands at 2086 and 2121 cm^{-1} decreased and a new band at 2005 cm^{-1} appeared. This band decayed with a lifetime of 3.33 ± 0.62 μs, corresponding to the growth of three new bands at 2092, 2032 and 1988 cm^{-1}, as seen in all previous experiments.

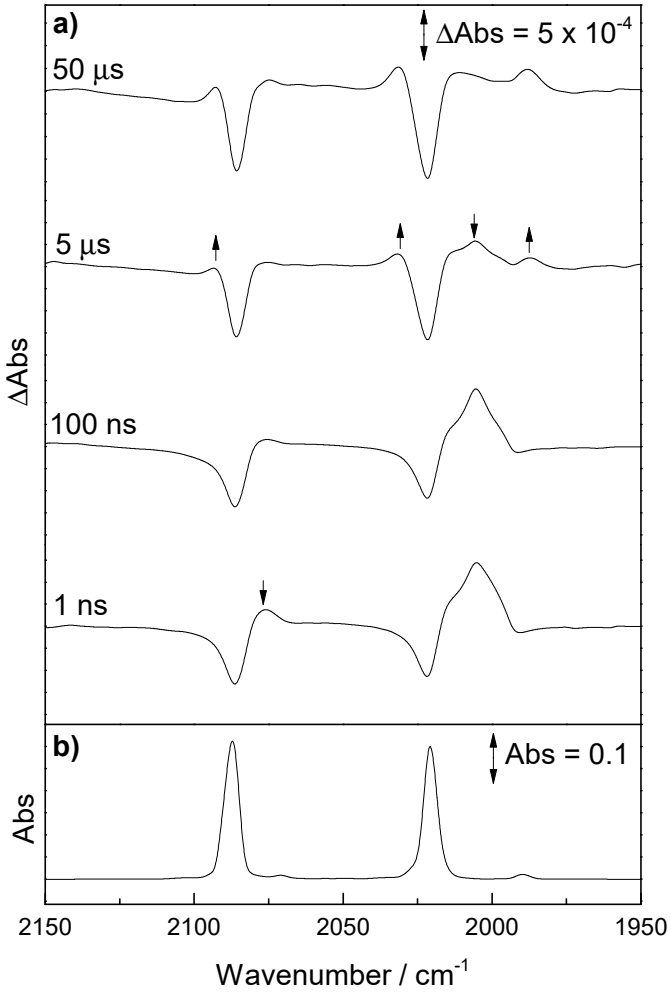

Figure 2.32: *a) ns-TRIR difference spectra at selected time delays for the 266 nm photolysis of Bp*Rh(CO)$_2$ in xenon doped perfluoromethylcyclohexane and b) Ground state FTIR spectrum of Bp*Rh(CO)$_2$ in perfluoromethylcyclohexane*

The band at 2005 cm^{-1} is assigned as the noble gas complex Bp*Rh(CO)Xe due to its lifetime being *ca.* two orders of magnitude higher than that of Bp*Rh(CO)(PFMCH) measured in the previous section. As it has in previous experiments, the decay of the solvated intermediate corresponds to the growth of the dimer species, shown in Figure 2.33, which again is stable for the remainder of the experiment.

The species that grows in is again assigned as the dimer species and is stable for the timeframe of the experiment. Present in this experiment, where it has not been previously, is a peak at 2075 cm^{-1}. This peak exhibits some interesting kinetics in that it decays and then grows again to ~30 % of its original intensity. This peak is hard to assign as it

could be one of many possibilities. One option is that it could be an intermediate in which two xenon atoms have bound to the intermediate, Bp*Rh(CO)$(Xe)_2$. Since this would satisfy the 18 electron rule, the prospect is possible. However, such a complex would be blueshifted with respect to Bp*Rh(CO)(Xe) (2000 cm^{-1}); therefore, this possibility is ruled out. The peak could be assigned to another form of dimer. As described before, the dimer [$(CO)_2$Rh(μ-Bp*)Rh$(CO)_2$] is known to have peaks in the infrared at 2017, 2071 and 2085 cm^{-1}.[119] This band seen here in TRIR at 2075 cm^{-1} occurs at a very similar wavenumber to the 2071 cm^{-1} reported by Banditelli *et al.*, and the reported bands at 2085 cm^{-1} and 2017 cm^{-1} occur close to the parent bleaches and may possibly be obscured. This band is very tentatively assigned to the dimer, [$(CO)_2$Rh(μ-Bp*)Rh$(CO)_2$], which also may be forming as a by-product of photolysis.

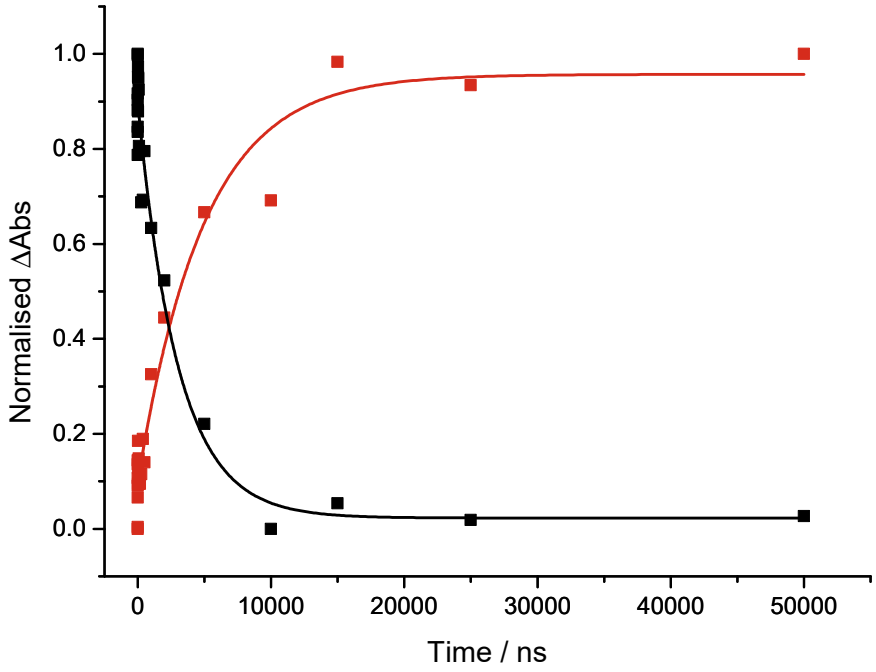

Figure 2.33: *Normalised TRIR kinetic traces for the decay of Bp*Rh(CO)(Xe) ($\tau = 3.0 \pm 0.5$ μs) at 2005 cm^{-1} and the growth of the proposed dimer species ($\tau = 4.9 \pm 0.8$ μs) at 2032 cm^{-1} following photolysis at 266 nm in xenon doped in perfluoromethylcyclohexane*

2.3.2.8 Comparison of Weakly Bonding Solvents

Table 2.3 summarises the ν(CO) of the solvated complexes and their respective lifetimes. The trend in lifetimes shows that the stability of the solvated complex decreases in the order: Bp*Rh(CO)(*n*-heptane) > Bp*Rh(CO)(*c*-pentane) (solvent = *c*-pentane) > Bp*Rh(CO)(*c*-pentane) (solvent = PFMCH) > Bp*Rh(CO)(ethane) > Bp*Rh(CO)Xe >> Bp*Rh(CO)(PFMCH). The lifetime of Bp*Rh(CO)(PFMCH) is much smaller (by two–three orders of magnitude) relative to the other intermediates, highlighting the extremely weakly coordinating nature of perfluorinated media, and their usefulness as a weakly coordinating solvent to facilitate bonding of alkanes and noble gases. All the ν(CO) of the complexes Bp*Rh(CO(L) have extremely similar wavenumbers, varying between 0 and 5 cm^{-1} at ambient temperature. The alkane and noble gas complexes Bp*Rh(CO)(cyclopentane) and Bp*Rh(CO)Xe vary in wavenumber by only 1 cm^{-1} in PFMCH. This is consistent with previous studies which have shown that CO stretching frequencies of alkane and noble gas solvate complexes vary in wavenumber by typically less than 1 cm^{-1}.[122] The lifetimes of all alkane complexes compared to the Xe complex are also fairly similar, both stable on the μs timescale. This similarity in wavenumber and lifetimes shows the important comparison that can be drawn between the coordinating properties of alkanes and noble gases.

The complexes are extremely long-lived, notably Bp*Rh(CO)(heptane) and Bp*Rh(CO)(*c*-pentane), which have a marked increase in lifetime when compared to other Rh–alkane complexes, which tend to C–H activate the alkane and hence are relatively short-lived. For example, the related complex Cp*Rh(CO)(*c*-pentane) has a lifetime of 10.2 ± 0.8 ns, over three orders of magnitude smaller than that of Bp*Rh(CO)(*c*-pentane).[116]

The lifetime of Bp*Rh(CO)(Xe) (3.3 ± 0.6 μs) is among some of the longest known transition metal–noble gas complexes. Only the rhenium complexes Cp'$Re(CO)_2$(Xe) are longer lived. While synthesised before at −50 °C, this is the first time to our knowledge that Bp*Rh(CO)(Xe) has been characterised at room temperature and pressure.

The long-lived nature of these complexes is interesting in relation to the nature of the complex Bp*Rh(CO)$_2$. It has been suggested that cationic metal complexes are able to make stronger bonds between the metal centre and a weakly bonding ligand due to their electron deficient nature. By their very nature sixteen electron metal complexes such as Bp*Rh(CO)$_2$ are electron deficient; therefore, it is hypothesised that a similar effect is taking place here.

Table 2.3: Infared ν(CO) bands and lifetimes (in μs) of Bp*Rh(CO)(X) (X = PFMCH, alkane or Xe) in different solvents

Compound	Solvent	ν(CO) / cm^{-1}	Lifetime / μs	Reference
Bp*Rh(CO)(PFMCH)	PFMCH	2000	0.05 ± 0.01	This work
Bp*Rh(CO)(*c*-pentane)	*c*-pentane	1998	71.5 ± 12.9	This work
	PFMCH	2006	35.3 ± 5.0	This work
Bp*Rh(CO)(*n*-heptane)	*n*-heptane	1998	114.3 ± 6.1	This work
Bp*Rh(CO)(C_2H_6)	PFMCH	2005	20.3 ± 1.6	This work
Bp*Rh(CO)Xe	PFMCH	2005	3.3 ± 0.6	This work
	*liq*Xe, -50 °C	1998	34.7 ± 4.5	98

2.3.3 Temperature Dependent TRIR Studies of Bp*Rh(CO)$_2$ with Weakly Coordinating Ligands

Following the successful characterisation of complexes Bp*Rh(CO)(X), where X = heptane, *c*-pentane, ethane and Xe, the TRIR at variable temperatures was undertaken to determine the activation energies, E_a, and Eyring parameters, the enthalpy and entropy of activation ($\Delta H^{\ddagger}$ and $\Delta S^{\ddagger}$, respectively), of the complexes. These experimental values will be compared to the computationally calculated values for the bond dissociation energy, BDE. This will give us an important comparison of the experimental and computational values, helping us to assess the accuracy of computationally calculated values, which will be useful for future work in Chapter 3.

The decay of the complexes Bp*Rh(CO)(X) were monitored at 5 different temperatures ranging between 15 and 60 °C (dependent on the boiling point of the solvent and the solubility of the complex in the respective solvent at low temperatures), and the results are summarised, alongside calculated rate constants and ln(k), in Table 2.4.

The calculated value for ln(k) was plotted again $\frac{1}{T}$, and also $\ln(\frac{k}{T})$ was plotted against $\frac{1}{T}$ to give Arrhenius and Eyring plots, typical examples of which are shown in Figure 2.34.

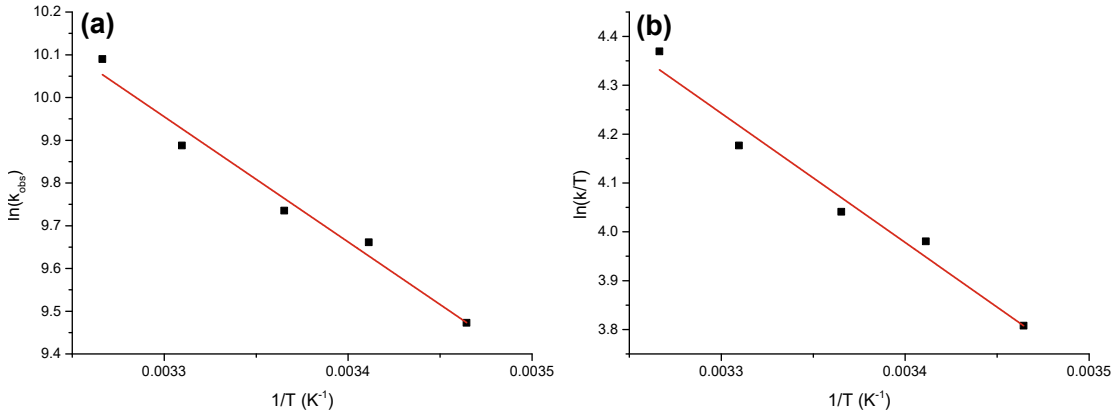

Figure 2.34: *Typical (a) Arrhenius and (b) Eyring Plots for the decay of Bp*Rh(CO)(X)*

From these plots, activation energies, E_a, and enthalpy and entropy of activation, $\Delta H^{\ddagger}$ and $\Delta S^{\ddagger}$, were calculated and are shown in Table 2.5. Eyring parameters provide a slightly

Table 2.4: Experimental lifetimes and calculated rate constants for the decay of Bp*Rh(CO)(X), where X = C_2H_6, C_5H_{10}, C_7H_{16} or Xe, at varying temperatures

	Temp / K	Lifetime / s	Rate Constant (k)	ln(k)
Bp*Rh(CO)(C_2H_6)	293.15	2.02×10^{-5}	4.94×10^{4}	5.13
	303.15	1.54×10^{-5}	6.51×10^{4}	5.37
	313.15	1.15×10^{-5}	8.71×10^{4}	5.63
	323.15	9.07×10^{-6}	1.10×10^{5}	5.83
	333.15	7.11×10^{-6}	1.41×10^{5}	6.05
Bp*Rh(CO)(*c*-C_5H_{10})	288.65	2.89×10^{-4}	1.30×10^{4}	9.47
	293.15	2.93×10^{-4}	1.57×10^{4}	9.66
	297.15	2.97×10^{-4}	1.69×10^{4}	9.74
	302.15	3.02×10^{-4}	1.97×10^{4}	9.89
	306.15	3.06×10^{-4}	2.42×10^{4}	10.09
Bp*Rh(CO)(*n*-C_7H_{16})	283.15	1.19×10^{-4}	8.38×10^{3}	9.03
	293.15	1.13×10^{-4}	8.84×10^{3}	9.09
	303.15	8.39×10^{-5}	1.19×10^{4}	9.39
	313.15	7.08×10^{-5}	1.41×10^{4}	9.56
	323.15	6.22×10^{-5}	1.61×10^{4}	9.68
Bp*Rh(CO)(Xe)	293.15	4.48×10^{-6}	2.23×10^{5}	12.32
	303.15	4.30×10^{-6}	2.33×10^{5}	12.36
	313.15	3.95×10^{-6}	2.53×10^{5}	12.44
	323.15	3.64×10^{-6}	2.75×10^{5}	12.52
	333.15	3.51×10^{-6}	2.85×10^{5}	12.56

clearer picture of the reaction mechanism compared to activation energies. Values of $\Delta S^{\ddagger}$ can help assign a reaction mechanism; generally large negative values of $\Delta S^{\ddagger}$ point towards an associative mechanism, whilst positive values would suggest a dissociative mechanism. However, calculations of $\Delta S^{\ddagger}$ must be carefully considered as there is large degree of error which comes from extrapolation of the data. For all complexes, both mechanisms were considered in calculations of $\Delta S^{\ddagger}$, with both resulting in a large negative value for $\Delta S^{\ddagger}$. Even with the potential for large errors in these values, the significant size of $\Delta S^{\ddagger}$ here is highly indicative of an associative mechanism. Moreover, several studies of metal–alkane complexes have shown that their reaction proceeds via an associative mechanism.[42,66] Therefore, the reaction is tentatively assigned as proceeding via an associative mechanism, and hence only ${}^{Ass}\Delta S^{\ddagger}$ are shown here.

Table 2.5: Experimentally determined Arrhenius and Eyring parameters for Bp*Rh(CO)X, where X = alkane or Xe

	E_a kJmol^{-1}	$\Delta H^{\ddagger}$ kJmol^{-1}	$\Delta S^{\ddagger}$ Jmol^{-1}	${}^{298}\Delta G^{\ddagger}$ kJmol^{-1}
Bp*Rh(CO)(C_2H_6)	18.8	16.2	-97.6	45.3
Bp*Rh(CO)(*c*-C_5H_{10})	24.4	22.0	-89.7	48.7
Bp*Rh(CO)(*n*-C_7H_{16})	13.4	10.9	-131	50.0
Bp*Rh(CO)(Xe)	5.31	2.72	-133	42.4

Notably, the Xe complex, Bp*Rh(CO)(Xe), also shows strong evidence of reacting with an associative mechanism. The complexes $CpM(CO)_2Xe$ (M = Mn or Re) were found to react with a dissociative reaction, in contrast to their alkane complex analogues. However, a study by Jina *et al.* found that the corresponding rhodium complexes, CpRh(CO)(Xe) and CpRh(CO)(alkane), both reacted via an associative mechanism, in contrast to the rhenium complexes. This led them to hypothesise that late transition metals react differently to early transition metals.[68] Our finding here is in keeping with this hypothesis. The same

work also found much lower $\Delta H^{\ddagger}$ values for the rhodium complexes in comparison to the rhenium complexes, (15.2 $kJmol^{-1}$ *vs.* 47.2 $kJmol^{-1}$ for Rh and Re, respectively). The calculated values found in this thesis are comparable to these values for rhodium, further supporting the theory that late transition metals react differently to early transition metals. Values of $\Delta S^{\ddagger}$ are also comparable to those reported for Cp'Rh(CO)(Xe) (-79 $Jmol^{-1}$).

Whilst the values for $\Delta S^{\ddagger}$ are relatively similar, the difference in $\Delta H^{\ddagger}$ varies significantly between complexes. For example the difference between Bp*Rh(CO)(c-C_5H_{10}) and Bp*Rh(CO)(Xe) is just under an order of magnitude (22.0 *vs.* 2.72 $kJmol^{-1}$, respectively). These values for $\Delta H^{\ddagger}$ give an indication of the bond strength between the ligand and the metal centre. Therefore, $\Delta H^{\ddagger}$ seems to be the most important factor in controlling the reaction which is in contrast to the findings of Long and coworkers, who found that $\Delta H^{\ddagger}$ remained relatively constant for a series of complexes of the form (η^6-arene)$Cr(CO)_2$(alkane).[43] Again, this supports the theory that early transition metals react differently to late transition metals.

Experimental activation parameters and computationally calculated bond dissociation energies values are compared in Table 2.6. It is important to note that the activation energy and bond dissociation energy are two distinct metrics. If the reaction proceeded by fully breaking the M–X bond before reforming the parent or further reacting, then the BDE and activation energy should be roughly the same. However, chemical reactions do not often proceed in this fashion, in many instances the reaction proceeds via one or more transition states, for example in an associative mechanism, where in the transition state the incoming ligand binds to the metal complex, temporarily increasing coordination at the metal centre. This would be a lower energy pathway and hence lead to a lower activation energy. The activation energy is also affected by many other things including solvent, temperature and the presence of other molecules like catalysts. Furthermore, for the reactions we are studying, we have hypothesised that they are proceeding via an associative mechanism by analysis of the $\Delta S^{\ddagger}$ values. This mechanism involves a lower energy transition state, and as such, in comparing the BDE and activation energy, one would expect the BDE

to be higher. Indeed, the values calculated here show a consistent overestimation by the computational BDE values by about 40 $kJmol^{-1}$. Whilst we cannot take much away from a direct comparison of the individual values, it is more useful to look at the correlation between the values in order to assess the accuracy of the computational results. Chandra and Uchimaru found good correlation between calculated C–H bond dissociation energies and experimental activation energies of haloethanes and halomethanes in their reaction with an OH radical.[123]

Table 2.6: Experimental activation energies and calculated bond dissociation energies for Bp*Rh(CO)X, where X = *c*-pentane and Xe

	Experimental Activation Energy (E_a) / $kJmol^{-1}$	Experimental $^{298}\Delta G^{\ddagger}$ / $kJmol^{-1}$	Calculated Bond Dissociation Energy (BDE) / $kJmol^{-1}$
Bp*Rh(CO)(C_2H_6)	18.8	45.3	58.3
Bp*Rh(CO)(*c*-C_5H_{10})	24.4	48.7	63.2
Bp*Rh(CO)(*n*-C_7H_{16})	13.4	50.0	60.6
Bp*Rh(CO)(Xe)	5.31	42.4	47.1

Figure 2.35 shows a graphical comparison of calculated bond dissociation energies and experimentally determined activation energies. Values for the Gibbs free energy, $\Delta G^{\ddagger}$, at 298 K have also been included for comparison. The values for the $\Delta G^{\ddagger}$ are closer in value to the calculated bond dissociation energies and follow the same trend except for *c*-pentane, where the BDE predicts a slight rise in energy, but experimentally there is a small decrease. Large errors in the calculation of $\Delta S^{\ddagger}$, as mentioned previously, can translate to errors in calculation of $\Delta G^{\ddagger}$. This may account for this small discrepancy.

The values for activation energy, as expected, are much lower than the values for BDE; however, all but *n*-heptane show good agreement with the general trend. Indeed, with the exception of *n*-heptane, the activation energies show a much better fit with the

calculated bond dissociation energies compared to Gibbs free energy. We can assess this by plotting activation energy against bond dissociation energy, as shown by Chandra and Uchimaru,[123] and the accuracy can be determined by the fit of a straight line. The plot of activation energy *vs.* bond dissociation energy is shown in Figure 2.36. The data for *n*-heptane is a clear outlier, with the activation energy much lower than predicted by the bond dissociation energy calculations. Discounting *n*-heptane, the other three data points show an excellent fit to a straight line, proving the accuracy of the computational calculations.

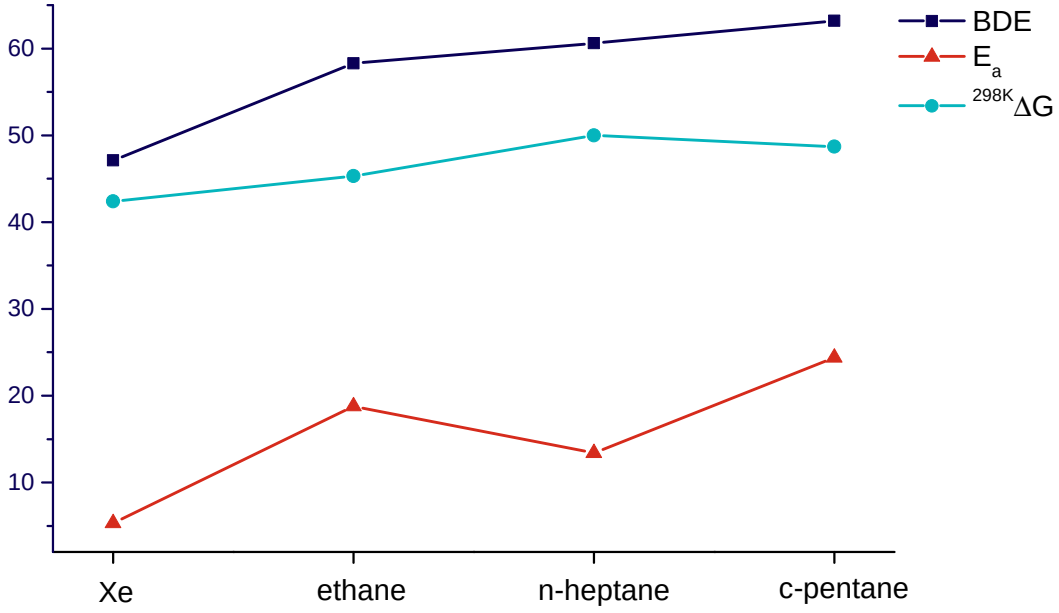

Figure 2.35: *Comparison of computationally calculated bond dissociation energies (BDE) and experimentally determined activation energies (E_a) and Gibbs free energy at 298 K ($^{289K}\Delta G$) for complexes of the form Bp*Rh(CO)(X), where X = Xe, ethane, n-heptane and c-pentane*

It is interesting that the activation energy of *n*-heptane (13.4 kJmol^{-1}) is low, even lower than that of ethane (18.8 kJmol^{-1}), especially when you take in to consideration that of all the complexes, it is the longest lived at room temperature (114.3 ± 6.1 μs).

Multiple computational studies have shown that heptane complexes bond dissociation energies are higher than those of short-chain alkanes, and experimentally lifetimes have also been shown to be longer than those of short chain alkanes. The BDE calculations

performed here follow all the known trends for alkane complexes; therefore, it seems unlikely that there is an error in them.

It seems more likely that there is an error in the activation energy value; however, due to time restraints we were unable to repeat the experiment. There are several factors consider as to why there is a discrepancy in the activation energy value for Bp*Rh(CO)(*n*-heptane). The solvent environments are not the same across all experiments, with the Bp*Rh(CO)(ethane) and Bp*Rh(CO)(Xe) experiments being performed in PFMCH, whilst Bp*Rh(CO)(*c*-pentane) and Bp*Rh(CO)(*n*-heptane) experiments were performed in their respective alkane solvents. This different solvent environment could have an effect on the activation energy; however, Bp*Rh(CO)(*c*-pentane) also has a different solvent environment but is found to fit well with the main trend.

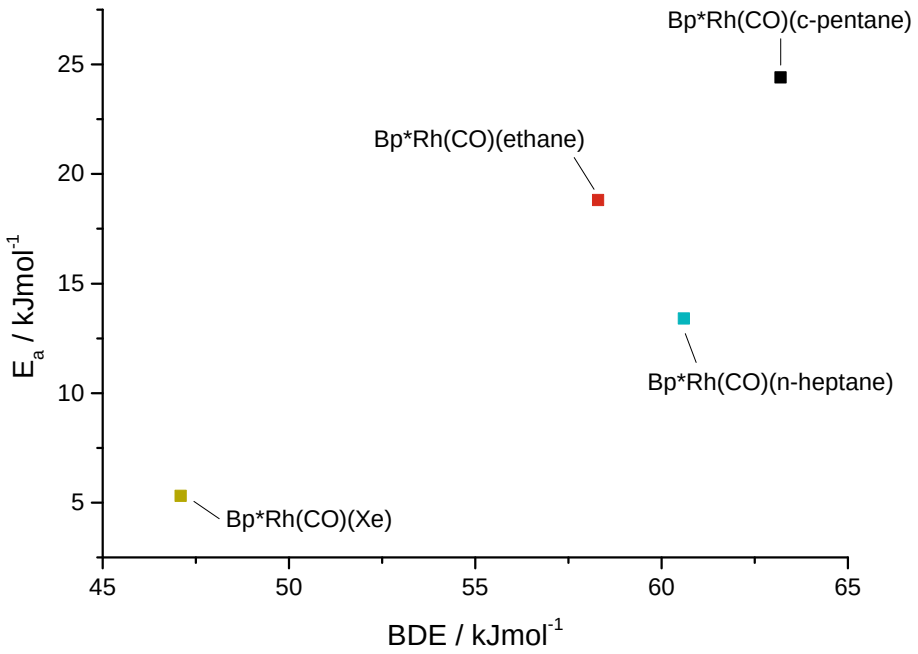

Figure 2.36: *Comparison of computationally calculated bond dissociation energies (BDE) and experimentally determined activation energies (E_a) and Gibbs free energy at 298 K ($^{289K}\Delta G$) for complexes of the form Bp*Rh(CO)(X), where X = Xe, ethane, n-heptane and c-pentane*

We consider that the *n*-heptane complex may react in a different way to the other complexes that results in the abnormal activation energy. However, it is clear from the

$\Delta S^{\ddagger}$ and $\Delta H^{\ddagger}$ values that the complex reacts via an associative mechanism, in the same way as all other studied complexes. It must be noted that *n*-heptane is a linear solvent, whilst PFMCH and *c*-pentane are cyclic solvents. Properties of linear and cyclic alkanes are known to be different and can effect chemistry.[5] It may be that as the X dissociates, the migration of X away from the complex may be slowed in the bulky cyclic solvent environment, slowing the rate of reaction and hence leading to an increased activation energy. However, we simply do not have enough data to support this theory.

It is clear that more experiments need to be completed on a range of different complexes and in different solvent environments to fully understand the trends in BDE and activation energy. There is clearly still much to learn about metal–alkane and metal–noble gas complexes. However, these results have shown that overall, the computational bond dissociation energies show good agreement with experimental parameters and still remain an excellent tool for predicting long-lived transition metal alkane and noble gas complexes.

2.4 Conclusions and Future Work

The photochemical reactions of $Tp^*Rh(CO)_2$ have been studied in a mixture of perfluorinated and alkane solvents. In the ns-TRIR PFMCH/cyclopentane mixture, there was the presence of peaks due to $Tp^*Rh(CO)$(*c*-pentane) which rearranges to form the C–H activated $Tp^*Rh(CO)(C_5H_9)H$. There was also a new peak which has been assigned tentatively as $Tp^*Rh(CO)(C_7F_{13})F$. The decay of $Tp^*Rh(CO)(\kappa^3$-cyclopentane) to form $Tp^*Rh(CO)(\kappa^2$-cyclopentane) was twice as slow in PFMCH/*c*-pentane than it was in neat *c*-pentane. Furthermore, the decay of $Tp^*Rh(CO)(\kappa^3$-cyclopentane) did not match the growth of $Tp^*Rh(CO)(\kappa^2$-cyclopentane) in PFMCH/*c*-pentane as it did in neat cyclopentane, alluding to the presence of another substance, which could be $Tp^*Rh(CO)(\kappa^3$-PFMCH). In the future, it is hoped that a perfluorous soluble analogue of $Tp^*Rh(CO)_2$ will be able to be synthesised so that its reactions be be probed in neat perfluorinated media to elucidate the reaction.

The photochemical reactions of sixteen electron $Bp^*Rh(CO)_2$ have been investigated by TRIR in weakly bonding solvents, resulting in the characterisation of $Bp^*Rh(CO)$(PFMCH), $Bp^*Rh(CO)$(alkane) (alkane = C_2H_6, C_5H_{10} and C_7H_{16}) and $Bp^*Rh(CO)$(Xe). The lifetimes of the complexes increased in the order $Bp^*Rh(CO)$(PFMCH) << $Bp^*Rh(CO)$(Xe) < $Bp^*Rh(CO)(C_2H_6)$ < $Bp^*Rh(CO)(C_5H_{10})$ < $Bp^*Rh(CO)(C_7H_{16})$. The lifetime of $Bp^*Rh(CO)$(PFMCH) was two to three orders of magnitude smaller than all other complexes, highlighting the extremely weakly bonding nature of PFMCH and its usefulness as a solvent with other weakly bonding ligands.

$Bp^*Rh(CO)$(alkane) and $Bp^*Rh(CO)$(Xe) were found to have remarkably long lifetimes, particularly $Bp^*Rh(CO)(C_7H_{16})$ (114.3 μs). The alkane complexes are particularly long-lived in comparison to other rhodium–alkane complexes, in which lifetimes are generally much shorter due to the process of C–H activation. Furthermore, the lifetime of $Bp^*Rh(CO)$(Xe) is also notable at 3.3 μs, which is an extremely long-lived xenon complex characterised under ambient conditions. To our knowledge the only longer-lived complexes at room temperature and pressure are $CpRe(CO)_2$(Xe) and $Cp^*Re(CO)_2$(Xe). We postu-

late that the sixteen electron and naturally electron deficient nature of Bp*Rh(CO)$_2$ is a factor in its ability to make long-lived complexes.

Variable temperature TRIR has revealed information about the activation energy and mechanism of reaction Bp*Rh(CO)(X) complexes. The largest activation energy was for Bp*Rh(CO)(cyclopentane) (E_a = 24.4 kJmol^{-1}) and the lowest was for Bp*Rh(CO)(Xe) (E_a = 5.31 kJmol^{-1}). The reactions of all complexes were found to proceed via an associative mechanism. Notably this includes Bp*Rh(CO)(Xe), which agrees with the hypothesis of Jina *et al.*, who found that Cp'Rh(CO)(Xe) reacted with a different mechanism to Cp'Re(CO)$_2$(Xe) (associative *vs.* dissociative, respectively), leading to the hypothesis that late transition metals react differently to early transition metals. $\Delta H^{\ddagger}$ was found to be the most important factor in controlling the reaction, with $\Delta S^{\ddagger}$ remaining relatively constant, in contrast to the findings of Long *et al.* when investigating reactions of early transition metals.

The accuracy of computational calculations of bond dissociation energy have been assessed by comparison with experimental activation energies. Computational calculations were found to accurately predict the trends of reactivity, cementing their usefulness in predicting long-lived metal–alkane and metal–xenon complexes. In the future we hope to conduct more variable temperature TRIR experiments to calculate the activation parameters of additional Bp*Rh(CO)(X) complexes in order to be able to make a more conclusive comparison with bond dissociation energy calculations. This includes conducting the variable temperature TRIR in a variety of solvents to assess the effect of cyclic and linear solvents on activation parameters.

Chapter 3

Bond Dissociation Energy Calculations of Non-Conventional Transition Metal Alkane Complexes

3.1 Introduction

Concurrent with the rapid growth and development of computers in the last three decades is the growth in computational chemistry. One of the great advantages of computational chemistry is that you can screen libraries of compounds relatively quickly, and one can even probe hypothetical chemical systems, or those that aren't stable under room conditions. Calculations of a molecule's energy, structure and frequency can go hand in hand with laboratory research and confirm experimental observations. Work in Chapter 2 has shown the accuracy of computational calculations and how they can be used to predict the dissociation energy of a particular bond, and this chapter aims to find long-lived alkane and noble gas complexes by screening bond dissociation energies of previously uninvestigated complexes.

Computational calculations can play an important role in the search for long-lived transition metal alkane and noble gas complexes. Chapter 2 has detailed the vast background

of these complexes; hence, we will go into no further detail here. DFT calculations calculating the bond dissociation energy (BDE) of the photogenerated transition metal fragment from a weakly bound alkane or noble gas will provide important predictions. Bond dissociation energy values are directly linked to the lifetimes of these short-lived complexes. A larger BDE corresponds to a stronger bond and hence a more stable and longer-lived complex. A detailed look into the literature surrounding calculated bond dissociation energies will be later in this introduction.

The basis of computational chemistry is that a molecules physical and chemical properties can be determined from its electronic structure. There are several quantum chemical methods available to study a molecules electronic structure. These include multi-configurational methods and coupled-cluster theory (both highly accurate and computationally expensive) and semi-empirical methods (fast but inaccurate). Density functional theory (DFT) is another widely used method to computationally model the properties of molecules, and it can provide good results at relatively low computational cost. DFT is the method that has been used in this work, and the theory behind it will henceforth be explained.

3.1.1 The Schrödinger Equation

The basis of theoretical chemistry and the equation at the core of quantum mechanics is the time-independent Schrödinger equation, which is represented mathematically in Equation 3.1. It is essentially a wave equation; describing the behaviour of molecular and atomic systems.

$$\hat{H}\Psi = E\Psi \tag{3.1}$$

In this equation $\hat{H}$ is the Hamiltonian operator for the system, E is the energy and Ψ is the wavefunction or eigenfunction.

The molecular Hamiltonian describes the interactions within a system of atoms, and is

a sum of the nuclear and electronic kinetic energies, $\hat{T}_N$ and $\hat{T}_e$, the nuclei-nuclei repulsion $\hat{V}_{NN}$, the electron–nuclei repulsion, $\hat{V}_{eN}$ and the electron–electron repulsion $\hat{V}_{ee}$;

$$\hat{H} = \hat{T}_N + \hat{T}_e + \hat{V}_{NN} + \hat{V}_{eN} + \hat{V}_{ee} \tag{3.2}$$

which can be written in atomic units as;

$$\hat{H} = -\sum_I \frac{1}{2M_I}\nabla_I^2 + \sum_I \sum_{J>I} \frac{Z_I Z_J}{|R_I - R_J|} - \sum_i \frac{1}{2}\nabla_i^2 \sum_i \sum_I \frac{Z_I}{|r_i - R_I|} + \sum_i \sum_{j>i} \frac{1}{|r_i - r_j|} \tag{3.3}$$

where M_I and Z_I are the nuclear masses and charges, respectively and $R_I - R_J$, $r_i - R_I$ and $r_i - r_j$ are the differences between the particle positions, where i and j label electrons and I and J label nuclei.

This complex equation for the molecular Hamiltonian can be simplified somewhat by the Born–Oppenheimer approximation.[124] This approximation allows for the separation of the nuclear and electronic energies based on the assumption that, due to the increased size of the nuclei compared to the electrons (nuclei are ~1800 times bigger), they are considered stationary on the electronic timescale. Using this approximation, the expressions for nuclear kinetic energies and nuclei–nuclei repulsion, $\hat{T}_N$ and $\hat{V}_{NN}$, are excluded from the expression for the Hamiltonian in Equation 3.3, so it then becomes the so-called electronic Hamiltonian;

$$\hat{H} = -\sum_i \frac{1}{2}\nabla_i^2 \sum_i \sum_I \frac{Z_I}{|r_i - R_I|} + \sum_i \sum_{j>i} \frac{1}{|r_i - r_j|} \tag{3.4}$$

Whilst this equation is much simpler, it is still a many-body problem which is too complex to solve. There are other approximations such as Hartree–Fock Theory,[125] which will not be discussed here, that attempt to simplify this equation so that it can be solved. However, one of the most common methods to solve this equation is Kohn–Sham density functional theory (KS-DFT).

3.1.2 Kohn–Sham Density Functional Theory

The basis of KS-DFT, referred to from now on simply as DFT, is expressing the total energy in terms of electron density instead of wavefunction. This was made possible by two theorems put-forward and proven by Hohenburg and Kohn.[126] The first theory is that the ground state properties of a many-electron system are uniquely determined by the electron density, E[ρ]. This means that the many-body electronic wavefunction, which is a function of 3N variables, and all but impossible to solve, can be written as a functional of electron density, which consists of just three variables. The second theorem defines an important property of the functional; stating that 'the electron density that minimizes the energy of the overall functional is the true electron density corresponding to the full solutions of the Schrödinger equation'.

These theorems showed it was possible to use the ground state density to calculate the properties of the system; however, it did not provide a way to calculate the ground state densities. The full electronic Hamiltonian shown in Equation 3.3 describes a system of interacting electrons; however, Kohn and Sham proposed a method to construct a model system from non-interacting electrons, which makes the Hamiltonian much easier to solve.[127] Thus, the electron density can be constructed from a non-interacting set of atomic orbitals, Equation 3.5.

$$E[\rho] = \sum_{i=1}^{N} \phi_i^*(r)\phi_i(r) \tag{3.5}$$

The total energy can now be expressed as a function of electron density, E[ρ], which is a function of position, ρ(r);

$$E[\rho] = T[\rho] + E_{ee}[\rho] + \int v_{eff}(r)\rho(r)dr + V_{xc}[\rho] \tag{3.6}$$

where T(ρ) is the kinetic energy of non-interacting electrons, $E_{ee}[\rho]$ is the interaction energy between electrons , v_{eff}(r) is the external potential and $V_{XC}[\rho]$ is the exchange-correlation potential, defined as:

$$V_{xc}[\rho] = \frac{\delta E_{XC}[\rho]}{\delta \rho(r)} \tag{3.7}$$

The Kohn–Sham equations effectively remove the complex inter-electron interactions from all but one term of the Hamiltonian; the exchange–correlation energy (exchange correlation functional, $E_{xc}[\rho]$). The $E_{xc}[\rho]$ accounts for the difference between classical and quantum mechanical electron–electron repulsion and the difference in energy between the fictitious non-interacting system and the real system.[128] All other parts of the Hamiltonian equation are now known and can be calculated, except for the $E_{xc}[\rho]$. Many methods have been developed to estimate the exchange–correlation energy, as the practicality of DFT depends on the accuracy of this approximation. In practice it is important to select a suitable exchange correlation functional that properly describes the system.

3.1.2.1 Exchange Correlation Functionals, Basis Sets and Effective Core Potentials

The simplest exchange-correlation functional is the local density approximation (LDA). This functional is based on the model of a uniform electron gas where the electron density is constant at all points in space.[129] LDA tends to overestimate the exchange-correlation energy, and does not perform well for systems where the density is not uniform. Therefore, a second method was developed that not only includes the local value of electron density but also accounts for the gradient of the density at each point. This is called generalised gradient approximation (GGA). The third method to approximate the exchange correlation functional is the hybrid method, which use a mixture of Hartree–Fock exchange and DFT exchange correlation. One example of a hybrid method is the B3LYP functional, which is one of the most commonly used functionals in DFT. One major drawback of this functional however is that it, somewhat obviously, does not perform well for non-covalent interactions, which is important for the transition metal complexes we wish to study. Recently developed hybrid-meta-GGA functionals have overcome this, such as the M06 functional which has been used in this work. This functional has been proven to perform well for transition metals and bond dissociation energy calculations.[130,131]

A basis set, such as 6-311G**, is needed to describe the molecular orbitals. Basis sets are sets of functions (basis functions) that describe the electronic wavefunction. In the linear combination of atomic orbitals (LCAO) these basis functions are atomic orbitals. For a completely accurate description of the wavefunction, and thus a 'complete basis set', an infinite number of basis functions would be needed.[132] Therefore, the size of the basis set affects the accuracy of the calculation. Larger basis sets are more accurate; however, come at a expensive computational cost.

As the size of the atom increases, so does the number of electrons. This requires an increasing number of basis functions, which increases the computational cost. These extra electrons are mostly core electrons which do not play a large part in bonding; therefore, this problem of a large basis set may be solved by modelling the core electrons with a suitable function.[133] This function is called the effective core potential (ECP). Additionally, the velocities of the core electrons of heavy atoms approach the speed of light, resulting in relativistic effects. These are minimal for first row transition metals but are more pronounced for second and third rows. ECPs account for these relativistic effects, where basis sets would not. ECPs have been used in this work for all transition metals and xenon.

3.1.2.2 Self-Consistent Field Procedure

DFT is a self-consistent field (SCF) procedure. From an initial estimate, the Kohn–Sham equations can be solved to yield the energy of a system. By the variational principle, this energy must be greater than or equal to the true ground state energy.[128] These equations are solved iteratively until they are self-consistent and hence the energy is minimised, for a schematic representation of this see Figure 3.1.

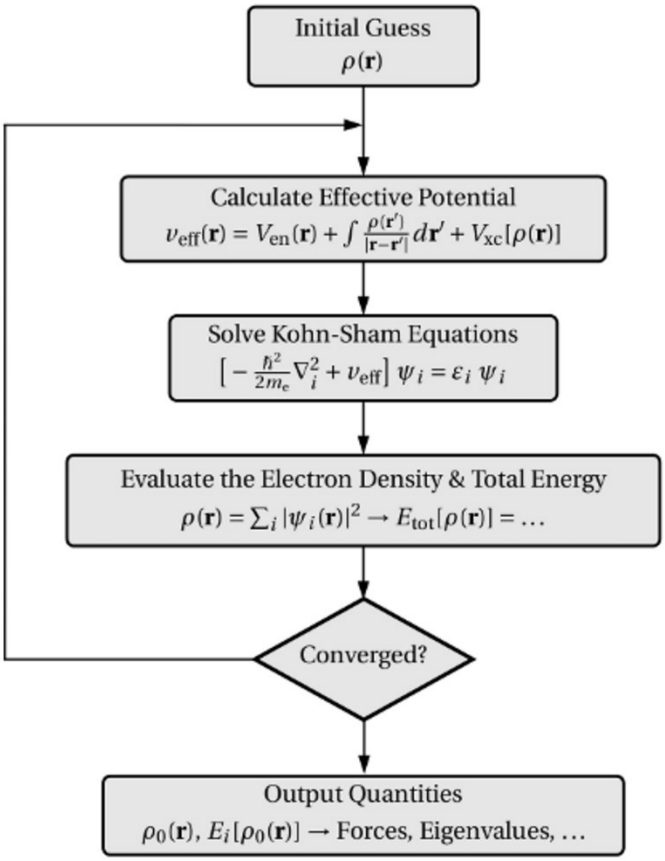

Figure 3.1: *Schematic representation of the self-consistency cycle in Kohn–Sham density functional theory calculations, reproduced from reference 134*

3.1.3 Bond Dissociation Energy Calculations

Once the energy of a chemical system has been determined by computational calculations, these energies can in turn be used to calculate the dissociation energy of a bond A–B.

In the following section, $E_Z^X(\mathrm{Y})$ refers to the energy of fragment Y, calculated with basis set X at geometry Z. In order to calculate the bond dissociation energy of a bond A–B, $\Delta \mathrm{E}_{AB}^{AB}(\mathrm{AB})$, a simple approach would be to subtract the energies of each fragment, $\mathrm{E}_{AB}^{A}(\mathrm{A})$ and $\mathrm{E}_{AB}^{B}(\mathrm{B})$, from the total energy of the bonded molecule, see Equation 3.8. $\mathrm{E}_{AB}^{A}(\mathrm{A})$ and $\mathrm{E}_{AB}^{B}(\mathrm{B})$ are the energies of the fragments for the geometry that they occupy in the complex, calculated using their own basis set.

$$\Delta E(AB) = E_{AB}^{AB}(AB) - E_{AB}^{A}(A) - E_{AB}^{B}(B) \tag{3.8}$$

However, in the energy calculation of the full complex, $\Delta E_{AB}^{AB}(AB)$, the basis functions from one fragment can compensate for the basis set incompleteness in the other fragment and vice versa, resulting in a lower calculated energy.[133] In other words, using a smaller basis set to describe the individual fragments will overestimate their energies, due to an inadequacy of the basis sets. This leads to an overestimation of the bond strength and this overestimation is called the basis set superposition error (BSSE). Using very large basis sets would decrease this error; however, for large systems this is not feasible. Therefore, the counterpoise correction method has been developed to estimate the BSSE. Some variations of this method exist, but a popular method, and the one used in this work, is shown in Equation 3.9.[128]

$$\Delta E^{CP}(AB) = [E_{AB}^{AB}(AB) - E_{AB}^{AB}(A) - E_{AB}^{AB}(B)] + [E_{AB}^{A}(A) - E_{A}^{A}(A)] + [E_{AB}^{B}(B) - E_{B}^{B}(B)] \tag{3.9}$$

There are several parts to this counterpoise corrected bond dissociation equation. The first, $E_{AB}^{AB}(AB) - E_{AB}^{AB}(A) - E_{AB}^{AB}(B)$, is a modified form of Equation 3.8, calculating the formation energy using a combined basis set. Here, the energies of fragments A and B, $E_{AB}^{AB}(A)$ and $E_{AB}^{A}(B)$, are calculated including basis functions for its relative missing fragment even though it is not actually present. These basis functions are referred to as ghost functions. As explained above, $E_{AB}^{AB}(A) \leq E_{AB}^{A}(A)$; hence, a lower and more accurate estimation of the bond dissociation energy is achieved.

The last part, $[E_{AB}^{A}(A) - E_{A}^{A}(A)] + [E_{AB}^{B}(B) - E_{B}^{B}(B)]$, is called the relaxation correction. It describes the energy required to adjust each fragment from its fixed complexed geometry, $E_{AB}^{A}(A)$, to its uncomplexed equilibrium geometry, $E_{A}^{A}(A)$.

By screening the BDEs of a large selection potential alkane and noble gas photo-products, we can determine potentially long-lived intermediates for experimental analysis. Furthermore, a large selection of compounds can be screened computationally in a fraction of the time it would take experimentally.

3.1.4 Literature Studies of Bond Dissociation Energies

A study by Cobar *et al.* calculated the bond dissociation energies of a series of $CpM(CO)_2$(alkane) (M = Mn or Re) and also a theoretical binuclear species, $[(CO)_2M(C_5H_4)C{\equiv}C(C_5H_4)M(CO)_2]$ (M = Mn or Re).[135] The highest calculated binding energy for the mononuclear $CpRe(CO)_2$(alkane) was for $CpRe(CO)_2$(cyclobutane) (13.1 kcal/mol) and in general, the binding energy was higher for cyclic alkanes compared to their linear counterparts. The calculations showed good agreement with experimental values calculated by variable temperature infrared measurements; for $CpRe(CO)_2$(cyclopentane) the experimental value was 7.7 kcal/mol versus 12.8 kcal/mol for the theoretical calculated value.[42,135] Notably, they found that the presence of a second metal site in binuclear $[(CO)_2Re(C_5H_4)C{\equiv}C(C_5H_4)Re(CO)_2]$ increased the binding energy of the alkane significantly, see Figure 3.2.

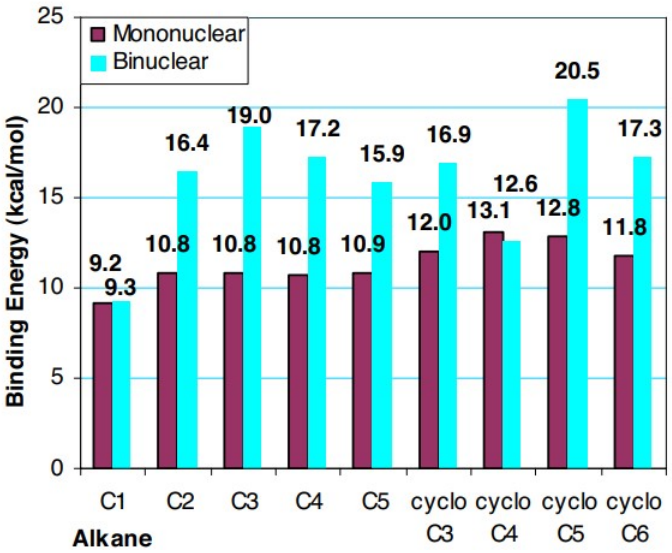

Figure 3.2: *Mononuclear $CpRe(CO)_2$(alkane) (purple) and binuclear $[(CO)_2Re(C_5H_4)C{\equiv}C(C_5H_4)Re(CO)_2]$ (cyan) binding energies in kcal/mol. C1–C5 represent linear alkanes methane to pentane, respectively, and cycloC3–cycloC6 represents cyclopropane to cyclohexane, respectively, reproduced from reference 135*

A detailed study into the binding energy of $CpRe(CO)_2(CH_4)$ by Chan and Ball,[136] systematically studied a range of functionals and basis sets to determine their accuracy in calculating the binding energy of this complex. Many DFT methods were compared

against the value of 65.9 kJmol^{-1} calculated by highly accurate coupled-cluster method.[136] There was a general underestimation from the DFT methods; however, they assessed that several DFT methods were cost-effective to study the bond dissociation energies of metal alkane complexes, including ωB987X-D, B3-PW91-D3, TPSSh-D3, and B98-D3. More recently Lu *et al.* also utilised coupled-cluster methods to calculate the binding energy of $CpRe(CO)_2(CH_4)$, calculating a value of 70.0 kJmol^{-1}, broadly agreeing with the previously described work.[137]

In the same work, the binding energies of a number of cationic rhenium and rhodium complexes were calculated, see Figure 3.3.

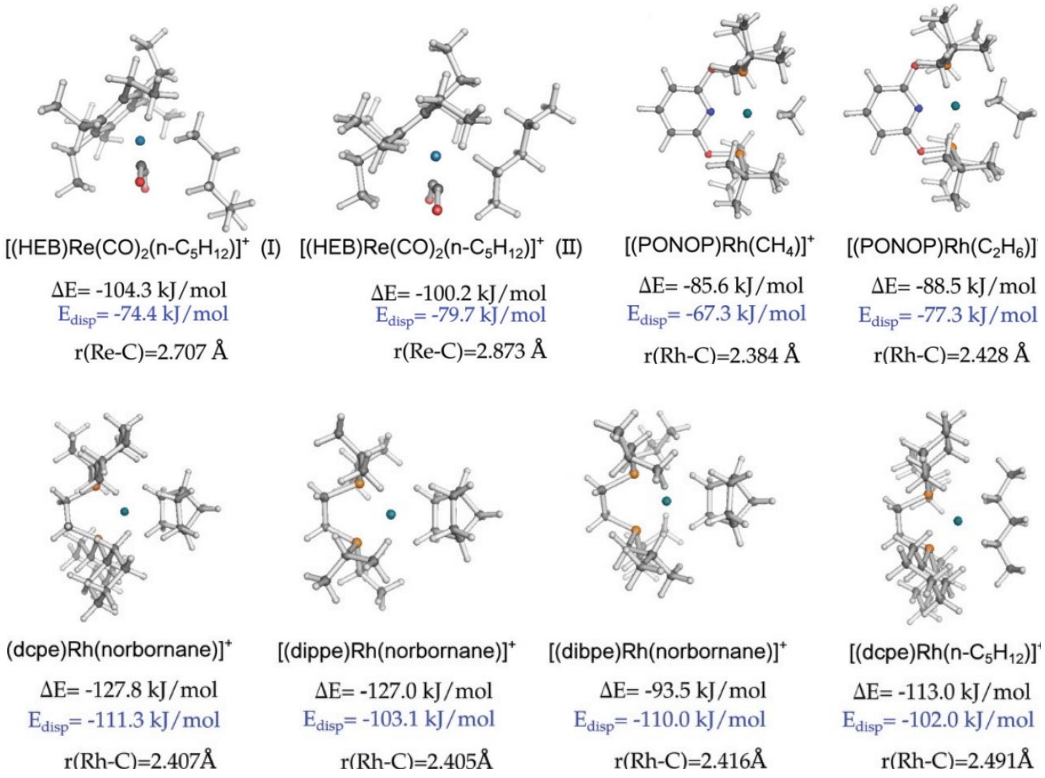

Figure 3.3: *Calculated structures, binding energies (ΔE), and London dispersion contribution (E_{disp}) for a number of transition metal complexes. M–C bond lengths are also shown. Reproduced from reference 137*

These included the complexes [(PONOP)Rh(alkane)]$^+$ which have been previously characterised by NMR,[50,51] and complexes [(L)Rh(norbornane)]$^+$ (L = dcpe, dippe, dibpe), and [(dcpe)Rh(n-C_5H_{12})]$^+$ which have been characterised experimentally by NMR and X-ray crystallography,[55] as described in Chapter 1. This interesting work shows the

magnitude of calculated bond dissociation energies corresponding to complexes stable enough to be structurally characterised. These bond dissociation energies range from 93.5–127.8 kJmol^{-1}, creating a good reference point for our calculations.

Recent work in our group has calculated the bond dissociation energy (BDE) of numerous transition metal alkane, noble gas and CO_2 complexes using DFT with the M06 functional and 6-311++G** basis set for all atoms except transition metals and Xe, where LANL08 and Def2-TZVPD were used, respectively.[138] It has previously been shown that accurate approximations of bond dissociation energy can be made with this method.[135] The work determined the bond dissociation energies of a vast number of alkane and noble gas complexes of transition metals from group V to group IX, and observed some important trends. These were;

(i) On descending a group, the BDE increased.

(ii) *n*-heptane complexes had a higher BDE than CH_4 or Xe

(iii) Upon moving across the periodic table, the BDE increases

(iv) Piano stool complexes typically formed complexes with higher BDE

(v) Cationic complexes were shown to result in a BDE of around 15–20 kJmol^{-1} higher than the analogous neutral complex

These calculations were in agreement with experimental observations of (i), (ii) and (iii), underlining the accuracy of bond dissociation energy calculations and their usefulness in predicting bond strengths.

3.1.4.1 Molecular Orbital Studies

Studies of the HOMO–LUMO gap between a number of neutral and cationic metal–alkane and noble gas complexes have shown that for cationic complexes the LUMO was significantly lower by around 3 eV. A lower LUMO would correspond to a smaller HOMO–LUMO gap leading to greater overlap between the two orbitals and hence a

stronger bond.[138] This has been proposed as a possible reason for why cationic complexes form stronger bonds compared to their neutral counterparts.

A DFT study by Ehlers *et al.*, of noble gas complexes of $M(CO)_5(X)$, where M = Cr, Mo or W and X = Ar, Kr or Xe, revealed the molecular orbital energy diagrams for these species, Figure 3.4.[139] They found that there was little change in the energy of the HOMO across the complexes; however, the energy of the LUMO was dependent on the metal centre, decreasing down the group (Cr > Mo > W), corresponding with an increase in bond strength. A decrease in the LUMO energy leads to a smaller gap between the HOMO and the LUMO, a better overlap between the orbitals and hence a stronger bond.

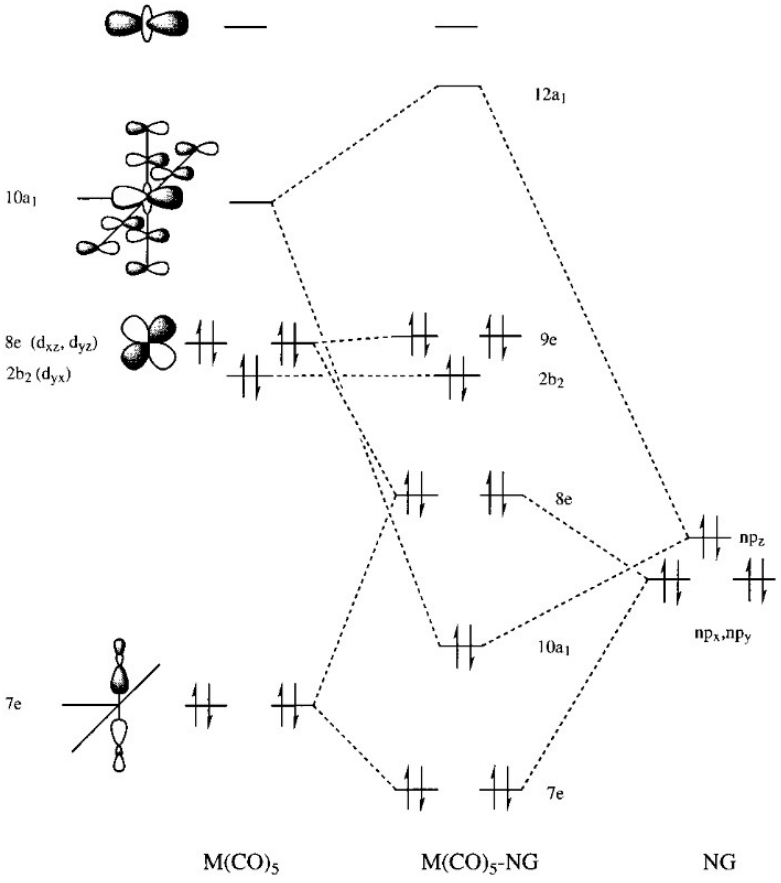

Figure 3.4: *Molecular orbital diagram for $M(CO)_5$–NG complexes, where NG = noble gas, reproduced from reference 139*

3.1.5 Designing Electron Deficient Transition Metal Complexes for Long-lived Metal Alkane and Noble Gas Complexes

As outlined by Grills and George, making a complex as electron deficient as possible would increase the strength of a metal–alkane or metal–noble gas bond.[70] This is because the energy of the metal fragments molecular orbitals are lowered, decreasing their ability to π-backbond and simultaneously increasing the overlap with the ligand p orbitals. In addition, the induced dipole moment in increased, increasing the electrostatic attraction between metal and ligand.

There are several ways to create electron deficiency at a metal centre. These will be explored in the following sections.

3.1.5.1 Sixteen and Seventeen Electron Complexes

Work in Chapter 2 has shown that the strength of the metal alkane and noble gas bond in complexes of sixteen electron Bp*Rh$(CO)_2$ was significant, leading to remarkably long-lived rhodium alkane and noble gas complexes. Sixteen electron complexes are by their nature electron deficient and the discoveries made in this thesis presented a new area to explore in that of electron deficient sixteen and seventeen electron transition metal complexes.

The group V hexacarbonyls are unique complexes in that they are seventeen electron radicals, V$(CO)_6$ in particular is relatively long lived. While Nb$(CO)_6$ and Ta$(CO)_6$ are not known to be stable at room temperature, Ta$(CO)_6$ was reportedly formed at low temperature in matrix isolation.[140] Their reactions generally centre around gaining an extra electron to become more stable; V$(CO)_6$ undergoes facile nucleophilic substitution by phosphine ligands to form V$(CO)_5$(L) where L = P$(OMe)_3$, P(O-*i*-Pr)$_3$ and P$MePh_2$.[141] V$(CO)_6$ also has both oxidising and reducing character, with its tendency to form the $[V(CO)_6]^-$ anion yet also possessing formal V(0) character.[142]

Whilst it is not expected that experimental work will be completed of group V M$(CO)_6$

complexes due to their unstable nature, especially $Nb(CO)_6$ and $Ta(CO)_6$, one of the great advantages of computational chemistry is that you can study systems that are not easily studied experimentally. A theoretical study on these seventeen electron radicals in comparison to their eighteen electron group VI analogues will still reveal if the electron deficient nature has an effect on the bond strength of the metal alkane or noble gas bond. Many studies into transition metal alkane and related complexes have shown that the strength of the bond increases as you move from group V across to group VII,;[41,42] however, it is hypothesised here that the electron deficient character of the group V hexacarbonyls may mean that they create stronger bonds with alkanes or noble gases in comparison to the group VI hexacarbonyls.

3.1.5.2 Cationic Complexes

Cationic complexes are another way to have an electron deficient centre. The positive charge strongly contracts the metal d-orbitals, greatly enhancing the electrostatic charge-polarizability attraction between the metal and the ligand.[70]

Work in our group has calculated the bond dissociation energy of $[(\eta^6\text{-}C_6H_6)Ir(CO)(Xe)]^+$ to be 100.3 $kJmol^{-1}$ compared to 62.0 $kJmol^{-1}$ for the analogous neutral CpIr(CO)(Xe). The same work studied a number of cationic complexes and compared them to their neutral analogues and found the cationic complexes had an increased BDE in every case.

In a significant experimental study by Ball and co-workers, the characterisation by IR and NMR at low temperature of a cationic complex of rhenium, $[(HEB)Re(CO)_2(alkane)][Al(OR^f)_4]$, where HEB = η^6-hexaethylbenzene, OR^f = perfluoro-*tert*-butoxy and alkane = cyclopentane or pentane was reported.[143] They found that this complex was significantly more stable than the analogous neutral complexes $(HEB)W(CO)_2(alkane)$ and $CpRe(CO)_2(alkane)$ under the same conditions.

Many of the chemical reactions of trispyrazolylborates have been described in Chapter 2. Much of the research has taken advantage of the highly tunable nature of the Tp ligand,

altering its properties by substitution of the R groups. However, Tp can be altered even further by changing the core boron atom to a carbon. This creates trispyrazolylmethane, Tpm, the neutral analogue of the Tp ligand, see Figure 3.5. In many of the trispyrazolylborate complexes the Tp can be directly replaced with a Tpm ligand to form a complex with a +1 charge compared to its Tp analogue.

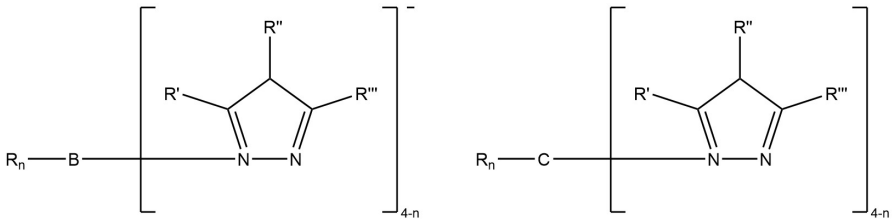

Figure 3.5: *General structure of a) trispyrazolylborate (Tp) ligand $[R_nB(pz)_{4-n}]^-$ and b) trispyrazolylmethane (Tpm) $[R_nC(pz)_{4-n}]$ ligand*

Another way to alter a complex to make it cationic is to swap a neutral carbonyl ligand for a positively charged nitrosyl (NO^+) ligand. If a complex contains both nitrosyl and carbonyl ligands, in a hypothetical photolysis, the carbonyl ligand will still dissociate, leaving an intermediate that is still positively charged, with the potential to form a long-lived alkane or noble gas complex. In our group, we have calculated the bond dissociation energy of both neutral $CpRe(CO)_3$ and cationic $[CpRe(CO)_2(NO)]^+$ derivatives. The bond dissociation energy of $[CpRe(CO)(NO)(c\text{-pentane})]^+$ was found to be much higher than $CpRe(CO)_2(n\text{-heptane})$ (110 $kJmol^{-1}$ *vs.* 62 $kJmol^{-1}$).

In addition, Khaluillin *et al.* found that replacing a CO ligand with a NO^+, which is more electron withdrawing than CO, led to methane binding more strongly to the metal, indeed it led on average to a 55 % stronger bond.[144] Using energy decomposition analysis (EDA), they determined that the increase in binding energy is due to increased forward donation and polarisation. Later, a comprehensive study by Thenraj and Samuelson came to a similar conclusion, testing a series of ligands and finding that metal–alkane binding energies were largest with complexes containing the electron withdrawing NO^+ ligand, and lowest with electron rich ligands such as NHC (NHC = *N*-heterocyclic carbene).[145] They

also used EDA to conclude that the orbital interaction energy term, ΔE_{orb}, is the major factor determining metal–alkane bond strength. As NO^+ ligand containing complexes bind most strongly to the alkane, this indicates electron donation from the alkane C–H σ-orbitals, rather than back-donation, appears most important in creating strong metal–alkane bonds.

3.2 Aims

Considering the techniques discussed in the Introduction to design electron deficient precursors for long-lived metal alkane complexes, there are a number of possible areas of investigation. Thus, the aims of this chapter are:

(i) To investigate the bond dissociation energies of alkane and noble gas derivatives of seventeen electron complexes $M(CO)_6$ (M = V, Nb or Ta).

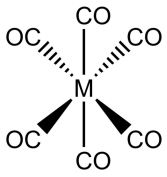

(ii) To investigate the bond dissociation energies of alkane and noble gas derivatives of complexes formed by replacing a CO with a NO in $M(CO)_6$ to form $M(CO)_5(NO)$ (M = V, Nb or Ta).

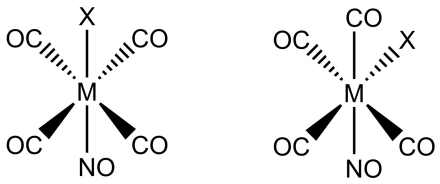

(iii) To investigate the bond dissociation energies of cationic metal–alkane or metal–noble gas derivatives of complexes formed by replacing a CO for a NO ligand in $Tpm'M(CO)_3$ to form $[Tpm'M(CO)_2(NO)]^+$ (Tpm' = Tpm or Tpm* and M = Cr, Mo or W).

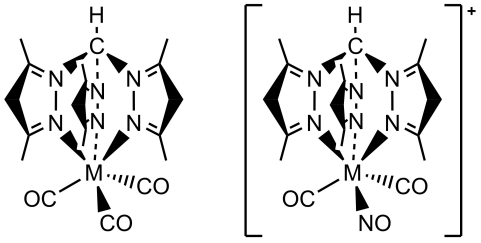

(iv) To investigate the bond dissociation energies of cationic metal–alkane or metal–noble gas derivatives of complexes formed by replacing a CO with a NO ligand in Tp'M(CO)$_3$ to form [Tp'M(CO)$_2$(NO)]$^+$ (Tp' = Tp or Tp* and M = Mn or Re).

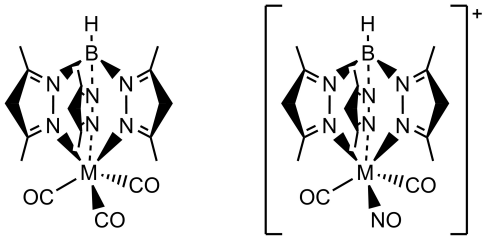

(v) To investigate the bond dissociation energies of cationic metal–alkane or metal–noble gas derivatives of complexes formed by replacing a Tp' ligand with Tpm' in Tp'M(CO)$_3$ to form [Tpm'M(CO)$_3$]$^+$ (Tp' = Tp or Tp*, Tpm' = Tpm or Tpm* and M = Mn or Re).

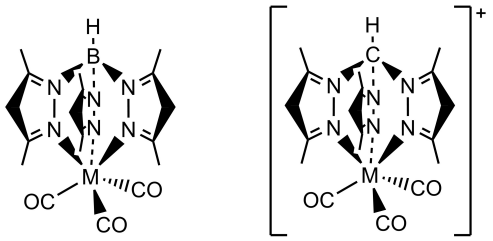

(vi) To investigate the bond dissociation energies of cationic metal–alkane or metal–noble gas derivatives of complexes formed by replacing a Bp' ligand with Bpm' in Bp'M(CO)$_2$ to form [Bpm'M(CO)$_2$]$^+$ (Bp' = Bp or Bp*, Bpm' = Bpm or Bpm* and M = Rh or Ir). These complexes would also be sixteen electron complexes, like their neutral analogues, therefore fulfilling two of the proposed criteria for creating long-lived metal alkane complexes.

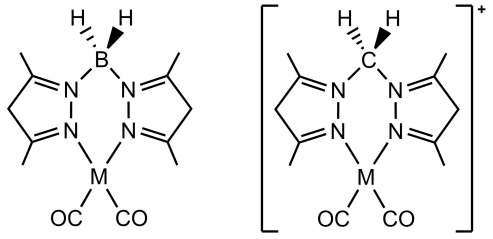

The bond dissociation energies of all complexes will be compared with their relevant eighteen electron or neutral analogues. Bond lengths will also be calculated and discussed to determine trends.

We have described in the Introduction how calculated LUMO energies of cationic complexes were found to be significantly lower than their neutral counterparts. Therefore, our final aim for this Chapter is thus:

(vii) To investigate LUMO energies of all complexes above to determine their relationship with relative bond dissociation energies.

3.3 Results

3.3.1 Bond Dissociation Energy Calculations of Group V Hexacarbonyl and Pentacarbonyl Nitrosyl Complexes

The first set of complexes to be investigated were seventeen electron $M(CO)_5X$, where M = V, Nb or Ta and X = CH_4, C_7H_{16} or CO_2. These complexes are to be investigated because we believe their non-conventional seventeen electron nature may lead to stronger alkane bonded complexes. Table 3.1 shows the results of bond dissociation energy (BDE) calculations for these complexes.

Table 3.1: Calculated bond dissociation energies for complexes of the form $M(CO)_5(X)$, where M = V, Nb or Ta and X = CH_4 or C_7H_{16}

Complex	BDE / kJmol^{-1}
$V(CO)_5$–CH_4	36.7
$V(CO)_5$–C_7H_{16}	45.3
$Nb(CO)_5$–CH_4	39.8
$Nb(CO)_5$–C_7H_{16}	48.3
$Ta(CO)_5$–CH_4	45.7
$Ta(CO)_5$–C_7H_{16}	55.3

The lowest BDE is for $V(CO)_5(CH_4)$, with a value of 36.7 kJmol^{-1}, and the highest is for $Ta(CO)_5(C_7H_{16})$ with a value of 55.3 kJmol^{-1}. The general trend follows the expected pattern; the BDE increases going down the group and CH_4 complexes are more weakly bound compared to C_7H_{16}.

These seventeen electron complexes can be compared to their analogous group VI complexes, $M(CO)_5(X)$ where M = Cr, Mo or W and X = CH_4 or C_7H_{16}, which are standard eighteen electron complexes. As described in Section 1.2.1, the strength of the

bond between an alkane and a metal centre generally increases on moving from Group V to Group VII. For example work within our group has shown that the BDE of the group V complexes $CpM(CO)_3(CH_4)$ (22.3–38.8 $kJmol^{-1}$) is much lower than the similar group VII complexes $CpM(CO)_2(CH_4)$ (42.3–54.9 $kJmol^{-1}$). Therefore, in a comparison between analogous group V $M(CO)_5(X)$ and group VI $M(CO)_5(X)$ complexes, one would expect an increase in the bond strength and hence BDE from group V to group VI. However, the complexes investigated here are not conventional eighteen electron complexes, and are expected to behave differently.

Figure 3.6 shows a comparison between the calculated values for such complexes. There is a clear decrease in BDE on moving across the group, which goes against known trends.

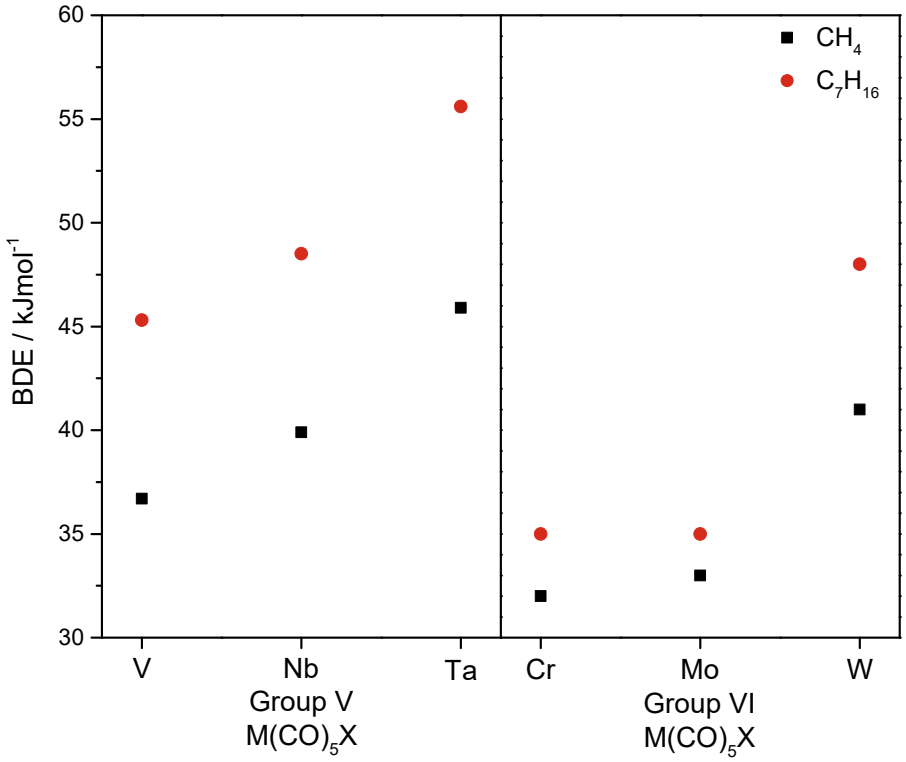

Figure 3.6: *Comparison of the bond dissociation energy of Group V and Group VI complexes of the type $M(CO)_5X$, where $X = CH_4$ or C_7H_{16}*

The Group V $M(CO)_5X$ complexes range from 4.5 to 13.5 $kJmol^{-1}$ higher than their Group VI analogues, with an average increase of 8.0 $kJmol^{-1}$. The main thing distin-

guishing these complexes is that Group VI $M(CO)_5(X)$ complexes are standard 18 electron complexes, whilst the Group V complexes are coordinatively unsaturated seventeen electron complexes. In Chapter 2, it was found that a coordinatively unsaturated sixteen electron rhodium complex bound relatively very strongly to the metal centre. We hypothesised that the inherently electron deficient nature of the sixteen electron complex was a factor in the remarkable strength of the bond. These calculations have added further proof that the non-conventional sixteen and seventeen nature of these complexes does indeed increase the strength of the metal–alkane bond.

Next, the group V complexes $M(CO)_4(NO)(X)$, where M = V, Nb or Ta and X = CH_4, C_7H_{16} or CO_2 were studied. In contrast to the previous complexes, these complexes have a standard 18 electron configuration. Additionally to consider are the different isomers of $M(CO)_4(NO)X$, of which there are two; $M(CO)_4(NO)$(ax-X) and $M(CO)_4(NO)$(eq-X), shown in Figure 3.7.

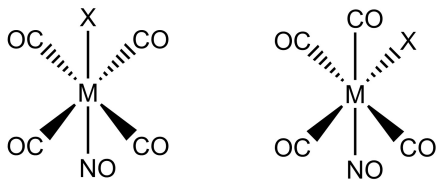

Figure 3.7: *Different isomers of $M(CO)_4(NO)X$, where X can lie axial or equatorial to the nitrosyl ligand*

As described in the Introduction, replacing a CO with a nitrosyl ligand has shown to result in a strengthening of the metal–alkane bond. Therefore, the BDE of these complexes will be calculated and compared to the seventeen electron $M(CO)_5X$ (M = V, Nb or Ta) calculated in the previous section, and also compared to analogous eighteen electron $M(CO)_5X$ (M = Cr, Mo or W) complexes.

Table 3.2 shows the results of bond dissociation energy calculations for $M(CO)_4(NO)(X)$. Again the trend follows as expected, with the BDE increasing as you descend the group, and with CH_4 forming weaker bonds compared to C_7H_{16}. The smallest BDE is hence for $V(CO)_4(NO)$(ax-CH_4) at 29.2 kJmol^{-1}, and the largest

is for $Ta(CO)_4(NO)(eq\text{-}C_7H_{16})$ at 47.1 kJmol^{-1}. For complexes with X in the equatorial position, the BDE is higher than the corresponding axial complex, with the exception of $Nb(CO)_4(NO)(eq\text{-}C_7H_{16})$ (39.9 kJmol^{-1}) which is lower than $Nb(CO)_4(NO)(ax\text{-}C_7H_{16})$ (40.1 kJmol^{-1}).

Table 3.2: Calculated bond dissociation energies for complexes of the form $M(CO)_4(NO)(X)$, where M = V, Nb or Ta and X = CH_4 or C_7H_{16}

Complex	BDE / kJmol^{-1}
$V(CO)_4(NO)$–$(eq\text{-}CH_4)$	31.7
$V(CO)_4(NO)$–$(ax\text{-}CH_4)$	29.2
$V(CO)_4(NO)$–$(eq\text{-}C_7H_{16})$	40.2
$V(CO)_4(NO)$–$(ax\text{-}C_7H_{16})$	38.3
$Nb(CO)_4(NO)$–$(eq\text{-}CH_4)$	33.3
$Nb(CO)_4(NO)$–$(ax\text{-}CH_4)$	32.6
$Nb(CO)_4(NO)$–$(eq\text{-}C_7H_{16})$	39.9
$Nb(CO)_4(NO)$–$(ax\text{-}C_7H_{16})$	40.1
$Ta(CO)_4(NO)$–$(eq\text{-}CH_4)$	39.6
$Ta(CO)_4(NO)$–$(ax\text{-}CH_4)$	38.1
$Ta(CO)_4(NO)$–$(eq\text{-}C_7H_{16})$	47.1
$Ta(CO)_4(NO)$–$(ax\text{-}C_7H_{16})$	46.6

In comparison to the previously studied seventeen electron complexes $M(CO)_5X$ (M = V, Nb or Ta and C = CH_4 or C_7H16), the BDE's are lower by around 5–8.5 kJmol^{-1}, see Figure 3.8, with an average decrease of 7.0 kJmol^{-1}. In the Introduction we suggested several ways to increase the strength of the metal–alkane bond. One method was to have an electron deficient complex (i.e., a sixteen or seventeen electron complex) and a second was

to swap a CO ligand for an NO ligand. These results suggests that the electron deficient effect of the seventeen electron $M(CO)_5X$ complexes is more effective than replacing a CO with an NO for creating a stronger bond between the metal and the alkane. This further highlights the importance of non-conventional complexes in the future to form long-lived alkane and noble gas complexes.

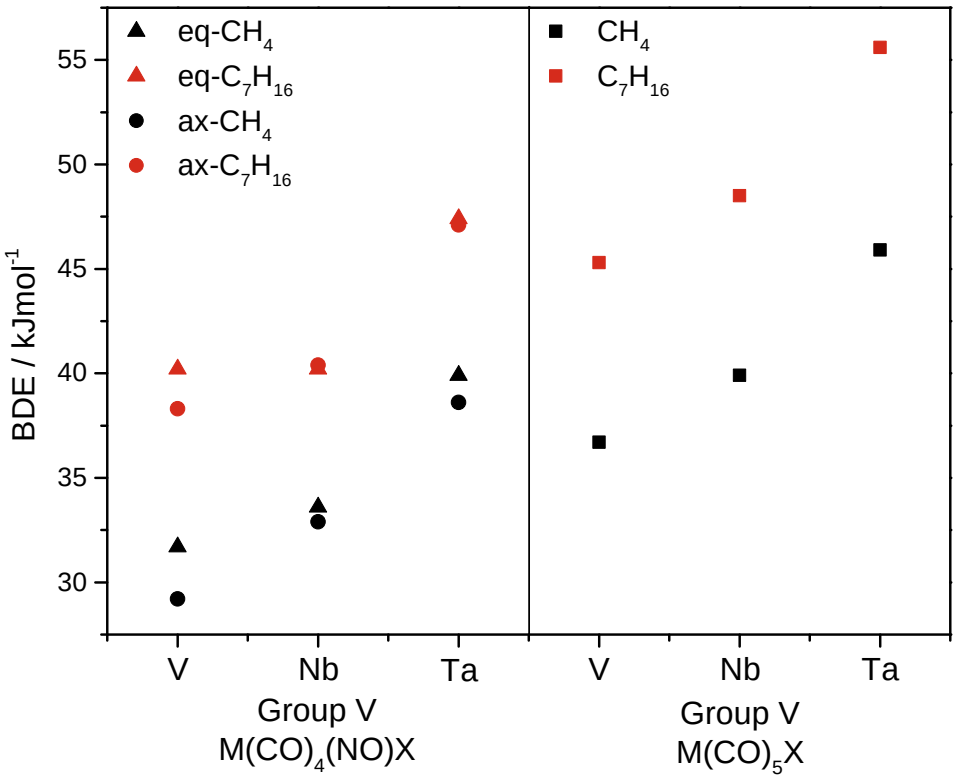

Figure 3.8: *Comparison of the bond dissociation energies of Group V $M(CO)_4(NO)X$ and Group V $M(CO)_5X$ complexes, where $X = CH_4$ or C_7H_{16}*

We have performed a second comparison with the Group VI hexacarbonyls. The $M(CO)_4(NO)(X)$ (M = V, Nb or Ta) bond dissociation energies are much more comparable to group VI $M(CO)_5(X)$ complexes, as seen in Figure 3.9. The Group VI $M(CO)_5X$ complexes range from 5.5 $kJmol^{-1}$ *lower* to 3 $kJmol^{-1}$ *higher* than their analogous Group V complexes. On average there is a decrease from Group V $M(CO)_4(NO)(X)$ complexes to Group VI $M(CO)_5(X)$ complexes of ~1 $kJmol^{-1}$. As we are comparing two standard eighteen electron complexes, according to well established trends in bond dissociation energies, we would expect the Group VI complexes to be higher in energy than the Group

V complexes. Since the values in BDE are relatively similar, it seems that the addition of a nitrosyl ligand has indeed increased the strength of the metal–alkane bond, as suggested by Khaluillin *et al.* [144]

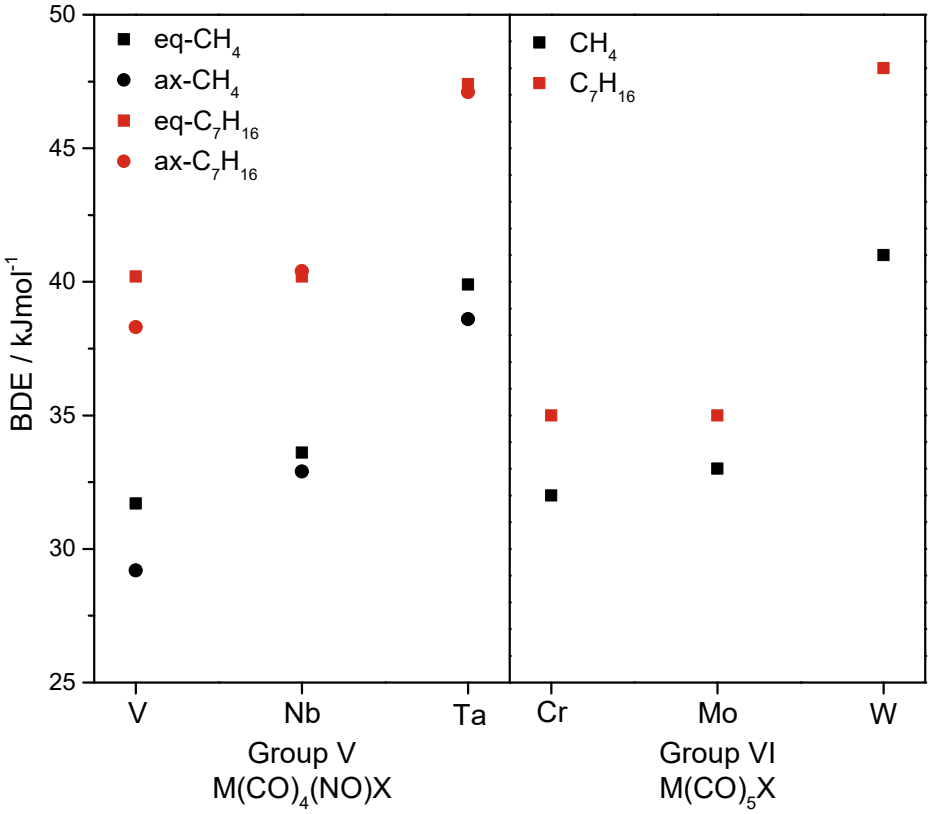

Figure 3.9: *Comparison of the bond dissociation energy of Group V $M(CO)_4(NO)X$ and Group VI $M(CO)_5X$ complexes, where $X = CH_4$ or C_7H_{16}*

3.3.1.1 Bond Length Studies

The bond lengths in group V $M(CO)_5X$ and $M(CO)_4(NO)X$ complexes were analysed. Shown in Table 3.3 are the bond lengths for $M(CO)_5X$, with labelled diagrams shown in Figure 3.10. The parent complexes $M(CO)_6$ (M = V, Na or Ta) all have equivalent M–C bond lengths for all CO ligands. All alkane bonded complexes show a small shortening of the M–C CO bonds compared to the parent complex, but this is most notable in the M–C bond perpendicular to the bonded alkane (M–C_6), which shows a contraction of 0.05–0.09 Å.

The bond lengths can also indicate the nature of the alkane bonding itself. All

complexes show that the shortest bond between the metal and the alkane is the bond to H_1. Interestingly, the bond length between the metal and H_2 is also significant enough for it to be considered a weak bond. These complexes seem to be exhibiting an η^2-H,H' type bond. The C_1–H_1 and C_1–H_2 bond lengths can also indicate the extent of bonding. Electron donation from the σ C–H bonding orbitals will lead to a weakening and hence a lengthening of the C–H bond. Indeed, all complexes show a lengthening of both the C_1–H_1 and C_1–H_2 bonds (between 0.01 and 0.03 Å) from traditional C–H alkane bond lengths (1.09 Å). In general the bond length between C_1 and H_1 are slightly longer than C_1 and H_2.

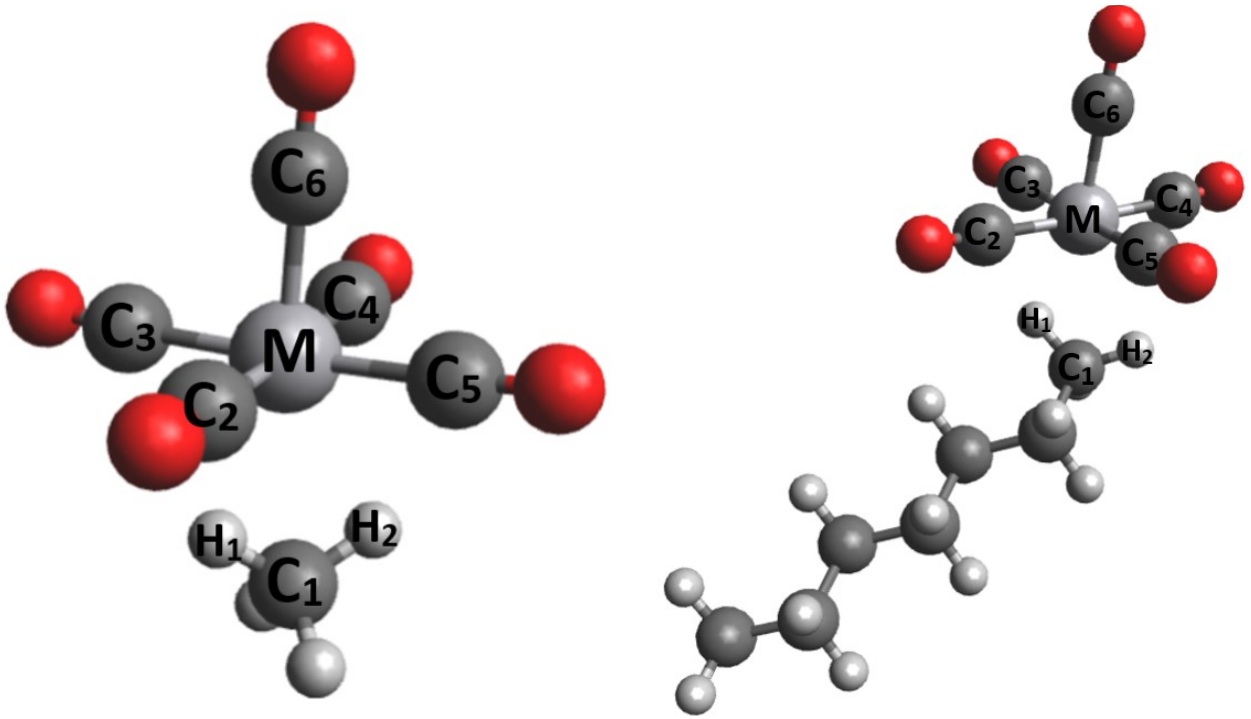

Figure 3.10: *Labelled diagrams of Group V $M(CO)_5X$ complexes, where $X = CH_4$ or C_7H_{16}*

Table 3.3: Selected calculated bond lengths (in Angstroms) for complexes of the form $M(CO)_5(X)$, where M = V, Nb or Ta and X = CH_4 or C_7H_{16}

	$M–C_1$	$M–H_1$	$M–H_2$	$C_1–H_1$	$C_1–H_2$	$M–C_2$	$M–C_3$	$M–C_4$	$M–C_5$	$M–C_6$
$V(CO)_6$	2.01	-	-	-	-	2.01	2.01	2.01	2.01	2.01
$V(CO)_5(CH_4)$	2.69	2.17	2.41	1.11	1.09	2.01	2.01	2.00	2.00	1.95
$V(CO)_5(C_7H_{16})$	2.70	2.08	2.49	1.12	1.10	2.00	2.01	2.00	2.00	1.96
$Nb(CO)_6$	2.19	-	-	-	-	2.19	2.19	2.19	2.19	2.19
$Nb(CO)_5(CH_4)$	2.84	2.35	2.50	1.10	1.10	2.19	2.18	2.17	2.17	2.10
$Nb(CO)_5(C_7H_{16})$	2.83	2.27	2.56	1.11	1.10	2.18	2.19	2.17	2.17	2.10
$Ta(CO)_6$	2.16	-	-	-	-	2.16	2.16	2.16	2.16	2.16
$Ta(CO)_5(CH_4)$	2.79	2.30	2.47	1.11	1.10	2.15	2.15	2.14	2.14	2.07
$Ta(CO)_5(C_7H_{16})$	2.79	2.23	2.52	1.12	1.10	2.15	2.15	2.14	2.14	2.07

Calculated bond lengths for $M(CO)_4(NO)$(eq-X) are shown in Table 3.4, with labelled diagrams shown in Figure 3.11. The complexes show a slight shortening of M–CO bonds compared to the parent, which again is most noticeable in the M–C bond opposite the bonded alkane, ($M–C_5$), which shortens by 0.07–0.10 Å. All complexes show that the shortest bond is between the metal and H_1 on the alkane, which in general is a significantly shorter distance than the bond between the metal and H_2 on the alkane. This is in contrast to the previously studied $M(CO)_5X$ complexes, which exhibited more of a η^2-H,H' bonded structure. Indeed, the $C_1–H_1$ bond shows a greater lengthening in general than that of $C_1–H_2$ from a normal C–H bond length (1.09 Å). The complexes with the greatest lengthening of the $C_1–H_1$ bonds correspond to complexes with the largest bond dissociation energy.

One complex that does not seem to follow the trend is $V(CO)_4(NO)$(eq-CH_4). All M–CO bonds have lengthened upon bonding of the alkane. We are not sure why this is this case, and more work is needed to understand this.

For the $M(CO)_4(NO)$(ax-X) structures, the bond lengths are shown in Table 3.5, and labelled diagrams in Figure 3.12. The M–CO bonds show no significant bond changes on binding to the alkane. However, all M–NO bonds exhibit a small shortening of the bond of ~0.05 Å. This is probably due to its position opposite the bonded alkane and mirrors the exaggerated shortening of the M–CO bond opposite the bonded alkane seen in the equatorial complexes. Again, in general the $M–H_1$ bond is the shortest bond to the alkane, and there is a significant difference in the $M–H_1$ and $M–H_2$ bonds in most complexes, in contrast to $M(CO)_5X$ complexes. The $C_1–H_1$ shows some small lengthening, which is most pronounced in the heptane bonded complexes. The $C_1–H_2$ bond also shows some lengthening; however, it is less significant than that of $C_1–H_1$. In this case, $V(CO)_4(NO)$(ax-CH_4) appears to follow the same trends as the other complexes, unlike its analogous equatorial complex.

Comparing the bond lengths in $M(CO)_4(NO)$(eq-X) and $M(CO)_4(NO)$(ax-X), in general the $M–H_1$ and $M–H_2$ bonds are shorter in $M(CO)_4(NO)$(eq-X), which ties well with the higher BDE of the equatorial complexes.

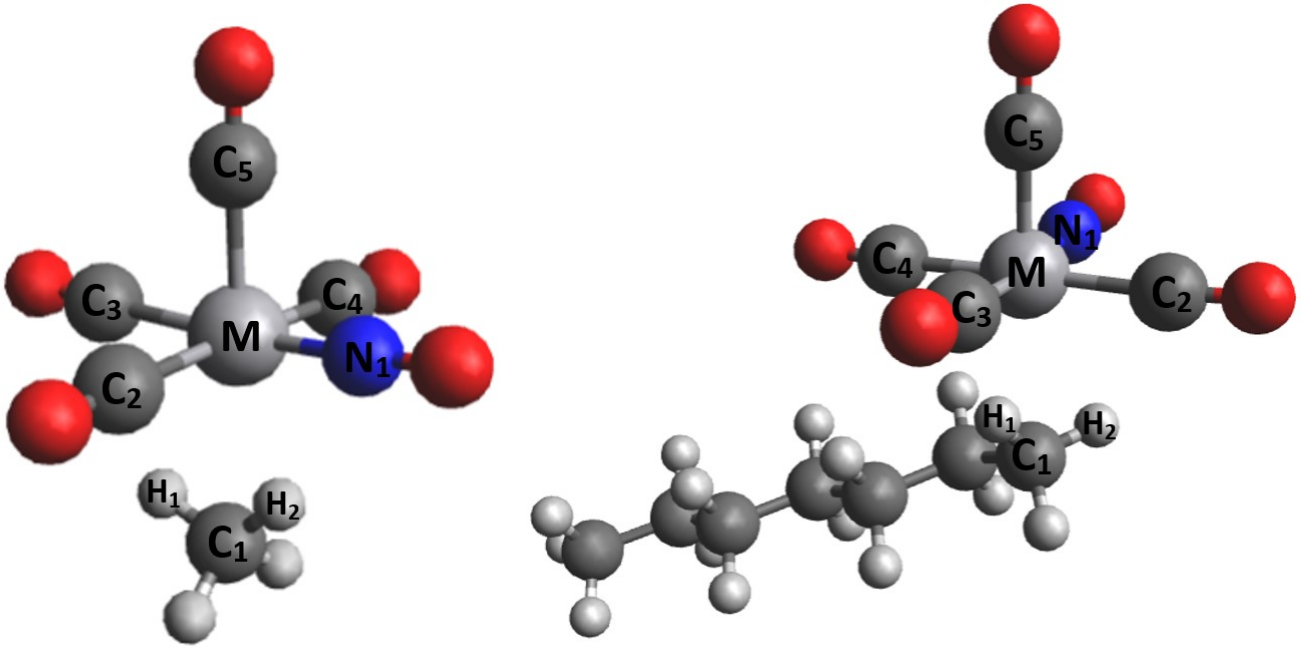

Figure 3.11: *Labelled structures of $M(CO)_4(NO)(eq\text{-}CH_4)$ (left) and $M(CO)_4(NO)(eq\text{-}C_7H_{16})$ (right), where M = V, Nb or Ta*

Table 3.4: Selected calculated bond lengths (in Angstroms) for complexes of the form $M(CO)_4(NO)(eq\text{-}X)$, where M = V, Nb or Ta and X = CH_4 or C_7H_{16}

	$M–C_1$	$M–H_1$	$M–H_2$	$C_1–H_1$	$C_1–H_2$	$M–C_2$	$M–C_3$	$M–C_4$	$M–C_5$	$M–N_1$
$V(CO)_5(NO)$	2.00	-	-	-	-	2.00	2.08	2.00	2.00	1.77
$V(CO)_4(NO)(eq\text{-}CH_4)$	2.76	2.10	2.65	1.11	1.09	2.10	2.13	2.10	2.04	1.76
$V(CO)_4(NO)(eq\text{-}C_7H_{16})$	2.82	2.05	2.79	1.12	1.09	2.00	2.09	1.99	1.93	1.76
$Nb(CO)_5(NO)$	2.19	-	-	-	-	2.19	2.29	2.19	2.19	1.92
$Nb(CO)_4(NO)(eq\text{-}CH_4)$	2.89	2.40	2.54	1.10	1.10	2.18	2.28	2.18	2.08	1.91
$Nb(CO)_4(NO)(eq\text{-}C_7H_{16})$	2.94	2.27	2.81	1.12	1.09	2.18	2.28	2.18	2.08	1.91
$Ta(CO)_5(NO)$	2.16	-	-	-	-	2.16	2.25	2.16	2.16	1.91
$Ta(CO)_4(NO)(eq\text{-}CH_4)$	2.84	2.35	2.51	1.10	1.10	2.14	2.23	2.14	2.06	1.90
$Ta(CO)_4(NO)(eq\text{-}C_7H_{16})$	2.90	2.22	2.77	1.12	1.09	2.15	2.23	2.14	2.06	1.90

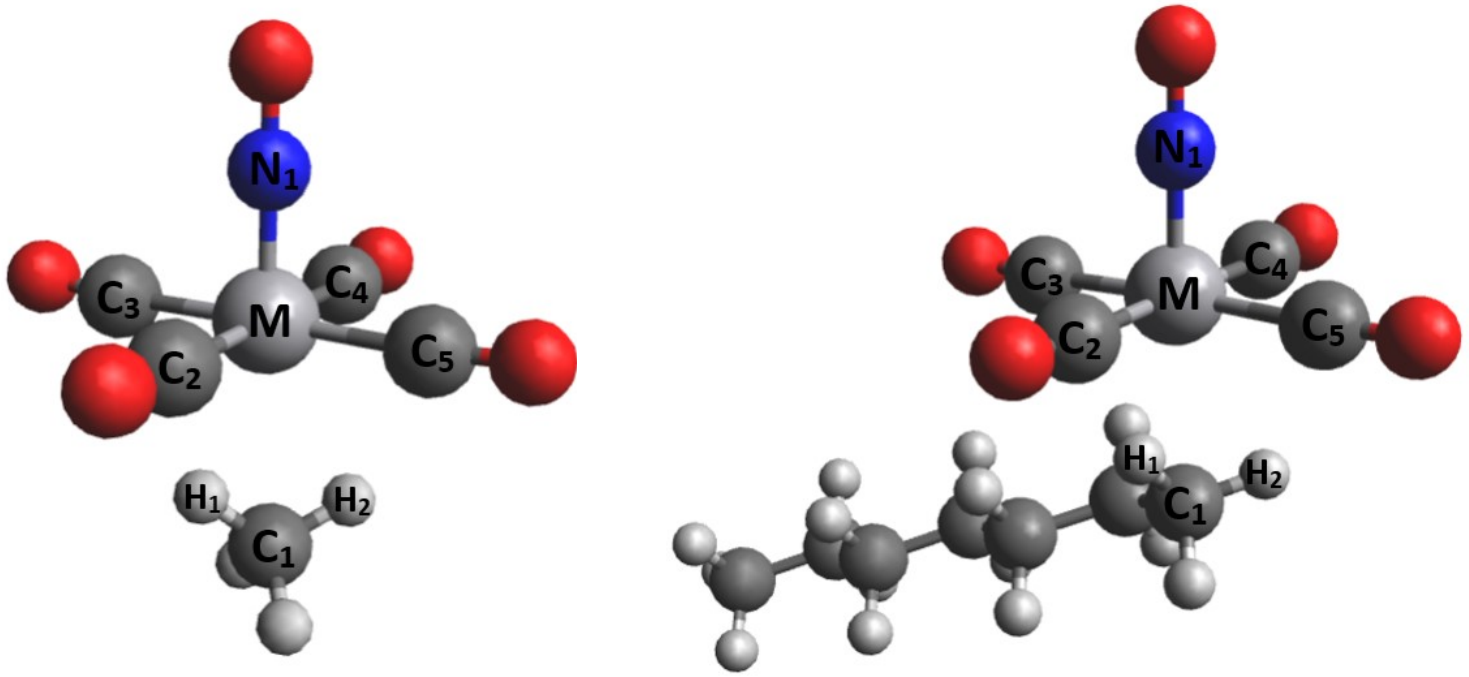

Figure 3.12: *Labelled structures of $M(CO)_4(NO)(ax\text{-}CH_4)$ (left) and $M(CO)_4(NO)(ax\text{-}C_7H_{16})$ (right), where M = V, Nb or Ta*

Table 3.5: Selected calculated bond lengths (in Angstroms) for complexes of the form $M(CO)_4(NO)(ax\text{-}X)$, where M = V, Nb or Ta and X = CH_4 or C_7H_{16}

	$M–C_1$	$M–H_1$	$M–H_2$	$C_1–H_1$	$C_1–H_2$	$M–C_2$	$M–C_3$	$M–C_4$	$M–C_5$	$M–N_1$
$V(CO)_5(NO)$	2.08	-	-	-	-	2.00	2.00	2.00	2.00	1.77
$V(CO)_4(NO)(ax\text{-}CH_4)$	2.80	2.21	2.56	1.10	1.09	2.00	2.01	2.01	2.01	1.73
$V(CO)_4(NO)(ax\text{-}C_7H_{16})$	2.85	2.08	2.83	1.12	1.09	2.00	2.00	2.00	2.01	1.73
$Nb(CO)_5(NO)$	2.29	-	-	-	-	219	2.19	2.19	2.19	1.92
$Nb(CO)_4(NO)(ax\text{-}CH_4)$	2.89	2.46	2.49	1.10	1.10	2.19	2.19	2.19	2.19	1.87
$Nb(CO)_4(NO)(ax\text{-}C_7H_{16})$	2.92	2.30	2.75	1.11	1.10	2.19	2.19	2.19	2.19	1.87
$Ta(CO)_5(NO)$	2.25	-	-	-	-	2.16	2.16	2.16	2.16	1.91
$Ta(CO)_4(NO)(ax\text{-}CH_4)$	2.84	2.43	2.44	1.10	1.10	2.15	2.15	2.15	2.15	1.85
$Ta(CO)_4(NO)(ax\text{-}C_7H_{16})$	2.88	2.25	2.72	1.12	1.10	2.15	2.15	2.15	2.15	1.86

3.3.1.2 LUMO Energies

Further work within our group measured the difference in energy of the LUMO for a series of cationic and neutral alkane and noble gas complexes, and found that the cationic metal fragments had a much lower energy LUMO by an average of 3 eV, citing the lower energy LUMO as reason for the stronger bond for cationic complexes. We are assuming that the energy of the HOMO of the binding alkane stays constant; therefore, only the LUMO of the metal fragments are listed. In Table 3.6 we have compared the energy of the LUMO of metal fragment of seventeen electron $M(CO)_5$ and eighteen electron $M(CO)_4(NO)$, where M = V, Nb or Ta, and also eighteen electron $M(CO)_5$ (M = Cr, Mo or W).

The results show that the LUMO is indeed lower for the seventeen electron group V metal fragments of $M(CO)_5$ than group VI $M(CO)_5$, by on average 0.51 eV, which is not as much as the ~3 eV difference calculated for cationic complexes in previous works, but is nonetheless still significant. These results have shown that the electron withdrawing nature of the seventeen electron complex has lowered the LUMO of the metal fragment, in a similar way that cationic complexes have been shown to do so.

The LUMO energies of group V $M(CO)_5$ fragments are also lower than group V $M(CO)_4(NO)$ fragments by an average of 0.64 eV. The LUMO energies of group V $M(CO)_4(NO)$ and group VI $M(CO)_5$ are comparable; however, the group VI $M(CO)_5$ are slightly lower by an average of 0.13 eV. These differences in LUMO energies between the complexes match well with the trends in bond dissociation energy values.

Table 3.6: Calculated LUMO energies for metal fragments of the type $M(CO)_5$ and $M(CO)_4(NO)$, where M = V, Nb or Ta (Group V) or M = Cr, Mo or W (Group VI)

	Complex	LUMO Energy / eV
Group V	$V(CO)_5$	-3.89
Seventeen Electron	$Nb(CO)_5$	-4.08
	$Ta(CO)_5$	-4.14
Group V	$V(CO)_4$(eq-NO)	-3.54
Eighteen Electron	$V(CO)_4$(ax-NO)	-3.46
	$Nb(CO)_4$(eq-NO)	-3.29
	$Nb(CO)_4$(ax-NO)	-3.13
	$Ta(CO)_4$(eq-NO)	-3.56
	$Ta(CO)_4$(ax-NO)	-3.40
Group VI	$Cr(CO)_5$	-3.59
Eighteen Electron	$Mo(CO)_5$	-3.35
	$W(CO)_5$	-3.65

3.3.2 Bond Dissociation Energy Calculations of Cationic Group VI Trispyrazolylmethane Complexes

Next we looked at the effect of replacing a CO ligand with an NO in the group VI complexes Tpm'M(CO)$_2$X to make cationic [Tpm'M(CO)(NO)X]$^+$, where Tpm' = Tpm or Tpm*, M = Cr, Mo or W and X = CH_4 or C_7H_{16}. Both addition of an NO ligand and the cationic nature is thought to increase the bond dissociation energy. The results of the calculations are shown in Table 3.7.

Table 3.7: Calculated bond dissociation energies for complexes of the form [Tpm'M(CO)(NO)X]$^+$, where Tpm' = Tpm or Tpm*, M = Cr, Mo or W and X = CH_4 or C_7H_{16}

Complex	BDE / kJmol^{-1}
[TpmCr(CO)(NO)–CH_4]$^+$	33.0
[Tpm*Cr(CO)(NO)–CH_4]$^+$	27.5
[TpmCr(CO)(NO)–C_7H_{16}]$^+$	44.8
[Tpm*Cr(CO)(NO)–C_7H_{16}]$^+$	38.7
[TpmMo(CO)(NO)–CH_4]$^+$	50.8
[Tpm*Mo(CO)(NO)–CH_4]$^+$	47.7
[TpmMo(CO)(NO)–C_7H_{16}]$^+$	61.5
[Tpm*Mo(CO)(NO)–C_7H_{16}]$^+$	56.9
[TpmW(CO)(NO)–CH_4]$^+$	52.7
[Tpm*W(CO)(NO)–CH_4]$^+$	55.4
[TpmW(CO)(NO)–C_7H_{16}]$^+$	71.9
[Tpm*W(CO)(NO)–C_7H_{16}]$^+$	65.3

The results follow the general trend for bond dissociation energies, with the

energies increasing on descending the group, and heptane complexes resulting in a higher BDE than methane complexes. Consequently, the lowest calculated BDE is for $[Tpm^*Cr(CO)(NO)(CH_4)]^+$ (27.5 $kJmol^{-1}$), and the highest is for $[TpmW(CO)(NO)(C_7H_{16})]^+$ (71.9 $kJmol^{-1}$). The Tpm complexes generally are calculated to have a higher bond dissociation energies than the Tpm* complexes, with the exception of $[TpmW(CO)(NO)(CH_4)]^+$ (52.7 $kJmol^{-1}$), which has a slightly lower BDE than $[Tpm^*W(CO)(NO)(CH_4)]^+$ (55.4 $kJmol^{-1}$). Discounting these complexes, the average difference between the Tpm* and Tpm complexes is 5.2 $kJmol^{-1}$. The Tpm* has two methyl groups on each pyrazole that are more electron donating than the hydrogens in the Tpm ligand. The electron donating character of the methyl groups will increase electron density on the pyrazole groups an increase electron donation to the metal centre. We hypothesise that in the more electron-rich metal centre is less available to accept electrons from the C–H σ-bond, thus resulting in a weaker bond.

We have also calculated the bond dissociation energies for analogous neutral complexes Tpm'$M(CO)_2(X)$ (M = Cr, Mo or W) (see Appendix A), and the comparison is shown in Figure 3.13. The cationic complexes typically have a BDE that is between 1.5 and 14 kJ mol^{-1} higher than their neutral analogues. This trend is for all complexes except for $[Tpm^*Cr(CO)(NO)(CH_4)]^+$ (27.5 $kJmol^{-1}$), which shows a slight decrease in BDE compared to $Tpm^*Cr(CO)_2(CH_4)$ (28.8 $kJmol^{-1}$). We will discuss this further in the bond length study. The average increase in energy on moving from neutral Tpm'$M(CO)_2X$ to $[Tpm'M(CO)(NO)(X)]^+$ is 7.1 $kJmol^{-1}$.

The values for BDE calculated here are in general 5–10 $kJmol^{-1}$ higher than other group VI alkane complexes calculated in our group. For example group VI $M(CO)_5(X)$ complexes range from 32–48 $kJmol^{-1}$ and (η^6-benzene)$M(CO)_2(X)$ complexes range from 33–53 $kJmol^{-1}$. The complex $[TpmW(CO)(NO)(C_7H_{16})]^+$ has a BDE of over 10 $kJmol^{-1}$ higher than any other tungsten complex calculated in our group. Therefore, these complexes present great promise for the study of long-lived group VI complexes.

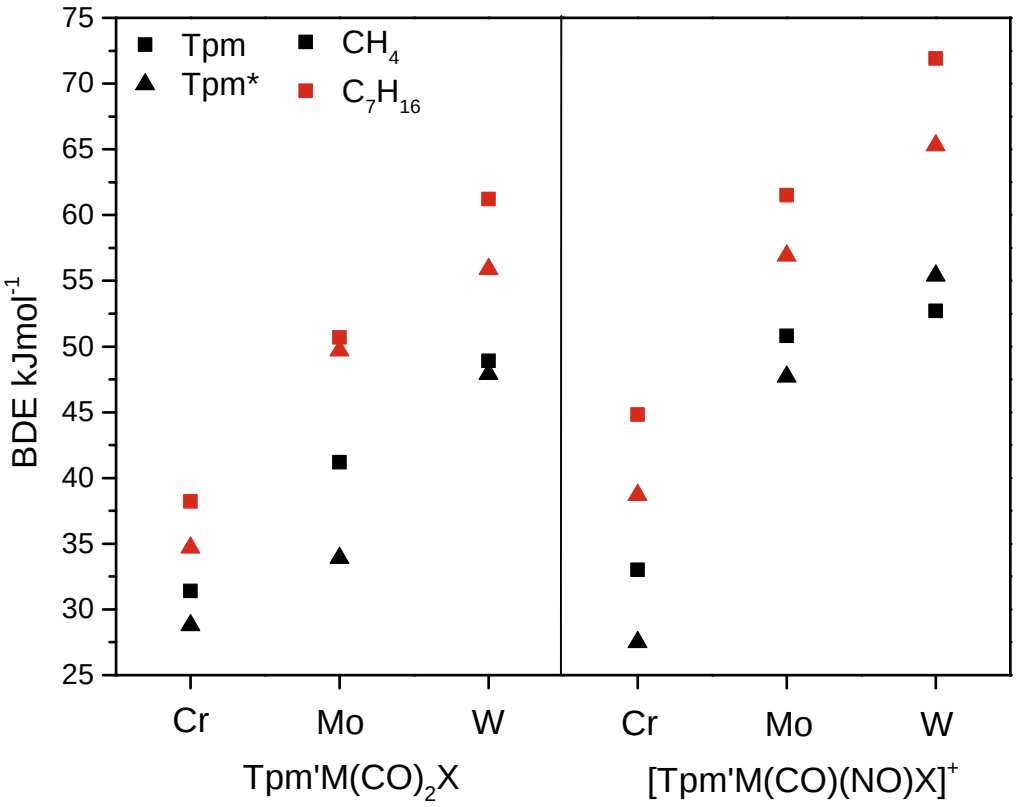

Figure 3.13: *Comparison of the bond dissociation energy of neutral Tpm'M(CO)$_2$X and cationic [Tpm'M(CO)(NO)X]$^+$ (where Tpm' = Tpm (square) or Tpm* (triangle), M = Cr, Mo or W and X = CH_4 (black) or C_7H_{16} (red))*

3.3.2.1 Bond Lengths Studies

Calculated bond lengths for [Tpm'M(CO)(NO)(X)]$^+$ complexes are shown in Table 3.8, alongside parent complexes [Tpm'M(CO)$_2$(NO)]$^+$ for comparison. Labelled diagrams are shown in Figure 3.14. The bond lengths show that in all cases, complexation of the alkane leads to a shortening of the M–N$_4$ bond, which is the nitrogen on the Tpm' ligand opposite the complexing alkane, of between 0.06 and 0.10 Å. This is expected after loss of a CO ligand and complexation of an alkane as the CO was much more strongly bound than the alkane. This mirrors the results in the previous section which saw a contraction of the bond directly opposite the bonded alkane in every case. All other metal-ligand bonds show no significant bond length changes.

For nearly all complexes, the M–H$_2$ bond is the shortest. The exceptions are

$[Tpm^*Cr(CO)(NO)(CH_4)]^+$, $[TpmCr(CO)(NO)(CH_4)]^+$ and $[TpmW(CO)(NO)(CH_4)]^+$, in which the alkane seems to be adopting a different geometry to all other complexes, with the $M–H_1$ bond, being the shortest. This may explain the unexpected bond dissociation energy results (these complexes were found to bind more weakly than expected). All complexes showed a lengthening of the C–H bond that was closest to the metal, with the lengthening equal to between 0.02 and 0.04 Å. The neighbouring C–H bond to the C–H bound to the metal did not exhibit an increase in bond length, suggesting that is it not involved in bonding.

As before, the complexes with the most significant increase in the length of the alkane C–H bond were the complexes with the highest bond dissociation energies.

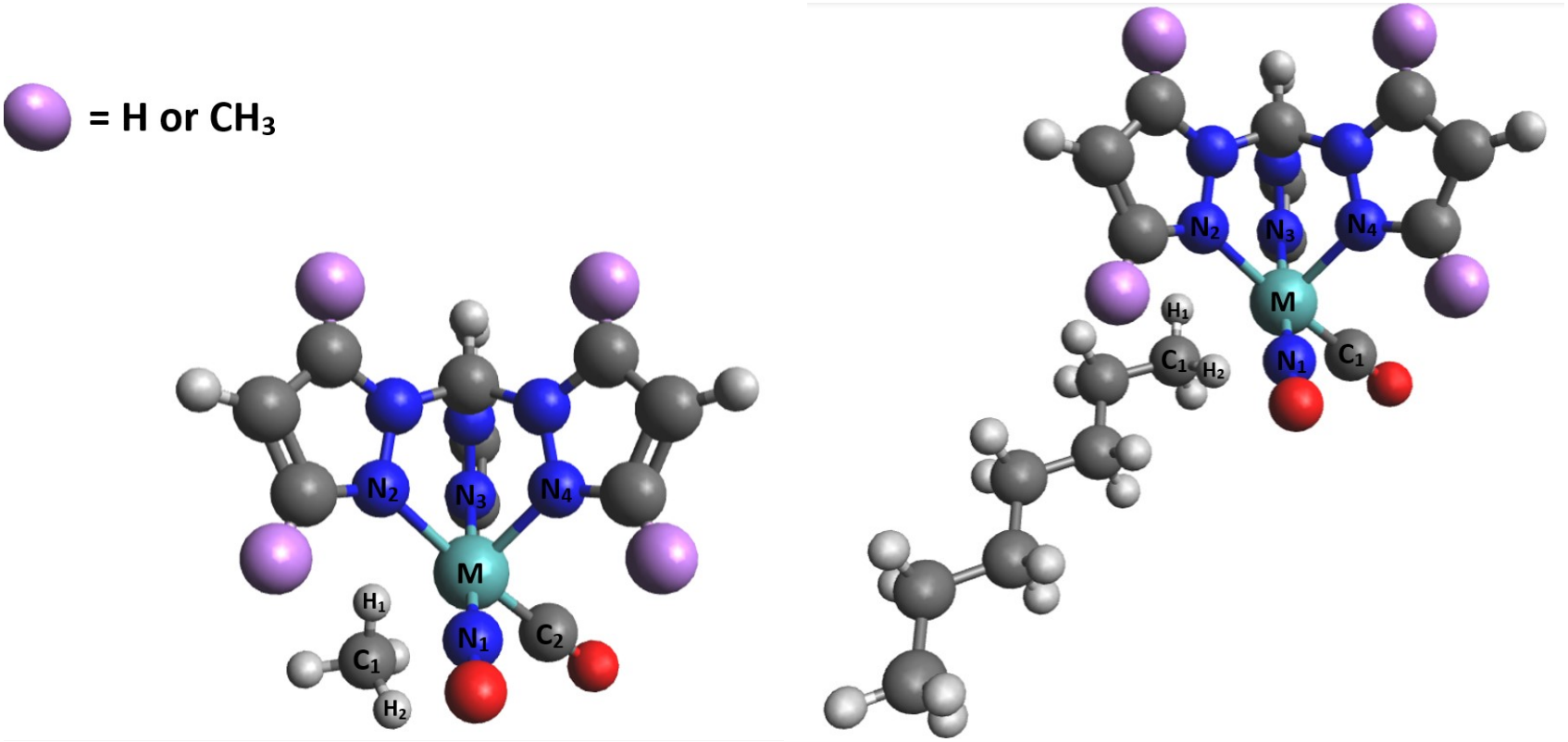

Figure 3.14: *Labelled structures of [Tpm'M(CO)(NO)(CH_4)]$^+$ (left) and [Tpm'M(CO)(NO)(C_7H_{16})]$^+$, where Tpm' = Tpm or Tpm* and M = Cr, Mo or W*

Table 3.8: Selected calculated bond lengths (in Angstroms) for complexes of the form [Tpm'M(CO)(NO)(X)]$^+$, where M = Cr, Mo or W and X = CH_4 or C_7H_{16}

	$M–C_1$	$M–H_1$	$M–H_2$	$C_1–H_1$	$C_1–H_2$	$M–C_2$	$M–N_1$	$M–N_2$	$M–N_3$	$M–N_4$
$[TpmCr(CO)_2(NO)]^+$	1.89	-	-	-	-	1.89	1.68	2.12	2.14	2.12
$[TpmCr(CO)(NO)(CH_4)]^+$	2.73	2.00	2.78	1.11	1.09	1.88	1.67	2.12	2.14	2.05
$[TpmCr(CO)(NO)(C_7H_{16})]^+$	2.76	2.75	1.94	1.12	1.09	1.88	1.67	2.12	2.14	2.06
$[Tpm*Cr(CO)_2(NO)]^+$	1.89	-	-	-	-	1.89	1.68	2.13	2.16	2.13
$[Tpm*Cr(CO)(NO)(CH_4)]^+$	2.82	2.05	3.10	1.11	1.09	1.87	1.67	2.13	2.15	2.06
$[Tpm*Cr(CO)(NO)(C_7H_{16})]^+$	2.88	2.91	2.01	1.09	1.12	1.87	1.67	2.13	2.16	2.06
$[TpmMo(CO)_2(NO)]^+$	2.03	-	-	-	-	2.03	1.82	2.28	2.29	2.28
$[TpmMo(CO)(NO)(CH_4)]^+$	2.71	2.87	2.06	1.09	1.12	2.00	1.80	2.29	2.29	2.18
$[TpmMo(CO)(NO)(C_7H_{16})]^+$	2.78	2.72	2.06	1.09	1.12	2.00	1.80	2.29	2.30	2.18

Table 3.8 continued: Selected calculated bond lengths (in Angstroms) for complexes of the form [Tpm'M(CO)(NO)(X)]$^+$, where M = Cr, Mo or W and X = CH_4 or C_7H_{16}

[Tpm*Mo(CO)$_2$(NO)]$^+$	2.03	-	-	-	-	2.03	1.82	2.27	2.29	2.27
[Tpm*Mo(CO)(NO)(CH$_4$)]$^+$	2.76	2.69	2.10	1.09	1.12	1.99	1.80	2.30	2.29	2.19
[Tpm*Mo(CO)(NO)(C$_7$H$_{16}$)]$^+$	2.82	2.72	2.08	1.09	1.12	1.99	1.80	2.29	2.31	2.19
[TpmW(CO)$_2$(NO)]$^+$	2.01	-	-	-	-	2.01	1.81	2.25	2.26	2.25
[TpmW(CO)(NO)(CH$_4$)]$^+$	2.77	2.08	2.76	1.12	1.09	1.98	1.79	2.25	2.26	2.15
[TpmW(CO)(NO)(C$_7$H$_{16}$)]$^+$	2.72	2.64	2.04	1.09	1.13	1.98	1.79	2.25	2.27	2.16
[Tpm*W(CO)$_2$(NO)]$^+$	2.01	-	-	-	-	2.01	1.81	2.25	2.27	2.25
[Tpm*W(CO)(NO)(CH$_4$)]$^+$	2.71	2.67	2.05	1.09	1.13	1.97	1.79	2.27	2.27	2.16
[Tpm*W(CO)(NO)(C$_7$H$_{16}$)]$^+$	2.77	2.69	2.05	1.09	1.13	1.97	1.79	2.26	2.29	2.16

3.3.2.2 LUMO Energies

The energies of the LUMO for the cationic metal fragment, [Tpm'M(CO)(NO)]$^+$ have been calculated and compared against LUMO values for the neutral metal fragment analogue, Tpm'M(CO)$_2$. The results are shown in Table 3.9.

Table 3.9: Calculated LUMO energies for metal fragments of the type Tpm'M(CO)$_2$ and [Tpm'M(CO)(NO)]$^+$, where Tpm' = Tpm or Tpm* and M = Cr, Mo or W

	Complex	LUMO Energy / eV
Neutral	TpmCr(CO)$_2$	-1.82
	Tpm*Cr(CO)$_2$	-1.71
	TpmMo(CO)$_2$	-1.88
	Tpm*Mo(CO)$_2$	-1.74
	TpmW(CO)$_2$	-1.88
	Tpm*W(CO)$_2$	-1.74
Cationic	[TpmCr(CO)(NO)]$^+$	-5.61
	[Tpm*Cr(CO)(NO)]$^+$	-5.28
	[TpmMo(CO)(NO)]$^+$	-5.44
	[Tpm*Mo(CO)(NO)]$^+$	-5.12
	[TpmW(CO)(NO)]$^+$	-5.55
	[Tpm*W(CO)(NO)]$^+$	-5.25

There is a clear difference between neutral and cationic LUMO energies with an average decrease of 3.6 eV. This is in keeping with work done previously in our group showing that cationic complexes typically had a lower LUMO energy than their neutral analogues by around 3 eV. We found a similar LUMO difference found here, but the BDE difference

is not as large. For example, in previous works an average LUMO decrease from neutral to cationic species of 3 eV corresponded to an average BDE increase of 17.4 kJmol^{-1},[138] whereas here the average increase is notably less, at 7.1 kJmol^{-1}. Therefore, there are still other factors, other than LUMO energies, that effect bond dissociation energy. Notably, there is also a difference between the LUMO energies of Tpm and Tpm* complexes of approximately 0.15 eV for the neutral complexes and approximately 0.3 eV for the cationic complexes. This lower LUMO energy for Tpm complexes correlates with a lower BDE and validates our hypothesis of a higher electron density of the metal due to the presence of methyl groups on the trispyrazolylmethane ligand.

3.3.3 Bond Dissociation Energy Calculations of Cationic Group VII Trispyrazolylborate and Trispyrazolylmethane Complexes

Work in our group has shown that on exchanging a CO in CpM(CO)$_2$(X) (where M = Mn or Re) for an NO to create cationic [CpM(CO)(NO)(X)]$^+$, the bond dissociation energy is increased significantly, for example the BDE of [CpRe(CO)(NO)(cyclopentane)]$^+$ was calculated to be 110 kJmol^{-1}. Therefore, we have looked into the bond dissociation energies of the related complexes [Tp'M(CO)(NO)(X)]$^+$ (Tp' = Tp or Tp* and M = Mn or Re), the results of which are shown in Table 3.10. The lowest calculated bond dissociation energy for these complexes was for [Tp*Mn(CO)(NO)(CH$_4$)]$^+$ (24.0 kJ mol^{-1}) and the highest was for [TpRe(CO)(NO)(C$_7$H$_{16}$)]$^+$ (74.9 kJ mol^{-1}). As expected, the BDE increased on moving from manganese to rhenium, and also on moving from CH$_4$ to C$_7$H$_{16}$. The difference between BDE of Tp and Tp* complexes is significant, with Tp complexes giving higher bond dissociation energies by around 12–18 kJ mol^{-1}. We found a similar increase in BDE between Tpm and Tpm* in calculation of group VI complexes in the previous section; however, the magnitude of the difference was slightly less for the group VI complexes. We again propose that the electron donating character of the methyl groups in Tp* increases electron donation to the metal centre. This increase in electron density means that the metal is less available to accept electrons from the σ-bond, thus leading to

a weaker bond.

Table 3.10: Calculated bond dissociation energies for complexes of the form [Tp'M(CO)(NO)X]$^+$, where Tp' = Tp or Tp*, M = Mn or Re and X = CH_4 or C_7H_{16}

Complex	BDE / kJmol^{-1}
[TpMn(CO)(NO)–CH_4]$^+$	39.1
[Tp*Mn(CO)(NO)–CH_4]$^+$	24.0
[TpMn(CO)(NO)–C_7H_{16}]$^+$	52.6
[Tp*Mn(CO)(NO)–C_7H_{16}]$^+$	35.1
[TpRe(CO)(NO)–CH_4]$^+$	57.0
[Tp*Re(CO)(NO)–CH_4]$^+$	45.3
[TpRe(CO)(NO)–C_7H_{16}]$^+$	75.2
[Tp*Re(CO)(NO)–C_7H_{16}]$^+$	60.9

The value of 75.2 kJmol^{-1} calculated for [TpRe(CO)(NO)(C_7H_{16})]$^+$ is relatively high, and the highest calculated thus far in this chapter. This is consistent with past work that has shown that bond dissociation energies increase on moving across from group V to group VII. The calculated BDE, however, is not as high at that calculated for similar cationic rhenium alkane complexes [CpRe(CO)(NO)(C_5H_{10})]$^+$ (110 kJmol^{-1}) and [BnRe(CO)$_2$(C_7H_{16})]$^+$ (89 kJmol^{-1}), where Bn = benzene.

The next complexes studied were cationic [Tpm'M(CO)$_2$X]$^+$, where M = Mn or Re, Tpm' = Tpm or Tpm* and X = CH_4 or C_7H_{16}. The results of bond dissociation energy calculations are shown in Table 3.11. The highest BDE was for [TpmRe(CO)$_2$(C_7H_{16})]$^+$ at 78.2 kJ mol^{-1} and the lowest was for [Tpm*Mn(CO)$_2$(CH_4)]$^+$ at 32.8 kJ mol^{-1}. The complexes range from 1.5–14 kJ mol^{-1} higher than the previously studied [Tp'M(CO)(NO)X]$^+$ complexes, with an average difference of 6.4 kJ mol^{-1}. The only exception is [TpmMn(CO)$_2$(C_7H_{16})]$^+$, which shows a slight decrease in BDE from

$[TpMn(CO)(NO)(C_7H_{16})]^+$ (51.7 to 52.6 kJ mol^{-1}, respectively). This is interesting as is suggested in work described in the Introduction, the methane in NO^+ ligand containing complexes bound the most strongly. We have found this not to be the case here. The highest BDE's are again for Tpm rather than the methyl containing Tpm* by around 5.5–9 kJ mol^{-1}. This is a slightly smaller difference compared to the difference between $[TpM(CO)(NO)(X)]^+$ and $[Tp*M(CO)(NO)(X)]^+$ complexes (12–18 kJ mol^{-1}).

Table 3.11: Calculated bond dissociation energies for complexes of the form $[Tpm'M(CO)_2X]^+$, where Tpm' = Tpm or Tpm*, M = Mn or Re and X = CH_4 or C_7H_{16}

Complex	BDE / $kJmol^{-1}$
$[TpmMn(CO)_2–CH_4]^+$	40.5
$[Tpm*Mn(CO)_2–CH_4]^+$	32.8
$[TpmMn(CO)_2–C_7H_{16}]^+$	51.7
$[Tpm*Mn(CO)_2–C_7H_{16}]^+$	42.8
$[TpmRe(CO)_2–CH_4]^+$	64.7
$[Tpm*Re(CO)_2–CH_4]^+$	59.1
$[TpmRe(CO)_2–C_7H_{16}]^+$	78.2
$[Tpm*Re(CO)_2–C_7H_{16}]^+$	70.4

As for previous investigations, the bond dissociations energies of analogous neutral complexes Tp'$M(CO)_2(X)$ (Tp' = Tp or Tp*, M = Mn or Re and X = CH_4 or C_7H_{16}) have been calculated (see Appendix A) and compared to the cationic complexes. The comparison of neutral group VII and cationic group VII complexes is shown in Figure 3.15. It shows a clear increase in bond dissociation energy from the neutral to cationic complexes. The only exception is the difference between $Tp*Re(CO)_2(CH_4)$ and $[Tp*Re(CO)(NO)(CH_4)]^+$ which shows a slight decrease to the cationic complex (46.7

to 45.3 kJ mol^{-1}). It also demonstrates the small increase from [Tp'M(CO)(NO)(X)]$^{+}$ to [Tpm'M(CO)$_2$(X)]$^{+}$ complexes. The cationic complexes range from 4–17 kJ mol^{-1} higher than their neutral counterparts and on average they are 10.6 kJ mol^{-1} higher. More specifically, For [Tp'M(CO)(NO)(X)]$^{+}$ complexes the average increase in BDE from their analogous neutral complexes is 8.5 kJmol^{-1}, whilst for the [Tpm'M(CO)$_2$(X)]$^{+}$ complexes, this average is slightly higher at 13.2 kJmol^{-1}.

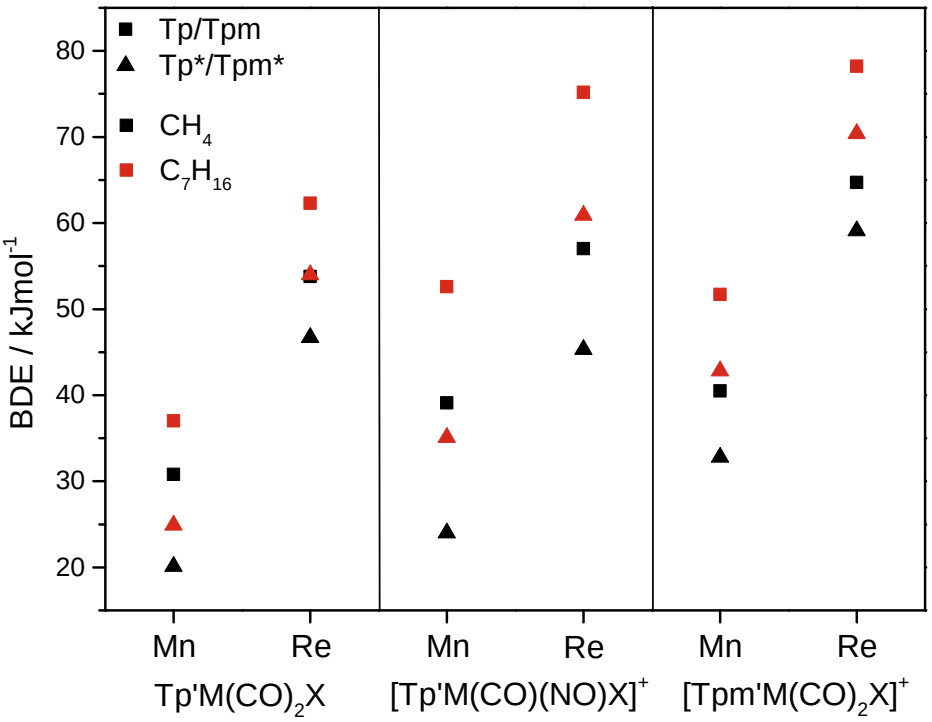

Figure 3.15: *Comparison of the bond dissociation energy of neutral Tp'M(CO)$_2$X with cationic [Tp'M(CO)(NO)X]$^{+}$ and [Tpm'M(CO)$_2$(X)]$^{+}$ (where Tp' = Tp (square) or Tp* (triangle), Tpm' = Tpm (square) or Tpm* (triangle), M = Mn or Re and X = CH$_4$ (black) or C$_7$H$_{16}$ (red))*

3.3.3.1 Bond Length Studies

Calculated bond lengths for complexes [Tp'M(CO)(NO)X]$^{+}$ and for comparison, for the parent complex [Tp'M(CO)$_2$(NO)]$^{+}$, are shown in Table 3.12. Labelled diagrams are shown in Figure 3.16. Complexation of the alkane leads to a contraction of the M–N$_4$ bond (the nitrogen opposite the bonding alkane) in all cases. This same contraction was also seen in the group VI complexes [Tpm'M(CO)(NO)X]$^{+}$. As we hypothesised before,

we assume this is due to the loss of a more strongly bonding CO ligand and its replacement by a weakly bonding alkane ligand, strengthening and hence shortening the M–N_1 bond. In all cases, the atom on the alkane closest to the metal is H_1, with the bond length ranging from 1.89–2.06 Å. The C_1–H_1 bond is lengthened from a normal C–H bond in all cases, showing that the alkane is indeed involved in bonding to the metal centre. The bonds are 0.02–0.05 Å longer than a normal C–H bond, with the longest C_1–H_1 bond belonging to $[TpRe(CO)(NO)(C_7H_{16})]^+$, which is reflected in the bond dissociation energy (this complex had the largest calculated BDE).

Calculated bond lengths for complexes $[Tpm'M(CO)_2X]^+$ and for reference, parent $[Tpm'M(CO)_3]^+$, are shown in Table 3.13. Labelled diagrams shown in Figure 3.17. Again, complexation of the alkane leads to a contraction of the M–N_1 bond (the nitrogen opposite the bonding alkane) in all cases. The shortest bond to the alkane is M–H_1, which ranges from 1.87–1.98 Å. This magnitude of this length however does not correlate with the magnitude of bond dissociation energy, for example the shortest M–H_1 bond (belonging to complex $[TpmMn(CO)_2(C_7H_{16})]^+$) does not correspond to the complex with the largest bond dissociation energy. The C_1–H_1 bond (the alkane C–H bonded to the metal) shows significant lengthening in all cases. In this case, the longest C_1–H_1 bonds do correspond to the strongest bond dissociation energies.

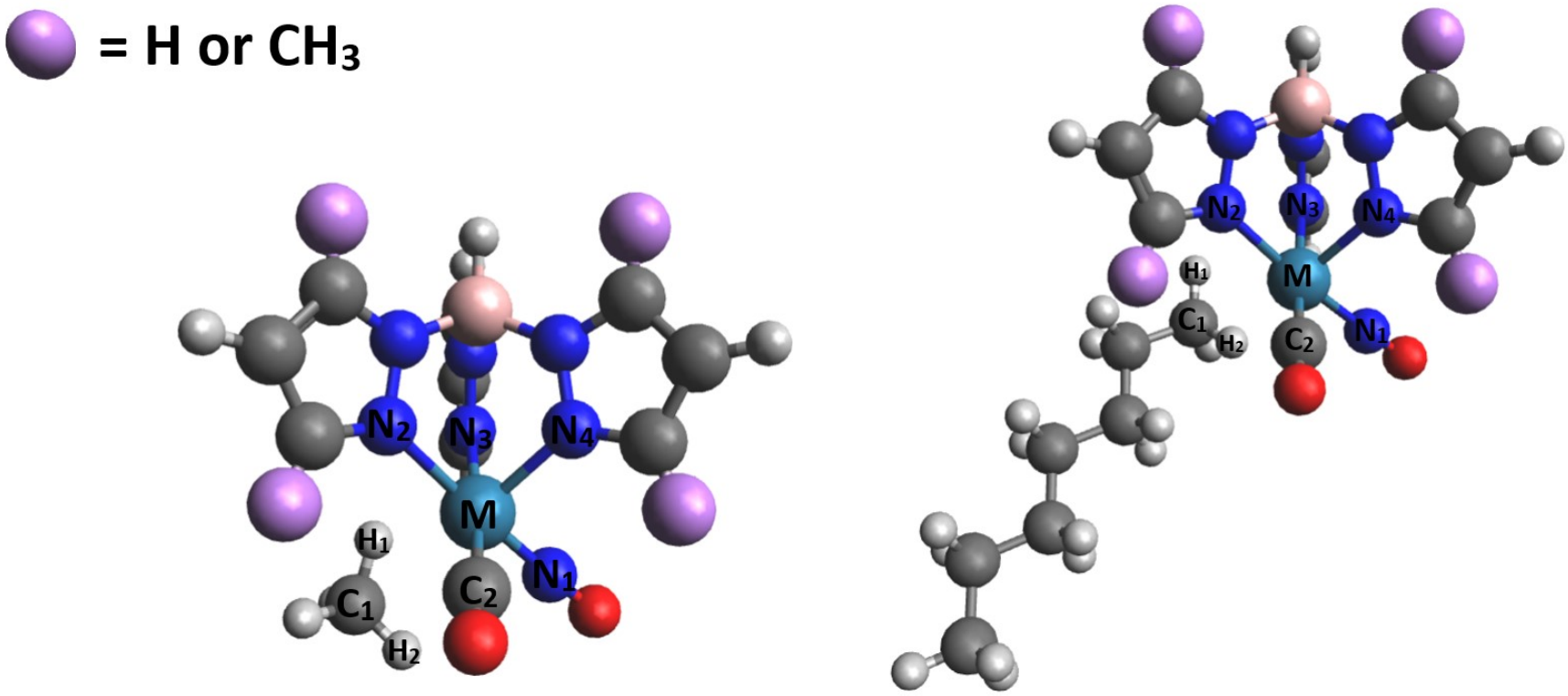

Figure 3.16: *Labelled structures of [Tp'M(CO)(NO)(CH_4)]$^+$ (left) and [Tp'M(CO)(NO)(C_7H_{16})]$^+$ (right), where Tp = Tp or Tp* and M = Mn or Re*

Table 3.12: Selected calculated bond lengths (in Angstroms) for complexes of the form [Tp'M(CO)(NO)(X)]$^+$, where Tp' = Tp or Tp*, M = Mn or Re and X = CH_4 or C_7H_{16}

	$M–C_1$	$M–H_1$	$M–H_2$	$C_1–H_1$	$C_1–H_2$	$M–C_2$	$M–N_1$	$M–N_2$	$M–N_3$	$M–N_4$
$[TpMn(CO)_2(NO)]^+$	1.89	-	-	-	-	1.89	1.66	2.03	2.02	2.02
$[TpMn(CO)(NO)(CH_4)]^+$	2.72	1.95	2.96	1.11	1.09	1.89	1.65	2.02	2.01	1.97
$[TpMn(CO)(NO)(C_7H_{16})]^+$	2.81	2.91	1.89	1.09	1.13	1.88	1.65	2.02	2.01	1.98
$[Tp*Mn(CO)_2(NO)]^+$	1.88	-	-	-	-	1.88	1.65	2.06	2.04	2.04
$[Tp*Mn(CO)(NO)(CH_4)]^+$	2.83	2.04	3.10	1.11	1.09	1.88	1.65	2.03	2.03	1.98
$[Tp*Mn(CO)(NO)(C_7H_{16})]^+$	2.98	3.07	2.02	1.09	1.12	1.88	1.65	2.04	2.03	1.98
$[TpRe(CO)_2(NO)]^+$	2.00	-	-	-	-	2.00	1.80	2.15	2.16	2.16
$[TpRe(CO)(NO)(CH_4)]^+$	2.75	2.04	2.78	1.12	1.09	1.97	1.78	2.15	2.16	2.09
$[TpRe(CO)(NO)(C_7H_{16})]^+$	2.76	2.74	1.98	1.09	1.14	1.97	1.78	2.16	2.16	2.10
$[Tp*Re(CO)_2(NO)]^+$	2.00	-	-	-	-	2.00	1.80	2.16	2.16	2.16
$[Tp*Re(CO)(NO)(CH_4)]^+$	2.81	2.06	3.03	1.12	1.09	1.96	1.78	2.16	2.17	2.09
$[Tp*Re(CO)(NO)(C_7H_{16})]^+$	2.85	2.84	2.02	1.09	1.13	1.96	1.78	2.17	2.18	2.09

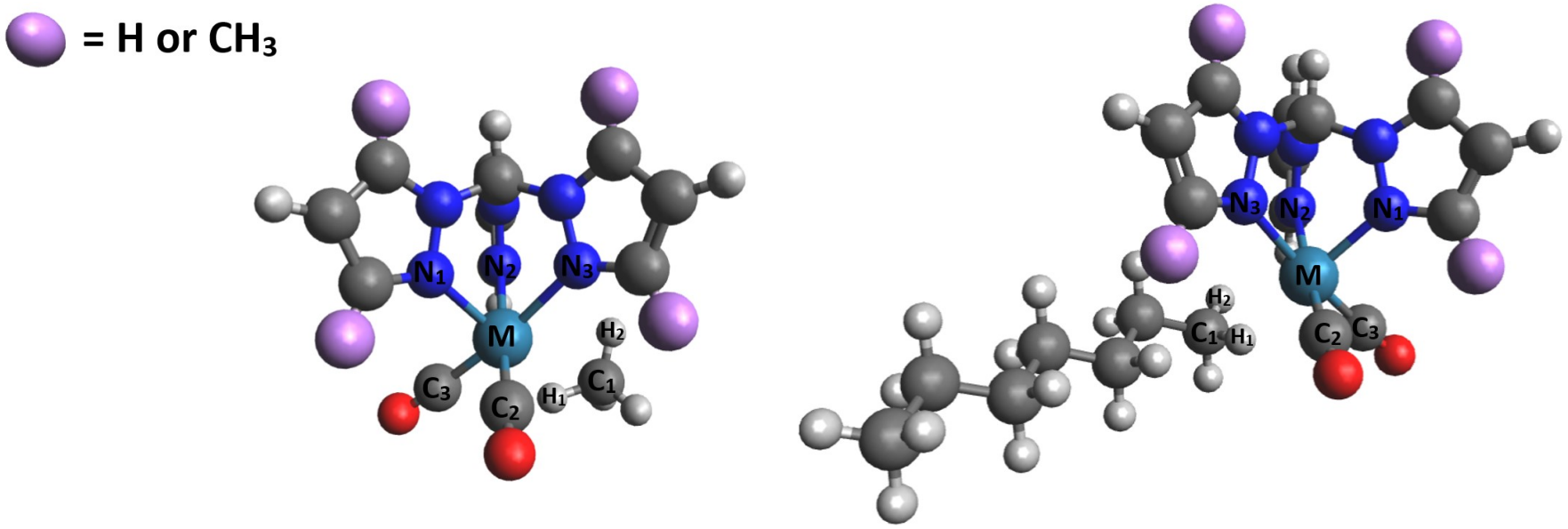

Figure 3.17: *Labelled structures of [Tpm'M(CO)$_2$(CH$_4$)]$^+$ (left) and [Tpm'M(CO)$_2$(C$_7$H$_{16}$)]$^+$ (right), where Tpm = Tpm or Tpm* and M = Mn or Re*

Table 3.13: Selected calculated bond lengths (in Angstroms) for complexes of the form [Tpm'M(CO)$_2$(X)]$^+$, where Tpm'= Tpm or Tpm*, M = Mn or Re and X = CH_4 or C_7H_{16}

	$M–C_1$	$M–H_1$	$M–H_2$	$C_1–H_1$	$C_1–H_2$	$M–C_2$	$M–C_3$	$M–N_1$	$M–N_2$	$M–N_3$
$[TpmMn(CO)_3]^+$	1.81	-	-	-	-	1.81	1.81	2.07	2.07	2.07
$[TpmMn(CO)_2(CH_4)]^+$	2.64	1.90	2.66	1.12	1.09	1.81	1.81	2.01	2.06	2.07
$[TpmMn(CO)_2(C_7H_{16})]^+$	2.72	1.87	2.76	1.12	1.09	1.80	1.80	2.01	2.07	2.07
$[Tpm*Mn(CO)_3]^+$	1.80	-	-	-	-	1.80	1.80	2.09	2.09	2.09
$[Tpm*Mn(CO)_2(CH_4)]^+$	2.72	1.96	2.69	1.11	1.09	1.80	1.80	2.02	2.09	2.09
$[Tpm*Mn(CO)_2(C_7H_{16})]^+$	2.80	1.93	2.84	1.12	1.09	1.80	1.80	2.02	2.09	2.09
$[TpmRe(CO)_3]^+$	1.93	-	-	-	-	1.93	1.93	2.22	2.22	2.22
$[TpmRe(CO)_2(CH_4)]^+$	2.64	1.96	2.66	1.13	1.09	1.90	1.90	2.11	2.22	2.22
$[TpmRe(CO)_2(C_7H_{16})]^+$	2.70	1.94	2.72	1.14	1.09	1.90	1.90	2.11	2.23	2.23
$[Tpm*Re(CO)_3]^+$	1.93	-	-	-	-	1.93	1.93	2.22	2.22	2.22
$[Tpm*Re(CO)_2(CH_4)]^+$	‘2.67	1.98	2.67	1.13	1.09	1.90	1.90	2.12	2.23	2.25
$[Tpm*Re(CO)_2(C_7H_{16})]^+$	2.73	1.96	2.71	1.14	1.09	1.90	1.90	2.12	2.24	2.24

3.3.3.2 LUMO Energies

The LUMO energies for the cationic metal fragments $[Tp'M(CO)(NO)]^+$ and $[Tpm'M(CO)_2]^+$ have been calculated and are shown in Table 3.14, with a comparison to the neutral analogue $Tp'M(CO)_2$.

Table 3.14: Calculated LUMO energies for metal fragments of the type $Tp'M(CO)_2$, $Tp'M(CO)(NO)$ and $Tpm'M(CO)_2$, where M = Re or Mn

	Complex	LUMO Energy / eV
Neutral	$TpMn(CO)_2$	-2.10
$Tp'M(CO)_2$	$Tp^*Mn(CO)_2$	-2.01
	$TpRe(CO)_2$	-2.26
	$Tp^*Re(CO)_2$	-2.15
Cationic	$[TpMn(CO)(NO)]^+$	-7.29
$[Tp'Mn(CO)(NO)]^+$	$[Tp^*Mn(CO)(NO)]^+$	-6.91
	$[TpRe(CO)(NO)]^+$	-6.86
	$[Tp^*Re(CO)(NO)]^+$	-6.48
Cationic	$[TpmMn(CO)_2]^+$	-5.58
$[Tpm'M(CO)_2]^+$	$[Tpm^*Mn(CO)_2]^+$	-5.25
	$[TpmRe(CO)_2]^+$	-5.69
	$[Tpm^*Re(CO)_2]^+$	-5.36

The clearly show that the LUMO energies for the cationic metal fragments are significantly lower than those of the neutral fragments, following trends seen so far in this chapter. The $[Tp'M(CO)(NO)]^+$ fragments are lower by roughly 5 eV, and the $[Tpm'M(CO)_2]^+$ fragments are lower by just over 3 eV. It is interesting that the $[Tp'M(CO)(NO)]^+$ fragments

have lower energy LUMOs than $[Tpm'M(CO)_2]^+$ fragments, as in BDE calculations, the $[Tpm'M(CO)_2(X)]^+$ complexes were higher than $[Tp'M(CO)(NO)(X)]^+$. Again this further confirms that LUMO energies are not the only factor affecting bond dissociation energies, as we have found in previous sections.

3.3.4 Bond Dissociation Energy Calculations of Cationic Group IX Bispyrazolylmethane Complexes

We have already shown in Chapter 2 that the alkane and noble gas complexes of $Bp^*Rh(CO)_2$ are extremely long-lived. Replacing the Bp* ligand with a Bpm or Bpm* will make the complex cationic, hence increasing the electron deficiency of the complex even further. Therefore, we wish to calculate the bond dissociation energies of alkane complexes of $[Bpm'M(CO)_2]^+$, (Bpm' = Bpm or Bpm*, M = Rh or Ir) see Figure 3.18. In addition to its cationic and hence electron deficient nature, the complex will retain its sixteen electron configuration, therefore combining two properties which have been shown to increase metal–X bond strength.

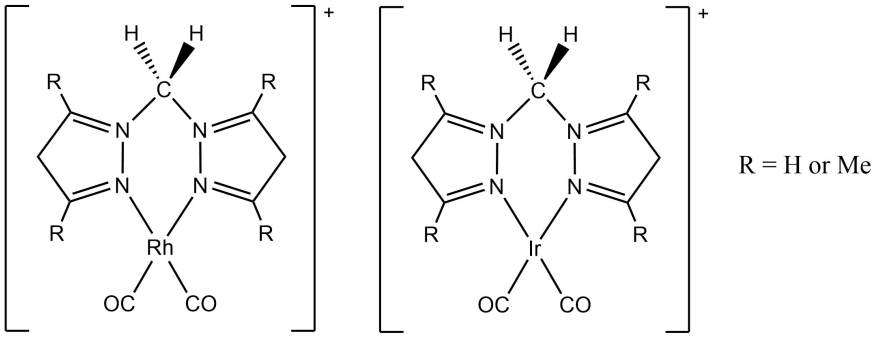

Figure 3.18: *Structures of the sixteen electron cationic complexes $[Bpm'Rh(CO)_2]^+$ and $[Bpm'Ir(CO)_2]^+$, where Bpm' = Bpm or Bpm**

Table 3.15 shows the results of bond dissociation energy calculations. As expected the BDEs increased from rhodium to iridium and increase from CH_4 to C_7H_{16}, with the lowest BDE belonging to $[Bpm^*Rh(CO)(CH_4)]^+$ (66.5 $kJmol^{-1}$) and the highest belonging to

$[BpmIr(CO)(C_7H_{16})]^+$ (112.3 kJmol^{-1}). The latter result is the highest we have calculated in this chapter, and amongst the highest calculated metal–alkane bond dissociation energies. As with previous investigations, the non-methyl containing $[BpmM(CO)(X)]^+$ complexes result in higher bond dissociation energies.

Table 3.15: Calculated bond dissociation energies for complexes of the form [Bpm'M(CO)(X)]$^+$, where Bpm' = Bpm or Bpm*, M = Rh or Ir and X = CH_4 or C_7H_{16}

Complex	BDE / kJmol^{-1}
$[BpmRh(CO)–CH_4]^+$	73.6
$[Bpm*Rh(CO)–CH_4]^+$	66.5
$[BpmRh(CO)–C_7H_{16}]^+$	85.0
$[Bpm*Rh(CO)–C_7H_{16}]^+$	78.2
$[BpmIr(CO)–CH_4]^+$	98.1
$[Bpm*Ir(CO)–CH_4]^+$	88.8
$[BpmIr(CO)–C_7H_{16}]^+$	112.3
$[Bpm*Ir(CO)–C_7H_{16}]^+$	103.4

All complexes show great promise for future long-lived metal alkane complexes. The longest-lived characterised metal–alkane complex (under room conditions), $CpRe(CO)_2$(*c*-pentane) was calculated to have a BDE of 62 kJmol^{-1}. All of the calculated values here are larger than this value, with the largest calculated value almost double this value. Structurally characterised rhodium complexes described in the Introduction were calculated to have bond dissociation energies in the range of 93.5–127.8 kJmol^{-1}. Three of the complexes here lie within that range, and therefore have significant potential to be stable enough for structural characterisation techniques like X-ray crystallography. If they were able to be synthesised, they could potentially be some of the longest lived alkane complexes. And

indeed, syntheses of $[BpmM(CO)_2][BF_4]$ (where M = Rh or Ir) and $[Bpm'Ir(CO)_2][BPh_4]$ (Bpm' = Bpm or Bpm*) have been previously reported.[146–149] However, their applications in the literature are solely limited to catalysis, namely for hydroamination reactions and alcoholysis of alcohols and hydrosilanes. To our knowledge they have not been studied as precursors for long-lived alkane complexes. Much of the problems with cationic species comes from the fact that the anion is often more strongly coordinating than an alkane, which leads to preferential bonding of the anion over any alkane. With exchange of the BF_4 and BPh_4 anion for a more weakly coordinating anion, these complexes would be excellent precursors for long-lived alkane and noble gas complexes. With successful anion exchanges having been performed for similar metal complexes, synthesis of these complexes remains a realistic goal.

Figure 3.19 shows a comparison of the bond dissociation energies between neutral Bp'M(CO)X (for BDE calculations see Appendix A) and cationic $[Bpm'M(CO)X]^+$.

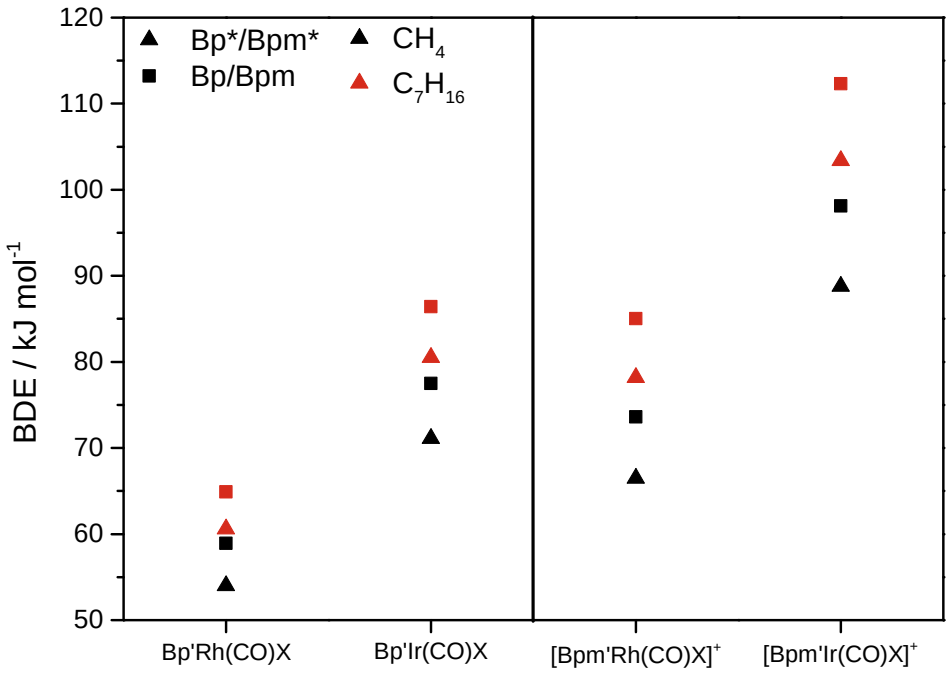

Figure 3.19: *Comparison of the bond dissociation energy of neutral Bp'M(CO)X and cationic $[Bpm'M(CO)X]^+$ (where Bp' = Bp (square) or Bp* (triangle), Bpm' = Bpm (square) or Bpm* (triangle), M = Rh or Ir and X = CH_4 (black) or C_7H_{16} (red))*

It clearly demonstrates an increase in the bond dissociation energy from neutral to

cationic complexes of between 12.5 and 26 kJmol^{-1}, with the largest increase from BpIr(CO)(C_7H_{16}) (86.4 kJmol^{-1}) to [BpmIr(CO)(C_7H_{16})]$^+$ (112.3 kJmol^{-1}). The average increase from neutral to cationic species is 19.0 kJmol^{-1}. Compared to previously studied group VI and VII complexes, this is a much bigger difference between neutral and cationic species, for example the average difference between group VI neutral and cationic species was 7.1 kJmol^{-1} and for group VII, the average difference was 9.4 kJmol^{-1}.

In Chapter 2, we studied the reactivity of Bp*Rh(CO)(alkane) complexes and found them to be remarkably long-lived, and proved that calculations accurately predict trends in bond dissociation energies. These calculations have shown that the cationic species BDE's are around a third higher than the neutral species; therefore, we can confidently predict that these cationic species will have a significantly longer lifetime than those of Bp*Rh(CO)(alkane).

3.3.4.1 Bond Length Studies

The calculated bond lengths for complexes of the form Bpm'M(CO)X (Bpm' = Bpm or Bpm*, M = Rh or Ir and X = CH_4 or C_7H_{16}) are shown in Table 3.16. The M–H_1 bond lengths are among the shortest we have calculated in this work, with three complexes calculated to have M–H_1 distances < 1.90 Å. The shorter distance between the metal and the hydrogen of the alkane is reflective of the stronger bond. This is also reflected in the C_1–H_1 bond lengths, the longest of which is 1.17 Å (for both BpmIr(CO)(C_7H_{16}) and Bpm*Ir(CO)(C_7H_{16})), which is a significant lengthening of a normal C–H bond (1.09 Å), and the longest we have calculated in this work. For all complexes, the shorter the M–H_1 distance, the longer the C_1–H_1 distance.

Replacing a strongly bonding CO ligand with a weakly bonding alkane has caused the bond between the metal and the second CO to shorten and therefore strengthen, again, mirroring previous results.

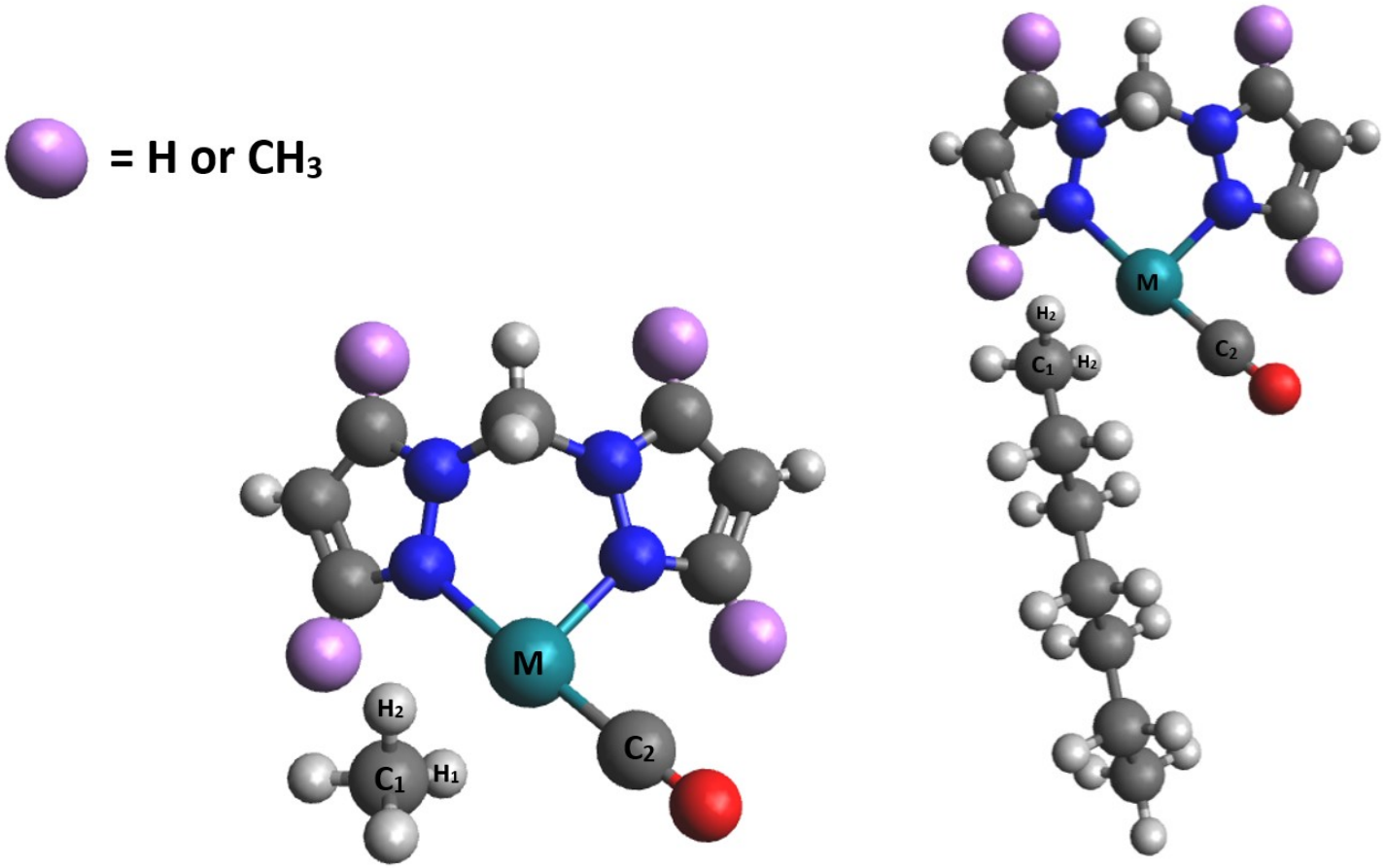

Figure 3.20: *Labelled structures of [Bpm'M(CO)(CH_4)]$^+$ (left) and [Bpm'M(CO)(C_7H_{16})]$^+$ (right), where Bpm' = Bpm or Bpm* and M = Rh or Ir*

Table 3.16: Selected calculated bond lengths (in Angstroms) for complexes of the form Bpm*M(CO)(X), where M = Rh or Ir and X = CH_4 or C_7H_{16}

	$M–C_1$	$M–H_1$	$M–H_2$	$C_1–H_1$	$C_1–H_2$	$M–C_2$
$[BpmRh(CO)_2]^+$	1.90	-	-	-	-	1.90
$[BpmRh(CO)(CH_4)]^+$	2.43	1.97	2.21	1.13	1.10	1.87
$[BpmRh(CO)(C_7H_{16})]^+$	2.48	1.87	2.36	1.15	1.10	1.87
$[Bpm*Rh(CO)_2]^+$	1.90	-	-	-	-	1.90
$[Bpm*Rh(CO)(CH_4)]^+$	2.69	1.95	2.26	1.13	1.10	1.87
$[Bpm*Rh(CO)(C_7H_{16})]^+$	2.49	1.87	2.38	1.15	1.10	1.87
$[BpmIr(CO)_2]^+$	1.87	-	-	-	-	1.87
$[BpmIr(CO)(CH_4)]^+$	2.40	1.85	2.34	1.16	1.10	1.85
$[BpmIr(CO)(C_7H_{16})]^+$	2.45	1.81	2.41	1.17	1.10	1.85
$[Bpm*Ir(CO)_2]^+$	1.87	-	-	-	-	1.87
$[Bpm*Ir(CO)(CH_4)]^+$	2.42	1.85	2.36	1.16	1.10	1.85
$[Bpm*Ir(CO)(C_7H_{16})]^+$	2.46	1.82	2.42	1.17	1.10	1.84

3.3.4.2 LUMO Energies

Again, we have calculated and compared the LUMO energies for the neutral Bp'M(CO)(X) and cationic $[Bpm'M(CO)(X)]^+$, where X = CH_4 or C_7H_{16}, the values of which are shown in Table 3.17. They show a difference between neutral and cationic complexes which on average is 3.6 eV, which continues the trend we have seen throughout this chapter. Again, the Bp/Bpm complexes exhibit a lower LUMO than the methyl containing Bp*/Bpm* complexes, which corresponds to a higher bond dissociation energy. Interestingly, however, whilst the iridium complexes were calculated to have a significantly higher bond

dissociation energy than their rhodium counterparts, their corresponding metal fragment LUMO energies are not as low as the rhodium LUMO energies. Previous works have shown that upon descending the group, LUMO energies decrease;[139] however, we have not found this to be the case for group IV metals. This further proves that LUMO energies are not the only factor in creating a strong metal–X bond.

Table 3.17: Calculated LUMO energies for metal fragments of the type Bp'M(CO) and [Bpm'M(CO)]$^+$, where Bp' = Bp or Bp*, Bpm' = Bpm or Bpm* and M = Rh or Ir

	Complex	LUMO Energy / eV
Neutral	BpRh(CO)	-3.07
	Bp*Rh(CO)	-2.83
	BpIr(CO)	-3.02
	Bp*Ir(CO)	-2.78
Cationic	[BpmRh(CO)]$^+$	-6.80
	[Bpm*Rh(CO)]$^+$	-6.42
	[BpmIr(CO)]$^+$	-6.72
	[Bpm*Ir(CO)]$^+$	-6.31

3.4 Conclusions and Future Work

The bond dissociation energies for a series of group V, VI, VII and IX complexes have been calculated. For group V hexacarbonyl derivatives of the form $M(CO)_5X$ (X = CH_4, C_7H_{16} or CO_2), the lowest BDE was for $V(CO)_5(CH_4)$ (36.7 $kJmol^{-1}$) and the highest was for $Ta(CO)_5(C_7H_{16})$ (52.9 $kJmol^{-1}$). All values for group V hexacarbonyl alkane complexes showed a significant increase in BDE in comparison to the analogous group VI hexacarbonyls by around 5–10 $kJmol^{-1}$. This goes against the general rule that the strength of the metal–alkane bond increases as you go across the groups. This anomaly was attributed to the seventeen electron, and hence electron deficient, nature of the group V hexacarbonyls. Furthermore, bond dissociation energies of alkane complexes of the group V eighteen electron $M(CO)_5(NO)$ were also found to be around 5–8 $kJmol^{-1}$ lower than their seventeen electron relatives, and were much more comparable to group VI $M(CO)_5(NO)$ complexes. Since the group V complexes are expected to be lower than their analogous group VI complexes, it appears that the addition of a NO ligand has indeed increased the bond dissociation energy. According to our calculation results, the electron deficient seventeen electron complex has a stronger effect on increasing the bond dissociation energy than the NO ligand. Analysis of the complexes' bond lengths showed some minor lengthening of the alkane C–H bonds of around 0.01–0.03 Å. The energies of LUMO of the metal fragments were also analysed to show that the LUMO of seventeen electron $M(CO)_5$ were slightly lower than those of standard eighteen electron $M(CO)_4(NO)$, which could account for the higher bond dissociation energy. The difference in LUMO energies however was not as significant as the difference found in previous work in our group between neutral and cationic complexes.

For cationic Group VI complexes, $[Tpm'M(CO)(NO)X]^+$, where Tpm' = Tpm or Tpm*, M = Cr, Mo or W and X = CH_4 or C_7H_{16}, the lowest BDE was for $[Tpm*Cr(CO)(NO)(CH_4)]^+$ at 27.5 $kJmol^+$ and the highest was for $[TpmW(CO)(NO)(C_7H_{16})]^+$ at 71.9 $kJmol^+$. The cationic nature of these complexes meant they these are the highest BDEs for group VI alkane complexes calculated

in our group. Again, analysis of the complexes' bond lengths showed some minor lengthening of the alkane C–H bonds of around 0.02–0.04 Å. For these complexes, the difference in LUMO energy between cationic metal fragments $[Tpm'M(CO)(NO)]^+$ and the neutral fragment $Tpm'M(CO)_2$ was significant, at around 3.6 eV. Previous work had calculated that an average of 3 eV difference in LUMO energy of the metal fragment between neutral and cationic complexes resulted in an average bond dissociation energy difference of 17.4 kJmol−1. The difference of 3.6 eV in LUMO energies here has only resulted in a 5–10 $kJmol^{-1}$ increase in BDE, therefore suggesting there are other factors involved.

Calculations into cationic group VII complexes, $[Tp'M(CO)(NO)(X)]^+$ and $[Tpm'M(CO)_2(X)]^+$, where Tp' = Tp or Tp*, Tpm' = Tpm or Tpm*, M = Mn or Re and X = CH_4 or C_7H_{16}, showed that the former nitrosyl complexes resulted in lower bond dissociation energies than the latter dicarbonyl complexes. The lowest BDE was for $[Tp*Mn(CO)(NO)(CH_4)]^+$ (24.0 $kJmol^{-1}$) and the highest was for $[TpmRe(CO)_2(C_7H_{16})]^+$ (78.2 $kJmol^{-1}$). The latter is a significant bond dissociation energy that is much larger than their neutral analogues and we can predict that experimentally they will result in extremely long-lived complexes. However, these BDE's were not as high as those calculated for other group VII cationic complexes such as $[CpRe(CO)_2(C_5H_{10})]^+$ (110 $kJmol^{-1}$) and $[BnRe(CO)_2(C_7H_{16})]^+$ (89 $kJmol^{-1}$). Again, there was a significant decrease in the LUMO energy for the cationic complexes by around 5 eV for $[Tp'M(CO)(NO)(X)]^+$ complexes and around 3 eV for $[Tpm'M(CO)_2(X)]^+$ complexes. Here, the bigger difference in LUMO energy has not resulted in a larger bond dissociation energies, as suggested in previous work. This again implies that LUMO energies are not the most important factor in BDE calculations.

Cationic relatives of the group IX complexes studied in Chapter 2, $[Bpm'M(CO)(X)]^+$ (Bpm' = Bpm or Bpm*, M = Rh or Ir and X = CH_4 or C_7H_{16}), were found to have the highest bond dissociation energies in this chapter, with the highest for $[BpmIr(CO)(C_7H_{16})]^+$ at 112.3 $kJmol^{-1}$. This is a significantly large bond dissociation energy and presents an inter-

esting new area of experimental research. The rhodium analogue, [Bpm*Rh(CO)$_2$][BF$_4$], has been synthesised experimentally in our group; therefore, eventual characterisation of [Bpm'Rh(CO)(alkane)]$^+$ and even [Bpm'Ir(CO)(alkane)]$^+$ remain a realistic goal. The cationic bispyrazolylmethane complexes showed a much more significant lengthening of the C–H bond of between 0.04 and 0.08 Å. This bond lengthening was particularly large for the iridium complexes, implying the increased electron density from the metal into the C–H antibonding orbitals is a key interaction here. Yet again, the LUMO values were significantly lower for the cationic metal fragments compared to the analogous neutral fragments by ~3.6 eV; however, the iridium fragment LUMO energies were higher than the analogous rhodium fragments. This is an unexpected trend which would be interesting to explore further in future work.

In all cases for the electron deficient complexes, the energy of the metal fragment LUMO energy was lowered, corresponding with an increase in BDE. We believe that this is a key reason why electron deficient complexes result in stronger bonds, as the overlap of the orbitals is better, see Figure 3.21; however, there are other factors that effect the magnitude of bond dissociation energy that warrant further investigations.

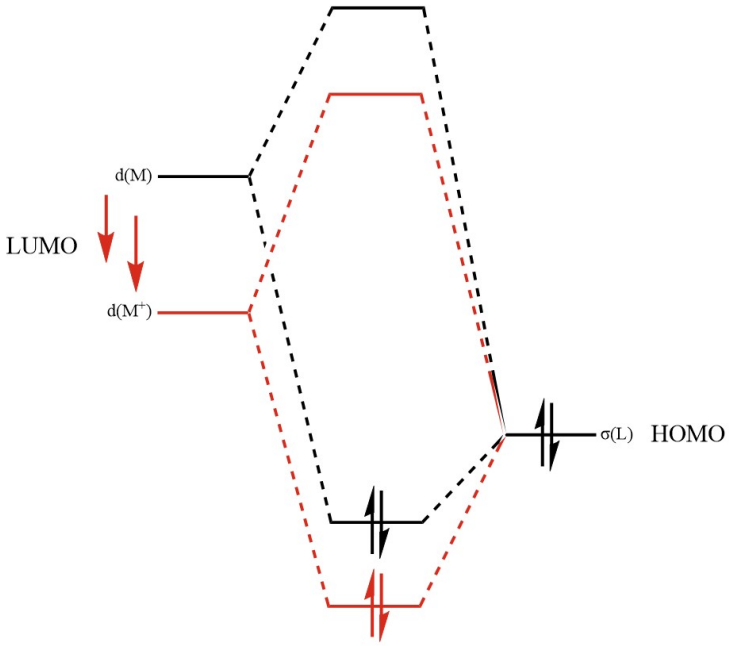

Figure 3.21: *Simplified molecular orbital diagram showing the bond between an alkane ligand and a metal d-orbital for a neutral (black) and a cationic (red) complex*

Chapter 4

Time-resolved Studies of Reactions of $CpM(CO)_3$ (M = Mn or Re) with Alkanes and Triethylsilane

4.1 Introduction

Thus far in this thesis we have studied the reactions of alkanes with transition metal complexes, and in particular we have focussed on the search for long-lived alkane σ-complexes. Understanding these complexes is vital to understanding the process of C–H activation; however, they are often incredibly short-lived, limiting study of their structure. Study of the reactions of other E–H bonds (E = H, Si, B, etc.) can provide a direct comparison to C–H bond reactions. These E–H bonds form '3-centre, 2-electron' bonds with transition metals, which often leads to activation of the E–H bond; therefore, there are many direct comparisons that can be drawn between these reactions and analogous reactions of C–H bonds. This Chapter will investigate the reactions of both Si–H and C–H bonds with metal centres. And there is a vast wealth of characterised transition metal silane complexes to draw comparisons from, as they are the second largest class of σ-complexes behind molecular hydrogen systems.[150]

4.1.1 Metal Silane Complexes

The bond between the silane and the metal centre arises from interaction between an empty metal d-orbital and the Si–H σ-bonding orbital. The increased basicity of a Si–H bond in comparison to a C–H bond makes it a better electron donor; hence, it is able to bind more strongly to the metal.[151] Just like the C–H bond in their alkane counterparts, the Si–H bond can be activated by a metal centre. The lower energy of the Si–H σ* antibonding orbital relative to C–H makes it a better π-acceptor,[152] leading to increased back-bonding from the metal centre, and a more facile dissociation of the Si–H bond. As such, metal silane complexes are found in various stages of Si–H activation, shown in Figure 4.1, ranging from a fully activated "2-centre, 2-electron" (2c, 2e) bond to any of the partially activated "3-centre, 2-electron" (3c, 2e) or bonds shown in between. The Si–H bond length in silane σ-complexes can range relatively quite widely from 1.6–1.9 Å (compared to a free Si–H bond at 1.5 Å), in contrast to H–H and C–H σ-complexes, whose lengths typically lie in a smaller range much closer to the length of free H–H and C–H bonds.[153]

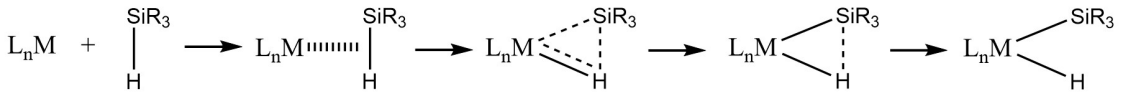

Figure 4.1: *Stages in Si–H bond activation by a transition metal centre, reproduced from reference 152*

The first recognised metal silane complex was reported in 1969 by Hoyano *et al.*,[154] that of $(C_6H_6)_2SiH_2Re_2(CO)_8$. Subsequently a wealth of complexes were characterised, in particular in work in the late 1980s by Schubert and co-workers. They published a number of works into metal silane bonds, the bulk of which is summarised in a comprehensive review.[155] These included characterisation of a number of silane complexes derived from $CpMn(CO)_2L$ (L = CO or PR_3). Structural data was primarily obtained from NMR studies by evaluation of coupling constants.[156]

Later, X-ray diffraction studies were used to study these complexes; however, this method can be unreliable as it fails to locate the hydrogen accurately. Neutron diffraction

studies, therefore, are a preferred method of analysis; however, there are few examples in the literature. McGrady *et al.* determined the structure of [Cp′Mn(CO)$_2$(η^2-HSiHPh$_2$)] (Cp′ = methylcyclopentadienyl) by neutron diffraction, see Figure 4.2, with bond lengths and angles calculated as; Mn–H(1) (1.575 Å), Si–H(1) (1.806 Å), Si–H(2) (1.501 Å), and H(1)–Si–H(2) 148.5°. This Si–H bond length was about 20 % longer than that of SiH$_4$. X-ray diffraction studies of its rhenium analogue, [Cp′Re(CO)$_2$(η^2-HSiHPh$_2$)], showed the Si–H bond to have lengthened even further to 2.19 Å,[157] suggesting full cleavage of the Si–H bond.

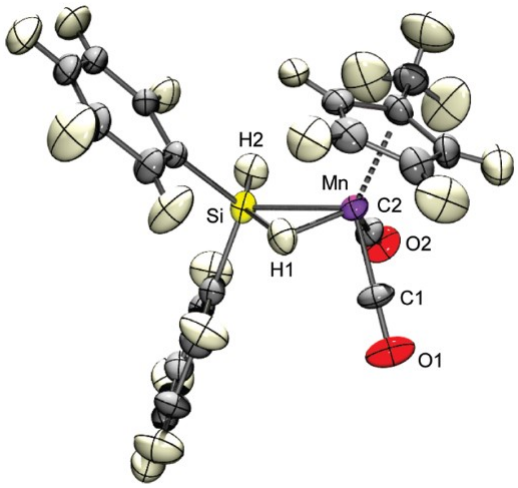

Figure 4.2: *Structure of [Cp′Mn(CO)$_2$(η^2-HSiHPh$_2$)], as determined by single crystal neutron diffraction, reproduced from reference 150*

However, not all interactions of silanes with a metal centre exist in a 3c, 2e σ-complex configuration. Yang *et al.* reported the structural and spectroscopic characterisation of an η^1 transition metal silane complex.[158] Treatment of [(POCOP)Ir(H)(acetone)][B(C$_6$F$_5$)$_4$] (POCOP = 2,6-[OP(^{t}Bu)$_2$]$_2$C$_6$H$_3$) with Et$_3$SiH in CD$_2$Cl$_2$ at 23 °C gave [(POCOP)Ir(H)(η^1-HSiEt$_3$)][B(C$_6$F$_5$)$_4$], see Figure 4.3. The Ir–Si distance (3.346 Å) and the Ir–H–Si angle (157°) were both indicative of an end on η^1-H interaction. DFT calculations supported experimental observations, calculating a Ir–Si distance of 3.38 Å and an Ir–H–Si angle of 161°. Calculations also showed that by either half or fully replacing the bulky ^{t}Bu groups on the PONOP ligand with methyl groups, the structure converted to the η^2-Si–H configuration. This demonstrates the influence

that sterics has on the binding mode, and how, by altering constituents on the ligand, the binding mode may be controlled. It is also an interesting case of η^1 bonding that is stable enough to be characterised.

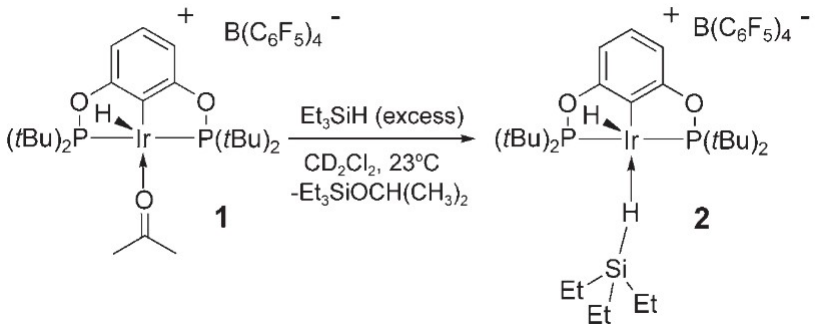

Figure 4.3: *Reaction mechanism to form [(POCOP)Ir(H)(η^1-HSiEt$_3$)][B(C$_6$F$_5$)$_4$] (**2**), reproduced from reference 158*

Much like studies of metal–alkane bonds, the reaction of metal complexes with silanes can be monitored by infrared spectroscopy, as the reporter ligand CO can indicate the type of bonding to the metal, and this is what this chapter will focus on. As described in Chapter 1, the reactions of CpM(CO)$_3$ (M = Mn or Re) are well-studied in the area of metal alkane complexes. This is because the CpM(CO)$_2$(alkane) complexes are the among the longest-lived metal alkane complexes, in particular CpRe(CO)$_2$(cyclopentane), which is the most stable known complex under ambient conditions, with a lifetime of 125 ms at room temperature. Study of the analogous silane reactions can provide more information on this important reaction.

4.1.1.1 Time-resolved Infrared Studies of the Reaction of CpMn(CO)$_3$ with Silanes

Much of the work on reactions of CpM(CO)$_3$ with silanes was undertaken by the Harris group. They investigated the reaction of CpMn(CO)$_3$ with triethylsilane by TRIR. Photolysis of CpMn(CO)$_3$ in triethylsilane led to the formation of an ethyl bound complex, CpMn(CO)$_2$(Et$_3$SiH), initially characterised in low temperature studies.[159] The proposed reaction mechanism is shown in Figure 4.4.

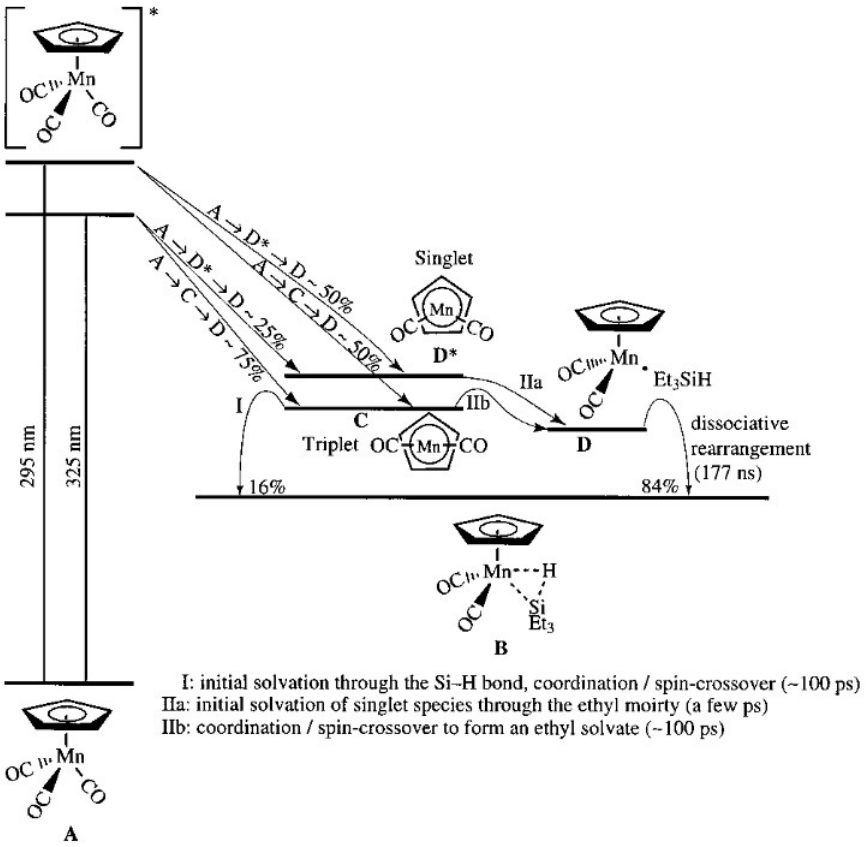

Figure 4.4: *Proposed reaction mechanism of Si–H bond activation by $CpMn(CO)_3$, reproduced from reference 111*

The ultrafast kinetics revealed formation of both the singlet and triplet form of coordinatively unsaturated $CpMn(CO)_2$. The ratio in which these were created was dependent on the excitation wavelength, with longer wavelength resulting in increased formation of the triplet species. Whilst there was no direct spectroscopic evidence of $^1CpMn(CO)_2$ (**D***) the mechanistic evidence implicated its existence. A later study by Kemnitz *et al.* has characterised both $^3CpMn(CO)_2$ and $^1CpMn(CO)_2$ by matrix isolation at 10K, confirming its existence.[160] The following spin forbidden crossover reaction of $^3CpMn(CO)_2$ (**C**) to $^1CpMn(CO)_2(Et_3SiH)$ (**D**) occurrs in *ca.* 100 ps. Formation of the 'Si–H activated' species can occur through one of two pathways; through direct formation from the coordinatively unsaturated dicarbonyl, $CpMn(CO)_2$ (**C**), occurring on the ps timescale, or through dissociative rearrangement of the ethyl bound complex, $CpMn(CO)_2(Et_3SiH)$ (**D**), occurring much more slowly on the ns timescale. While the shift to higher energy of the

ν(CO) of 'activated' $CpMn(CO)_2H(SiEt_3)$ is characteristic of bond activation, the Si–H bond length, calculated by DFT, was not sufficiently long enough to confirm actual Si–H bond cleavage. The complex was assigned as an η^2 Si–H σ-complex, $CpMn(CO)_2(\eta^2$-Si–$HEt_3)$, with significant $CpMn(CO)_2(H)(SiEt_3)$ character, and is henceforth referred to as 'partially activated'.

The reaction of silanes with $CpMn(CO)_3$ has also been studied in alkane solvents. Work in our group has shown that, interestingly, the partial Si–H activation proceeds via an alkane bonded intermediate in the reaction of $CpMn(CO)_3$ in tributylsilane doped heptane. TRIR investigations found that, as the reaction above, both the triplet and singlet dicarbonyls were produced on photolysis. Again, there were two routes to forming the partially activated $CpMn(CO)_2(SiBu_3)H$; the first being direct formation from the triplet dicarbonyl $^3CpMn(CO)_2$, occurring in a few ps. The second, in contrast the reaction in neat silane, occurs through a heptane bonded intermediate, see Figure 4.5. This step, occurring on the microsecond timescale, is several orders of magnitude longer than dissociative rearrangement from the ethyl-bound $CpMn(CO)_2(Et_3SiH)$ seen in neat triethylsilane. The authors found no evidence of formation of the $CpMn(CO)_2(Bu_3SiH)$ intermediate, owing to the low concentration of silane used in the experiment and lack of spectroscopic evidence.

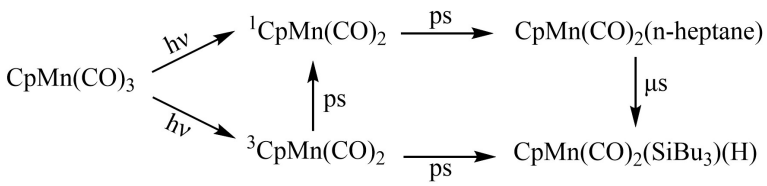

Figure 4.5: *Proposed reaction mechanism of Si–H bond activation by $CpMn(CO)_3$, reproduced from reference 111*

Investigations into the reactions of $CpRe(CO)_3$ with silanes were also conducted. The reaction has been found to proceed somewhat differently in comparison to its manganese analogue, see Figure 4.6. Only the singlet species, $^1CpRe(CO)_2$ (**G***), is formed upon photolysis. There are again two pathways to form the Si–H activated product;

through solvation of the ethyl moiety to form $CpRe(CO)_2(Et_3SiH)$ (**G**) and further dissociative rearrangement to form $CpRe(CO)_2(H)(SiEt_3)$ (**F**), or through direct formation from $^1CpRe(CO)_2$ (**G***). The former is, as it was for Mn, a much slower process, occurring on the microsecond timescale, whilst the latter occurs in a few picoseconds.

DFT calculations of the Si–H bond length revealed that full oxidative addition takes place in the Re complex, in contrast to the manganese complex. This is associated with the more electron rich nature of rhenium, allowing for greater π-backbonding and hence easier Si–H bond dissociation. This was observed in the infrared spectra in the greater shift of the ν(CO) of $CpRe(CO)_2(H)(SiEt_3)$ from the parent $CpRe(CO)_3$ than that of $CpMn(CO)_2(H)(SiEt_3)$ from $CpMn(CO)_3$.

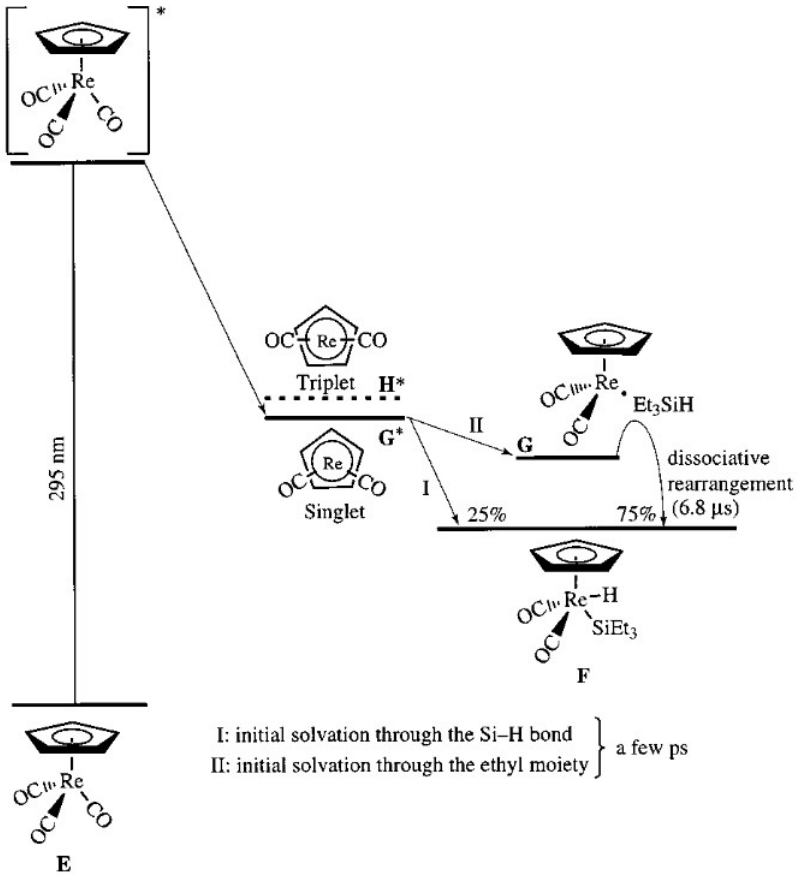

Figure 4.6: *Proposed reaction mechanism of Si–H bond activation by $CpRe(CO)_3$, reproduced from reference 111*

Work in our group has also investigated the reaction of $CpRe(CO)_3$ in *n*-heptane with 0.25 M tributylsilane but only identified the one photoproduct, $CpRe(CO)_2$(*n*-heptane),

on the timescale studied (1 ms). This is in contrast to the same reaction with $CpMn(CO)_3$, where the Si–H activation product was made via the *n*-heptane bonded intermediate. The authors proposed that this was due to the exceptionally long-lived nature of $CpRe(CO)_2$(*n*-heptane).

A recent computational study by Zhang and Su calculated the energies of all intermediates and transition states for both the triplet and singlet states, finding that photolysis of $CpMn(CO)_3$ generates both a singlet and triplet dicarbonyl whereas photolysis of $CpRe(CO)_3$ can only lead to the singlet dicarbonyl excited state.[161] Dependent on the energy of excitation, either the triplet or singlet channel is more favoured (higher energy favours the singlet state), see Figure 4.7. All these observation were in agreement with experimental observations.

Another notable finding of this study is the nature of the transition states. In particular the transition state labelled by the authors as Mn-S_0-Cpx, Mn-T_1-Cpx and Re-S_0-Cpx, see Figure 4.7. For the manganese intermediate, for both Mn-T_1-Cpx and Mn-S_0-Cpx, the geometry of this intermediate is clearly an η^1 geometry, with a Mn–H–Si angle of 155.4° and 138.8°, respectively. However, for the rhenium intermediate, Mn-S_0-Cpx, it is more representative of an η^2 intermediate, with a Re–Si–H angle of 87.3°. This is certainly a notable finding, with the authors additionally noting that "Mn-S_0-Cpx should be easily detected by experiments" due to its complexation energy being low. However, the intermediate in this reaction has been determined to be an η^2 intermediate.

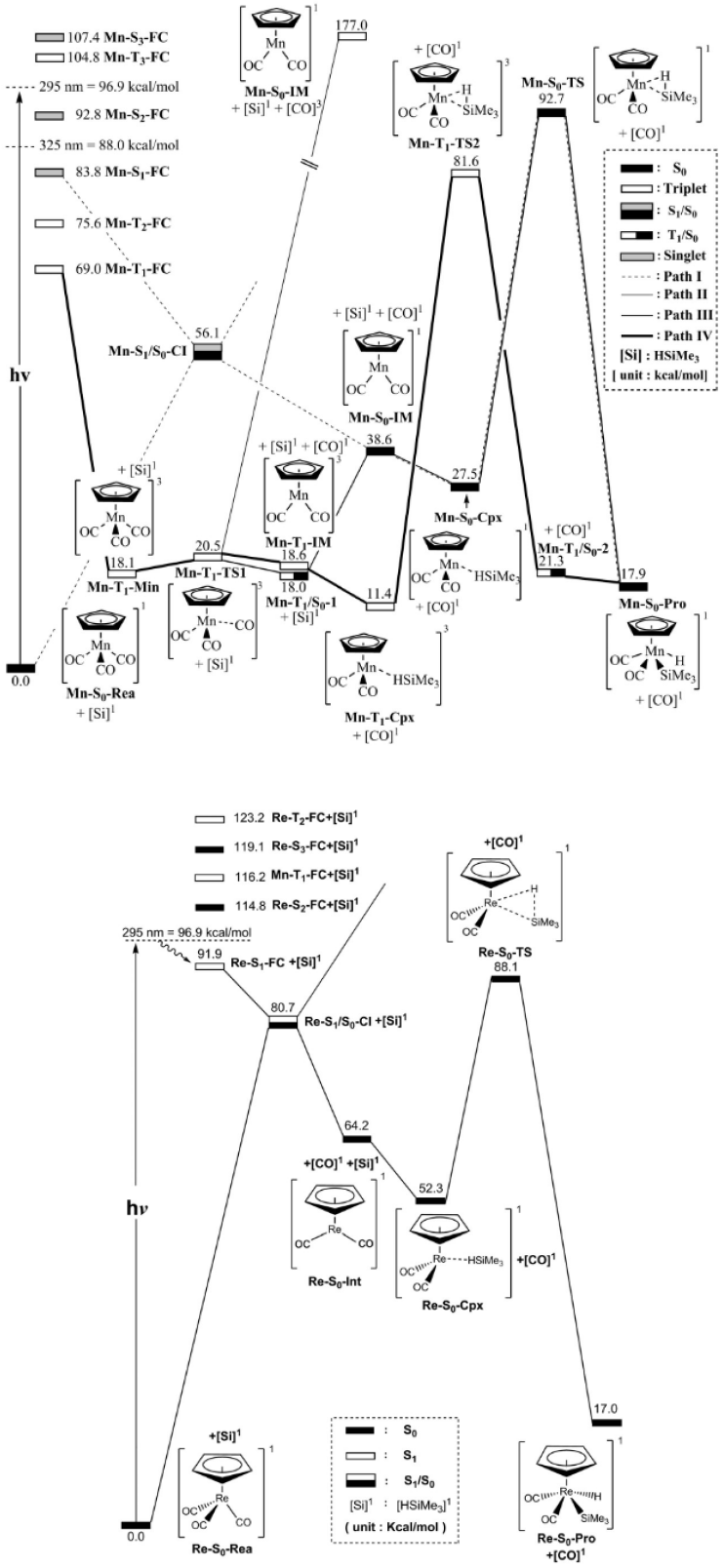

Figure 4.7: *Computed energy profiles of photochemical reactions of $CpMn(CO)_3$ (top) and $CpRe(CO)_3$ (bottom) with energies in kcal mol^{-1}, reproduced from reference 161*

4.1.2 E–H Bonding Reaction Trajectories

As discussed in Chapter 1, the key intermediate in C–H activation is widely accepted to be the σ-complex, see Figure 4.8. σ-complexes can be defined as a complex with a ligand containing a σ-E–H bond (E = H, C, Si, B, etc.), which is acting as a two-electron donor to the metal, resulting in a 'two-electron, three-centre' bond. Since interactions between a C–H bond and a metal centre were first discovered by Ibers and Maitlis in the 1960's,[162,163] many studies have sought to elucidate the true nature of this interaction.

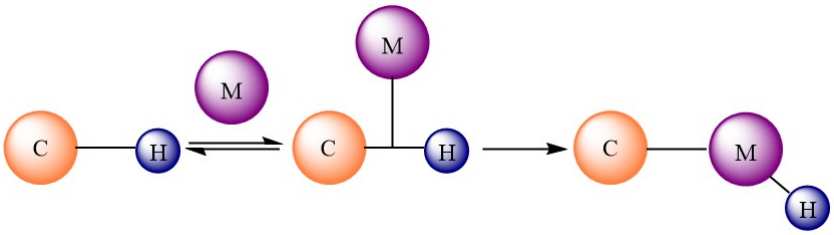

Figure 4.8: *Proposed mechanism for C–H activation, involving the key 'σ-complex' intermediate. Adapted from reference 33*

In a transition metal-(EH) complex, the electrons in the E–H σ bond are donated into an empty metal d orbital. In addition, electron density from the metal is back-donated to the E–H σ* anti-bonding orbitals, an interaction unique to transition metal σ-complexes, see Figure 4.9. An isolable complex must have some back-bonding; however, strong back-donation will lead to E–H bond activation.[151] These weak E–H donors form the most stable complexes with transition metals, suggesting that the back-donation component of the bond is important and stabilises the bond to a degree.[164]

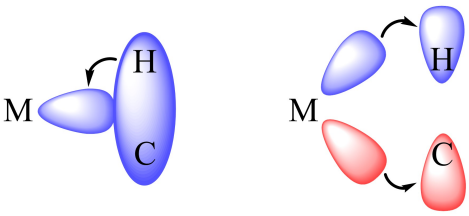

Figure 4.9: *Possible bonding interactions between a transition metal and a C–H bond. Left, an empty d-orbital accepts electrons from the C–H σ bond. Right, back-donation from the filled metal d-orbital to the C–H antibonding orbital. Reproduced from reference 151.*

Several binding modes of the alkane to the metal centre have been considered over many decades of research, see Figure 4.10(a). There is another class of interaction called 'agostic' interactions, which is intramolecular coordination of a C–H bond to a transition metal, Figure 4.10(b). We now know from experimental and theoretical observations, mainly X-ray crystallography, that most transition metal σ-complexes exist in the η^2-E,H conformation; however, there are some exceptions. These studies were detailed in Chapter 1.

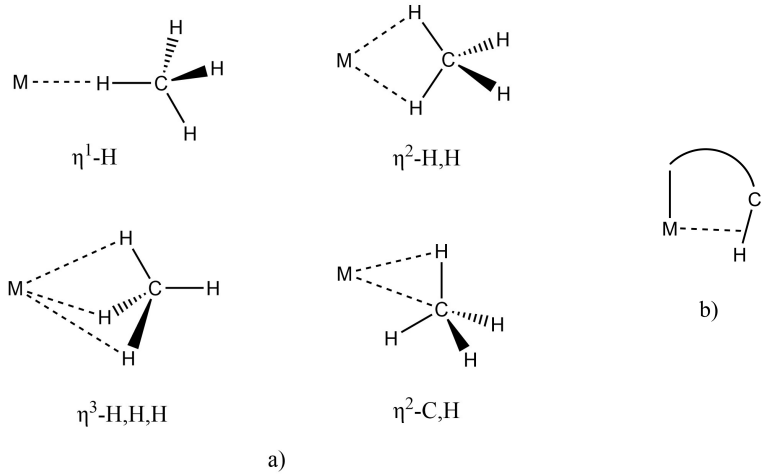

Figure 4.10: *a) Possible coordination modes of CH_4 to a metal, adapted from reference 36 and*
b) Coordination in an 'agostic' transition metal C–H σ-complex, adapted from reference 165

This section will discuss the reaction mechanisms of addition of H_2, C–H and Si–H bonds to a metal centre. As described above, it is widely accepted that this mechanism proceeds via a transition metal σ-complex, and many structural studies have shown that the majority of these transition metal σ-complexes exist in an η^2-(E,H) configuration. However, there is some speculation about the reaction mechanism, and how the E–H approaches the metal.

The first computational studies were into the reaction mechanism of addition of hydrogen to a metal centre. In the first study by Dedieu and Strich in 1979, the addition of H_2 to $RhCl(PH_3)_3$ (a model for Wilkinson's catalyst) was studied. They only studied the hydrogen approaching the metal with a perpendicular approach, i.e., an η^2 configuration.

However, the authors noted that rough preliminary calculations indicated that at the beginning of the reaction, the hydrogen approaching the metal in an end-on η^1 fashion is preferred over the side-on η^2 approach.[166]

Further works have supported these early studies. Saillard and Hoffmann calculated the energies of two different geometrical approaches of both H_2 and CH_4 to $Cr(CO)_5$. They found that although the perpendicular approach is stabilised somewhat, energetically H_2 favoured a parallel approach to the metal. However, CH_4 favoured a perpendicular approach, see Figure 4.11.[167]

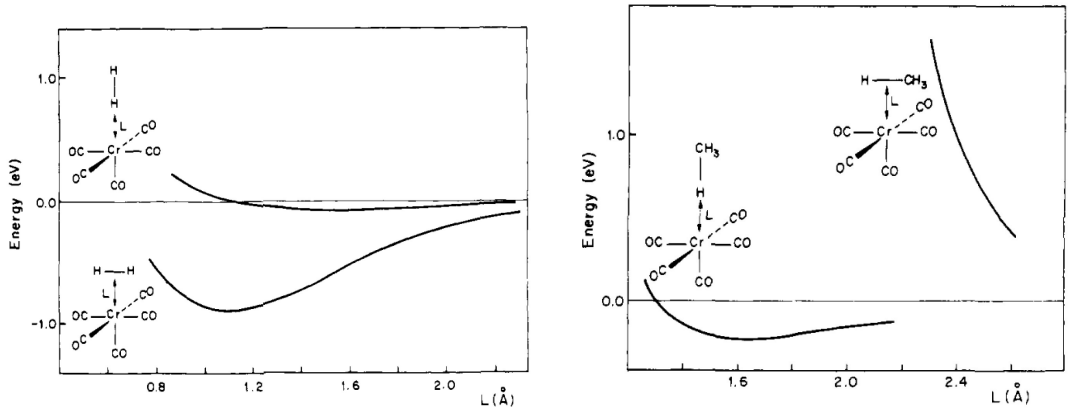

Figure 4.11: *Total energy of the perpendicular and parallel approaches of H_2 (left) and CH_4 (right) to $Cr(CO)_5$, reproduced from reference 167*

An assessment of the molecular orbitals reveals the reasons for this. In the parallel approach, the H_2 xz-σ* overlap is large; however, for CH_4, the corresponding component is small, and mismatched with the C–H σ* orbitals, Figure 4.12. In addition, there is a substantial overlap between the metal xz and the occupied σ C–H orbital, and in fact, this repulsive effect has a higher contribution over the attractive forces. The authors called this a dominance of the 'two-orbital four-electron repulsions' over the attractive bonding forces.

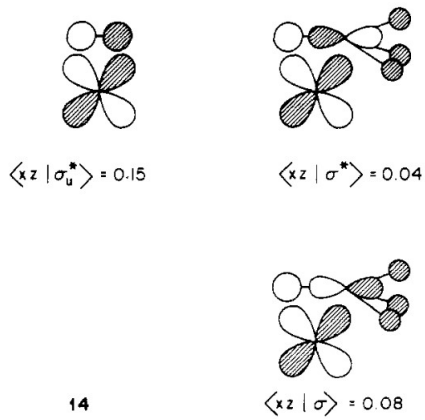

Figure 4.12: *Molecular orbitals of H_2 (left) and CH_4 (right) in a parallel (η^2) approach to the metal and their interaction with the metal d_{xz} orbitals, reproduced from reference 167*

Whilst most studies on the reaction trajectory of E–H bonding to a metal are theoretical, a handful of interesting studies have used the Bürgi–Dunitz structure-correlation method[168] to give an 'experimental' trajectory of the reaction. First, Schubert *et al.* used this method to predict the reaction trajectory of Si–H with a metal, by studying a series of reactions of SiR_3H to $CpMn(CO)_3$.[169,170] The silane was found to approach the metal with the hydrogen ahead, with the Si–H bond then pivoting, increasing the M–Si interaction, leading to eventual cleavage of the Si–H bond, see Figure 4.13.[155,170]

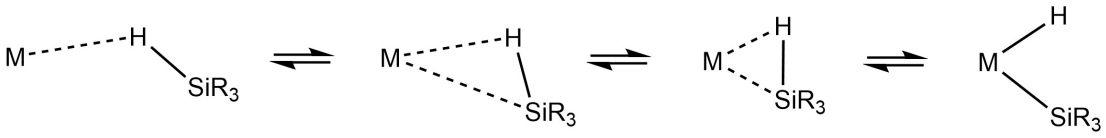

Figure 4.13: *Proposed trajectory for the reaction between Si–H and M, adapted from reference 155*

An in-depth study by Crabtree *et al.* used the same method to study addition of C–H to a metal centre. Figure 4.14 shows the results of this analysis. Their results were remarkably similar to those of Schubert *et al.*, with the alkane approaching the metal 'hydrogen first' with a M–H–C angle of 130°. The C–H then rotates and the bond lengthens, leading to eventual C–H cleavage.[171]

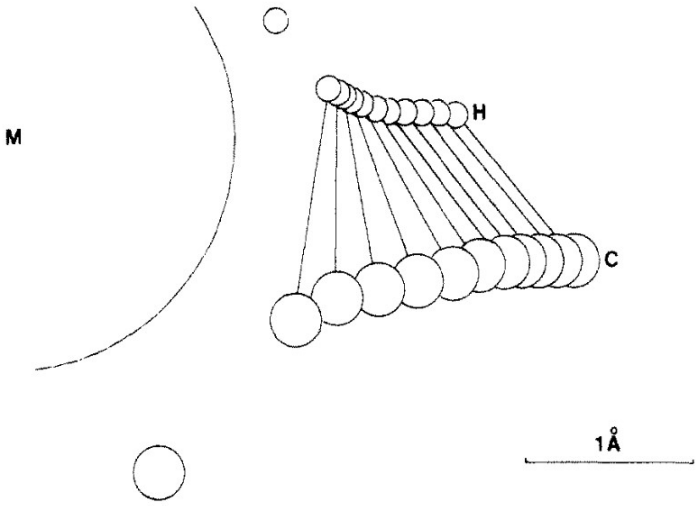

Figure 4.14: *A representation of the trajectory of the reaction between C–H and M, reproduced from reference 171. The trajectory shows the C–H approaching the metal with an M–H–C bond angle of 130°. The C–H bond then rotates and elongates before breaking. Reproduced from reference 171.*

They postulated that the off-axis (M–H–C < 180°) approach may be favoured for two reasons. One; by maximising the metal d_σ orbital overlap with the C–H σ bond. The C–H bonding pair of electrons is donating to the empty d orbital, see Figure 4.15, left. And two; due to the increased availability of the C–H σ* antibonding orbitals for backbonding from the metal, Figure 4.15, right. Such bonding is only available in the off-axis geometry. Both these processes serve to weaken the C–H bond.[171]

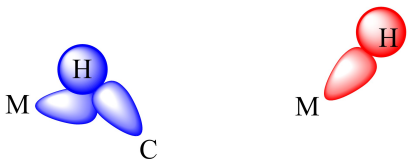

Figure 4.15: *Possible bonding interactions between a transition metal and a C–H bond when the M–H–C bond angle is equal to 130°. Left, an empty d-orbital accepts electrons from the C–H bond. Right, back-donation from the filled metal d-orbital to the C–H antibonding orbital. Adapted from reference 171.*

More modern DFT calculations have improved on previous works by optimising the transition geometry, as opposed to fixing the approaching alkane in a parallel or perpendicular geometry. While this previous approach has provided a simple but effective energy

comparison, the exact orientation of any intermediates remained unknown. Song and Hall studied the coordination of CH_4 to CpRh(CO) using MP2 calculations.[172] They calculated that the CH_4 approaches the metal with the Rh–H–C bond angle equal to 125.7°, in very good agreement with the experimental observations of Crabtree. Again, the calculations showed a rotation and an elongation of the C–H bond as it approached the metal, see Figure 4.16. The authors found that the interaction between Rh and C plays a significant role in determining the orientation of the C–H bond as it approaches the metal. Therefore, it seems that the identity of the metal may play an important role in whether the C–H bond approaches in an η^1 or η^2 fashion.

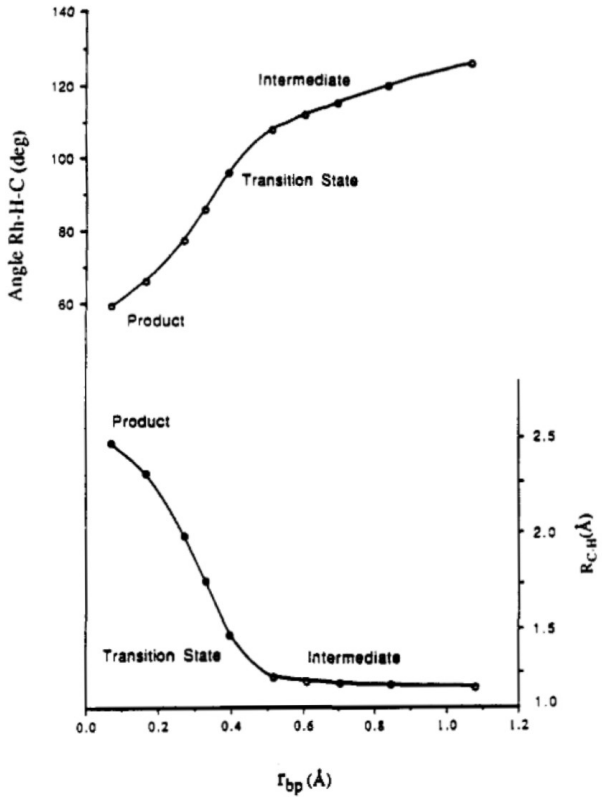

Figure 4.16: *Calculated changes in Rh–H–C bond angle and C–H bond length (R_{C-H}) as the distance between Rh and CH_4 (r_{bp}) changes in the reaction between CpRh(CO) and CH_4. Reproduced from reference 172.*

A more recent DFT study by Macgregor *et al.* has also concluded that in the addition of H_2 to $[M(PH_3)_4]$ (M = Ru, Fe or Rh^+), at long M–H_2 distances, an η^1 configuration is preferred. As the M–H_2 distance decreases, the H_2 rotates to an η^2 conformation.[173]

In addition, they calculated the activation energy of the η^1/η^2 'swing' and found that the η^1/η^2 'swing' of the reaction of $M(PH_3)_4$ with H_2 (M = Ru and Fe) proceeded with no activation energy. Whilst for same process in the reaction of $[Rh(PH_3)_4]^+$ with H_2, the activation energy was > 4 kcal mol^{-1}.

In photochemical C–H activation by a transition metal, a coordinatively unsaturated intermediate is essential for initial bonding of the alkane. As a result of this, in the early stages of the reaction the most important process is electron transfer from the σ bond to the metal. Therefore, it certainly makes sense that at the beginning of the reaction that the approach is with the hydrogen head-on. In Chapter 2, we described the DFT study of the addition of alkanes to $TpRh(CO)_2$. The first intermediate in this reaction was calculated to be an η^1 bound alkane; κ^3-TpRh(CO)(η^1-alkane).[91,96]

Three centre, two electron bonds occur most commonly when one of the three centres is a hydrogen,[164] implying that the small size of the hydrogen allows it to closely approach the metal, where this may not be possible with other atoms. This adds further support to a perpendicular approach with the hydrogen 'leading'.

Whilst there is much theoretical evidence to support the existence of an η^1-complex in the mechanism of C–H bonding and further activation to the metal, there is little experimental evidence. In practice, it is likely that these η^1-complexes are too short lived to be seen experimentally. However, in this Chapter, we will use TRIR to show evidence of η^1 bonding in alkanes. To support these observations, we have also used another time-resolved method, time-resolved X-ray absorption spectroscopy.

4.1.3 Time-resolved X-ray Absorption Spectroscopy

A brief introduction to time resolved extended X-ray absorption spectroscopy (TR-EXAFS) was given in Chapter 1, detailing the study in which TR-EXAFS was used to determine W–C bond lengths in $W(CO)_5$(heptane). This study was used to confirm the phenomenon of 'chain-walking', a process where the binding of heptane to the metal centre rapidly interchanges between C–H bonds in the chain. A further introduction will be given here.

Some key advantages of X-ray absorption spectroscopy (XAS) are that it can be used in all media, most importantly in liquids, in contrast to conventional X-ray diffraction (XRD) studies, where the sample to be analysed must be a highly organised crystal. A second advantage is that it is element specific, as the bonding energy of the core shell is different for each atom; thus, by changing the energy of the X-ray photons, elements can be specifically targeted. This carries the added advantage that solvent or impurities will have no effect unless they contain the absorbing element. Lastly, XAS can give detail of the electronic and geometric structure of the element in question.[174]

In X-ray absorption spectroscopy, X-rays are absorbed by an electron in a tightly bound quantum core level (i.e., 1s or 2s orbital) of an atom. The energy of the X-ray photon must be greater than the energy of the binding energy of this core level in order for absorption to occur. Once the energy is absorbed by the electron, it is ejected from the atom, with any excess energy given to it.

Once the electron has been ejected, there are two pathways for the decay of the excited state. These are; X-ray fluorescence, where the core level hole is filled by an electron of higher energy and thus ejecting an X-ray, and Auger emission, where an electron drops from a higher level and a second electron is emitted, see Figure 4.17. Both of these decay pathways have discrete energies and hence are characteristic of the absorbing atom.[175]

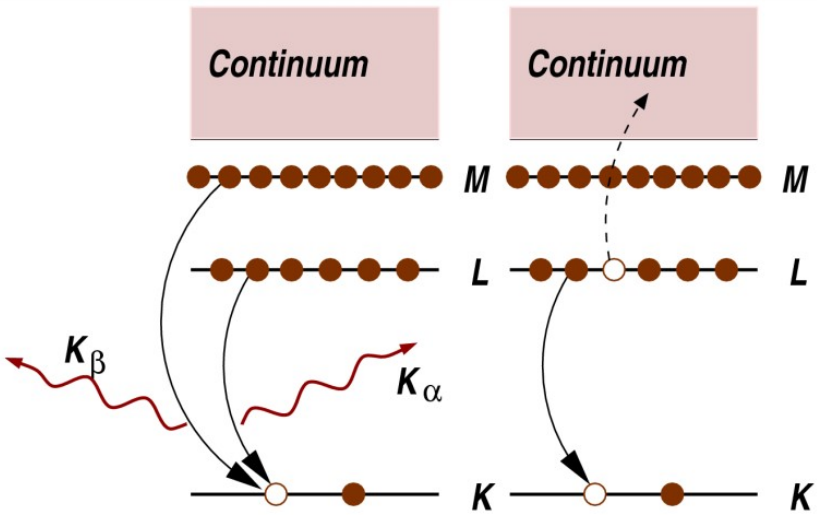

Figure 4.17: *Representation of the decay of the excited state by X-ray fluorescence (left) and Auger emission (right), reproduced from reference 175*

At the specific energy at which the electron is ejected, there is a sharp increase in absorption in the spectrum, referred to as the leading edge. These edges are named after the core orbital from which they originate, i.e., K-edge, L-edge, etc. There are two important regions of an XAS spectrum, the X-ray absorption near edge structure (XANES), which is the region in the spectrum just beyond the leading edge, and extended X-ray absorption fine structure (EXAFS), which is the region approximately >50 eV beyond the edge, see Figure 4.18.[176]

The XANES region is harder to quantitatively interpret that the EXAFS; however, this region of the spectrum has a much larger signal than the EXAFS, thus lending itself better to lower concentration solutions or more complex sample environments. This region is highly sensitive to changes in oxidation state, coordination number and geometry. As such, the XANES region can be used as a fingerprint to crudely interpret the structure.[175] The EXAFS can be analysed quantitatively to determine the bond lengths, coordination number and nature of the neighbouring atoms of the absorbing atom.[177]

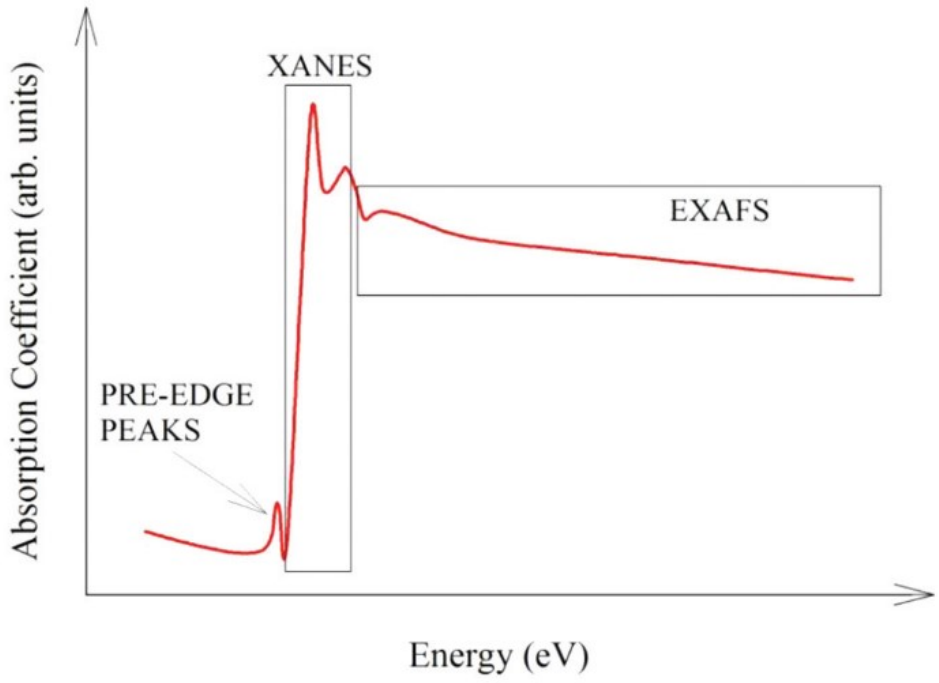

Figure 4.18: *Schematic representation of an X-ray absorption spectrum, reproduced from reference 178*

The outgoing electron can be scattered by neighbouring atoms to the absorbing atom, which can return back to where it originated. The XANES region features are mostly caused by multiple scattering events, whilst the EXAFS region consists of mainly single scattering events.[179] Oscillations in the EXAFS are due to the interference of the outgoing electron with back-scattered electrons from neighbouring atoms. These oscillations can be described using the EXAFS equation, see Equation 4.1, where f(k) and δ(k) are scattering properties of the neighbouring atoms, λ(k) is the photoelectron mean free path, N is the number of neighbouring atoms, R is the distance to the neighbouring atom and σ^2 is the disorder in the neighbour distance.

$$\chi(k) = \sum_j \frac{N_j f_j(k) e^{-2R_j/\lambda(k)} e^{-2k^2\sigma_j^2}}{kR_j^2} sin[2kR_j + \delta_j(k)] \tag{4.1}$$

If we know f(k), δ(k) and λ(k), we can work out R, N and σ^2.

To carry out time-resolved X-ray absorption spectroscopy (TR-EXAFS), one requires intense, energy tunable X-ray pulses, the best source of which is currently synchrotron radiation. Synchrotron radiation has the added bonus of high stability. The time resolution of this is limited to the intrinsic synchrotron pulse duration, which is typically 50–100 ps. However, recently, a specialised insertion device has been developed that allows for pulse durations on the femtosecond timescale to be reached.[180]

A typical TR-EXAFS experiment will be much like a classical pump–probe experiment, with a UV pump laser to excite the sample spatially overlapping with the X-ray probe beam. The probe beam occurs at twice the frequency of the pump beam to allow for a 'pump on' and 'pump off' spectra to be taken, giving a difference spectra. TR-EXAFS is not as well established as TR-IR, with relatively few experiments, limited by the availability of a suitable X-ray source. However, modern advancements mean that TR-XAS is becoming increasingly common, with the introduction of 'table-top' experiments.[181–184] Recent advancements in TR-EXAFS in inorganic chemistry include the structural elucidation of intermediates in the photochemical reaction of $[Fe^{II}(bpy)_3]^{2+}$. The population

mechanism was identified to be ^{1}MLCT → ^{3}MLCT → ^{5}T, with the quintet state being populated in approximately 150 fs.[185] In work by the same group, they were able to analyse the bond lengths in $[Fe^{II}(bpy)_3]^{2+}$ with subpicometer precision, with the Fe–N bond elongation calculated to be 0.203 ± 0.008 Å.[186] Similarly, the structure of the triplet excited state of $[Pt_2(P_2O_5\ H_2)_4]^{4-}$ was determined in solution at 150 ns after excitation, with the authors noting a contraction of the Pt–Pt bond (0.31 Å), and observing for the first time the lengthening of the Pt–P bonds by 0.01 Å.[187]

The sole TR-XAS study of a metal carbonyl complex remains the study described in Chapter 1, where TR-XAS was used to elucidate the bond lengths in various $W(CO)_6$ derivatives, namely $W(CO)_5$(heptane), $W(CO)_5(HSiBu_3)$, $W(CO)_5$(Xe) and $W(CO)_5$(PFMCH). In work contained in the Chapter we aim to extend the current body of work on TR-XAS of metal carbonyls by investigating the reactions of $CpMn(CO)_3$ and $CpRe(CO)_3$ in alkanes and triethylsilanes.

4.2 Aims

Combined TRIR and TR-XAS have proven to be incredibly useful tool in the characterisation of metal alkane complexes. Silane complexes are a useful comparative study for alkane complexes, and as we have detailed in the Introduction, display interesting reactivity when studied alongside alkanes. We have described how the reactions of $CpMn(CO)_3$ and $CpRe(CO)_3$ proceed in silane and silane/alkane mixtures. As yet, these reactions remain unstudied by TR-XAS. Thus, the aims of this chapter are as follows:

(i) To investigate the reaction of $CpMn(CO)_3$ in heptane and varying concentrations of triethylsilane by TRIR in order to establish suitable concentrations of dopant (i.e., triethylsilane) for TR-EXAFS experiments.

(ii) To increase the concentration of triethylsilane in comparison to previous studies of the reaction of $CpRe(CO)_3$ in heptane and triethylsilane, and study the reaction by TRIR in order to fully elucidate the reaction mechanism.

(iii) To extend the time-resolved infrared investigations into reactions of $CpM(CO)_3$ (M = Mn or Re) in heptane and triethylsilane by investigating the reaction with TR-EXAFS.

When investigating aim (ii) we observed some interesting features of the reaction of $CpRe(CO)_3$ in neat triethylsilane and triethylsilane/heptane mixtures. Therefore, several new aims arose for this work. These are:

(iv) To investigate the reactions of $CpRe(CO)_3$ in a series of linear and cyclic alkanes and deuterated alkanes by ns-TRIR.

(v) To investigate the affect of temperature on reactions in (iv) by studying the variable temperature TRIR to afford kinetic parameters.

4.3 Results I

This results section is dedicated to aims (i), (ii) and (iii). As described in the Introduction, much of the studies of $CpM(CO)_3$ (M = Mn or Re) in neat alkanes and silanes have been conducted by Harris *et al.* We will repeat much of this work and also the work detailed in our group on the reactions in alkane/silane mixtures. This work is vital for gathering information for future TR-XAS experiments.

4.3.1 TRIR Investigations into the Reactions of $CpMn(CO)_3$ in Triethylsilane and *n*-heptane

We will study the ns-TRIR of $CpMn(CO)_3$ in neat triethylsilane, neat heptane and triethylsilane/heptane mixtures before assessing the effect of changing concentration of triethylsilane in heptane/triethylsilane mixtures.

4.3.1.1 ns-TRIR of $CpMn(CO)_3$ in Neat Triethylsilane

The results of the photolysis of $CpMn(CO)_3$ in triethylsilane are shown in Figure 4.19. Our results appear consistent with previous work.[111] Early time spectra show, alongside the bleach of the parent bands, the appearance of two new bands at 1895 and 1961 cm^{-1} which decay concurrently with the growth of a further two new bands at 1917 and 1978 cm^{-1}, see Figure 4.20. Mono-exponential fits of the data give a lifetime for the decay of the first species as 146 ± 14 ns, and 96 ± 7 ns for the growth of the second. These species, on comparison to lifetimes and peak locations in previous works, are assigned to the species $CpMn(CO)_2(Et_3SiH)$ and 'partially activated' $CpMn(CO)_2(H\text{-}SiEt_3)$, respectively.

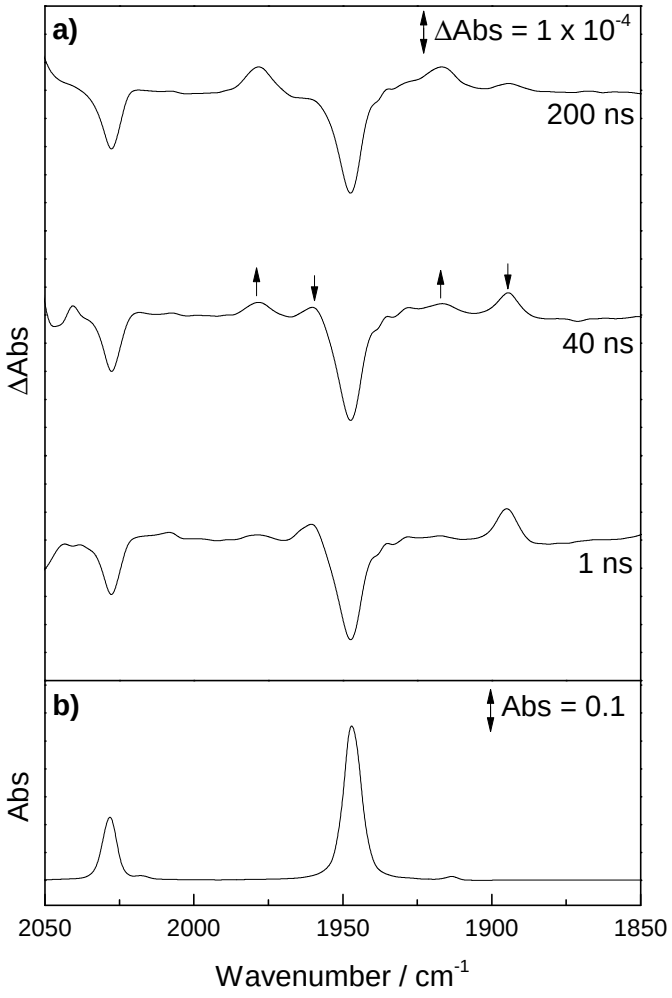

Figure 4.19: *a) ns-TRIR difference spectra at selected time delays for the 266 nm photolysis of $CpMn(CO)_3$ in neat triethylsilane and b) Ground state FTIR spectrum of $CpMn(CO)_3$ in triethylsilane*

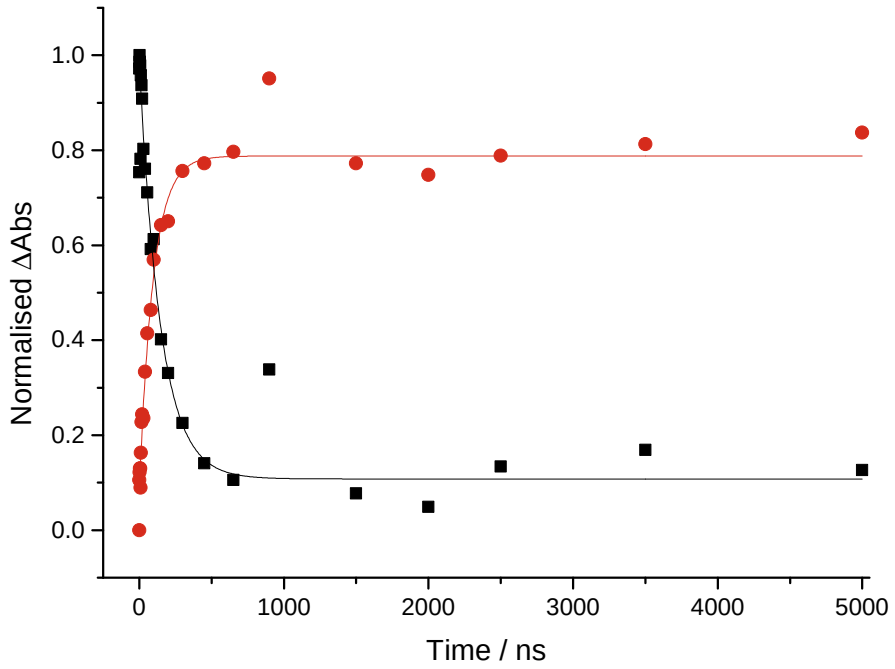

Figure 4.20: *Normalised TRIR kinetic traces for the decay of $CpMn(CO)_2(Et_3SiH)$ (τ = 146 ± 14 ns) at 1894 cm^{-1} and the growth of $CpMn(CO)_2(SiEt_3)H$ (τ = 96 ± 7.0 ns) at 1979 cm^{-1} following photolysis at 266 nm in triethylsilane*

4.3.1.2 ns-TRIR of $CpMn(CO)_3$ in *n*-heptane

The results of the ns-TRIR of $CpMn(CO)_3$ in neat heptane are shown in Figure 4.21. After ten nanoseconds, there are two new peaks in the spectrum, alongside the bleach of the parent bands. These new peaks occur at 1958 and 1894 cm^{-1} and are seen to decay with a lifetime of 69.8 μs, concurrent with the growth of two new peaks at 1976 and 1916 cm^{-1}, see Figure 4.22. Upon comparison to the literature, the peaks at 1958 and 1894 cm^{-1} are assigned to $CpMn(CO)_2$(heptane). The intermediate $CpMn(CO)_2$(heptane) is known to decay to form the dimer $Mn_2Cp_2(CO)_5$;[188] therefore, the peaks at 1976 and 1916 cm^{-1} are assigned to this species.

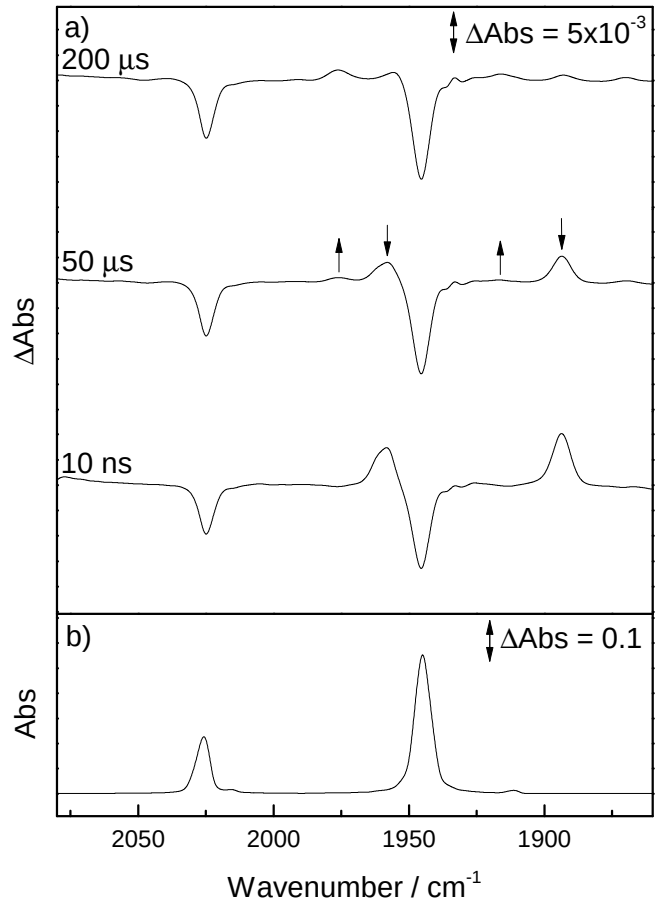

Figure 4.21: *a) ns-TRIR difference spectra at selected time delays for the 266 nm photolysis of $CpMn(CO)_3$ in n-heptane and b) Ground state FTIR spectrum of $CpMn(CO)_3$ in n-heptane*

There are five peaks associated with this species; however, two of them are obscured by the parent bands. The final peak is found in the bridging CO region at 1777 cm^{-1}, due to a single bridging CO.[189] As we have not probed the bridging CO region in this experiment, we cannot provide concrete evidence for formation of this dimer species, however, since this is a known photoproduct and $CpMn(CO)_3$ is not known to C–H activate alkanes, we can assign the final photoproduct as the dimer $Mn_2Cp_2(CO)_5$.

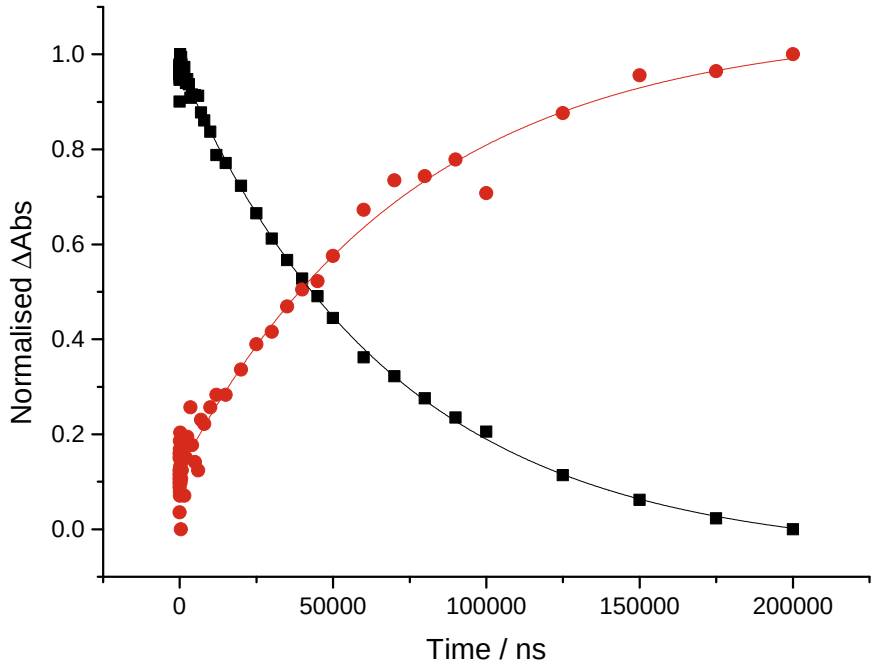

Figure 4.22: *Normalised TRIR kinetic traces for the decay of $CpMn(CO)_2$(n-heptane) (τ = 69.8 ± 1.5 µs) at 1894 cm^{-1} and the growth of $Mn_2Cp_2(CO)_5$ (τ = 75.5 ± 7.0 µs) at 1917 cm^{-1} following photolysis at 266 nm in n-heptane*

4.3.1.3 ns-TRIR of $CpMn(CO)_3$ in *n*-heptane Doped with Triethylsilane (30–240 mM)

The ns-TRIR of $CpMn(CO)_3$ in triethylsilane doped heptane at varying concentrations of triethylsilane was conducted in order to deduce a suitable concentration of triethylsilane to use for subsequent TR-EXAFS experiments.

Figure 4.23 shows the typical ns-TRIR spectra recorded upon photolysis of $CpMn(CO)_3$ in heptane and triethylsilane (30–240 mM). Two peaks at 1893 and 1957 cm^{-1} appear in the early time spectra, decaying at a rate in the order of tens of microseconds, at the same rate as growth of two new bands at 1914 and 1975 cm^{-1}. The first intermediate was assigned to the species $CpMn(CO)_2$(heptane), on comparison to the literature. The species $CpMn(CO)(Et_3SiH)$ is also as considered as a possibility for this peak; however, on comparison to the previous experiment, where the lifetime of the species $CpMn(CO)(Et_3SiH)$ was found to be on the ns timescale, this possibility was ruled out. The mono-exponential nature of the decay and the relatively low concentration of triethylsilane also supports this

hypothesis. The final photoproduct at 1914 and 1975 cm^{-1} is assigned as the partially activated $CpMn(CO)(SiEt_3)H$, in comparison to previous works. Previous work in our group has shown that the reaction of $CpMn(CO)_3$ in a mixed alkane and tributylsilane solvent results in the Si–H activated product via an alkane intermediate.

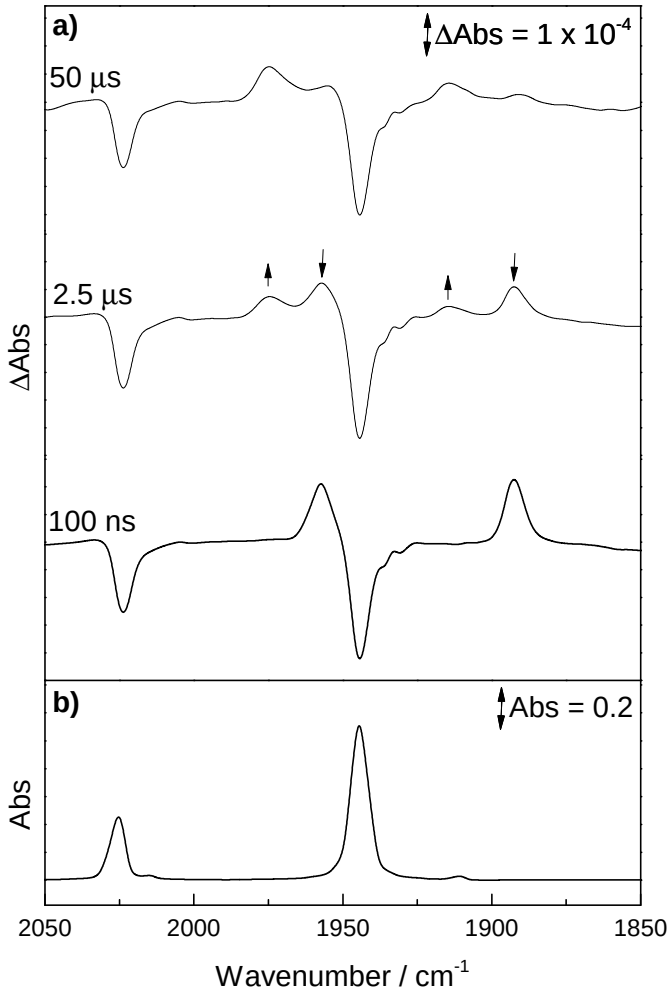

Figure 4.23: *a) ns-TRIR difference spectra at selected time delays for the 266 nm photolysis of $CpMn(CO)_3$ in heptane doped triethylsilane (120 mM) and b) Ground state FTIR spectrum of $CpMn(CO)_3$ in heptane*

The decay of the intermediate $CpMn(CO)_2$(heptane) (τ = 2.87 ± 0.07 μs) matches the growth of the final photoproduct $CpMn(CO)(SiEt_3)H$ (τ = 3.03 ± 0.10 μs), see Figure 4.24. The lifetime of $CpMn(CO)_2$(heptane) in neat heptane solvent was 69.8 μs, which is a 25x increase on the rate here. Therefore, the presence of the competing triethylsilane

has significantly reduced the lifetime of $CpMn(CO)_2$(heptane).

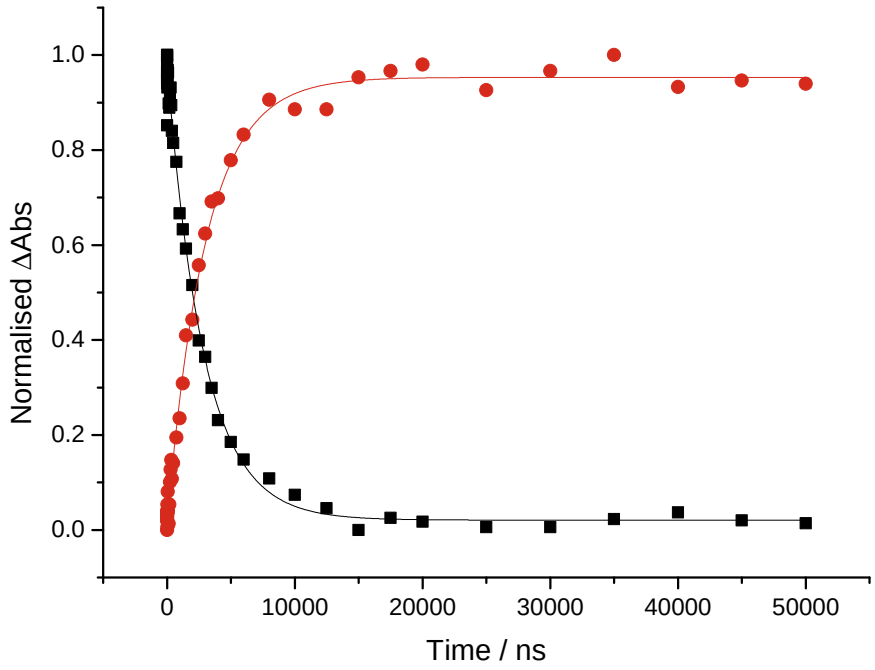

Figure 4.24: *Normalised TRIR kinetic traces for the decay of $CpMn(CO)_2$(n-heptane) (τ = 2.87 ± 0.07 µs) at 1891 cm^{-1} and the growth of $CpMn(CO)_2(SiEt_3)H$ (τ = 3.03 ± 0.10 µs) at 1914 cm^{-1} following photolysis at 266 nm in n-heptane*

We investigated the effects of changing the concentration of the triethylsilane in the rate of decay of $CpMn(CO)_2$(heptane). Table 4.1 shows the values of the rate constant, k_{obs}, with different concentrations of triethylsilane. The lowest concentration studied was 30 mM of triethylsilane, which resulted in a lifetime of 6.9 µs for $CpMn(CO)_2$(heptane), and the highest was 240 mM, which gave a lifetime of 1.5 µs for $CpMn(CO)_2$(heptane). There was a clear trend in that decreasing the concentration of triethylsilane lead to an increase in the lifetime of the intermediate product, clearly shown in Figure 4.25.

Table 4.1: Values for the lifetime of $CpMn(CO)_2$(heptane) in heptane/triethylsilane with varying concentrations of triethylsilane

Triethylsilane Concentration / mM	k_{obs} / s^{-1}
30	1.45×10^5
60	2.07×10^5
120	3.47×10^5
180	4.99×10^5
240	6.54×10^5

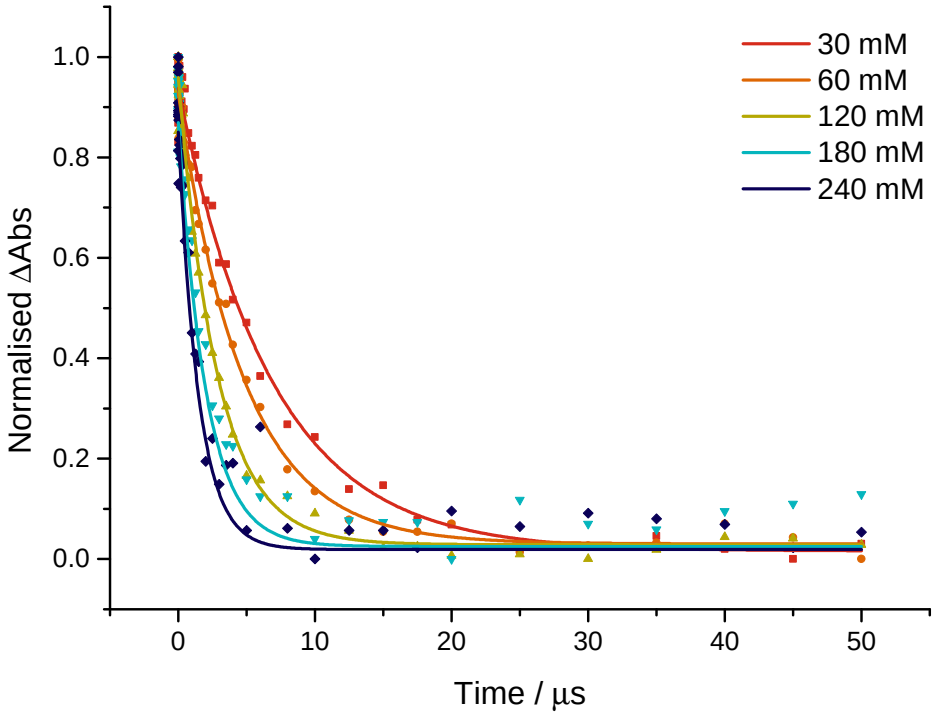

Figure 4.25: *TRIR kinetic traces for the decay of $CpMn(CO)_2$(n-heptane) at various concentration of triethylsilane*

The Stern–Volmer equation, Equation 4.2, can give important information about the rate at which triethylsilane is 'quenching' the reaction of $CpMn(CO)_2$(heptane) to form $CpMn(CO)_2(SiEt_3)H$.

$$\frac{\tau_0}{\tau} = 1 + K_{SV}[Q] \tag{4.2}$$

where τ_0 and τ are the fluorescence lifetimes in absence and presence of quencher, respectively, K_{SV} is the Stern–Volmer constant and [Q] is the concentration of quencher.

In the case of dynamic quenching, where the quencher interferes with the excited state *after* it has been formed, this equation becomes:

$$\frac{\tau_0}{\tau} = 1 + k_q \tau_0 [Q] \tag{4.3}$$

where k_q is the quenching constant.

Therefore, by plotting τ_0/τ against concentration of triethylsilane, we can obtain a Stern–Volmer plot, Figure 4.26.

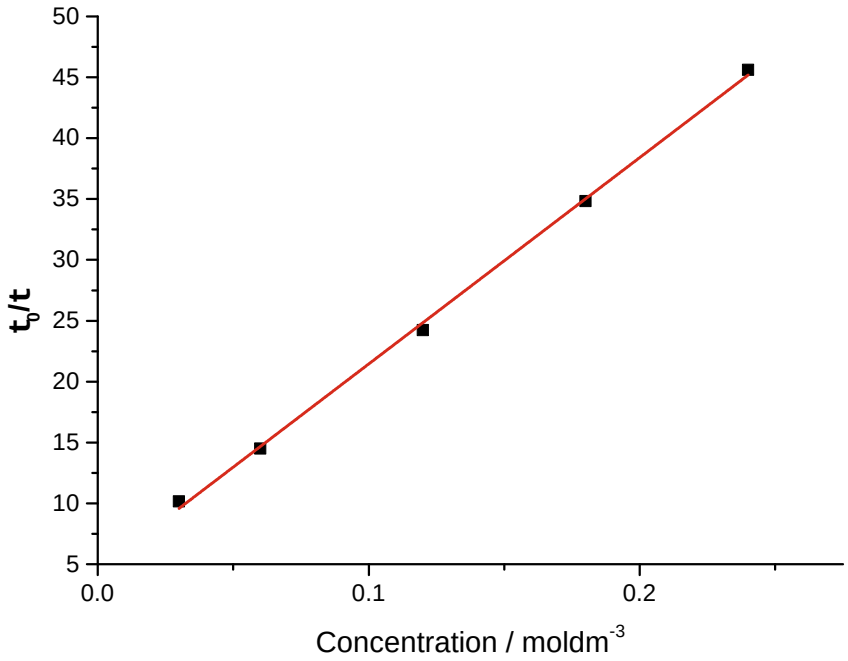

Figure 4.26: *Stern–Volmer plot for the decay of $CpMn(CO)_2$(n-heptane) in different concentration solutions of triethylsilane*

This gives a value for the Stern–Volmer constant, K_{SV}, as 169.5 M^{-1} and the quenching constant, k_q, as 2.43×10^6. This is key information for future TR-XAS experi-

ments, where reaction monitoring is limited to the first few microseconds. Therefore, it is important to find the correct concentration of triethylsilane where the reaction from $CpMn(CO)_2$(heptane) to $CpMn(CO)_2(SiEt_3)H$ occurs in a few microseconds. With information that gives the rate at which triethylsilane 'quenches' this reaction, we can easily find the correct concentration to use for TR-XAS experiments.

A summary of the ν(CO) frequencies and lifetimes of all photoproducts of the reactions studied in the section are shown in Table 4.2.

Table 4.2: Summary of infrared ν(CO) frequencies and lifetimes (in μs) of $CpMn(CO)_2X$ (where X = heptane or triethylsilane) and their relative activation products in different solvent environments

Species	Solvent	Wavenumber	Lifetime / μs
$CpMn(CO)_2$(heptane)	heptane	1959, 1894	69.8
	heptane/$SiHEt_3$ (120mM)	1957, 1893	2.84
$Mn_2Cp_2(CO)_5$	heptane	1976, 1916	long-lived
$CpMn(CO)_2(SiHEt_3)$	$SiHEt_3$	1961, 1895	0.15
$CpMn(CO)_2(SiEt_3)H$	$SiHEt_3$	1978, 1917	long-lived
	heptane/$SiHEt_3$ (120 mM)	1975, 1914	long-lived

The data shows that on moving from neat heptane to heptane/triethylsilane, all carbonyl peaks blueshift slightly. Both final photoproducts, $Mn_2Cp_2(CO)_5$ and $CpMn(CO)_2(SiEt_3)H$ are long-lived and do not decay on the timescale of the experiments.

4.3.2 TRIR Investigations into the Reactions of $CpRe(CO)_3$ in Triethylsilane and *n*-heptane

The analogous reactions of the rhenium equivalent, $CpRe(CO)_3$, were then studied. Previous work has shown that the reactivity can vary between the two manganese and rhenium complexes; therefore, we expect some differences in our results.

4.3.2.1 ns-TRIR of $CpRe(CO)_3$ in Neat Triethylsilane

The ns-TRIR of $CpRe(CO)_3$ in neat triethylsilane is shown in Figure 4.27.

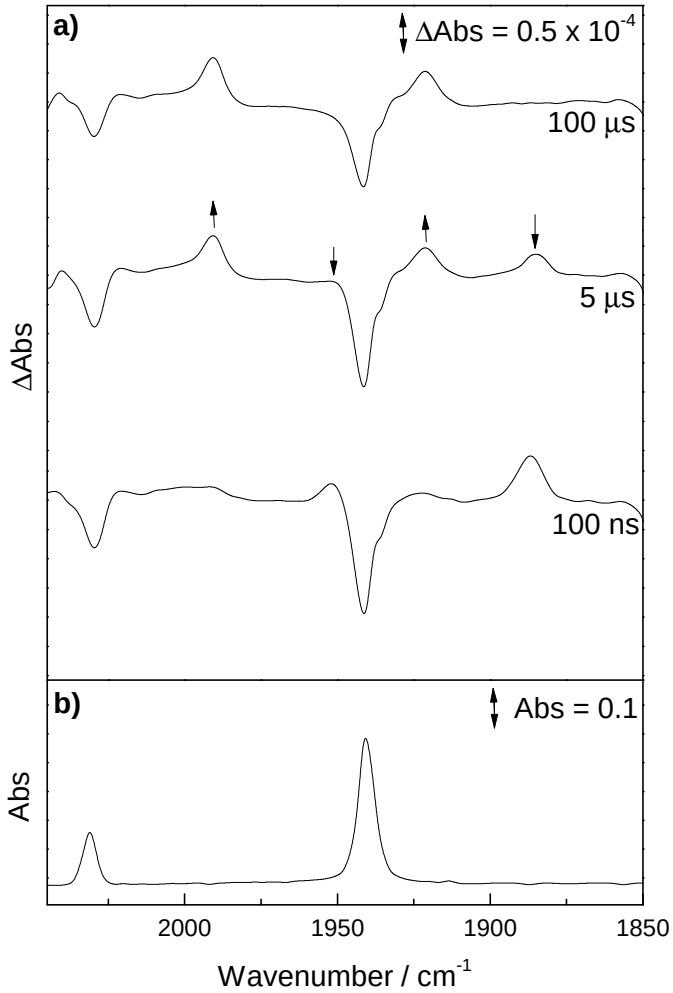

Figure 4.27: *a) ns-TRIR difference spectra at selected time delays for the 266 nm photolysis of $CpRe(CO)_3$ in neat triethylsilane and b) Ground state FTIR spectrum of $CpRe(CO)_3$ in triethylsilane*

At 100 ns we see the bleach of the parent peaks and the appearance of two new peaks at 1887 and 1952 cm^{-1}. These peaks decay at the same rate as the growth of two peaks at 1921 and 1991 cm^{-1}, Figure 4.28. The intermediate peaks are assigned to the species $CpRe(CO)_2(Et_3SiH)$ and the final photoproduct peaks are assigned to the Si–H activated species $CpRe(CO)_2(H)(SiEt_3)$, on comparison to previous experiments. The photoproduct peaks of $CpRe(CO)_2(H)(SiEt_3)$ shift to a higher wavenumber relative to the parent in comparison to those in the manganese experiment, indicative of the increased extent of Si–H cleavage that is well-documented for the rhenium case.

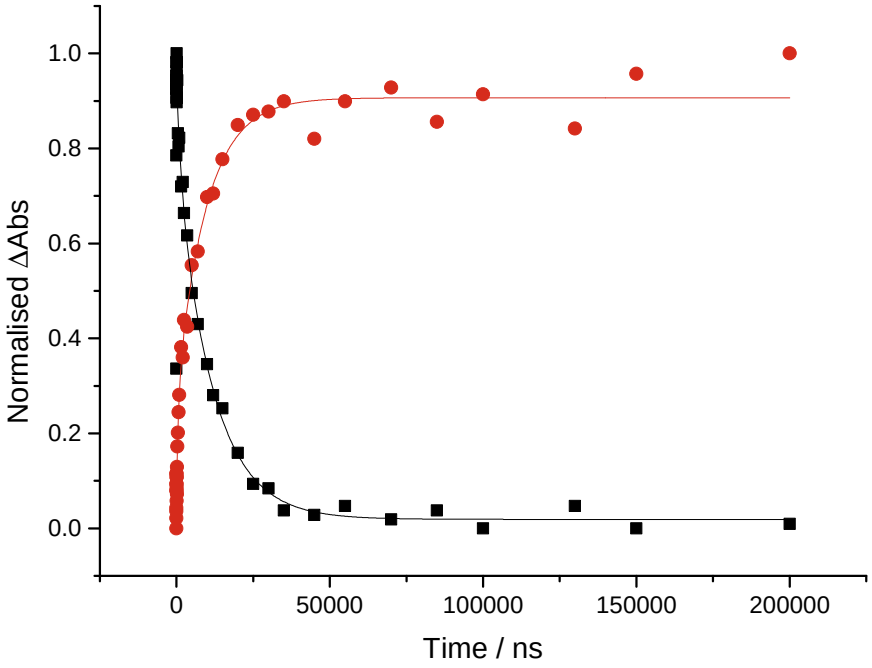

Figure 4.28: *Normalised TRIR kinetic traces for the decay of $CpRe(CO)_2(Et_3SiH)$ (τ_1 = 11.6 ± 1.2 μs, τ_2 = 1.4 ± 0.7 μs) at 1885 cm^{-1} and the growth of $CpRe(CO)_2(SiEt_3)H$ (τ_1 = 9.6 ± 1.2 μs, τ_2 = 0.6 ± 0.2 μs) at 1989 cm^{-1} following photolysis at 266 nm in triethylsilane*

Both the decay and the growth of these peaks can be fitted to a bi-exponential decay process, consisting of a fast component (τ = 1.4 μs) and a slow component (τ = 11.7 μs). Previous analyses of this experiment did not find a bi-exponential decay for this reaction, only finding that the decay could be fitted to a standard mono-exponential, attributed to the decay of $CpRe(CO)_2(Et_3SiH)$ and the growth of $CpRe(CO)_2(H)(SiEt_3)$. Several reasons

for this bi-exponential decay here have been considered.

The possibility that we may be seeing the decay of a vibrationally hot species was briefly considered; however, the lifetime of the fast component of the decay (τ = 1.4 μs) is not on the typical timescale for the decay of these kinds of species. Moreover Harris and co-workers investigated the ultrafast kinetic of the reaction of $CpRe(CO)_3$ in triethylsilane, and found all vibrationally hot intermediates had decayed away within the first few picoseconds.[111]

The presence of a contaminant may be causing a biexpoential decay. If there were traces of heptane, or indeed any other alkane solvent that may bind to the ligand, it could be the case that two intermediate photoproducts may from in tandem; $CpRe(CO)_2(Et_3SiH)$ and $CpRe(CO)_2$(*n*-heptane), occurring at approximately the same wavenumber. They would decay with a different rate constant and would certainly cause a bi-exponential decay process. However, great care was taken to completely dry the experimental equipment before introducing the reagents. Moreover upon repetition of the experiment, the same results were obtained.

On closer inspection of the peak at 1887 cm^{-1}, it appears to blueshift over time, see Figure 4.29. The peak at 1952 cm^{-1} also shows some evidence of a shift; however, due to its smaller absorbance and position at the edge of the parent bleach, this is harder to determine.

Laser drift was considered as a possible cause for this shift; however, if this was the case, then you would expect to see a shift in other peaks, i.e., the parent bleaches, which is not seen here. Therefore, this possibility was ruled out.

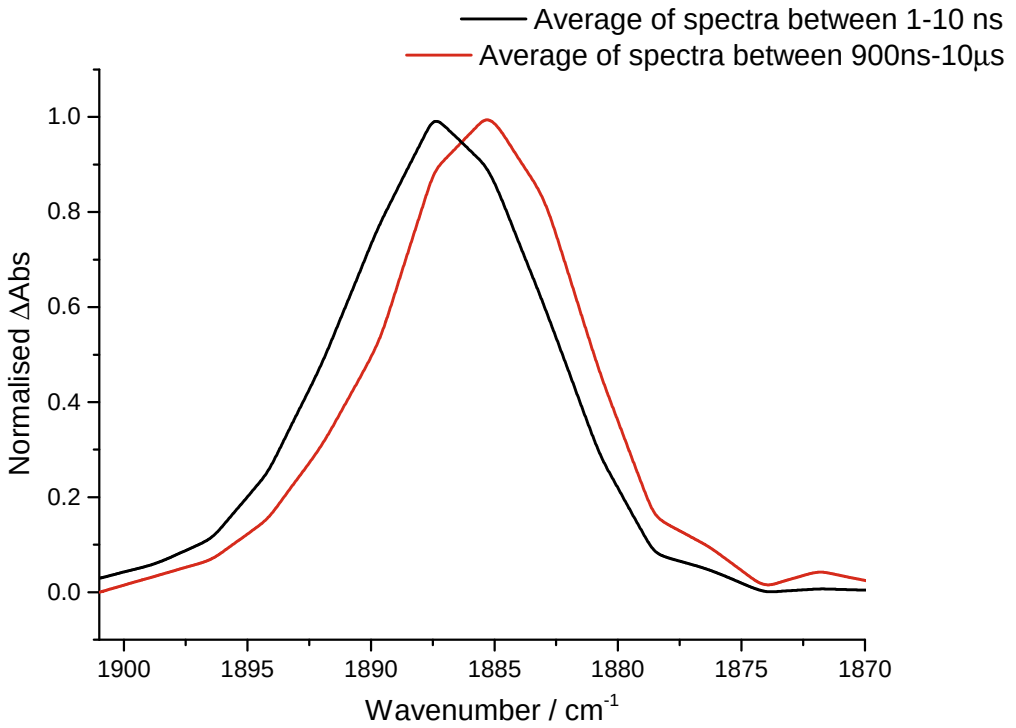

Figure 4.29: *Normalised average of spectra between 1–10 ns (black) and 900 ns–10 µs (red) after photolysis of $CpRe(CO)_3$ in triethylsilane*

The apparent production of two species may be attributed to the simultaneous formation of both $CpRe(CO)_2(SiHEt_3)$ and $CpRe(CO)_2(Et_3SiH)$, see Figure 4.30. Since the theory that they are being made in tandem has been proposed previously in the literature, this is altogether possible. However, this blueshift was not noted in previous experiments. Moreover, if, as suggested, they are being formed in tandem, then the peak would appear broadened rather than the shift we observe. The shift in wavenumber suggests a change from one structure to another, rather than the presence of two products simultaneously.

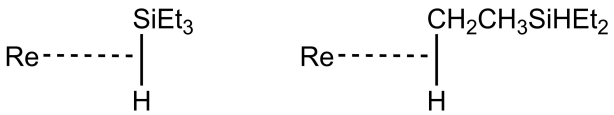

Figure 4.30: *Representation of η^1-H–$SiEt_3$ and η^2-Si–HEt_3 bonding in $CpRe(CO)_2(SiHEt_3)$*

Another explanation has been theorised, where the bonding of the triethylsilane is moving from η^1-H–$SiEt_3$ to η^2-Si–HEt_3, Figure 4.31. This possibility will be discussed further in Section 4.4.

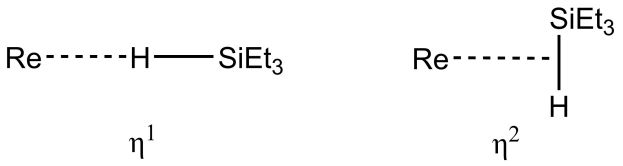

Figure 4.31: *Representation of η^1-$HSiEt_3$ and η^2-$SiHEt_3$ bonding in $CpRe(CO)_2(SiHEt_3)$*

4.3.2.2 ns-TRIR of $CpRe(CO)_3$ in *n*-heptane Doped with Triethylsilane (2–5 M)

Previous work in our group has found that on doping tributylsilane (0.25 M) in a solution of $CpRe(CO)_3$ in *n*-heptane, there was only one photoproduct formed, $CpRe(CO)_2$(*n*-heptane), on the timescale of the reaction (1 ms). We expect that the reaction will follow the same reaction path as that of manganese, i.e., the *n*-heptane bound intermediate will directly form the Si–H activated $CpRe(CO)_2(H)(SiEt_3)$. However, this has not been seen experimentally before. The previous work proposed that the stability of $CpRe(CO)_2$(*n*-heptane) is too great that the creation of $CpRe(CO)_2H(SiBu_3)$ is not seen on the millisecond timescale. Therefore, we have used a much higher concentration of triethylsilane to increase the rate of reaction and hence decrease the lifetime of $CpRe(CO)_2$(heptane) significantly enough so that its decay can be seen within the timescale of the experiment. Therefore, concentrations between 2 and 5 M triethylsilane were used. Figure 4.32 shows the results of photolysis of $CpRe(CO)_3$ in triethylsilane (2 M) doped in heptane.

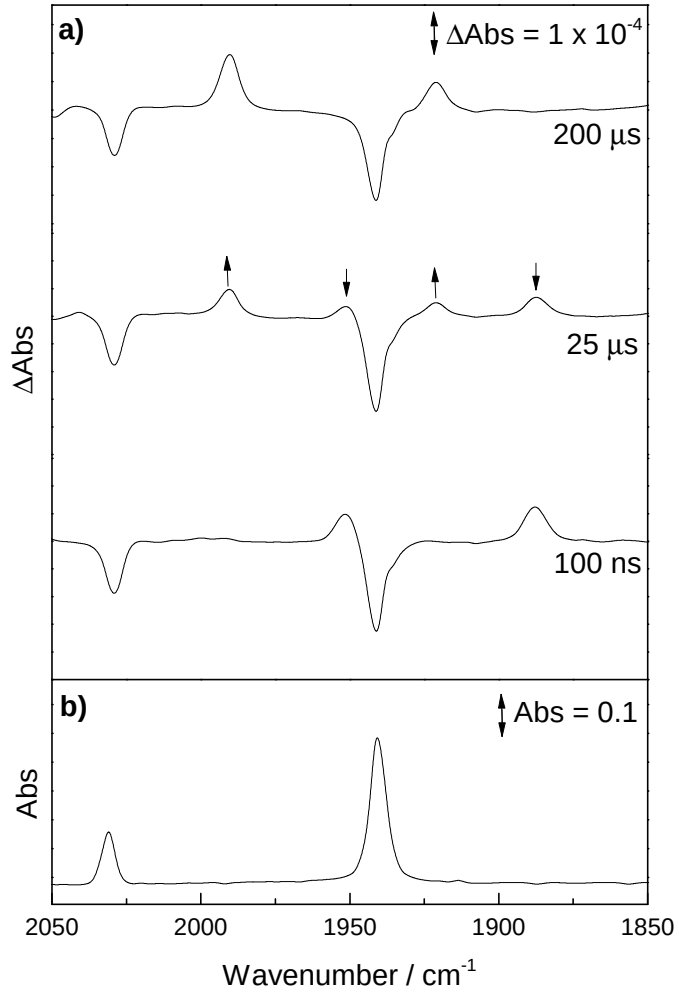

Figure 4.32: *a) ns-TRIR difference spectra at selected time delays for the 266 nm photolysis of $CpRe(CO)_3$ in heptane doped triethylsilane (2 M) and b) Ground state FTIR spectrum of $CpRe(CO)_3$ in heptane*

Photolysis results in the bleach of the parent peaks and the appearance of two new peaks at 1877 and 1952 cm^{-1}. These decay concurrently with the growth of a further two species at 1990 and 1921 cm^{-1}, Figure 4.33. These species are assigned as $CpRe(CO)_2$(heptane) and $CpRe(CO)_2(H)(SiEt_3)$, respectively, on comparison to the reactions of the analogous manganese complex. Both the decay of the intermediate and the growth of the photoproduct, as in the previous experiment, can be fitted to a bi-exponential decay process. This consists of a fast component (τ = 1.4 ± 0.4 μs) and a slow component (τ = 64.4 ± 3.0 μs). The fast component has a remarkably similar lifetime to the fast component from the previous experiment in neat triethylsilane.

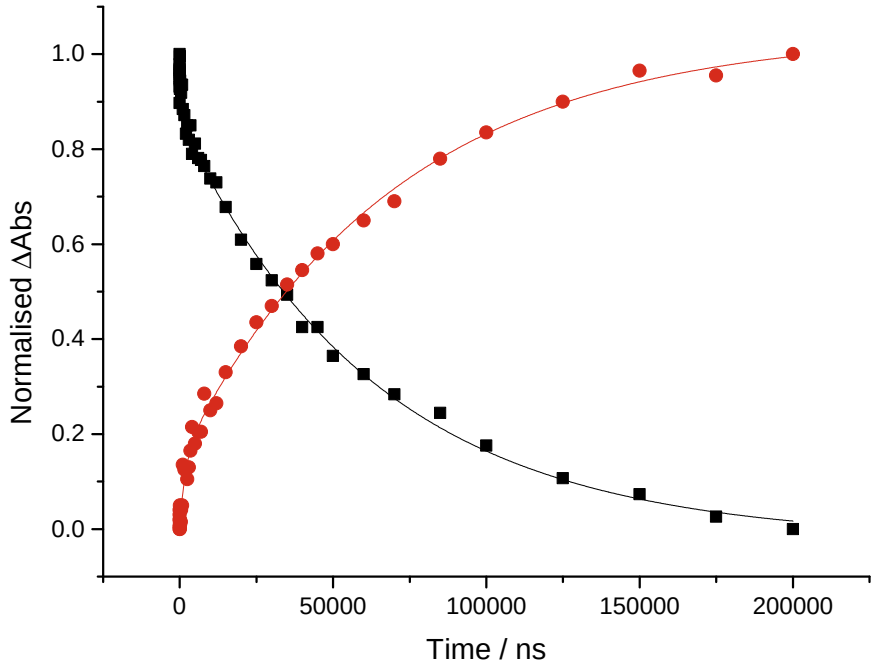

Figure 4.33: *Normalised TRIR kinetic traces for the decay of the peak at 1887 cm^{-1} (τ_1 = 64.4 ± 3.0 μs, τ_2 = 1.4 ± 0.4 μs) and the growth of the peak at 1921 cm^{-1} (τ_1 = 69.9 ± 4.5 μs, τ_2 = 1.9 ± 0.5 μs) following photolysis of CpRe(CO)$_3$ at 266 nm in heptane and triethylsilane (2M)*

On taking a closer look at the 1887 cm^{-1} peak, again we can see there is a blueshift over time, Figure 4.34. The blueshift here is less significant than the previous experiment, shifting here by ~ 1 cm^{-1}, whereas the previous experiment was ~ 2 cm^{-1} blueshift.

One of the theories we provided for the nature of the bi-exponential decay in the previous experiment was that CpRe(CO)$_2$(SiHEt$_3$H) and CpRe(CO)$_2$(Et$_3$SiH) were being formed simultaneously. If that were true then we would not expect to see a shift in the peak in this experiment as we are expecting to form CpRe(CO)$_2$(heptane) exclusively, as was seen in the analogous manganese experiment. The metal here can only bond to a CH$_3$ or a CH$_2$ on the heptane, which would not be expected to result in a noticeable shift of wavenumber. However, the concentration of triethylsilane in the analogous manganese experiment was negligible, effectively ruling out production of CpMn(CO)$_2$(SiHEt$_3$). Here the concentration of triethylsilane is much higher; therefore, it is more likely that we may be forming CpRe(CO)(SiHEt$_3$) and CpRe(CO)$_2$(heptane) simultaneously.

Therefore, simultaneous formation of $CpRe(CO)_2$(heptane) and $CpRe(CO)_2(SiHEt_3)$ could account again for the bi-exponential nature of the decay. All in all, this data is inconclusive, and more experimental data needs to be collected to form a reasonable conclusion. This phenomenon has been explored further in Section 4.4.

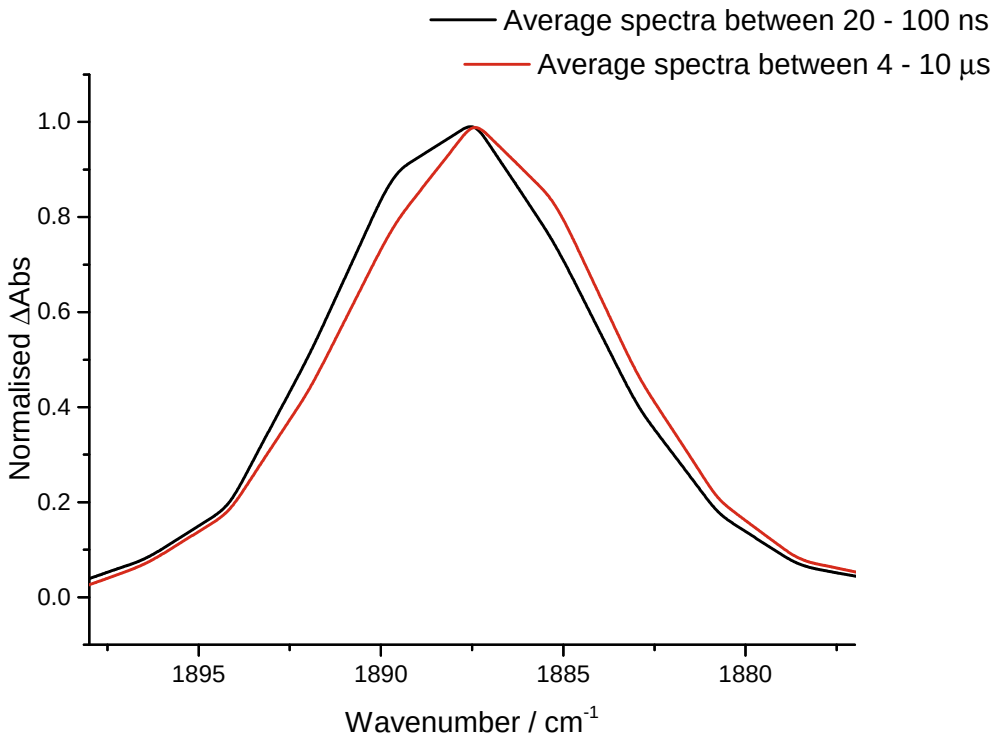

Figure 4.34: *Normalised average of spectra between 20–100 ns (black) and 4–10 µs (red) after photolysis of $CpRe(CO)_3$ in triethylsilane doped heptane*

As with the analogous experiment with $CpMn(CO)_2$, we investigated the effects of changing the concentration of the triethylsilane in the rate of decay of $CpRe(CO)_2$(heptane). Table 4.3 shows the values of the rate constant, k_{obs}, with different concentrations of triethylsilane. The lowest concentration studied was 2 M of triethylsilane, which resulted in a lifetime of 65.1 µs for $CpRe(CO)_2$(heptane), and the highest was 5 M, which gave a lifetime of 14.5 µs for $CpRe(CO)_2$(heptane). There was a clear trend in that decreasing the concentration of triethylsilane lead to an increase in the lifetime of the intermediate product.

Table 4.3: Values for the lifetime of $CpRe(CO)_2$(heptane) in heptane/triethylsilane with varying concentrations of triethylsilane

Triethylsilane Concentration / M	k_{obs} / s^{-1}
2	1.54×10^4
3	2.26×10^4
4	4.25×10^4
4.5	5.04×10^4
5	6.92×10^4

The Stern–Volmer plot for this reaction is shown in Figure 4.35. As we have not measured the value of τ_0 in this work, we have plotted $1/\tau$ (k_{obs}) (instead of τ_0/τ) against concentration of triethylsilane. This gives a value of 1.74×10^4 for the quenching constant, k_q.

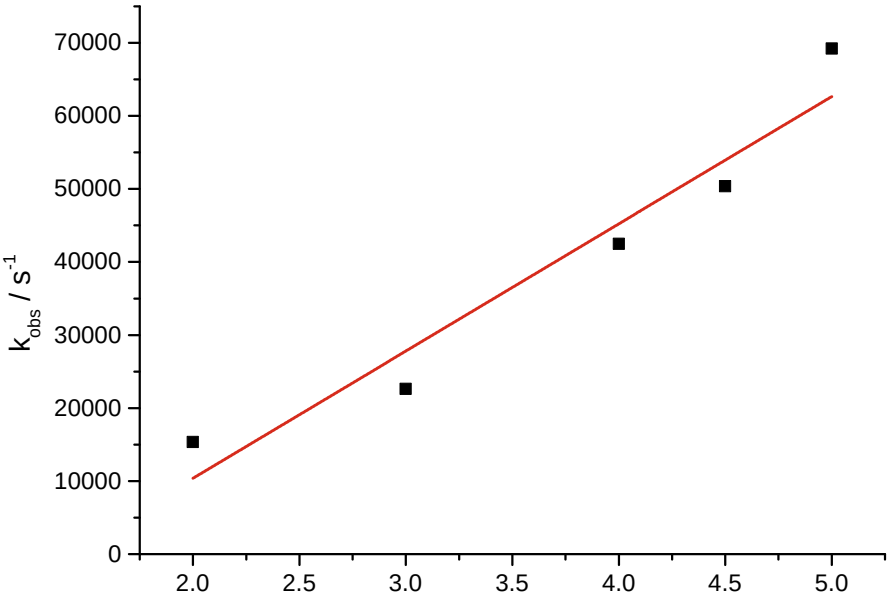

Figure 4.35: *Stern–Volmer plot for the decay of $CpRe(CO)_2$(n-heptane) in different concentration solutions of triethylsilane*

From this data, we can see that the reaction of $CpRe(CO)_3$ in *n*-heptane/triethylsilane is unsuitable for study with TR-EXAFS, as the lifetime of $CpRe(CO)_2$(*n*-heptane) is too long to study its change to $CpRe(CO)_2H(SiEt_3)$, even at extremely high concentrations of triethylsilane.

A summary of the ν(CO) frequencies and lifetimes of all photoproducts are shown in Table 4.4. The data shows that in both neat *n*-heptane and the *n*-heptane/triethylsilane mix, the intermediate and final photoproduct peaks are at nearly identical wavelengths. This suggests that in *n*-heptane/triethylsilane mixtures, the $CpRe(CO)_3$ is predominantly dissolved in the triethylsilane. Indeed, due to the large concentrations of triethylsilane needed to significantly reduce the lifetime of the *n*-heptane bonded complex, the relative quantities of *n*-heptane and triethylsilane were almost equal. Therefore, this observation seems reasonable.

Clearly more investigations need to take place into the peak shifting phenomenon observed for the triethylsilane and *n*-heptane bonded intermediates. This will be undertaken in the next results section.

Table 4.4: Summary of infrared ν(CO) frequencies and lifetimes (in μs) of $CpRe(CO)_2X$ (where X = heptane or triethylsilane) and their relative activation products in different solvent environments

Species	Solvent	Wavenumber	Lifetime / μs
$CpRe(CO)_2$(heptane)	heptane/$SiHEt_3$ (2 M)	1952*, 1877*	64.4
$CpRe(CO)_2(SiHEt_3)$	$SiHEt_3$	1952*, 1885*	11.7
$CpRe(CO)_2(SiEt_3)H$	$SiHEt_3$	1990, 1921	long-lived
	heptane/$SiHEt_3$ (2 M)	1990, 1921	long-lived

*exhibits a ~1–2 cm^{-1} peak shift at early time, final peak locations are shown

4.3.3 Preliminary Time-resolved X-ray Absorption Spectroscopy (TR-XAS) Studies

One of the original aims of the X-ray absorption spectroscopy (XAS) experiments was to study the reaction of $CpMn(CO)_3$ in triethylsilane doped *n*-heptane. This was to study the structural changes in the photoproducts $CpMn(CO)_2$(*n*-heptane) and $CpMn(CO)_2H(SiEt_3)$. However, unfortunately the monochromator at the Advanced Photon Source in Illinois could not give a good quality or stable output at low energy for manganese; thus, we were unable to study manganese reactions.

Therefore, we solely studied the reactions of $CpRe(CO)_3$. XAFS studies of $CpRe(CO)_3$ in neat triethylsilane were performed at the Advanced Photon Source (APS), Argonne National Laboratory, Illinois, USA. Studies were undertaken in collaboration with Drs. Xiaoyi Zhang and Jin Yu of the APS, Professor Andrew Dent and Dr. Stuart Bartlett of the Diamond Light Source, and Mr Edward Bowman of the University of Nottingham.

Figure 4.36 shows the ground state X-ray absorption spectrum (XAS) of $CpRe(CO)_3$ in neat triethylsilane (a), along with the XAS difference spectrum recorded at 2–3 μs (black) and 8–9 μs (red) following 266 nm photolysis of $CpRe(CO)_3$ in $SiHEt_3$ under He (b). The ground state spectrum shows a large absorption edge at 10.533 keV and small oscillations in the higher energy region, which are are characteristic of the coordination geometry and nature of the ligands around the metal. The difference spectrum shows a bleach of the original absorption edge, and a strong positive absorption at 10.530 keV, i.e., a shift to lower energy of the absorption edge. This red shift is indicative of an increase in electron density at the rhenium after irradiation, consistent with the loss of a CO and hence loss of electron back-bonding. There are some weak oscillations; however, the high energy end of the difference spectrum is relatively noisy.

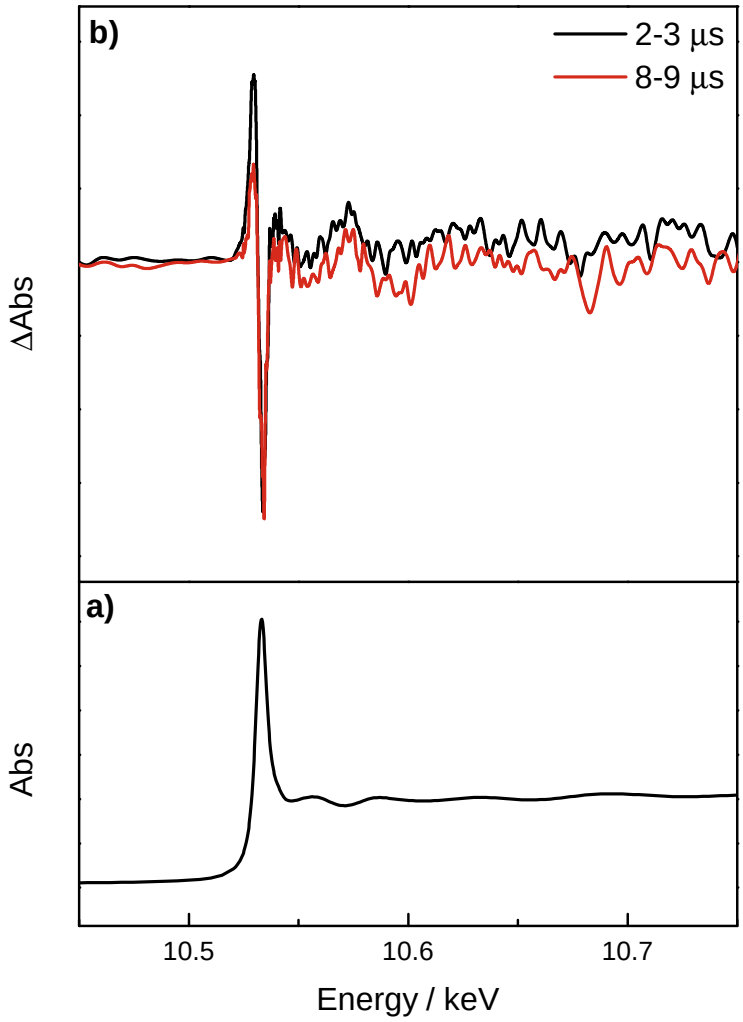

Figure 4.36: *a) Re L_{III}-edge XAS spectrum of $CpRe(CO)_3$ before excitation, and b) Re L_{III}-edge XAS difference spectrum of $CpRe(CO)_3$ 2–3 µs after excitation (black) and 8–9 µs after excitation (red)*

We can see a clear decrease in the absorption edge at 10.530 keV from 1–2 µs after excitation to 8–9 µs after excitation. This is in agreement with what we observe in the ns-TRIR data, where we saw the decay of $CpRe(CO)_2(SiHEt_3)$ with a lifetime of 11.7 µs. We would perhaps expect to the concurrent growth of new peaks due to the change in coordination environment when $CpRe(CO)_2H(SiEt_3)$ is formed (as seen in the ns-TRIR); however, there is no noticeable formation of new peaks. However, this may be because the spectra are relatively noisy, and further in-depth analysis is needed.

In the ns-TRIR of $CpRe(CO)_3$ in triethylsilane, we see a ~2 cm^{-1} blueshift of the peaks

due to $CpRe(CO)_2(SiHEt_3)$ over time, which is indicative of an increase in electron density around the metal. The lifetime of this process is expected to be around 1 μs. Therefore, we are looking for a similar change in the XAS data. Figure 4.37 shows a comparison of the XANES region of the peak at 10.530 keV at 1–2 μs (black) and 4–5 μs (red). There is a visible redshift in the absorption edge, again indicative of an increase in electron density around the metal.

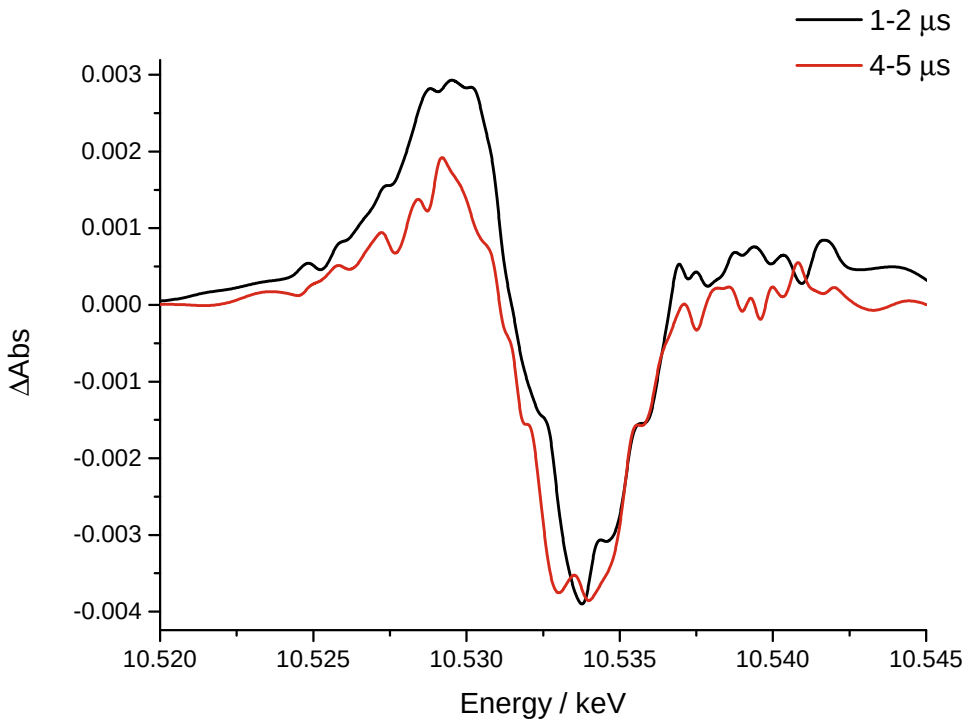

Figure 4.37: *Comparison of the XANES region 1–2 μs (black) and 4–5 μs after photolysis of $CpRe(CO)_3$ in triethylsilane*

This clearly supports the ns-TRIR data, and lends further evidence for the existence of an η^1 intermediate. Further in-depth analysis of the TR-EXAFS spectra will hopefully reveal more detailed information about the coordination environment around the metal to provide additional support for the presence of an η^1 intermediate.

4.4 Results II

This results section is dedicated to aims (iv) and (v). In Section 4.3 we observed a small peak shift in the intermediates in experiments with $CpRe(CO)_3$. Therefore, we will investigate this phenomenon further by measuring the ns-TRIR of $CpRe(CO)_3$ in a number of alkane solvents, namely *n*-heptane, *n*-hexane and *c*-hexane. We will then undertake variable temperature ns-TRIR to ascertain the affect of temperature on this reaction and determine activation parameters.

4.4.1 TRIR Investigations into the Reactions of $CpRe(CO)_3$ in a Series of Linear, Cyclic and Deuterated Alkanes

4.4.1.1 ns-TRIR of $CpRe(CO)_3$ in *n*-heptane

First, the ns-TRIR of $CpRe(CO)_3$ in neat *n*-heptane was studied. This is a well studied reaction as the photoproduct, $CpRe(CO)_2$(*n*-heptane) is one of the longest known alkane complexes. Therefore, within the nanosecond timescale, we do not expect to see the decay of this species. However, if, as we observed in Section 4.3, there is a small shift in the photoproduct peaks, we will be able to observe this.

The results of this experiment are shown in Figure 4.38. As a result of photolysis, the parent peaks bleach with the appearance of two new peaks centred at 1969 and 1895 cm^{-1}, which do appear to blueshift over the course of the experiment by ~2 cm^{-1} to form peaks centred at 1967 and 1893 cm^{-1}. Where is was not observed in the experiment in the analogous experiment in triethylsilane in Section 4.3, there is a shift in the peak on the shoulder of the parent bleach ($\sim$ 1969 cm^{-1}). The final photoproduct peak locations are the same as reported peaks for $CpRe(CO)_2$(*n*-heptane), and these shifts have not been noted previously in the literature. However, the previous literature experiments would have been conducted on a much longer timescale, as the decay of the photoproduct is on the order of milliseconds. Therefore, this relatively fast process may have been missed. Average spectra over 10–50 ns and also over 10–25 μs for both photoproduct peaks are

shown in Figure 4.39.

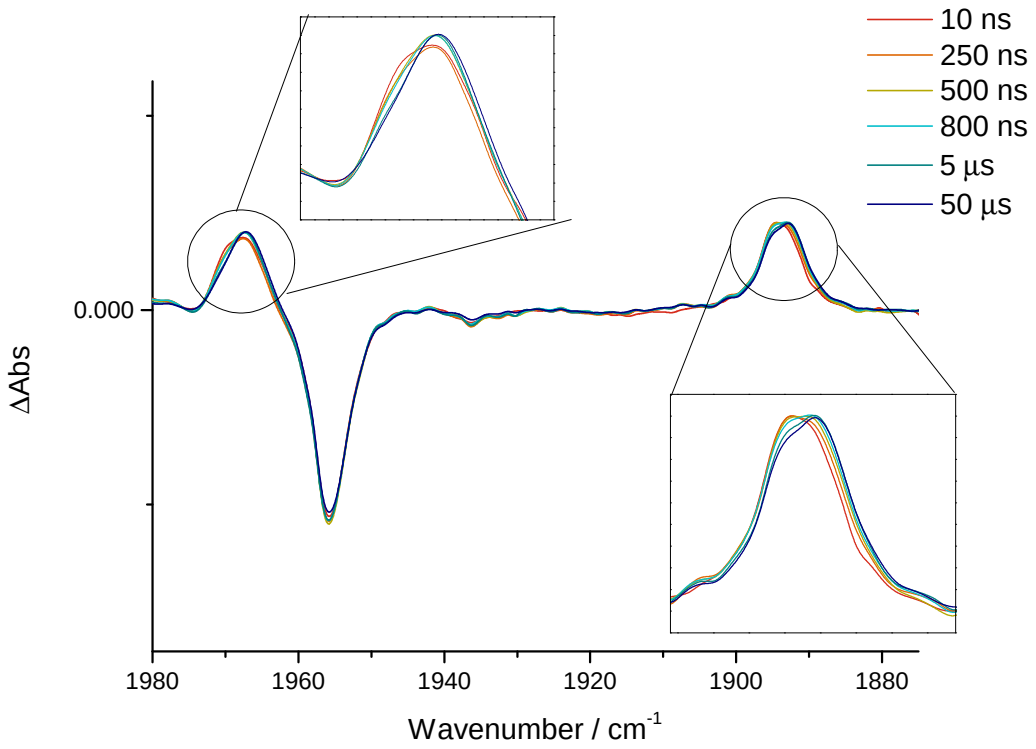

Figure 4.38: *ns-TRIR difference spectra at selected time delays for the 266 nm photolysis of $CpRe(CO)_3$ in n-heptane*

The nature of these shifts is very interesting. Laser drift, as it was in Section 4.3, was considered as a possible cause for this shift, and again, as there was no observable shift in the parent peaks, this possibility was ruled out. There is only one dopant in solution; therefore, there is only species present to bond to the metal, i.e., $CpRe(CO)_2$(*n*-heptane). In Chapter 4, it was difficult to distinguish whether the peak shift was due to the presence of multiple complexes, as there were two different binding sites on triethylsilane (bonding can occur through the Si–H bond or through the C–H bond on an ethyl group). In this case there is no such possibility; therefore, an intramolecular change seems more likely.

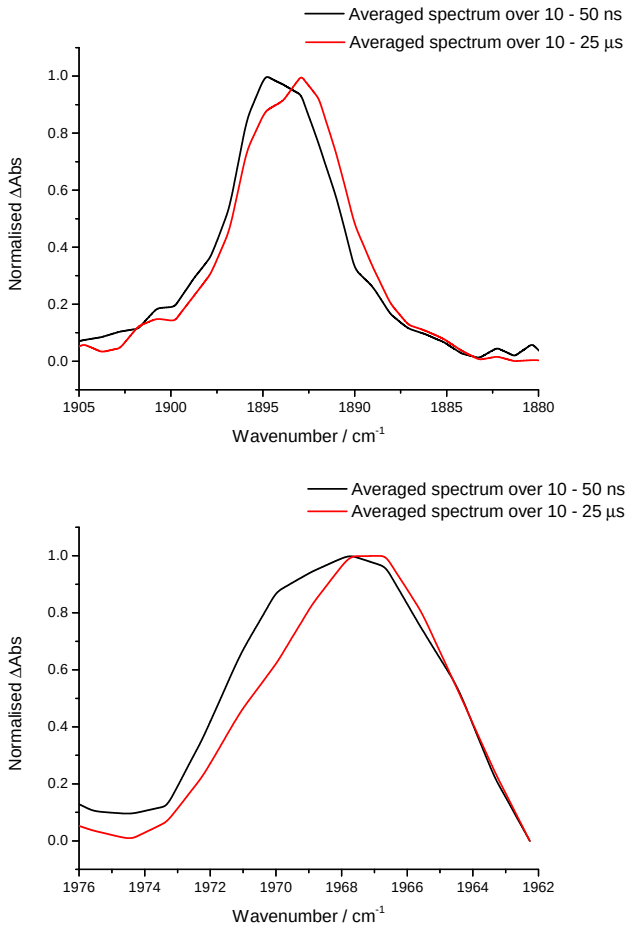

Figure 4.39: *Normalised average spectra between 10–50 ns (black) and 10–25 µs (red) following the 266 nm photolysis of $CpRe(CO)_3$ in n-heptane*

One such intramolecular change that has been experimentally proven for complexes of this type, is a process called 'chain-walking', where the bond moves from the end CH_3 units to the CH_2 units.[52,57] However, these alkanes were shown by NMR experiments to rapidly interchange between CH_3 and CH_2 bonds in alkanes in a equilibrium-like process. This kind of rapidly interchanging process would not be seen in the infrared as the two peaks would appear as one broadened peak. Therefore, this possibility will not be considered further.

It must be considered that an impurity has been introduced into the solution; however, great care was taken to minimise the possibility of this occurrence. Therefore, this possibility is not excluded, but is not considered further.

The theory that we previously proposed for the same reaction in triethylsilane is

proposed again here, namely the bonding is changing from end-on η^1-CpRe(CO)$_2$(H–$CH_2C_6H_{13}$) to η^2-CpRe(CO)$_2$(C–HC_6H_{15}). As we have seen in the Introduction, many theoretical studies have shown that the alkane approaches the metal centre 'hydrogen first', followed by a rotation of the C–H bond; however, this has not been observed experimentally.

A consideration of the electron density will hopefully uncover why this shift is observed. A shift to lower wavenumber as seen here is indicative of an increase in electron density around the metal. One way we can look at the electron density is by considering that moving from an η^1-complex to an η^2-complex is effectively like moving from a two-centre two-electron bond to a two-centre three-electron bond, leading to an increase in electron density. As the bond rotates, the C–H bond is more available to donate to the empty metal d-orbital, again increasing electron density. The shift in this experiment (*n*-heptane) is less than the shift observed in the experiment observed in Chapter 4 for the same experiment in triethylsilane. Si–H bonds are better electron donors so this supports our theory of η^1–η^2 as on rotation of the bond, the Si–H donates more electron density to the metal and hence leads to a larger shift to lower wavenumber.

However, a second way to view it is that on rotation of the C–H bond from η^1 to η^2, the C–H σ* antibonding orbitals are more available for back-bonding from the metal, which would decrease electron density on the metal.

We therefore suggest that there is a simultaneous increase in electron density from increased donation from the C–H bond to the empty metal d-orbital and a decrease from back-bonding of the metal to the C–H anti-bonding orbitals. The experimental results suggest that overall the dominant influence is from increased donation from the C–H bond which leads to increased electron density on the metal and a shift to lower wavenumber.

Due to the overlap in the two peaks, the single point kinetic data is noisy and we are unable to extract reliable lifetime data. Therefore, the global analysis was conducted to deduce the nature of lifetime of these two apparent excited states. The results of the excited state calculation are shown in Figure 4.40, with global analysis calculating two

clear separate excited states, the first with peaks at 1967 and 1893 cm^{-1} and the second with peaks at 1966 and 1892 cm^{-1}.

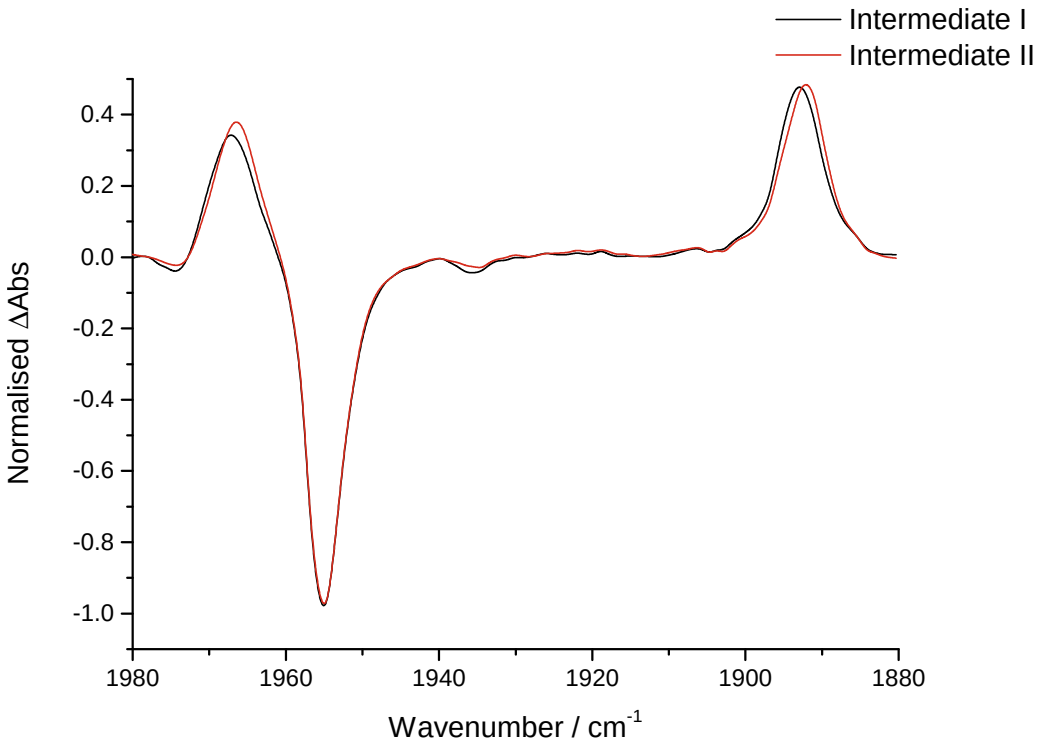

Figure 4.40: *Normalised excited state spectra generated from global analysis following 266 nm photolysis of $CpRe(CO)_3$ in n-heptane*

The lifetime of the decay of the first intermediate was found to match the growth of the second, with a lifetime of 882.1 ns, Figure 4.41. This lifetime is similar to the fast component of the bi-exponential decay in the experiments in Chapter 4 (882 ns *vs.* 1.4 μs). The lifetime of the complex $CpRe(CO)_2$(*n*-heptane) is approximately 400 μs.[42] Therefore, this proposed η^1 intermediate is relatively short-lived in comparison to its η^2 relative. This can explain why other such shifts have not been reported for other complexes, as $CpRe(CO)_2$(*n*-heptane) is one of the longest lived complexes observed at room temperature and pressure. Other complexes that are shorter lived may react via the same η^1 intermediate but it may be too short lived to be observed even by time-resolved methods.

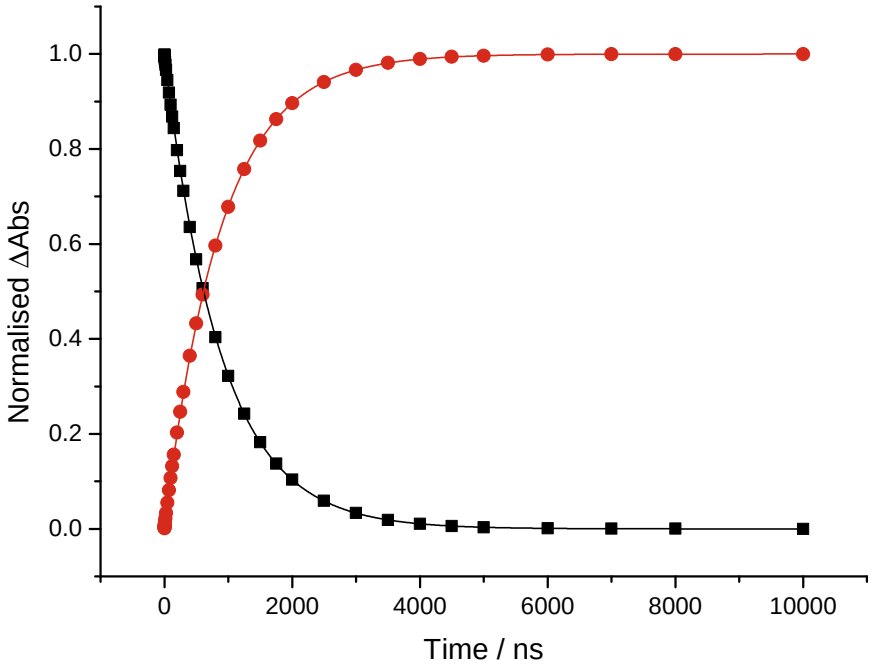

Figure 4.41: *Normalised excited state kinetics generated from global analysis following 266 nm photolysis of CpRe(CO)$_3$ in n-heptane, showing the decay of intermediate I and growth of intermediate II (τ = 882.1 ns)*

4.4.1.2 ns-TRIR of CpRe(CO)$_3$ in *n*-hexane

The ns-TRIR was investigated in hexane solvent to see whether the shift still occurs in a different linear alkane. As with CpRe(CO)$_2$(*n*-heptane), the lifetime of CpRe(CO)$_2$(*n*-hexane) is on the order of milliseconds; therefore, the decay of this species is not expected to be seen on the timescale of this experiment. The results are shown in Figure 4.42. There is an initial photoproduct at 1879 cm^{-1} and 1954 cm^{-1} which appears to blueshift over time by 1–2 cm^{-1} to form the final photoproduct at 1878 cm^{-1} and 1952 cm^{-1}, which matches the profile of CpRe(CO)$_2$(*n*-hexane). We hypothesised in the previous section that the shift seen in the analogous experiment in heptane could be due to an impurity in the solvent. Due to the observation of the same magnitude of shift in both hexane and heptane, with both shifts occurring on a similar timescale, we can rule out the an impurity as the cause, as it is highly unlikely that the same impurity would be present in the two

different solvents.

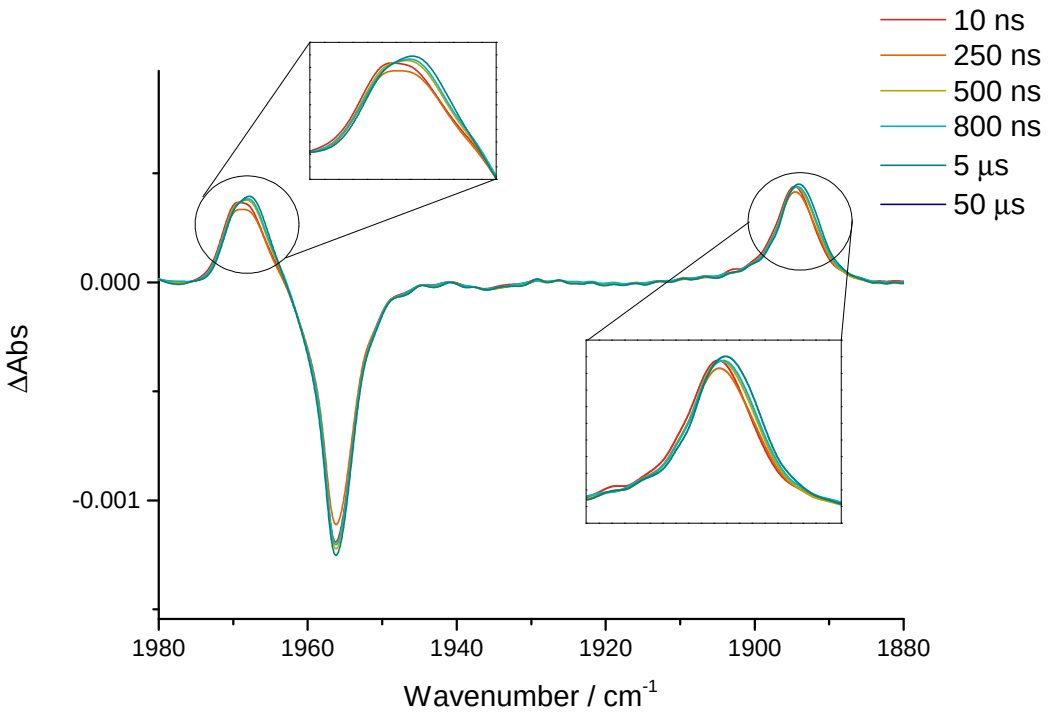

Figure 4.42: *ns-TRIR difference spectra at selected time delays for the 266 nm photolysis of $CpRe(CO)_3$ in n-hexane*

The average of the spectra between 5–20 ns (black) and 3–8 µs (red) is shown in Figure 4.43, clearly showing the 1–2 cm^{-1} shift in both peaks at 1879 and 1954 cm^{-1}.

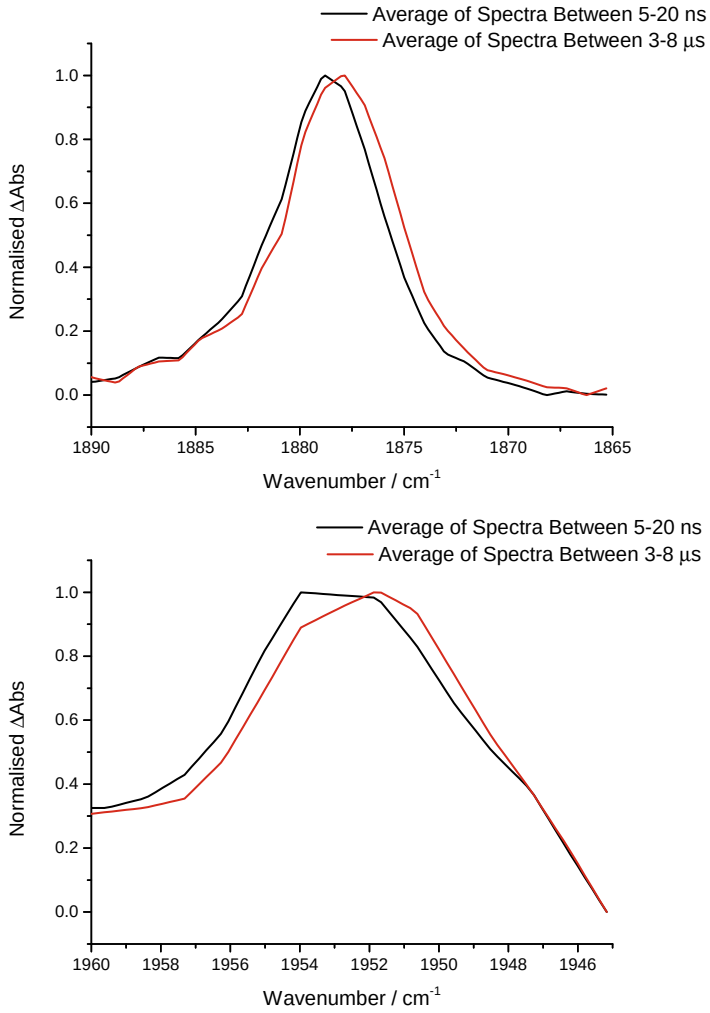

Figure 4.43: *Normalised average spectra between 5–20 ns (black) and 3–8 µs (red) of the peaks at 1879 cm^{-1} (top) and 1954 cm^{-1} (bottom) following the 266 nm photolysis of CpRe(CO)$_3$ in n-hexane*

Again, due to the close proximity of the peaks, the single point kinetic data was difficult to obtain and was fairly noisy; therefore, global analysis was undertaken to distinguish the excited states and deduce the lifetime of the shift. The calculated excited state spectra are shown in Figure 4.44, again showing two clear excited states, the first with peaks at 1970 and 1895 cm^{-1}, and the second with peaks at 1968 and 1894 cm^{-1}. The shift in the peaks (1–2 cm^{-1}) is of the same magnitude as the experiment in *n*-heptane; therefore, excited state I is assigned tentatively as η^1-CpRe(CO)$_2$(H–CH$_2$C$_5$H$_{11}$), and excited state II as η^2-CpRe(CO)$_2$(C–HC$_5$H$_{13}$).

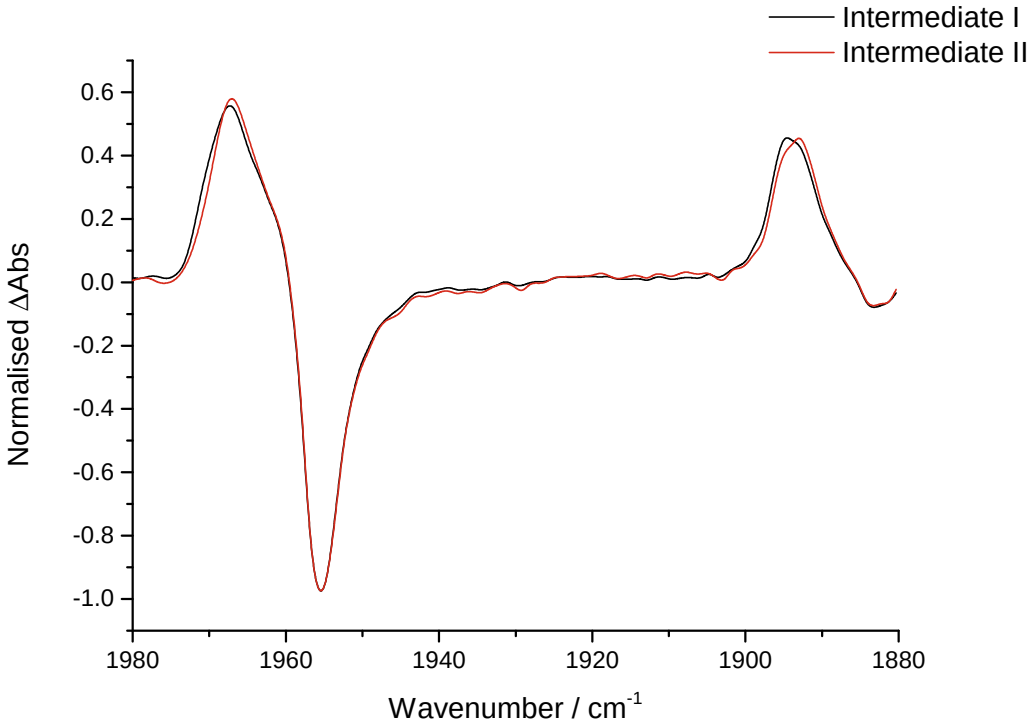

Figure 4.44: *Normalised excited state spectra generated from global analysis following 266 nm photolysis of $CpRe(CO)_3$ in n-hexane*

The lifetime of the decay of 'Intermediate I' and the growth of 'Intermediate II' was found to match, with a lifetime of 509 ns, Figure 4.45. This is a faster lifetime of decay than that of the same process in heptane solvent, which had a lifetime of 882 ns. The lifetime of $CpRe(CO)_2$(*n*-heptane) is known to be longer than that of $CpRe(CO)_2$(*n*-hexane). This difference in lifetime of the related η^1-complexes is consistent with the difference in lifetimes of their related η^2-complexes, supporting assignment of the intermediate as η^1-$CpRe(CO)_2(H–CH_2C_5H_{11})$.

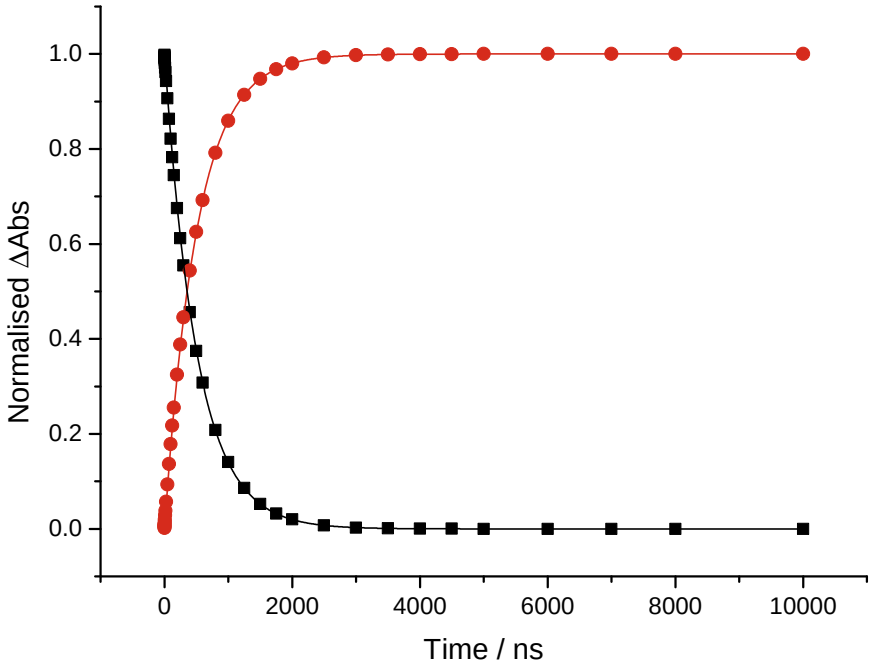

Figure 4.45: *Normalised excited state kinetics generated from global analysis following 266 nm photolysis of $CpRe(CO)_3$ in n-hexane, showing the decay of intermediate I and growth of intermediate II ($\tau = 509.3$ ns)*

4.4.1.3 ns-TRIR of $CpRe(CO)_3$ in *c*-hexane

The ns-TRIR was investigated in cyclohexane to see if the shift was present in a cyclic alkane. The results are shown in Figure 4.46. They show that upon excitation, there is a decrease in the parent peaks and the appearance of two new peaks at 1890 and 1966 cm^{-1}, which do not appear to shift. This photoproduct can be assigned as $CpRe(CO)_2$(c-hexane), bonded in an η^2 fashion. This peak does not decay, which is consistent with previous literature results, as the lifetime of this product is on the milliseconds timescale. If the shift that we see in previous experiments is in fact the bonding changing from η^1 to η^2, and since the only difference between cyclohexane and *n*-hexane/*n*-heptane is its cyclic nature, this suggests that there may be a steric factor which prevents the alkane from approaching the metal in an η^1 fashion. We have already described in the Introduction examples of how sterics can affect the orientation of alkane and silane complexes. The experiment was

repeated in cyclohexane-d_{12}, with the same result, namely, no shift in the photoproduct peak of $CpRe(CO)_2$(cyclohexane-d_{12}).

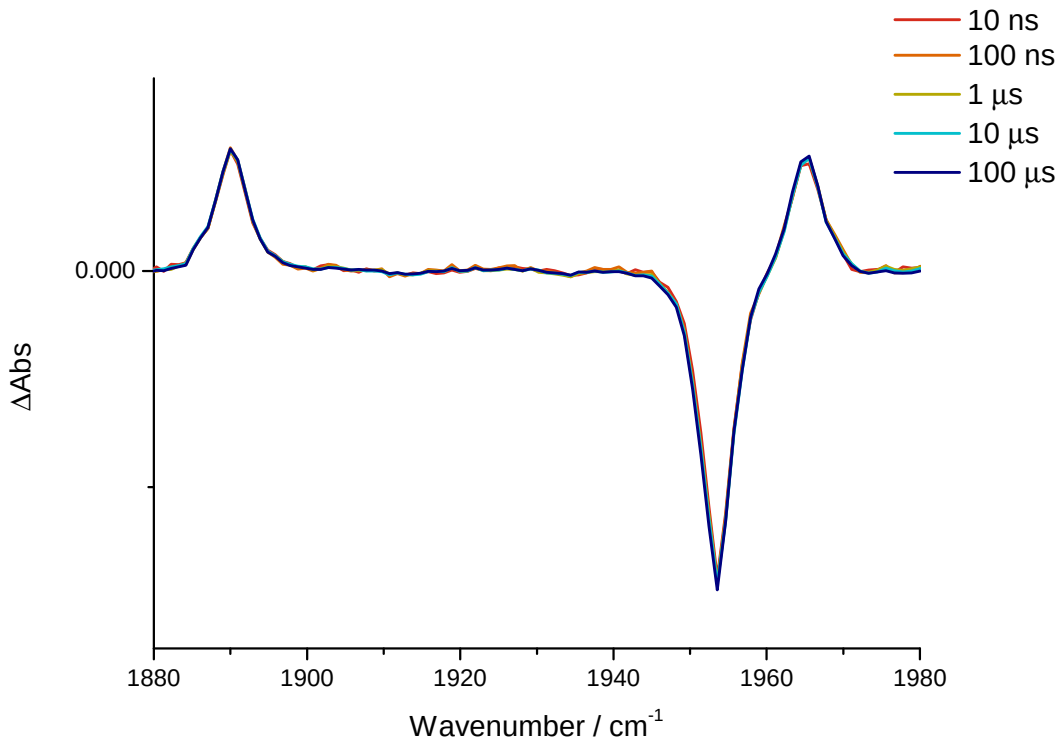

Figure 4.46: *ns-TRIR difference spectra at selected time delays for the 266 nm photolysis of $CpRe(CO)_3$ in cyclohexane*

We also consider that the reaction of $CpRe(CO)_2(\eta^1$-cyclohexane) to $CpRe(CO)_2(\eta^2$-cyclohexane) may be occurring; however, the reaction may occur too quickly for us to see on the nanosecond timescale. The reaction was repeated in the ps-TRIR; however, again, no discernable shift was seen.

4.4.1.4 ns-TRIR of $CpRe(CO)_3$ in *n*-hexane-d_{14}

The ns-TRIR was performed in deuterated hexane, as it was hypothesised that with the difference between deuterium and hydrogen, the magnitude of the shift between the proposed η^1-$CpRe(CO)_2(D–CD_2C_5D_{11})$ and η^2-$CpRe(CO)_2(C–DC_5D_{13})$ might be different than that of η^1-$CpRe(CO)_2(H–CH_2C_5H_{11})$ and η^2-$CpRe(CO)_2(C–HC_5H_{13})$. The results are shown in Figure 4.47, clearly showing the decrease in the parent peaks, and the appear-

ance of two new peaks at 1954 and 1878 cm^{-1} which blueshift over time to form peaks at 1952 and 1877 cm^{-1}. The presence of the same magnitude peak shift as seen in both experiments in heptane and hexane further rules out the possibility that this shift is caused by an impurity.

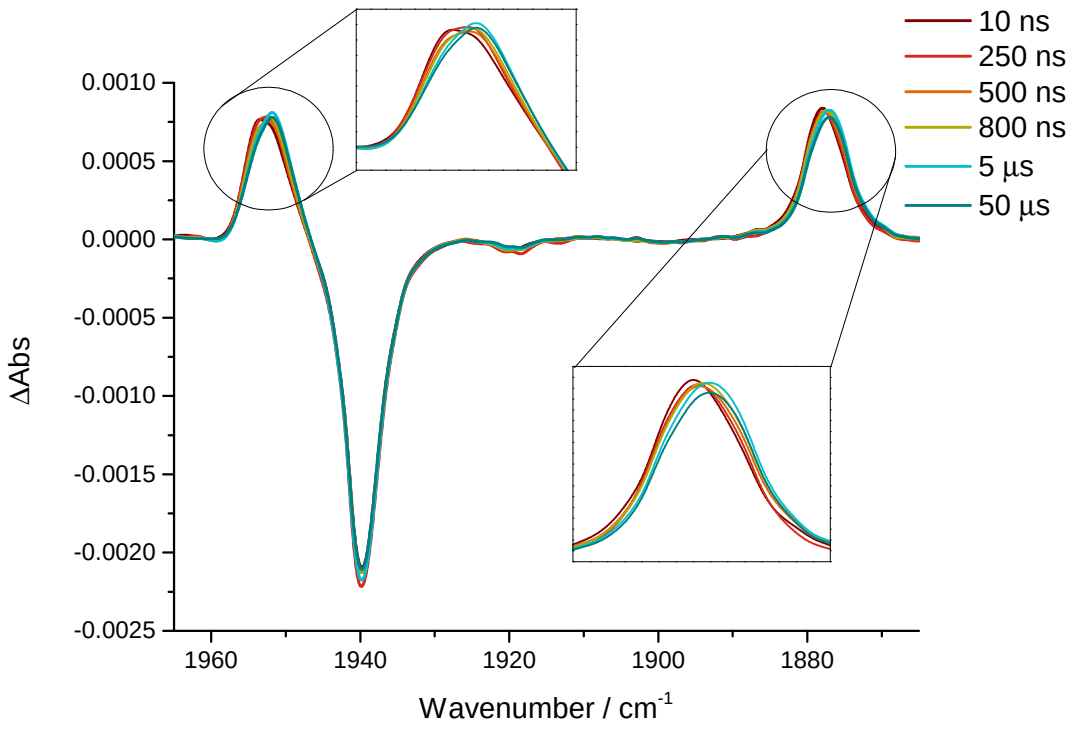

Figure 4.47: *ns-TRIR difference spectra at selected time delays for the 266 nm photolysis of CpRe(CO)$_3$ in hexane-d_{14}*

In Figure 4.48, the difference between the photoproduct peaks in hexane (black) and hexane-d_{14} (red) at 10 ns (solid line) and 5 µs (dashed line) is shown. The peak at ~1885 cm^{-1} exhibits a small blueshift in hexane-d_{14}; however, the peak at ~1953^{-1} does not appear to shift. If anything, the peak appears less broad in hexane-d_{14}. A blueshift indicates an increase in electron density around the metal.

An in-depth analysis of the peaks showed that the peak shift in hexane was 0.98 cm^{-1} and 2.21 cm^{-1} for the peaks at ~1885 cm^{-1} and ~1953 cm^{-1}, respectively, whist in hexane-d_{14} the shifts were calculated to be 0.95 cm^{-1} and 2.09 cm^{-1}.

Whilst there is minor evidence of a smaller shift in hexane-d_{14}, there is still error in the calculations of peak location so we cannot say with confidence that there is significance in

these values. This difference in peak shift would support assignment of the intermediate as an η^1 bonded alkane species.

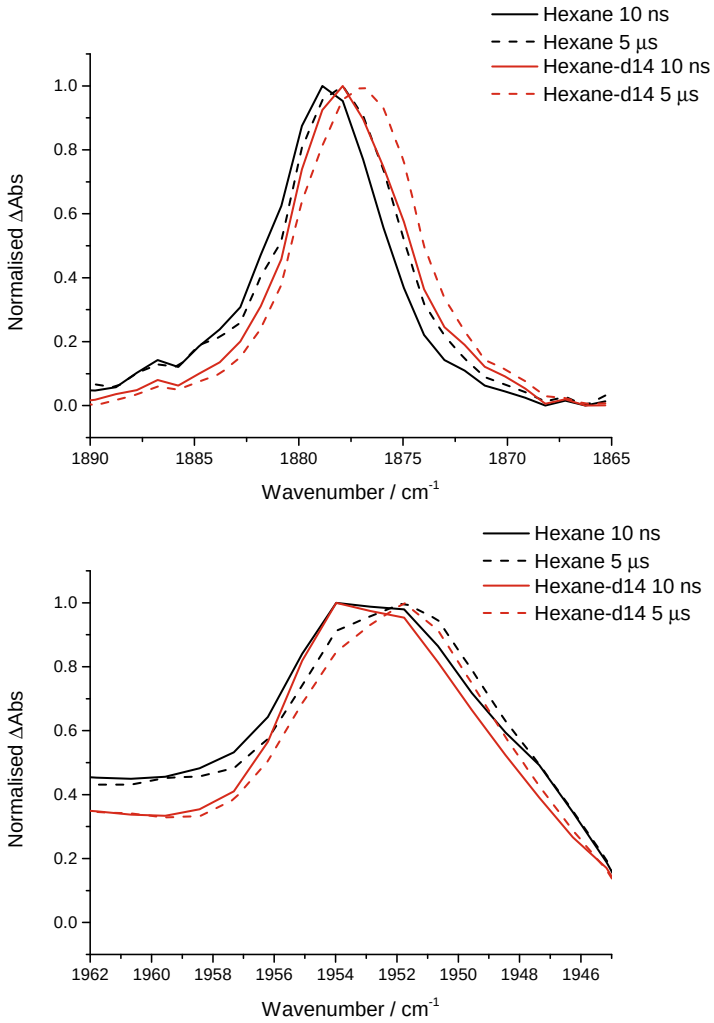

Figure 4.48: *Normalised spectra at 10 ns (solid line) and 5 µs (dashed line) following the 266 nm photolysis of CpRe(CO)$_3$ in n-hexane (black) and n-hexane-d$_{14}$ (red)*

4.4.2 Temperature Dependent TRIR Studies of CpRe(CO)$_3$ in Linear Alkanes

The TRIR at variable temperatures was conducted to gain insight into the kinetic parameters of the reaction. The results are shown in Table 4.5. Primarily, the rate of decay was measured in 10 degree intervals, but interestingly, at elevated temperatures in hexane, the peak shift was less apparent. This was not observed for heptane, see Figure 4.49.

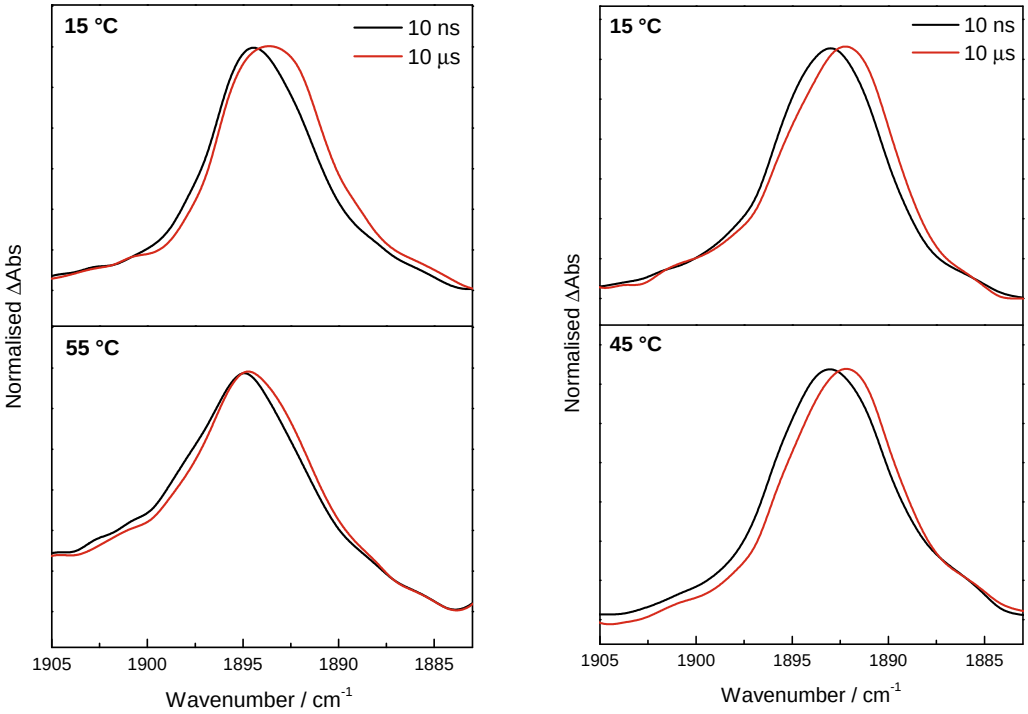

Figure 4.49: *Comparison of observed peak shift at 10 ns (black) and 10 µs (red) at low and high temperature for CpRe(CO)$_2$(η^1-hexane) (left) and CpRe(CO)$_2$(η^1-heptane) (right)*

The rate of decay of the proposed η^1 species was then measured at temperatures of five degree intervals from 15 to 35 °C for hexane and 15 to 45 °C for heptane. The results are shown in Table 4.5, showing the lifetime, rate constant (k_{obs}) and ln(k_{obs}). ln(k_{obs}) and ln($\frac{k}{T}$) were then plotted against $\frac{1}{T}$ to give Arrhenius and Eyring plots, respectively, typical examples of which are shown in Figure 4.50.

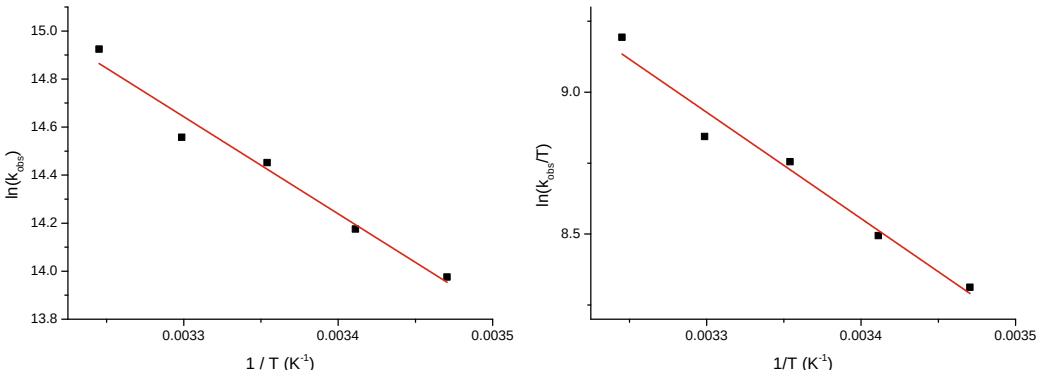

Figure 4.50: *Typical Arrhenius (left) and Eyring (right) plots for the proposed rearrangement reaction CpRe(CO)$_2$(η^1-alkane) to CpRe(CO)$_2$(η^2-alkane) (alkane = n-heptane or n-hexane)*

Table 4.5: Experimental lifetimes and calculated rate constants for the decay of $CpRe(CO)_2(\eta^1$-alkane) (alkane = *n*-hexane or *n*-heptane) at varying temperatures

	Temp / K	Lifetime / s	Rate Constant (k_{obs}) s^{-1}	$\ln(k_{obs})$
$CpRe(CO)_2(\eta^1$-$C_6H_{14})$	288.15	8.52×10^{-7}	1.17×10^6	13.98
	293.15	6.98×10^{-7}	1.43×10^6	14.18
	298.15	5.29×10^{-7}	1.89×10^6	14.45
	303.15	4.76×10^{-7}	2.10×10^6	14.56
	308.15	3.30×10^{-7}	3.03×10^6	14.92
$CpRe(CO)_2(\eta^1$-$C_7H_{16})$	288.65	1.19×10^{-6}	8.40×10^5	13.64
	293.15	8.22×10^{-7}	1.22×10^6	14.01
	298.15	8.82×10^{-7}	1.13×10^6	13.94
	303.15	3.84×10^{-7}	2.61×10^6	14.77
	308.15	3.36×10^{-7}	2.97×10^6	14.91
	313.15	5.22×10^{-7}	1.92×10^6	14.47
	318.15	5.23×10^{-7}	1.91×10^6	14.46

These plots were then used to calculate activation energy, E_a, and enthalpy and entropy of activation, $\Delta H^{\ddagger}$ and $\Delta S^{\ddagger}$, respectively. $^{298K}\Delta G^{\ddagger}$ has also been calculated, and all kinetic parameters are shown in Table 4.6.

As discussed in Chapter 2, kinetic parameters can point towards a reaction mechanism, in particular, the value of $\Delta S^{\ddagger}$ can indicate an associative or dissociative mechanism. Large, negative values of $\Delta S^{\ddagger}$ suggest an associative mechanism, whilst positive values would suggest a dissociative mechanism. Again, calculations of $\Delta S^{\ddagger}$ must be carefully considered, as there is a large degree of error that can be introduced by extrapolation of the data. However, the $\Delta S^{\ddagger}$ values calculated here are only small negative or a small positive value. Therefore, we can probably rule out an associative mechanism and assign

the reaction as a dissociative or an interchange mechanism.

Considering the proposed mechanism of η^1-H to η^2-C,H and the mechanistic studies described in the introduction, namely that the C–H bond rotates as it approaches the metal, it would be more fitting to assign the reaction as an interchange mechanism. This is because in the proposed approach of the C–H bond, there is no dissociation. Therefore, we tentatively assign this as an interchange mechanism.

The activation energy and enthalpy of activation are relatively large, which would suggest a large energy barrier to overcome in going from η^1 to the η^2 bonded species.

The heptane intermediate has a larger activation energy, $\Delta H^{\ddagger}$ and $\Delta S^{\ddagger}$ and also a marginally larger ${}^{298}\Delta G^{\ddagger}$ than the hexane intermediate. This is reflective of the longer lifetime of the heptane intermediate.

Table 4.6: Experimentally determined Arrhenius and Eyring parameters for $CpRe(CO)_2X$, where X = η^1-heptane or -hexane

	E_a kJmol^{-1}	$\Delta H^{\ddagger}$ kJmol^{-1}	$\Delta S^{\ddagger}$ Jmol^{-1}	${}^{298K}\Delta G^{\ddagger}$ kJmol^{-1}
$CpRe(CO)_2\eta^1$-heptane	41.2	38.7	4.4	37.4
$CpRe(CO)_2\eta^1$-hexane	33.6	31.1	−20.6	37.2

4.5 Conclusions and Future Work

In Section 4.3, we have repeated known literature experiments, the photochemical reaction of $CpMn(CO)_3$ in triethylsilane, *n*-heptane and lastly triethylsilane doped *n*-heptane. Photolysis of $CpMn(CO)_3$ in both neat triethylsilane and neat *n*-heptane led to the formation of $CpMn(CO)_2(SiHEt_3)$ and $CpMn(CO)_2$(*n*-heptane), respectively. The former decays with a lifetime of 146 ± 14 ns to form the partially activated Si–H photoproduct; $CpMn(CO)_2(SiEt_3)H$. The *n*-heptane bonded intermediate is much more long-lived, decaying with a lifetime of 69.8 μs, making it 1000× less reactive than the analogous silane intermediate. It decays to form the known dimer $Mn_2Cp_2(CO)_5$. For the photolysis in triethylsilane (120mM) doped *n*-heptane, we found good agreement with past studies, as photolysis leads to creation of $CpMn(CO)_2$(*n*-heptane) which decays with a lifetime of 2.87 ± 0.07 μs to form the 'partially Si–H activated' product $CpMn(CO)_2H(SiEt_3)$. We have conducted the experiment with varying concentrations of triethylsilane, where we found that lower concentrations led to a longer lifetime of the heptane bonded intermediate. Measuring the lifetimes at varying concentrations enabled us to measure the the Stern–Volmer constant, at 169.5 M^{-1}. This is key information needed for future TR-XAS experiments. In future work, we hope to study the reaction of $CpMn(CO)_3$ in triethylsilane doped *n*-heptane by X-ray absorption spectroscopy, in order to probe the structure of the intermediate $CpMn(CO)_2$(*n*-heptane) and photoproduct $CpMn(CO)_2H(SiEt_3)$.

We have repeated the experiments for $CpRe(CO)_3$ in triethylsilane and triethylsilane doped *n*-heptane. In neat triethylsilane we find photolysis results in production of $CpRe(CO)_2(SiHEt_3)$, which decays with a bi-exponential decay, the first component with a lifetime of 1.4 μs, and the second at 11.7 μs. This decay is concurrent with the growth of the Si–H activated species $CpRe(CO)_2(SiEt_3)H$. Previously in the literature, the lifetime was found to decay via a simple mono-exponential decay, with a lifetime of 7.2 μs. We have found that the peaks due to $CpRe(CO)_2(SiHEt_3)$ exhibit a ~2 cm^{-1} shift in wavenumber, a phenomenon never noted before in the literature, and not seen in the analogous reaction with $CpMn(CO)_3$. We have hypothesised that the shift in wavenumber is due to

the Si–H bonding changing from η^1 to η^2.

In the reaction of $CpRe(CO)_3$ in triethylsilane doped *n*-heptane, we have found that the reaction follows the same path as $CpMn(CO)_3$, namely the heptane bonded intermediate, $CpRe(CO)_2$(*n*-heptane) directly leads to the Si–H activated product, $CpRe(CO)_2(SiEt_3)H$. Previous work in our group was unable to determine this reaction, as the concentration of triethylsilane used was not high enough to monitor the decay of $CpRe(CO)_2$(*n*-heptane) on the timescale studied (1 ms). We have used a much high concentration of triethylsilane (2 M) to be able to monitor this reaction on the timescale of our TRIR setup. At 2 M of triethylsilane, the species $CpRe(CO)_2$(*n*-heptane) decays with again a bi-exponential decay, with the first component at 1.4 ± 0.4 μs, and the second at 64.4 ± 3.0 μs. We measured this decay at variying concentraions of triethylsilane (2–5 M) again finding that the higher the concentration, the shorter the lifetime of the intermediate. We were able to ascertain the value of the quenching constant at 1.74×10^4. This reaction was deemed unsuitable for study in TR-EXAFS, as the heptane bonded intermediate is too long-lived. Again, in this experiment the intermediate peak exhibits a ~1 cm^{-1} shift in wavenumber, slight smaller than the shift seen in neat triethylsilane. We have tentatively assigned this as the bonding changing from η^1 bonded *n*-heptane to η^2 bonded *n*-heptane; however, further investigations were needed to support this.

Preliminary TR-XAS studies of $CpRe(CO)_3$ in triethylsilane have been reported, showing a small shift in the absorption edge upon photolysis at 266 nm. This is indicative of a decrease in electron density around the metal. Additionally, we note a small redshift in the absorption edge from between 1–2 μs and 4–5 μs, again indicative of a decrease in electron density around the metal. This is reminiscent of the blueshift in the ν(CO) of the intermediate $CpRe(CO)_2(SiHEt_3)$ seen in the ns-TRIR. This further supports assignment of an η^1 intermediate; however, further analysis of the TR-EXAFS spectra is needed to hopefully determine structural information about the photoproducts.

In Section 4.4, we have studied the reactions of $CpRe(CO)_3$ in neat *n*-heptane, *n*-hexane, *n*-hexane-d_{14} and c-hexane to further explore this peak shifting phenomenon. The photoly-

sis of $CpRe(CO)_3$ in all alkanes led to the production of photoproducts $CpRe(CO)_2$(alkane), which are well known to be among the longest lived alkane bonded species; therefore, we did not see their decay on the timescale of our reaction. However, in neat *n*-heptane and *n*-hexane, we again saw a $\sim$1 cm^{-1} shift in the $CpRe(CO)_2$(n-alkane) photoproduct peaks. We have again tentatively assigned this as the alkane bonding changing from η^1 to η^2. The fact that this shift was seen in multiple experiments shows that it is a real shift. The photolysis of $CpRe(CO)_3$ in cyclohexane resulted in formation of $CpRe(CO)_2$(c-hexane), whose photoproduct peaks were not seen to shift at all. We propose that sterics may be a factor.

Global analysis was conducted on both $CpRe(CO)_2$(*n*-heptane) and $CpRe(CO)_2$(*n*-hexane) experiments to deduce the kinetics of this peak shifting. The proposed $CpRe(CO)_2(\eta^1$-heptane) intermediate was found to decay with a lifetime of 882.1 ns, corresponding to the growth of $CpRe(CO)_2(\eta^2$-heptane). The proposed $CpRe(CO)_2(\eta^1$-hexane) intermediate was found to be slightly shorter-lived, decaying with a lifetime of 509 ns, again corresponding to the growth of $CpRe(CO)_2(\eta^2$-hexane).

The photolysis of $CpRe(CO)_3$ in deuterated *n*-hexane was investigated to compare to the analogous reaction in normal *n*-hexane. The peak locations for $CpRe(CO)_2(\eta^1$-hexane) and $CpRe(CO)_2(\eta^1$-hexane-d_{14}) were found to be slightly different; however, there was little to no difference in the magnitude of the peak shift.

Finally, the variable temperature TRIR was conducted for the reactions of $CpRe(CO)_3$ in *n*-heptane and *n*-hexane, to deduce the activation parameters for these reactions. The activation energy for $CpRe(CO)_2(\eta^1$-heptane) and $CpRe(CO)_2(\eta^1$-hexane) was measured to be 41.2 and 33.6 $kJmol^{-1}$, respectively. The entropy of activation for $CpRe(CO)_2(\eta^1$-heptane) and $CpRe(CO)_2(\eta^1$-hexane) was found to be 4.4 and -20.6 $kJmol^{-1}$, respectively, suggesting a dissociative or an interchange mechanism. We suggest that in the intramolecular rearrangement of $CpRe(CO)_2(\eta^1$-alkane) to form $CpRe(CO)_2(\eta^2$-alkane), an interchange mechanism is more likely.

An in-depth density functional theory investigation is needed on the reactions of

$CpRe(CO)_3$ in triethylsilane and alkanes in order to assess the transition states of the reaction to support experimental observations os a possible η^1 intermediate. We have performed TR-EXAFS experiments on the photolysis of $CpRe(CO)_3$ in heptane at the APS in Illinois; however, these results need to be processed. It is hoped that in the future we can use structural data obtained from these experiments to confirm the process of η^1 to η^2 conversions.

Chapter 5

Variable Temperature TRIR Investigation into the Photochemical and Photophysical Reactions of a Rhenium Tetracarbonyl Bipyridine Complex

5.1 Introduction

Thus far in this work, we have focussed on reactions of metal carbonyl species, where upon irradiation with UV light, a carbonyl ligand is ejected to form a highly reactive sixteen (or even fourteen) electron species that will bind with a weakly bonding alkane, silane or noble gas ligand. These reactions are photochemical, where a chemical change has been induced by light. In this chapter, we will explore the *photophysical* reactions, i.e., the non-chemical changes induced by light, and the following photochemical reactions that they may incur, of rhenium tetracarbonyl bypyridine complexes.

Photophysical processes occur when a molecule absorbs a photon of appropriate

energy, promoting an electron into an excited state. This electronic transition from the ground state ($\mathbf{S}_0$) to an excited state ($\mathbf{S}_1$ or $\mathbf{S}_2$) takes place in the order of femtoseconds. This energy can be released in a number of ways; non-radiative decay (vibrational relaxation, internal conversion and intersystem crossing) or through emission of light, also called radiative decay (fluorescence or phosphorescence), see Figure 5.1. Chemical reactions may occur if the energy can't be released via radiative or non-radiative decay, to form a photoproduct of different chemical make-up than the ground state.

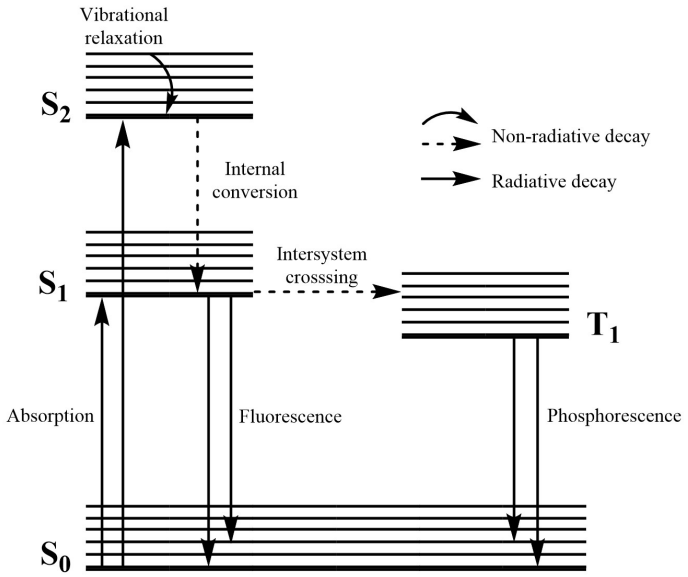

Figure 5.1: *Jablonski Diagram*

Fluorescence is a fast process (typically between 10^{-6} and 10^{-9} s) as it is formally spin-allowed. Comparatively, phosphorescence is relatively long-lived, owing to the fact that is a formally spin-forbidden process.

5.1.1 Photophysical Reactions of Transition Metal Complexes

There are several different possible electronic transitions in a transition metal complex that result in several different excited states, which are:

(i) Ligand centred (LC) or intraligand (IL) excited states, arising from transitions between energy levels from the same ligand;

(ii) Interligand change transfer (ILCT) excited states, arising from transitions between energy levels of two different ligands;

(iii) Metal centred (MC) or ligand field (LF) excited states, arising from transitions between the energy levels of the metal d-orbitals;

(iv) Ligand-to-metal-charge-transfer (LMCT) excited states, arising from transitions from the ligand to the metal; and

(v) Metal-to-ligand-charge-transfer (MLCT) excited states, arising from transitions from the metal to the ligand.

Which of these is the emitting state depends on which has the lowest energy, which in turn depends on the nature of the ligand, the metal and the complex geometry.[190] Assignments of the emitting state can be made by observing features in a complexes absorption and luminescence spectra. MLCT and LMCT states usually occur at lower energy and are generally intense transitions. Transitions between the ligand orbitals tend to lie at a comparatively higher energy than these charge transfer transitions.

Attracting much interest over the last forty years for their vast array of photophysical properties are d^6 metal complexes, such as Re(I), Ru(II), Os(II) and Ir(III). Generally, d^6 metal complexes display an octahedral geometry, where the ligands surrounding the metal split the d-orbitals into three lower and two higher levels, with the electrons occupying the three lower levels. The extent of this splitting is dependent on the ligands surrounding the metal and also the nature of the metal itself. Polypyridine ligands such as those studied in this Chapter exert fairly strong crystal field splitting. As for the metal, the 4d and 5d electrons of second and third row metals have a larger spatial distribution than the 3d electrons of first row metals,[191] also leading to greater splitting. As such, in second and third row d^6 metal complexes, such as Re(I), Ru(II), Os(II) and Ir(III), the splitting is large enough that the e_g orbitals lie energetically above the ligand π^* orbitals. Therefore, on photoexcitation, the electron is promoted from the HOMO (the metal t_{2g} orbitals) to the LUMO, (the ligand π^* orbitals) see Figure 5.2. This results in a metal-to-ligand-charge-

transfer (MLCT) excited state, which is often long-lived, and is the reason behind these complexes unique photophysical and photochemical properties.

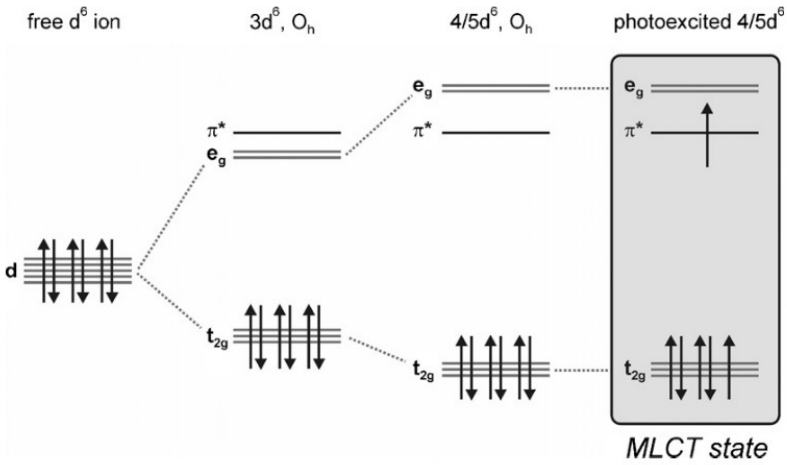

Figure 5.2: *Simplified molecular orbital diagram for d^6 polypyridine complexes, reproduced from reference 191*

Some of the first and most well-studied rhenium species are $Re(CO)_3(LL)X$ species, where LL = bidentate diimine and X = a halogen. The excited state properties of these complexes usually occur through their lowest triplet excited state; therefore, the nature of the lowest energy acceptor ligands (almost always the diimine ligand) plays an important role in determining the photophysical and/or photochemical properties.[192] Excited state properties of these complexes can be easily tuned by modification of the diimine ligand and also the halogen ligand. Such diverse photophysical and photochemical properties has led to a vast array of different uses, including as emitters for electroluminescence devices,[193,194] as a light absorber in dye-sensitised solar cells[195] and most notably as photocatalysts for CO_2 reduction.[196–198]

The typical Jablonski diagram for a $Re(CO)_3LLX$ species is shown in Figure 5.3. Due to the ^{1}MLCT lying close in energy on the shoulder of the ^{1}LC, on excitation, both excited states can be populated simultaneously. These excited states undergo inter-system crossing to form a triplet state, which unlike their singlet states are different in energy. This state further relaxes either back to the ground state.[192] Since the resulting ^{3}MLCT and ^{3}LC

states lie at different energies, emission characteristics of these two states can be used to distinguish between them. The ^{3}MLCT excited states often show a broad structureless emission at *ca.* 600 nm and ^{3}LC states show a strong vibronic emission around 500 nm.

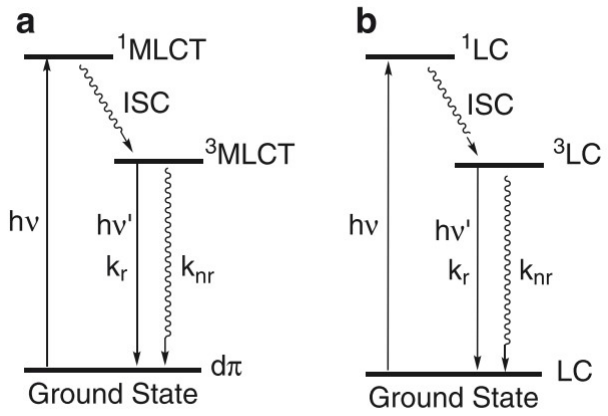

Figure 5.3: *Schematic Jablonski diagram for the photochemical and photophysical transitions that occur in $Re(CO)_3(LL)X$, including a) The MLCT model and b) the LC model, reproduced from reference 192*

The accessibility of these states can be altered by temperature. A study by Sacksteder *et al.* showed that measuring the emission of $ReL(CO)_3X$ (where L = 2,2-bipyridine, 1,10-phenanthroline, or 5-phenyl-1,10-phenanthroline and X = substituted pyridine or quinoline) at 77 K caused the phosphorescence to switch from the ^{3}MLCT state to the ^{3}LC state. They explained this by citing the changes in energy of the MLCT with temperature.[199]

A second study has also revealed the importance of temperature on excited states. Koike *et al.* found that in the photochemical reaction of $[Re(X_2bpy)(CO)_3(PR_3)]^+$ with CH_3CN to make $[Re(X_2bpy)(CO)_2(PR_3)(CH_3CN)]^+$, the quantum yields of the reaction increased with temperature.[200] This strongly suggested that the photochemical ligand substitution reaction occurs via an excited state thermally accessible from the ^{3}MLCT state, see Figure 5.4.

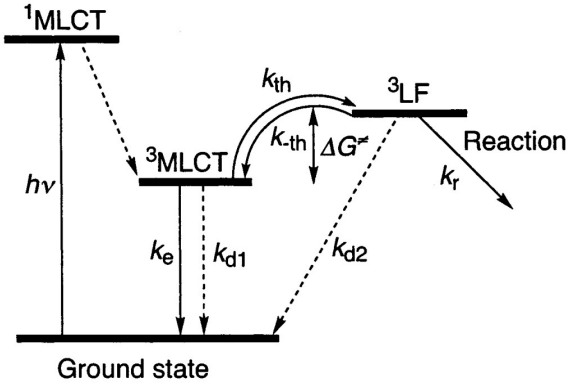

Figure 5.4: *Jablonksi diagram for the photochemical reaction of* $[Re(X_2bpy)(CO)_3(PR_3)]^+$ *in* CH_3CN*, reporoduced from reference 200*

As described above, the lowest energy excited state transfer in these complexes is usually an MLCT. However, in reality, occupied frontier orbitals can mix, resulting in mixed-character excited states. This mixing is due to two factors; 1) the delocalisation of the optical orbitals and 2) the combination of multiple one-electron transitions in one electronic transition.[201] The energies of the ^{3}MLCT and the ^{3}LC excited states are often close in energy, leading to increased possibility of state mixing.[201]

Density functional theory (DFT) and time-dependent density functional theory (TD-DFT) can be used to determine the exact nature of the excited state transitions. For example, a study by Kirgan *et al.* showed that in $[Re(CO)_3(bpy)Cl]$, the HOMO contained $\geq$ 50 % Re_d character, with ~20 % contributions from both CO and Cl. The LUMO consisted of $\geq$ 80 % diimine ligand π^* character. Therefore, the lowest energy optical transition was assigned as a metal-ligand-to-ligand charge transfer transition (MLLCT).[202] DFT and TD-DFT have become useful tools to elucidate the exact nature of excited states.

5.1.2 Photophysical and Photochemical Reactions of Rhenium Tetracarbonyl Complexes

There are some downsides of $Re(CO)_3(LL)X$ type complexes, in that they often have low emissive quantum yields, short excited state lifetimes and low energy emission maxima. In a bid to solve this problem, in the early 1990's Shaver *et al.* investigated the

photophysics of a number of rhenium tetracarbonyl complexes.[203] Indeed, the complex $[Re(CO)_4(bpym)][BF_4]$ (bpym = 2,2-bipyrimidine) was found to have vastly different properties to its tricarbonyl relatives. The excited state lifetime of $[Re(CO)_4(bpym)][BF_4]$ was found to be over an order of magnitude larger than that of $[Re(CO)_3(bpym)Cl]$, with Shaver postulating that substituting the Cl with a strong field CO ligand decreases the non radiative decay channel.[203] Further investigations on several other complexes, including $[Re(CO)_4(bpy)]^+$ (bpy = 2,2'-bipyridine), $[Re(CO)_4(dmb)]^+$ (dmb = 4,4'-dimethyl-2,2'-bipyridine) and $[Re(CO)_4(phen)]^+$ (phen = 1,10-phenanthroline), revealed that changing the diimine ligand can vastly change the photophysical properties of the complex, as represented by the UV/Vis and emission spectra shown in Figure 5.5.[204]

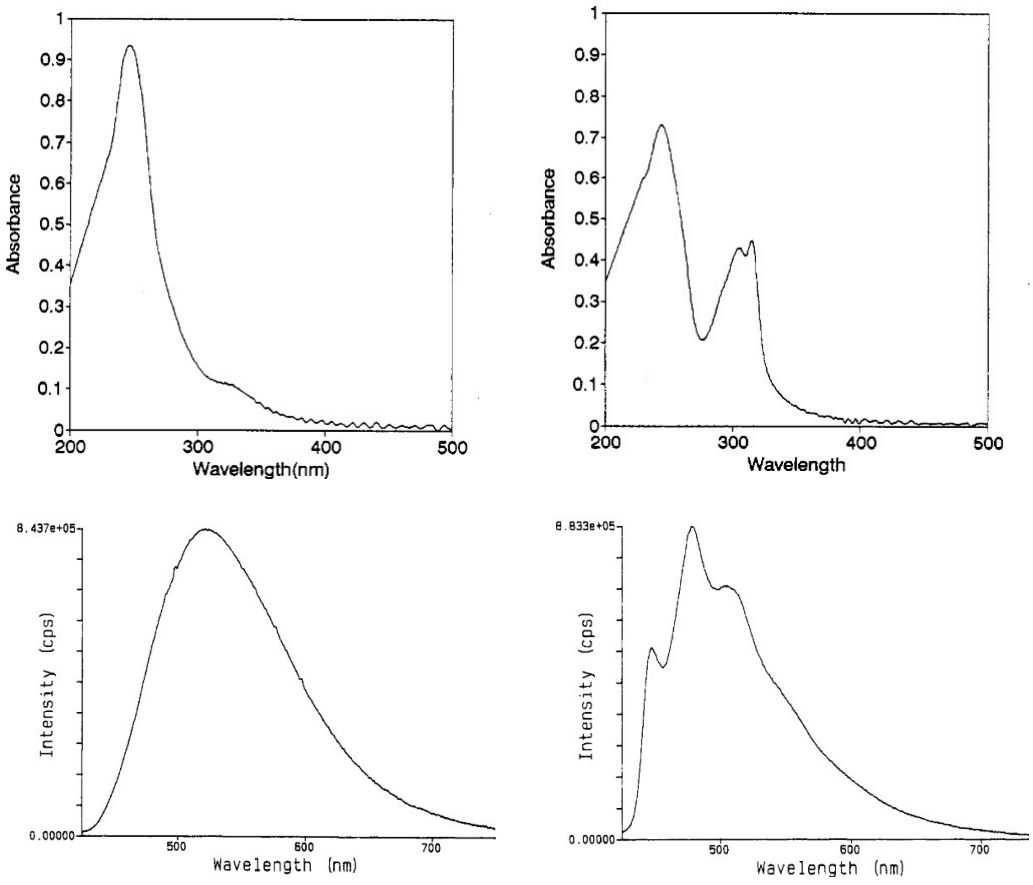

Figure 5.5: *UV/Vis spectra of $[Re(CO)_4(bpym)][CF_3SO_3]$ (top left) and $[Re(CO)_4(bpy)][CF_3SO_3]$ (top right), and emission spectra of $[Re(CO)_4(bpym)][CF_3SO_3]$ (bottom left) and $[Re(CO)_4(bpy)][CF_3SO_3]$ (bottom right) reproduced from reference 204*

The infrared spectra of rhenium tetracarbonyl diimine complexes contain four infrared bands consistent with the binding modes $1A_1$, $2A_1$, B_1 and B_2, as shown in Figure 5.6. For $[Re(CO)_4(bpy)]^+$, the ground state infrared bands in the ν(CO) region are observed at 1969, 2011, 2029 and 2123 cm^{-1}, corresponding to the B_2, $2A_1$, B_1 and $1A_1$ modes, respectively.[205]

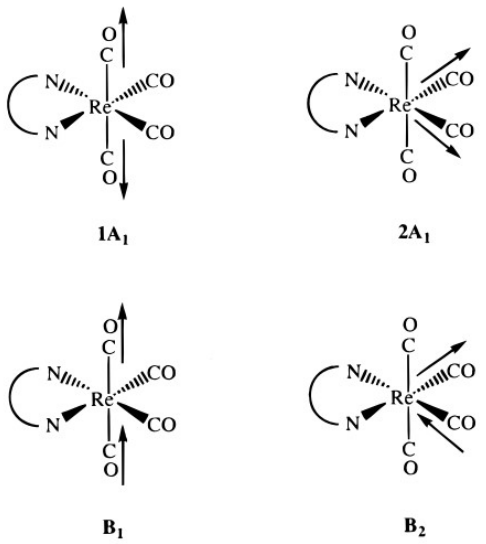

Figure 5.6: *Different infrared modes of $[Re(LL)(CO)_4]^+$ complexes, where LL = α, α'-diimine ligand, reproduced from reference 205.*

Time-resolved infrared spectroscopy can be used to determine excited states of transition metal carbonyl complexes. For ^{3}MLCT states, a shift to higher energy is expected relative to the ground state, as electron density is decreased at the metal centre, decreasing π-backbonding between the metal and CO ligand, hence increasing the strength of the CO bond. This can result in shifts of the ν(CO) bands of over 40 cm^{-1}.[206,207] For ^{3}LC states, whilst there is no direct change in electron density at the metal centre, the ligand becomes a slightly better donor in the excited state.[205] This donates a small amount of electron density to the metal, resulting in a small decrease in energy of the ν(CO) (< 10 cm^{-1}).[207]

Previously to work carried out in our group, there was a sole report in the literature of the TRIR of rhenium tetracarbonyl diimine complexes. Bernhard *et al.* conducted the TRIR of $[Re(LL)(CO)_4]^+$ (where LL = 2,2'-bipyridine (bpy), 4,4'-dimethyl-2,2'-bipyridine (dmb), or 1,10-phenanthroline (phen)) in 1,2-dichloroethane.[205] Using an excitation wavelength

of 355 nm they saw an initial excited state with bands at 1973, 2014, 2033 and 2118 cm^{-1}, see Figure 5.7. They assigned this excited state as a mixed ^{3}MLCT/LC state, which was observed for all three complexes investigated. Contrary to previous reports of other complexes,[208,209] the bands corresponding to the $2A_1$, B_1 and B_2 modes shifted slightly to higher energies, while the bands of the $1A_1$ mode shifted to slightly lower energy. The characteristic shift to lower energy for an LC state (< 10 cm^{-1}) was thought to be counteracted by the larger shift to higher energy of the MLCT state (> 40 cm^{-1}). The work here most agreed with previous work by Strouse *et al.*, who, by using low temperature single crystal absorption, assigned the lowest lying electronic state of $[Re(LL)(CO)_4]^+$ to be 1–3% MLCT character with an LC state.[210,211]

The excited state had a lifetime of around 2 μs, after which dissociation of CO led to the final photoproduct with bands around 1950 and 2050 cm^{-1}, consistent with the structure *fac*-$[Re(LL)(CO)_3(DCE)]$ (DCE = 1,2-dichloroethane). Formation of the photoproduct was reported to be 100 % efficient. They postulated that the photodissociation was unlikely from the LC excited state, but more likely from the ^{3}MLCT state or a low-lying ligand field (LF) state.

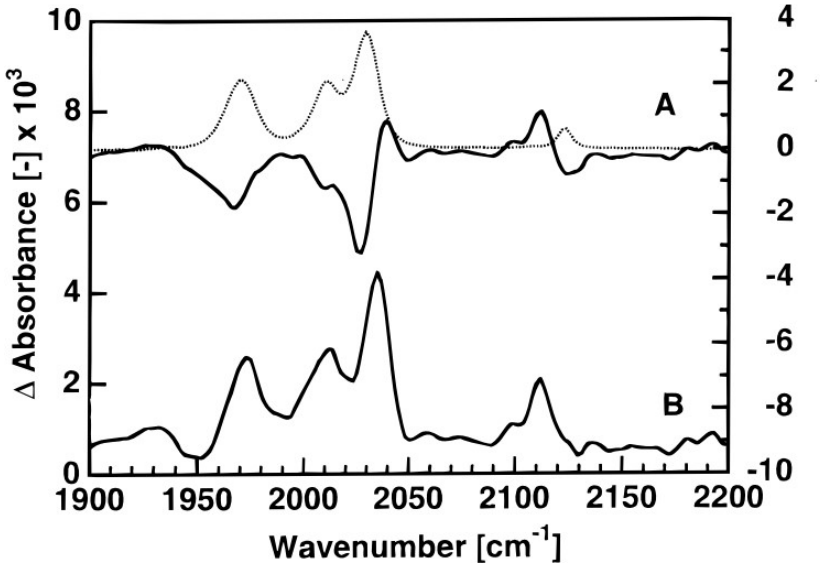

Figure 5.7: *TRIR difference spectra of $[Re(CO)_4(bpy)]^+$ at 298 K in 1,2-dichloroethane (A, solid line), alongside the ground-state spectrum (A, dotted line). The calculated excited state spectrum is shown in B, reproduced from reference 205.*

More recent work in our group, however, has contradicted these results, with the ps-TRIR and ns-TRIR of $[Re(CO)_4(bpy)][PF_6]$ used to observe two excited states instead of the one reported by Bernhard *et al.*[212] Figure 5.8 shows the results of global analysis to separate the overlapping excited states. State I (in black) decayed with a lifetime of around 150 ns. The second excited state (in red), assigned to a mixed ILCT/MLCT state, matched the previously reported excited state by Bernhard, decaying with a lifetime of around 2 μs. As reported previously in the literature, the final photoproduct was assigned to the CO loss product $Re(CO)_3(bpy)(CH_2Cl_2)$.

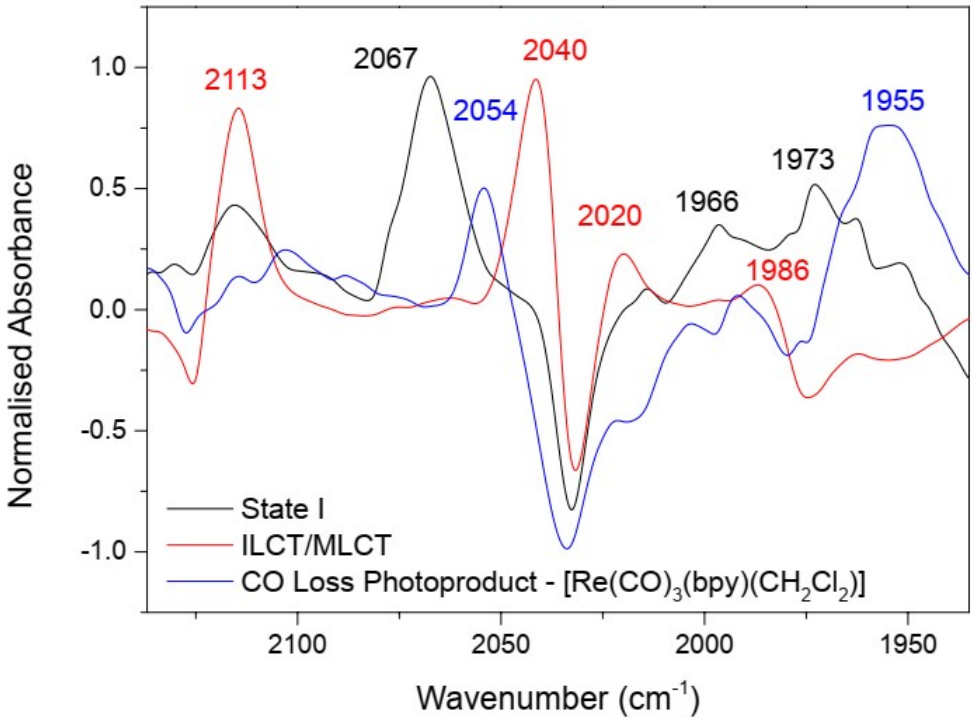

Figure 5.8: *Normalised excited state spectra following 355 nm excitation of $[Re(CO)_4(bpy)][PF_6]$ in dichloromethane, following results of global analysis, reproduced from reference 212*

TD-DFT (time-dependent density functional theory) calculations were used to help with assignment of these excited states. The calculations confirmed the presence of the newly observed excited state, 'State I', which was assigned as a mixed ILCT/MLCT, similar to the previously observed state. Figure 5.9 shows the results of the calculations into the distribution of the electronic charge. In a vacuum, the majority of the electron density

moves from the metal to the ligand, i.e., it is a mostly MLCT character excited state. However, when calculations were performed in CH_2Cl_2 and CH_3CN, the distributions changed significantly. The higher energy state calculations show electron density transfer from the bpy to the axial CO and also from the Re to the CO in both CH_2Cl_2 and CH_3CN, i.e., a mixed ILCT/MLCT state.

The lower energy state calculations show slightly different character with a significant amount of electron density moving from the metal to the bpy ligand but with also some contribution from the CO ligands to the bpy. This further supports State I's assignment as a mixed MLCT/ILCT state with more MLCT character.

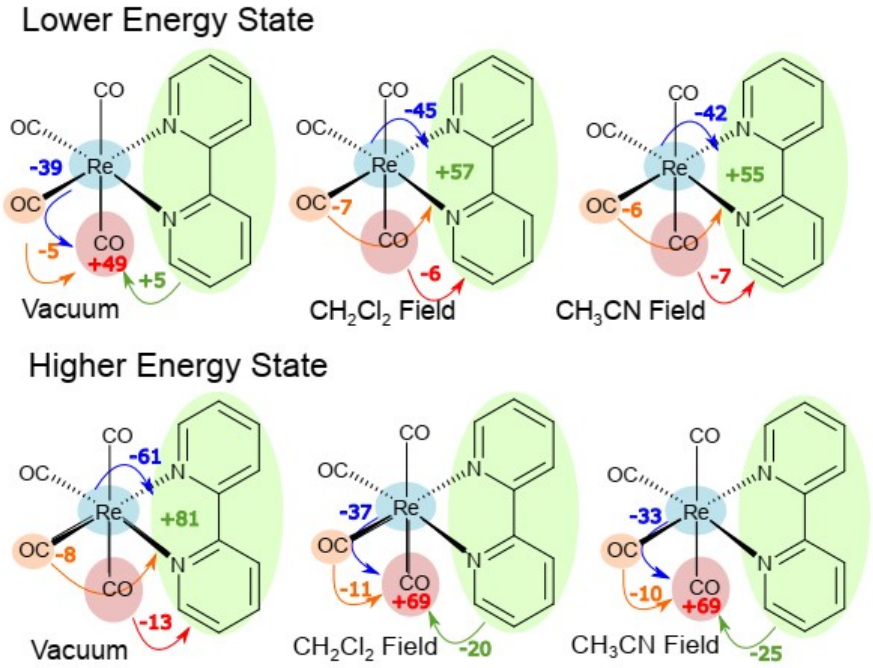

Figure 5.9: *Movement of electron density that occurs in the lower and higher energy states in a vacuum (left), CH_2Cl_2 (middle) and CH_3CN (right), as calculated by TD-DFT, reproduced from reference 212*

The proposed Jablonksi diagram for this reaction is shown in Figure 5.10, proposing that CO loss occurs from 'State II' or the mixed ^{3}ILCT/MLCT state. This was observed experimentally as the decay of State II matched the growth of the photoproduct. The study also found that excitation at 266 nm only led to the formation of one excited state, 'State II', which decayed in 900 ns to form the solvated CO loss photoproduct.

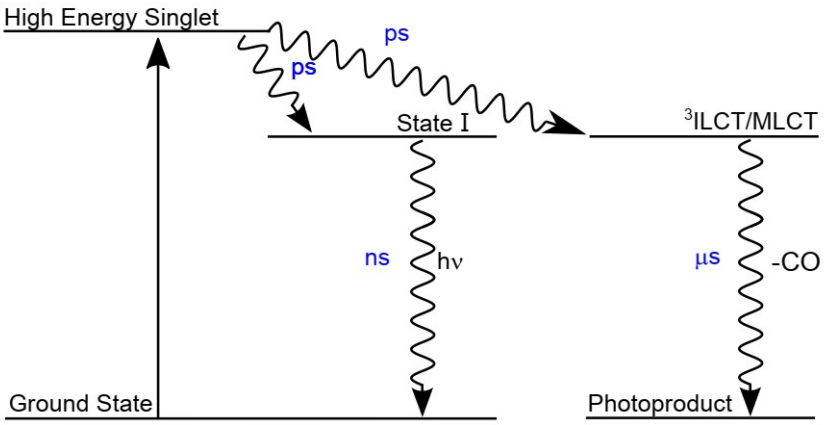

Figure 5.10: *Proposed Jablonski diagram for the photochemical and photophysical reactions of [Re(CO)$_4$(bpy)][PF$_6$] following excitation at 355 nm, reproduced from reference 212*

A second study in our group looked at the influence of the substituents on the bipyridine, see Figure 5.11. It was found that with an electron donating group on the bpy ligand, CO loss was more likely to occur. Where electron withdrawing groups were present, CO loss became a much less favoured pathway.[121] The author suggested that with increasing electron withdrawing character of the substituents on the bpy, the less MLCT character the mixed ILCT/MLCT excited state contains. However, on investigation of the ν(CO) shift from the parent, which for a state containing less MLCT character would be expected to shift to lower energy, the bands for the EWG containing groups, were seen to redshift. The lifetime of the two excited states also decreased on increasing the electron withdrawing capabilities of the substituents on the bpy.

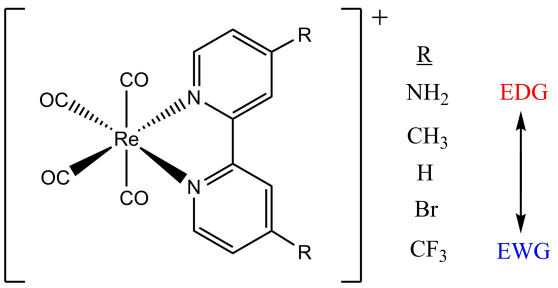

Figure 5.11: *The structure of Re(CO)$_4$(4,4'-R$_2$-bpy) complexes studied*

5.1.3 Marcus Theory of Electron Transfer

The photophysical reactions we have so far discussed in this Introduction are electron transfer reactions, where charge is transported from one part of the molecule to another. Simple transition state theory fails to model solution-phase electron transfer reactions properly. In contrast to classical chemical reactions, in simple electron transfer reactions, no chemical bonds are broken or formed so a different picture is needed to describe the process. Whilst no chemical bonds are made or broken, bond lengths and angles can however change. In addition, the surrounding solvent shell must readjust to the change in charge distribution. To account for all of this, in Nobel prize winning work, Rudolph A. Marcus developed Marcus theory,[213] to explain 'outer-sphere, self-exchange' reactions. This has been widely used in the literature to accurately describe electron transfer. Marcus theory will be introduced here to the extent necessary for understanding of the work in this thesis.

Marcus theory uses Morse potentials to describe the reaction coordinate, see Figure 5.12, and these curves are approximated mathematically as parabolas. During the fast electron transfer process, nuclei have no time to shift position; thus, the electron transfer occurs mainly at or near the intersection of the reactant and product potential energy curves.[214] Therefore, the intersect of the parabolas is a good estimation for the transition state of the reaction.[215]

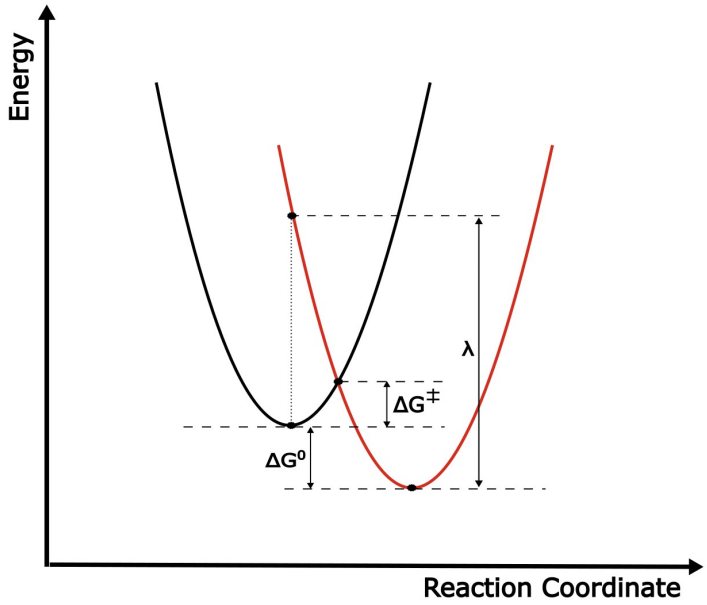

Figure 5.12: *Reactant and product free energy wells for an electron transfer reaction, modified from reference 216*

$\Delta G^{\ddagger}$, the free energy barrier, is given by the equation;

$$\Delta G^{\ddagger} = \frac{1}{4\lambda}(\lambda + \Delta G^{0})^{2} \tag{5.1}$$

where ΔG^{0} is the overall free energy change of the reaction (also referred to as the driving force) and λ is the reorganisation energy. Marcus describes λ as the 'energy input necessary to alter the structure of solvated reactants to match that of solvated products, before electron transfer takes place'.[213,217] It accounts for vibrations of the molecules and from the polarization changes in the dielectric solvent environment.[218] Substituting the expression for $\Delta G^{\ddagger}$ in Equation 5.1 into the Arrhenius rate equation gives the rate of reaction for electron transfer, k_{ET}, as:

$$k_{ET} = Aexp\left(\frac{-(\Delta G^{0} + \lambda)^{2}}{4\lambda k_{B}T}\right) \tag{5.2}$$

One of the most important predictions from Marcus theory stems from the quadratic dependence of $\Delta G^{\ddagger}$ on ΔG^{0}. This shows that as the driving force of the reaction increases, the rate of reaction increases, reaching a maximum at $-\Delta G^{0} = \lambda$. However, when $-\Delta G^{0}$

$> \lambda$, the rate *decreases* as the driving force increases. This is called the Marcus inverted region and is represented graphically in Figure 5.13. Experimental evidence of the inverted region would not be found until about 20 years after it was first postulated by Marcus.[219,220]

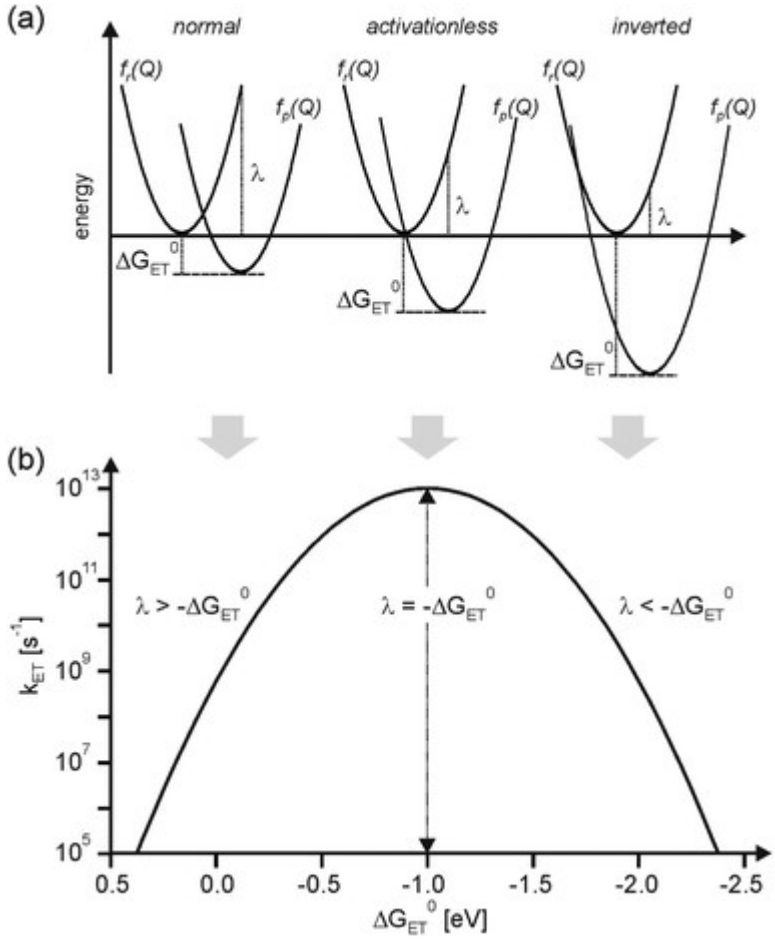

Figure 5.13: *a) Reactant and product energy wells for three different scenarios, and b) The dependence of the rate of reaction for an electron transfer process on reaction free energy (ΔG^0), reproduced from reference 221*

As mentioned above, the reorganizational energy, λ, has a component accounting for polarisation changes in the dielectric solvent environment. The equation to calculate λ, which we will not go into in detail here, shows that the maximum rate of reaction occurs when the free energy change of the reaction equals the sum of the solvent and vibrational reorganisation energies.[220] As a result of this dependence of λ on the solvent environment, some notable differences in reaction rates have been observed in different solvents. Work by Closs *et al.* showed that on decreasing the polarity of the solvent in the

intramolecular electron transfer reactions of a series of compounds, the maximum rate of reaction occurred at increasingly less negative free energies of reaction.[220] This effectively shifts the maxima of the curve in Figure 5.13(b) to the left.

Advances in DFT calculations mean that by calculating the vertical energy gap between excited states of interest a Marcus-type parabola can be constructed.[222] These calculations can also help us estimate $\Delta G^{\ddagger}$, ΔG^{0}, λ and the electron transfer rate.[223] In this work, Marcus theory has been used to construct Marcus type parabolas to help describe different reactivity in different solvents.

5.2 Aims

The affect of temperature on photophysical reactions has been documented in several studies, some of which we have described in the Introduction. We have also described the reactions of $[Re(CO)_4(bpy)][PF_6]$, where recent work in our group has revealed reactivity which had not previously been described in the literature. However, as yet, the temperature dependence of this reaction remains unstudied.

Thus, the aims of this chapter are as follows:

(i) To study the reactions of $[Re(CO)_4(bpy)][PF_6]$ in dichloromethane and acetonitrile at varying temperatures to determine the effect of temperature on the photophysics of these reactions.

(ii) Use density functional theory calculations to help interpret experimental observations.

5.3 Results

5.3.1 Temperature Dependent TRIR Studies of $[Re(CO)_4(bpy)][PF_6]$ in Dichloromethane

First, the ns-TRIR of $[Re(CO)_4(bpy)][PF_6]$ in dichloromethane at 355 nm excitation was investigated at room temperature to repeat previous work. The results are shown in Figure 5.14. After 10 ns there are five new peaks in the spectrum at 2113, 2062, 2039, 2017 and 1984 cm^{-1}, alongside a bleach of the parent bands.

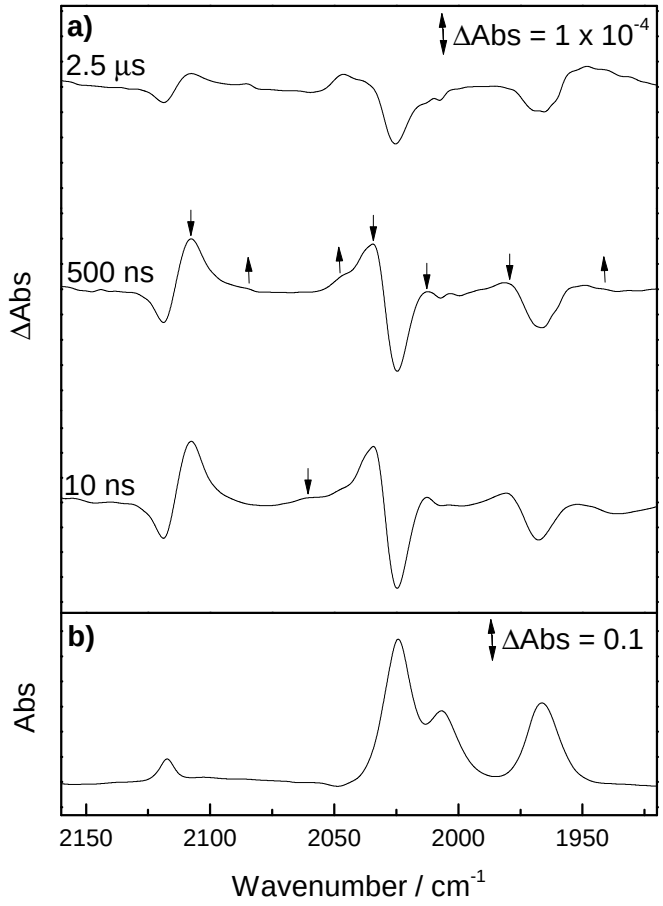

Figure 5.14: *a) ns-TRIR difference spectra at selected time delays for the 355 nm photolysis of $[Re(CO)_4(bpy)][PF_6]$ in dichloromethane and b) Ground state FTIR spectrum of $[Re(CO)_4(bpy)][PF_6]$ in dichloromethane*

These are assigned to two different species, with the peak at 2062 cm^{-1} decaying with a different rate to the remaining four peaks. This peak at 2062 cm^{-1} is assigned to 'State

I', first observed in previous work in our group. This state has previously been assigned as a ^{3}ILCT/MLCT excited state with emissive character. The second photoproduct with peaks at 2113, 2039, 2017 and 1984 cm^{-1} is also a mixed ^{3}ILCT/MLCT state, also seen in previous works. These four peaks decay by the end of the experiment with the growth of three peaks at 2091, 2052 and 1948 cm^{-1}. The final photoproduct is assigned to the CO loss photoproduct $Re(CO)_3(bpy)(CH_2Cl_2)$.

The single point kinetics of the intermediate species and photoproduct were analysed; however, it is important to note that these values are not particularly reliable because many of the excited state species peaks are overlapping and there may be complex behaviour between the excited states. We think it is important to discuss them; however, as there are some differences between the kinetics in dichloromethane and in acetonitrile, as will become clear later in the Chapter. The 'State I' kinetics were analysed from its sole peak at 2062 cm^{-1} and are shown in Figure 5.15. The decay of this peak could be fitted to a bi-exponential decay, with τ_1 = 41.8 ± 27.5 ns and τ_2 = 298 ± 173 ns. Note the large errors in these values.

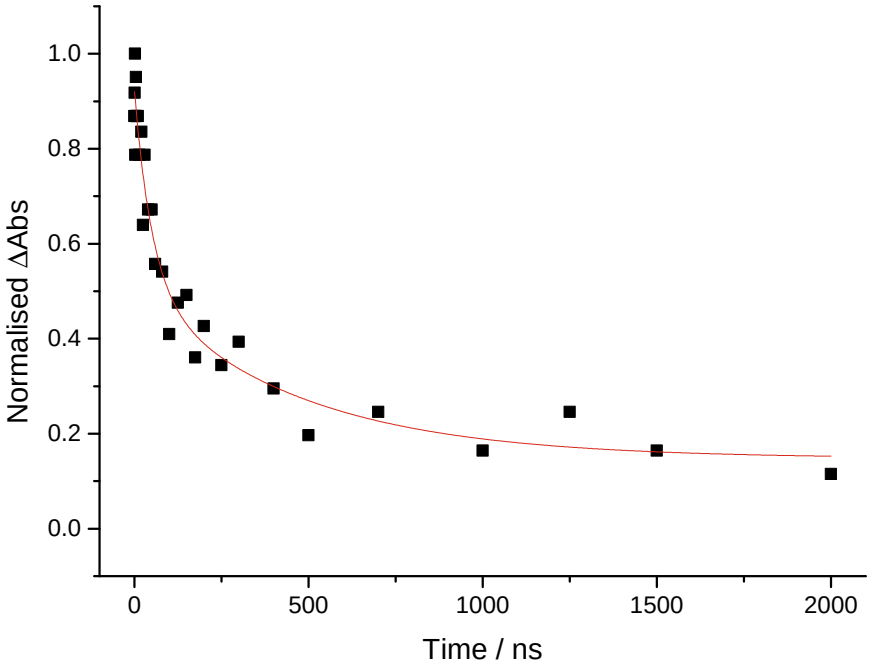

Figure 5.15: *Normalised TRIR kinetic traces for the decay of 'State I' at 2062 cm^{-1} (τ_1 = 41.8 ± 27.5 ns, τ_2 = 298 ± 173 ns) following 355 nm photolysis of [Re(CO)$_4$(bpy)][PF$_6$] in dichloromethane*

The bi-exponential decay of this peak could be due to many reasons; there could be two species present at this peak, which is not unexpected given that several excited states can form after photolysis. A second reason for this decay could be that 'State I' is decaying to form two different species, again, equally likely due to the nature of these excited states. Additionally, there could be another excited state decaying to form State I, which in turn decays back to the ground state, resulting in the apparent biexponential decay.

Kinetic analysis of 'State II' was taken from the peak at 2113 cm^{-1} due to it not overlapping with any other peaks and its strong absorbance. The decay could be fitted to a mono-exponential and also a bi-exponential with excellent fitting (0.999 R^2 values for both fittings). The lifetime for the mono-exponential decay is calculated to be 2.42 ± 41.2 µs, the bi-exponential decay gives values of τ_1 = 815 ± 579 ns and τ_2 = 2.78 ± 0.32 µs. Analysis of the other peaks assigned to 'State II' at 2039 and 1984 cm^{-1} fit better to a mono-exponential decay, agreeing with the value of 2.42 µs. Therefore, we conclude that the mono-exponential gives a better fit. It is possible that there are two different species present at the peak at 2113 cm^{-1} causing this apparent bi-exponential decay.

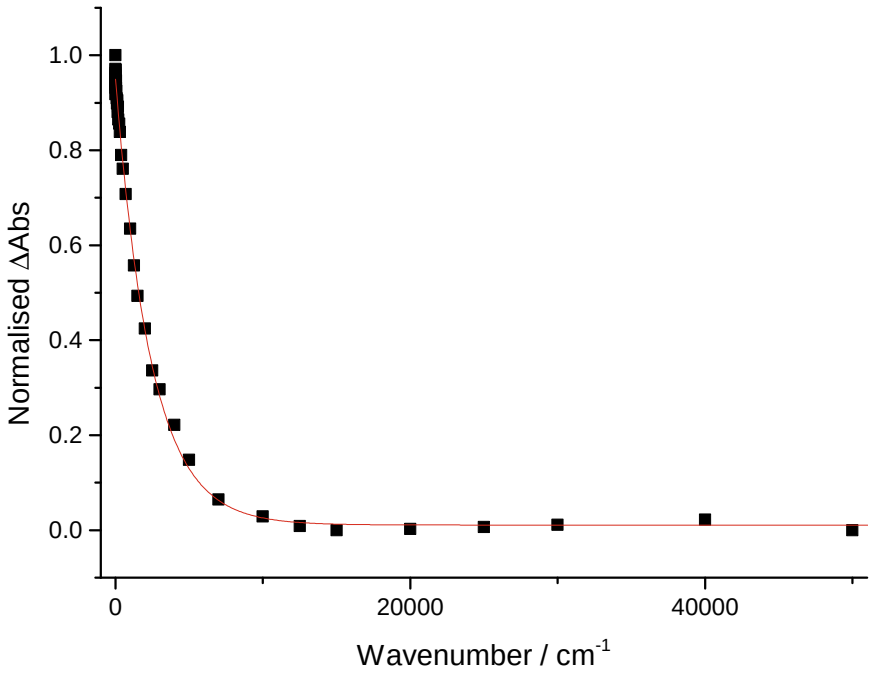

Figure 5.16: *Normalised TRIR kinetic traces for the decay of 'State II' at 2113 cm^{-1} (τ = 2.42 ± 41.2 µs) following 355 nm photolysis of [Re(CO)$_4$(bpy)][PF_6] in dichloromethane*

The kinetics of the formation of the photoproduct were analysed from the peak at 1948 cm^{-1}, again, due to it not overlapping with other peaks and its strong absorbance. The kinetics are shown in Figure 5.17. The growth could be fitted to a standard mono-exponential growth, with a lifetime of 1.37 ± 0.78 μs. This does not match the decay of 'State II' nor 'State I'. In previous work, the decay of 'State II' was found to match the growth of the photoproduct. We have not found this to be true here from analysis of the single point kinetics; however, these kinetics are very complex due to the presence of several excited states with overlapping bands. It is entirely possible there may be other excited state(s), different to both the observed 'State I' and 'State II', complicating analysis.

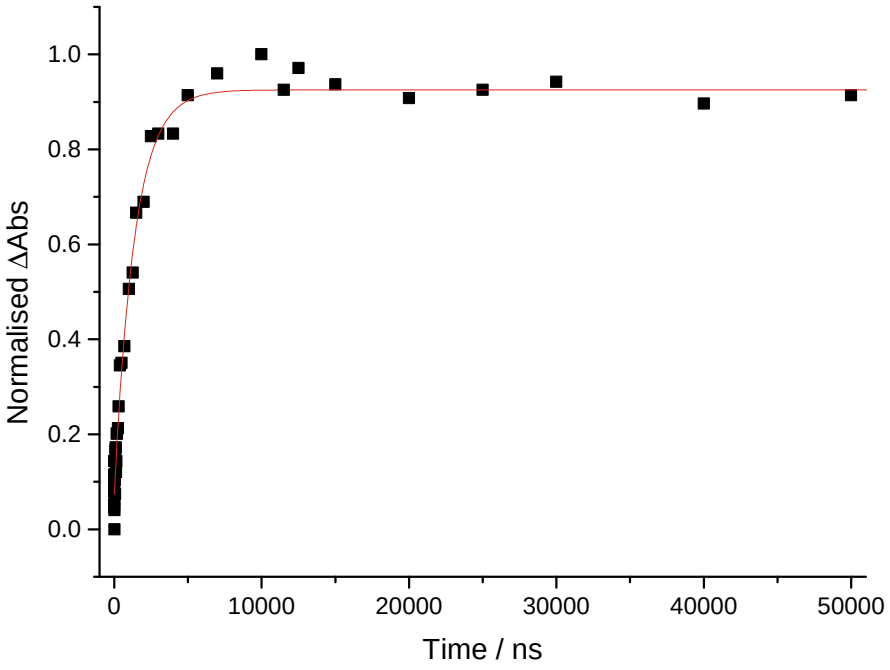

Figure 5.17: *Normalised TRIR kinetic traces for the formation of the photoproduct at 1948 cm^{-1} (τ = 1.37 ± 0.78 μs) following 355 nm photolysis of [Re(CO)$_4$(bpy)][PF$_6$] in dichloromethane*

The results from the analysis of single point kinetics are summarised in Table 5.1.

Global analysis was undertaken to distinguish between the two observed excited states, as the bands are overlapping. The results of this are shown in Figure 5.18, showing the individual calculated excited state spectra for the three species observed following

Table 5.1: Values for the lifetimes of decay of 'State I', 'State II' and for the growth of the photoproduct (in μs) under ambient conditions for the reaction of $[Re(CO)_4(bpy)][PF_6]$ in dichloromethane

		Lifetime / μs		
Species	Wavenumber / cm^{-1}	τ_{dec1}	τ_{dec2}	τ_{gro}
'State I'	2062	0.04	0.30	-
'State II'	2113, 2039, 2017, 1984	2.42	-	-
Photoproduct	2091, 2052, 1948	-	-	1.37

photolysis. State I is shown in black, State II is shown in red and the CO loss photoproduct is shown in blue.

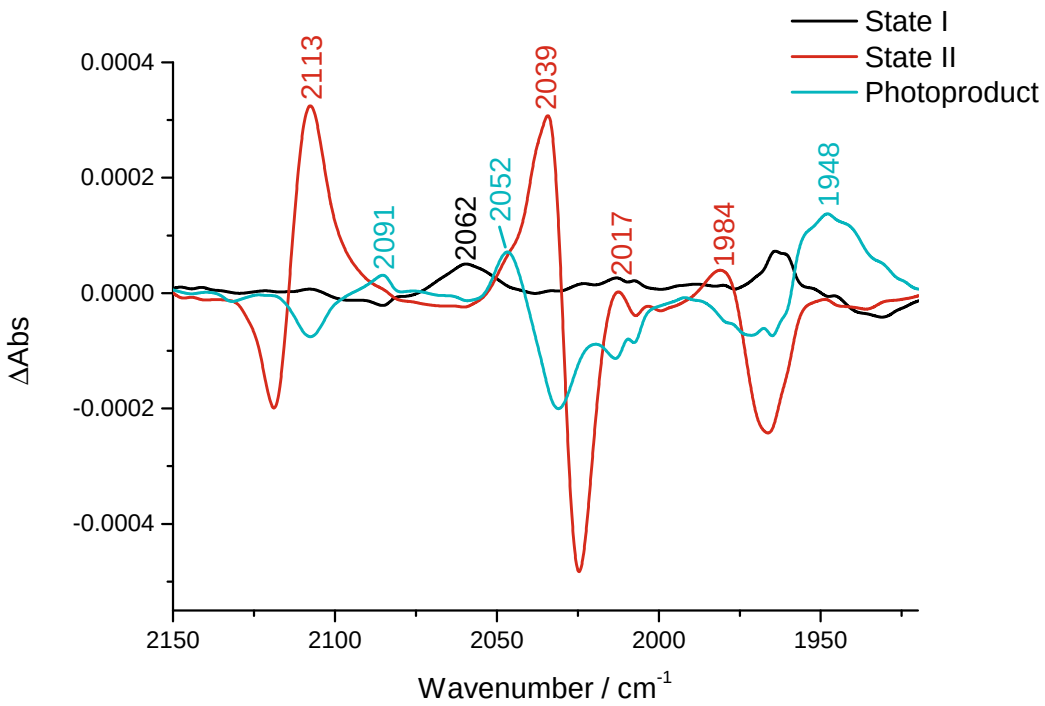

Figure 5.18: *Excited state spectra generated from global analysis following 355 nm photolysis of $[Re(CO)_4(bpy)][PF_6]$ in dichloromethane*

Global analysis was also used to deduce the kinetics of these excited states, and the kinetic traces calculated by global analysis are shown in Figure 5.19. State I is short lived, with a lifetime of 197 ns. State II decays concurrently with the growth of the CO loss

photoproduct (τ = 2.42 μs). This is in good agreement with previous work, which found a lifetime of 100 ± 10 ns for State I and a lifetime of 2.9 ± 0.3 μs for the decay of State II and the growth of the final photoproduct. It is also in general in good agreement with single point kinetic lifetimes.

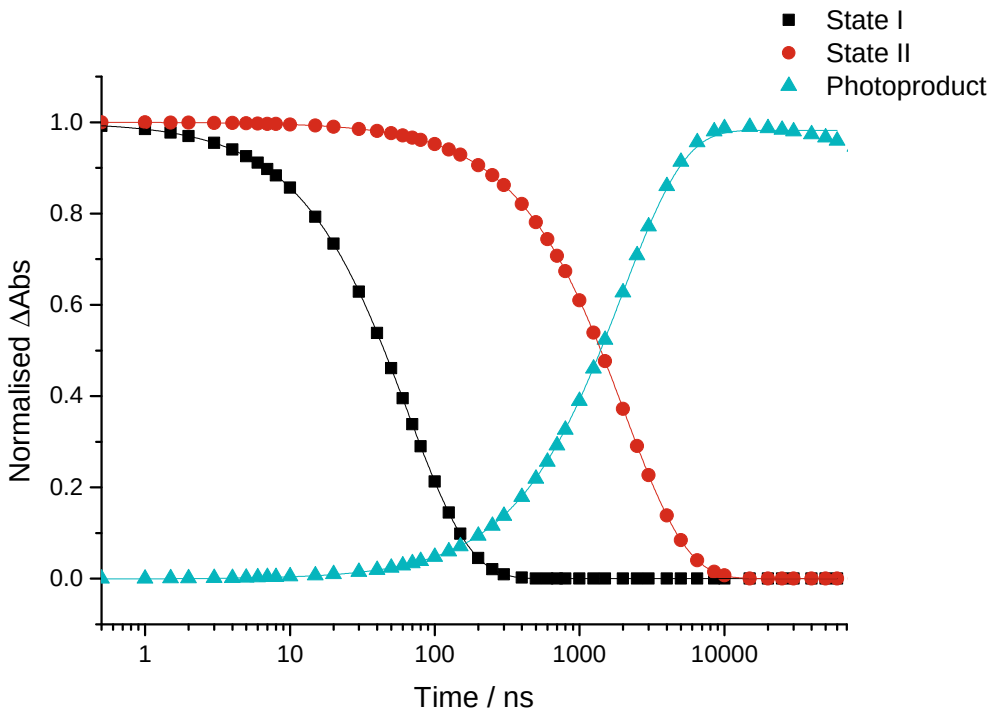

Figure 5.19: *Normalised excited state kinetics generated from global analysis following 355 nm photolysis of [Re(CO)$_4$(bpy)][PF$_6$] in dichloromethane, showing the decay of State I (black) (τ = 197 ns) and the concurrent decay and growth of State II (red) and the photoproduct (blue) (τ = 2.42 μs)*

The ns-TRIR at varying temperatures was then undertaken to see the effect of temperature on formation of the excited states. The ns-TRIR was measured in five degree intervals from 5 to 35 °C and results from selected temperatures are shown in Figure 5.20. At all temperatures, the same photoproducts were observed, namely State I at 2062 cm^{-1}, State II at 2113. 2039, 2017 and 1984 cm^{-1}, and the CO loss photoproduct at 2091, 2052 and 1948 cm^{-1}. There were no new peaks observed at low or high temperature. Analysis of the single point kinetics shows no dependence on temperature for either the decay of State I, State II or the growth of the photoproduct, see Table 5.2. However, if the data at 15 °C is discounted as an outlier, the decay of State II does appear to decrease with an increase

in temperature.

Table 5.2: Values for the lifetimes of decay of 'State I', 'State II' and for the growth of the photoproduct (in μs) at varying temperatures for the reaction of $[Re(CO)_4(bpy)][PF_6]$ in dichloromethane

Temperature / °C	Lifetime / μs			
	Decay of State I		Decay of State II	Growth of Photoproduct
	τ_1	τ_2		
5	0.06	0.86	3.16	1.20
10	0.08	0.87	2.90	1.47
15	0.17	1.13	3.33	1.47
20	0.04	0.40	2.52	1.01
25	0.04	0.30	2.42	1.33
30	0.09	0.62	2.21	1.06
35	0.03	0.55	2.05	0.92

A visual inspection of the spectra shows that at the highest temperature (35 °C) there may be an increased production of the photoproduct, based on an increased absorbance; however, there is little difference between 5 and 20 °C, Figure 5.20.

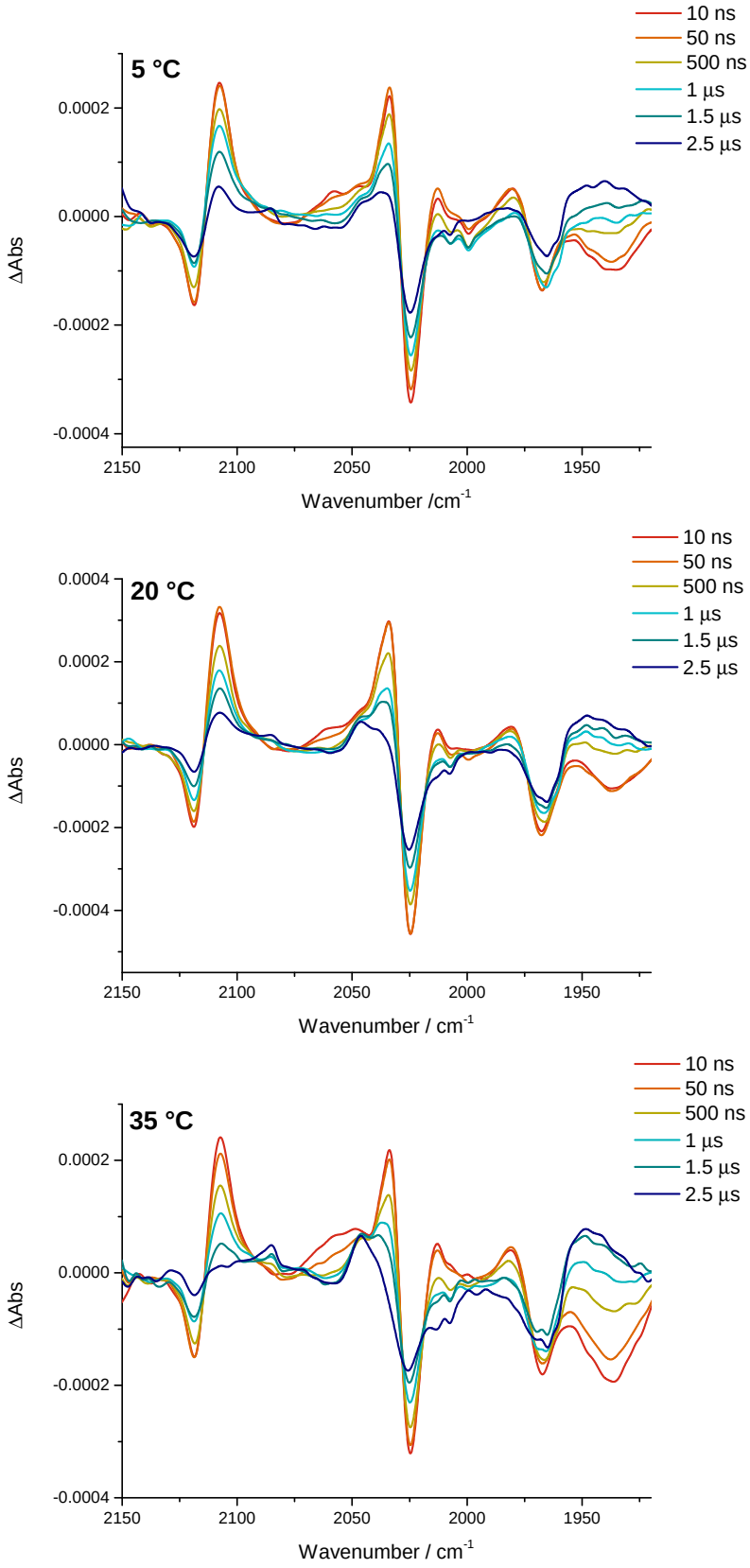

Figure 5.20: *ns-TRIR difference spectra at selected time delays for the 355 nm photolysis of [Re(CO)$_4$(bpy)][PF$_6$] in dichloromethane at 5 degrees (top left), 20 degrees (top right) and 35 degrees (bottom)*

Upon kinetic analysis of the photoproduct peak at 1943 cm^{-1}, there is indeed increased formation of photoproduct at 30 and 35 °C; however, there is no trend in the lower temperatures, Figure 5.21. Overall, there is little evidence for any change in photoproduct formation with temperature. The boiling point of dichloromethane did not allow us to increase the temperature further.

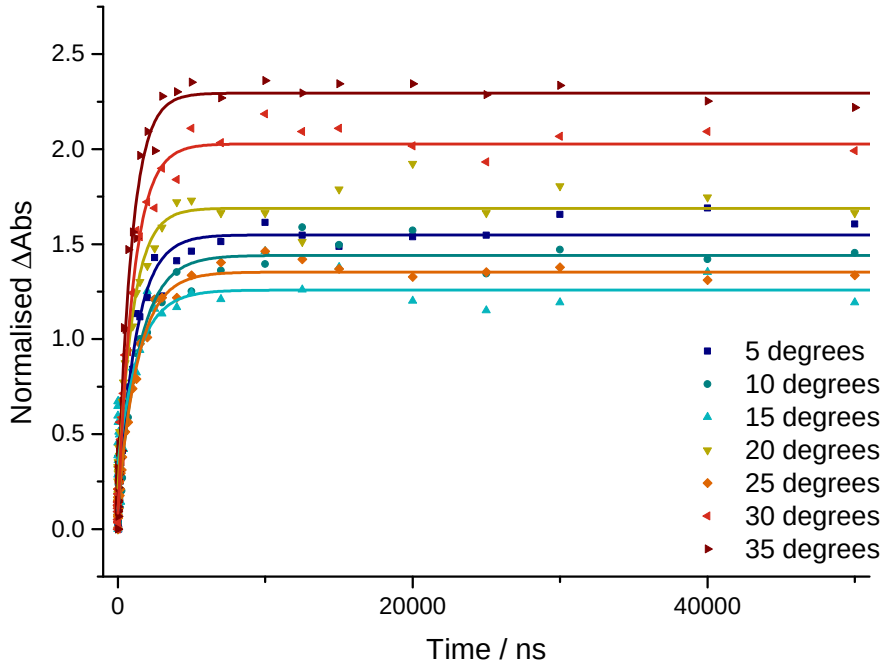

Figure 5.21: *Normalised kinetic traces from the growth of the photoproduct peak at 1943 cm^{-1} at varying temperatures following 355 nm photolysis of $Re(CO)_4(bpy)$ in dichloromethane*

Figure 5.22 shows the kinetics of the reformation of the parent band at 2030 cm^{-1}. As the temperature increases, there is no real trend in reformation of the parent band. If there was an increase in photoproduct production, then we might expect to see a decrease in the reformation of the parent species. This data supports the observation of no increase in photoproduct formation. There might be minor evidence to suggest that as the temperature increases, the parent reformation decreases; however, we cannot say this with any real certainty as the change in absorbance between temperatures is too little.

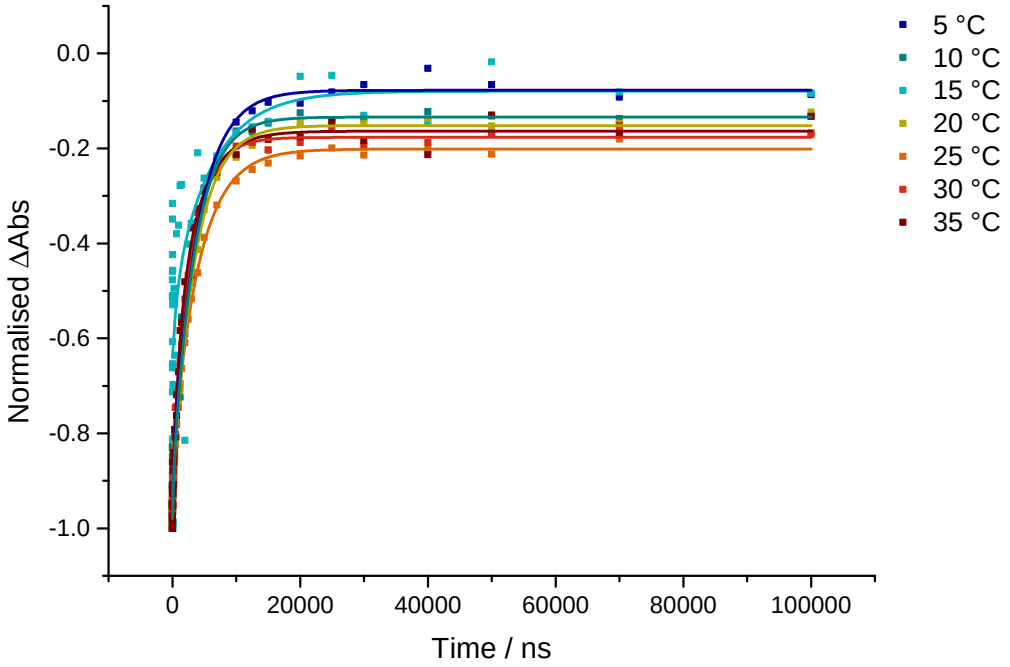

Figure 5.22: *Proposed Jablonski diagram for the photochemical and photophysical reactions of [Re(CO)$_4$(bpy)][PF$_6$] following excitation at 355 nm, reproduced from reference 212*

Global analysis was again used to deconvolute the excited state spectra at all temperatures. Global analysis showed the production of two excited states at all temperatures and the final photoproduct peaks. The lifetimes of the photoproduct formation analysed by global analysis, as with the single point kinetics, do not show any trends with temperature, and therefore will not be discussed in any further detail here.

Upon an increase in temperature upon photolysis of [Re(CO)$_4$(bpy)][PF$_6$] in dichloromethane, there is little evidence of an increase in photoproduct production. In addition, the lifetimes of decay of State I and State II show no dependence on temperature, and indeed, neither does lifetime of the growth of the photoproduct.

5.3.2 Temperature Dependent TRIR Studies of $[Re(CO)_4(bpy)][PF_6]$ in Acetonitrile

We continued with the ns-TRIR of $[Re(CO)_4(bpy)][PF_6]$ in acetonitrile at room temperature to, again, repeat and corroborate previous work in the group. The results are shown in Figure 5.23.

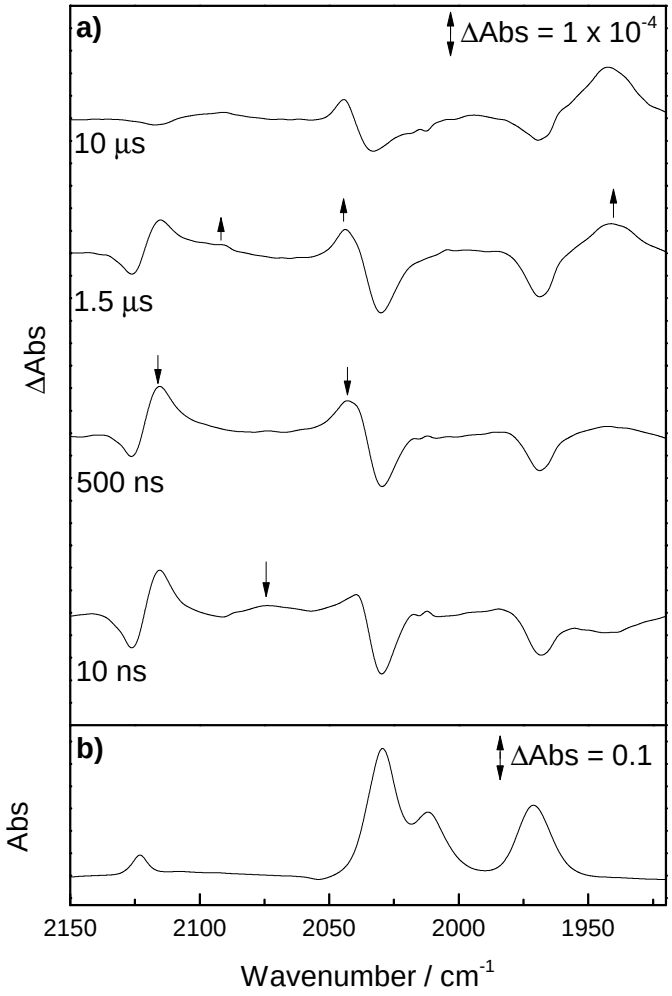

Figure 5.23: *a) ns-TRIR difference spectra at selected time delays for the 355 nm photolysis of $[Re(CO)_4(bpy)][PF_6]$ in acetonitrile at room temperature and b) Ground state FTIR spectrum of $[Re(CO)_4(bpy)][PF_6]$ in acetonitrile at room temperature*

After 10 nanoseconds, there is a small broad peak at 2071 cm^{-1}, as seen in the experiment in dichloromethane and also previous work in acetonitrile. This peak is hence assigned to State I. There are also several other peaks present in the spectrum at 10 ns;

2115, 2040, 2012 and 1983 cm^{-1}. These are assigned to the species referred to as State II, also seen in previous dichloromethane experiment and previous work in acetonitrile. By 1.5 microseconds, these peaks are starting to decay with the growth of three new peaks at 2090, 2044 and 1943 cm $^{-1}$, assigned as the photoproduct $Re(CO)_3(bpy)(CH_3CN)$, all in good agreement with previous work.

Again, the single point kinetics of the intermediates and photoproduct were analysed; however, as with the analogous experiment in dichloromethane, they may not be the true lifetimes of the excited states due to the overlapping excited state peaks. The kinetics of 'State I', taken from the decay of its only peak at 2071 cm^{-1} are shown in Figure 5.24.

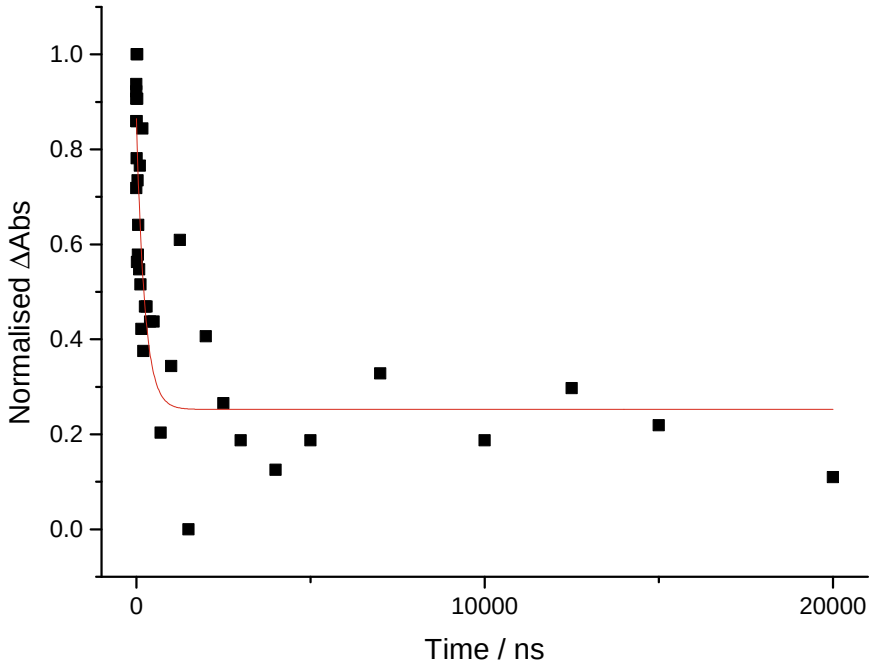

Figure 5.24: *Normalised TRIR kinetic traces for the decay of 'State I' at 2071 cm^{-1} (τ = 181 ± 62 ns) following 355 nm photolysis of $[Re(CO)_4(bpy)][PF_6]$ in acetonitrile*

The kinetics are noisy due to the weak absorbance of the peak; however, its decay can be fitted to a mono-exponential decay with τ = 181 ± 62 ns. This is in contrast to the decay of 'State I' in dichloromethane, which could only be fitted to a bi-exponential decay. We postulated that in dichloromethane, there could be another excited state present around the same peak distorting the kinetics. Since the only thing that has changed is

the solvent, it is unlikely this is the case, as another excited state would be expected to be present in acetonitrile as well. Therefore, it appears that the mechanism may be different in dichloromethane to acetonitrile. We will discuss this further later in the chapter. The lifetime for 'State I' determined here by single point kinetics, agrees well with previous work, which found a lifetime of 160 ± 30 ns for same process.

Kinetic analysis of 'State II' was, like the experiment in DCM, taken from the peak at 2115 cm^{-1} due to it not overlapping with any other peaks, and its strong absorbance. The decay is shown in Figure 5.25, giving a lifetime of 5.03 ± 0.32 μs. This does not agree well with previous work, which found a decay of 2.1 ± 0.4 μs for the decay of State II in acetonitrile. Analysis of the other peaks assigned as State II at 2038 and 2012 cm^{-1} give values of 2.64 ± 0.25 and 2.37 ± 0.31 μs, respectively. These values are in much better agreement with previous work. In the previous experiment in dichloromethane, the kinetics at 2115 cm^{-1} could be fitted to both a bi-exponential or a mono-exponential. We postulated that there may be another excited state species present that was causing this anomaly. The results here also support the presence of another excited state at 2115 cm^{-1}.

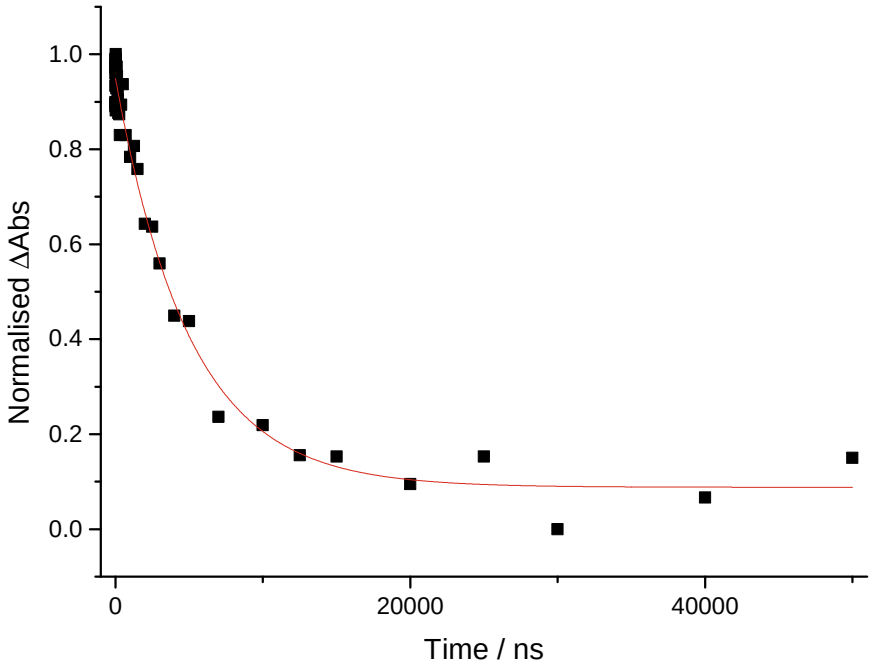

Figure 5.25: *Normalised TRIR kinetic traces for the decay of 'State II' at 2115 cm^{-1} (τ = 5.03 ± 0.32 μs) following 355 nm photolysis of [$Re(CO)_4(bpy)$][PF_6] in acetonitrile*

The kinetics of the formation of the photoproduct were analysed from the peak at 1940 cm^{-1}, again, due to it not overlapping with other peaks and its strong absorbance. The kinetics are shown in Figure 5.26. The growth could be fitted to a bi-exponential growth, with τ_1 = 528 ± 305 ns and τ_2 = 2.17 ± 0.83 µs. This is unlike the reaction in DCM, which was fitted to a standard mono-exponential. In previous work, the decay of 'State II' was found to match the growth of the photoproduct. Here the decay of 'State II' at 2115 cm^{-1} is over double the lifetime of the growth of the photoproduct. However, the kinetics of the other peaks assigned to State II (2.64 ± 0.25 and 2.37 ± 0.31 µs) are much more comparable to τ_2 (2.17 ± 0.83 µs). We think that the single point kinetics do support the formation of the photoproduct from State II. Again, these kinetics are very complex due to the presence of several excited states with overlapping bands. It is quite likely there may be other excited state(s), different to both the observed 'State I' and 'State II', complicating analysis.

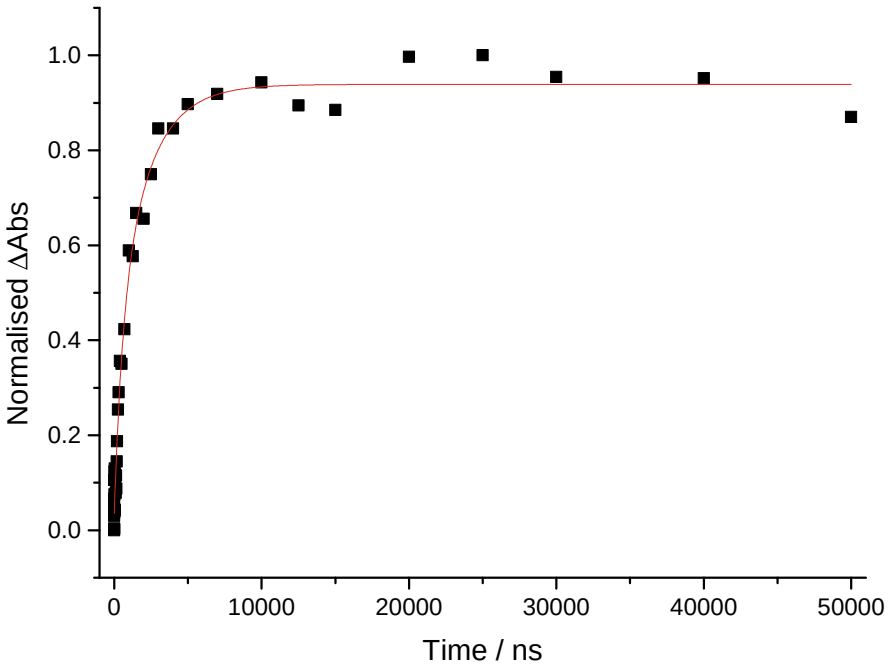

Figure 5.26: *Normalised TRIR kinetic traces for the formation of the photoproduct, $Re(CO)_3(bpy)(CH_3CN)$, at 1940 cm^{-1} ($\tau_1 = 528 \pm 305$ ns, $\tau_2 = 2.17 \pm 0.83$ µs) following 355 nm photolysis of $[Re(CO)_4(bpy)][PF_6]$ in acetonitrile*

The global analysis was again undertaken to de-convolute the excited state spectra. The

results of global analysis are shown in Figure 5.27. The results are in general agreement with previous data, showing the species 'State I' at 2071 cm^{-1} (black), 'State II' at 2115, 2040, 2012 and 1983 cm^{-1} (red) and the photoproduct $Re(CO)_3(bpy)(CH_3CN)$ at 2090, 2044 and 1943 cm^{-1} (blue).

The lifetimes of excited states were also calculated by global analysis, Figure 5.28. The lifetime of 'State I' as calculated by global analysis is 921 ns, which is in poor agreement with the single point kinetic analysis (which found $\tau = 181 \pm 62$ ns) and also with previous works. The decay of state II was seen to equal the growth of the photoproduct, with a lifetime of 5.5 μs, which again, is in poor agreement with previous work, which found a lifetime of 2.1 ± 0.4 μs. This value of 5.5 μs however, shows better agreement with the single point kinetics (5.1 ± 0.3 μs) analysed at the peak at 2115 cm^{-1}.

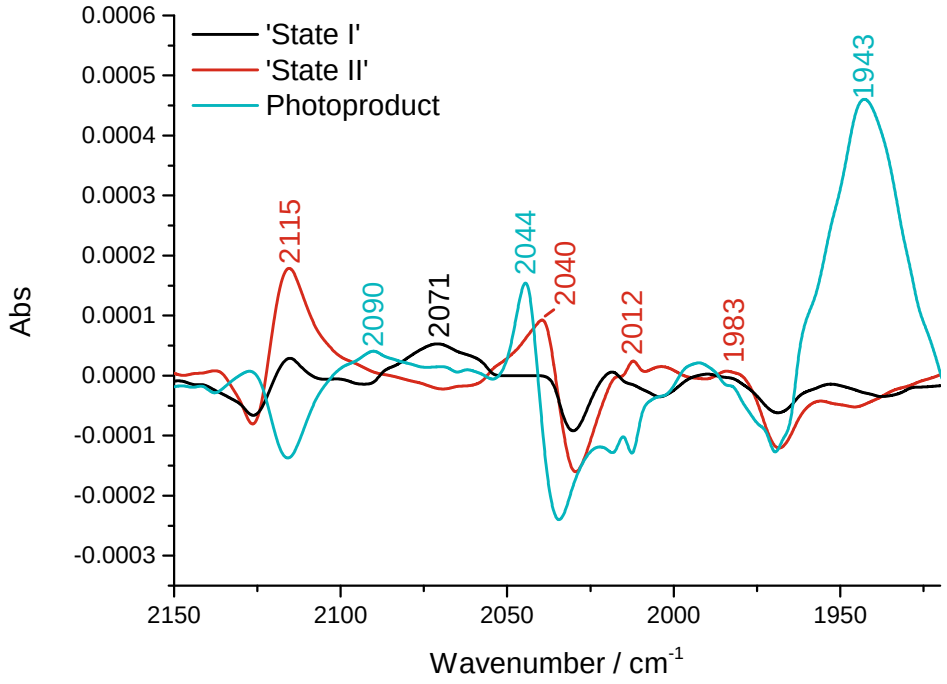

Figure 5.27: *Excited state spectra generated from global analysis following 355 nm photolysis of $[Re(CO)_4(bpy)][PF_6]$ in acetonitrile*

Overall, the peak locations derived from global analysis agree with previous results; however, the calculated lifetimes do not, and moreover do not agree with the single point kinetic data. Many different kinetic models were tested during global analysis, with

many different reaction pathways tested, but all gave largely similar results. We think that there may be a more complex mechanism occurring which is beyond the scope of our modelling software. Analysis of the single point kinetic data has shown that the mechanism appears different in dichloromethane and acetonitrile. This would support our hypothesis. Without using a better kinetic modelling software, we cannot draw definite conclusions on the reaction mechanism from this data.

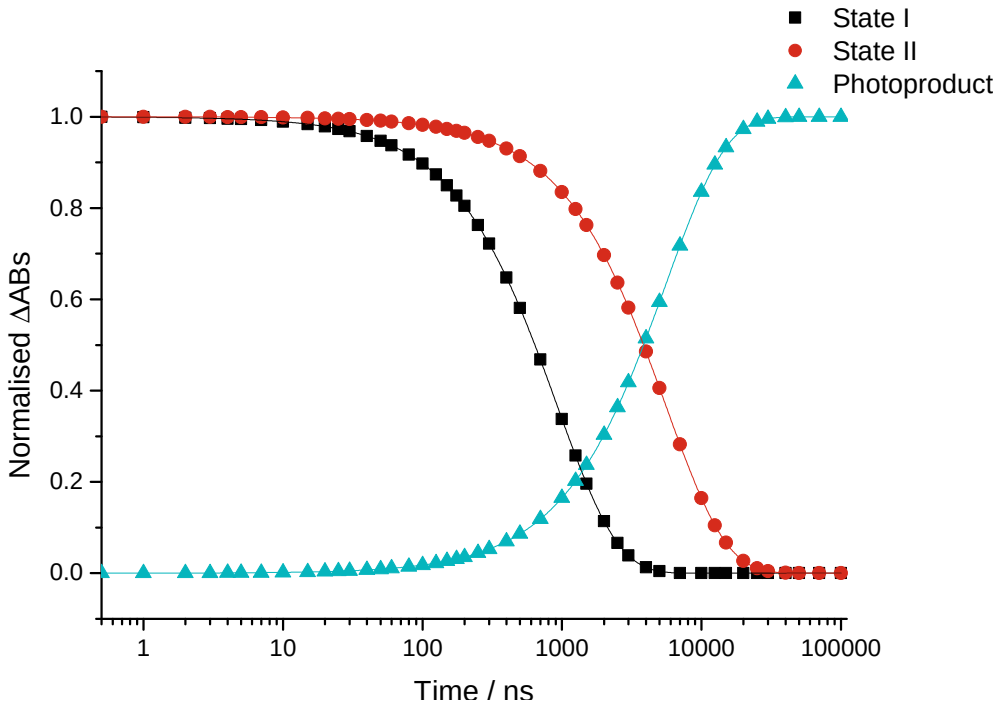

Figure 5.28: *Normalised excited state kinetics generated from global analysis following 355 nm photolysis of [Re(CO)$_4$(bpy)][PF$_6$] in acetonitrile, showing the decay of State I (black) (τ = 921 ns), and the concurrent decay and growth of State II (red) and the photoproduct (blue) (τ = 5.5 μs)*

The affect of temperature on the reaction of [Re(CO)$_4$(bpy)][PF$_6$] in acetonitrile was studied by conducting the ns-TRIR at intervals of 10 degrees between 15 and 55 °C. The higher boiling point of acetonitrile allowed for a broader temperature range than that of the dichloromethane experiment. The results from selected temperatures are shown in Figure 5.29. Compared to the dichloromethane experiment, there is a much clearer increase in photoproduct production at higher temperatures, on consideration of the relative absorbance of the photoproduct peaks. This growth in height with temperature is shown in Figure 5.30.

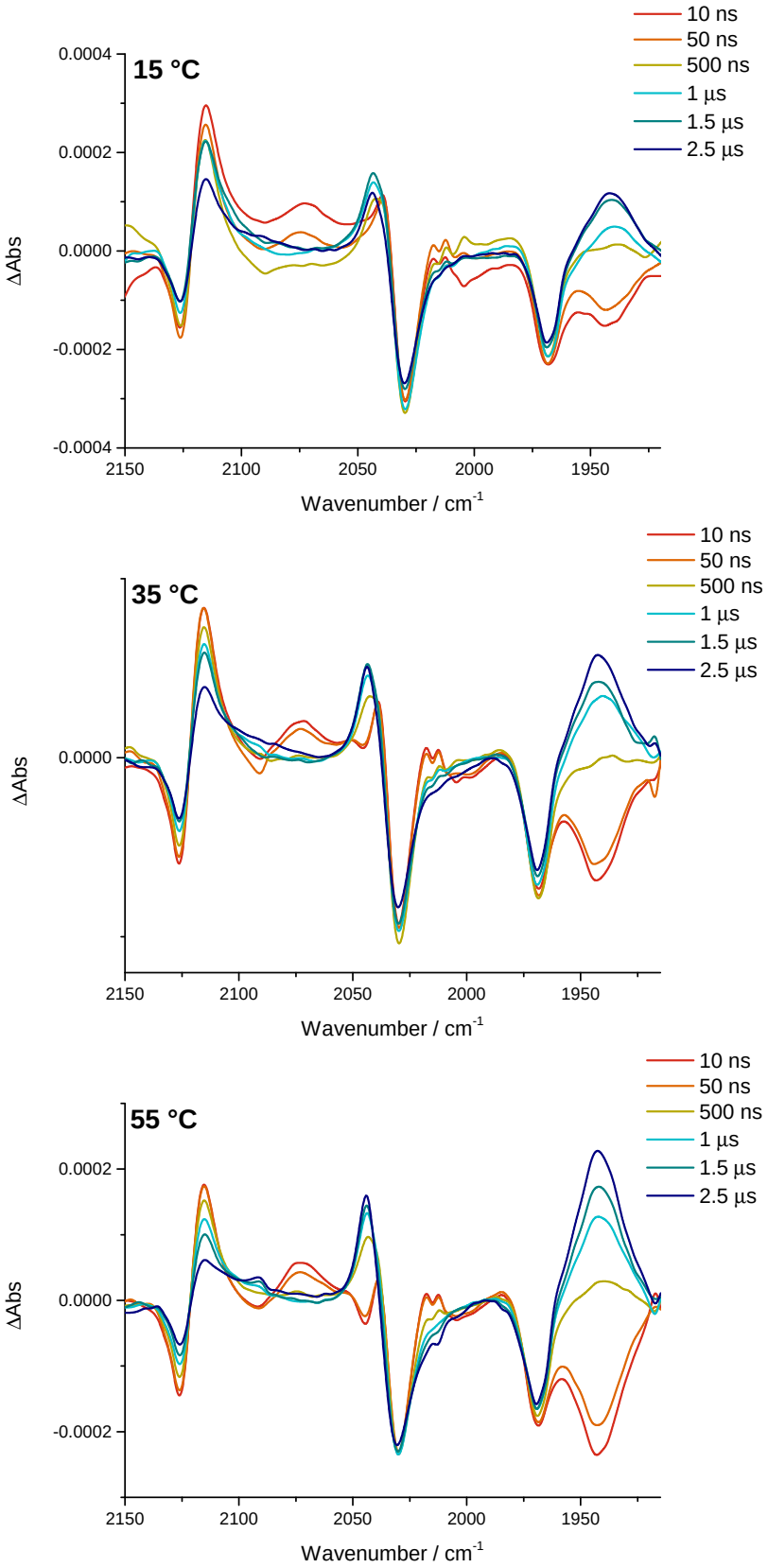

Figure 5.29: *ns-TRIR difference spectra at selected time delays for the 355 nm photolysis of [Re(CO)$_4$(bpy)][PF$_6$] in acetonitrile at 15 degrees (top), 35 degrees (middle) and 55 degrees (bottom)*

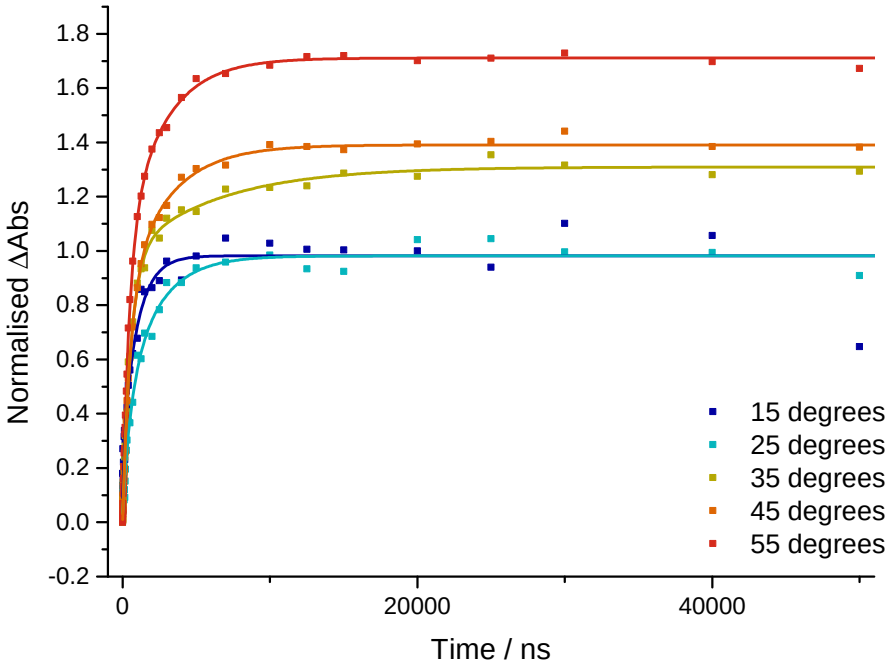

Figure 5.30: *Normalised kinetic traces from the growth of the photoproduct peak at 1943 cm^{-1} at varying temperatures following 355 nm photolysis of $Re(CO)_4(bpy)$ in acetonitrile*

We analysed the reaction kinetics by global analysis; however, as with the room temperature experiment, the lifetimes, particularly of 'State I' did not show good agreement with the single point kinetics. Therefore, we have only analysed the single point kinetic data for these experiments. These values for the lifetime of decay of 'State I' and 'State II' and the growth of the photoproduct at different temperatures are shown in Table 5.3. There are a few clear trends, in contrast to the dichloromethane data, which displayed no clear trend in lifetimes. The lifetime of decay of 'State I' increases with temperature, with the shortest lifetime at 15 °C (130 ± 64 ns) and the longest at 55 °C (326 ± 53 ns). The lifetime of decay of 'State II' decreases with temperature, with the shortest lifetime at 55 °C (2.97 ± 0.11 μs) and the longest at 15 °C (5.71 ± 0.52 μs). The growth of the photoproduct appears to have no trend with temperature.

This increase in lifetime of State I with temperature is very interesting. This is contradictory to what we found with the analogous reaction in dichloromethane, where

Table 5.3: Values for the lifetimes of decay of 'State I', 'State II' and for the growth of the photoproduct (in μs) at varying temperatures for the reaction of $[Re(CO)_4(bpy)][PF_6]$ in acetonitrile

Temperature / °C	Lifetime / μs			
	Decay of State I	Decay of State II	Growth of Photoproduct	
			τ_1	τ_2
15	0.13	5.71	0.09	0.92
25	0.18	5.03	0.54	2.17
35	0.20	4.26	0.56	6.12
45	0.25	3.68	0.50	2.82
55	0.34	2.97	0.45	2.61

there was no discernable trend. This could suggest that there is a competing process, one that is longer lived but becomes more favourable at higher temperatures, i.e., a transfer from State I to another state. This may be to State II or a different excited state.

Figure 5.31 shows the kinetics of the reformation of the parent band at 2030 cm^{-1}. As the temperature increases, the reformation of the parent band decreases, complimenting the observation of an increase in the photoproduct formation. The decay of State I has previously been found to decay to the parent state.[121] This observation of decreased reformation of the parent supports our hypothesis that there is a transfer from State I to another state. An increased transfer from State I to another state would decrease the parent reformation pathway from State I and and increase the photoproduct formation pathway from the other state, both of which have been observed in the variable temperature ns-TRIR experiments.

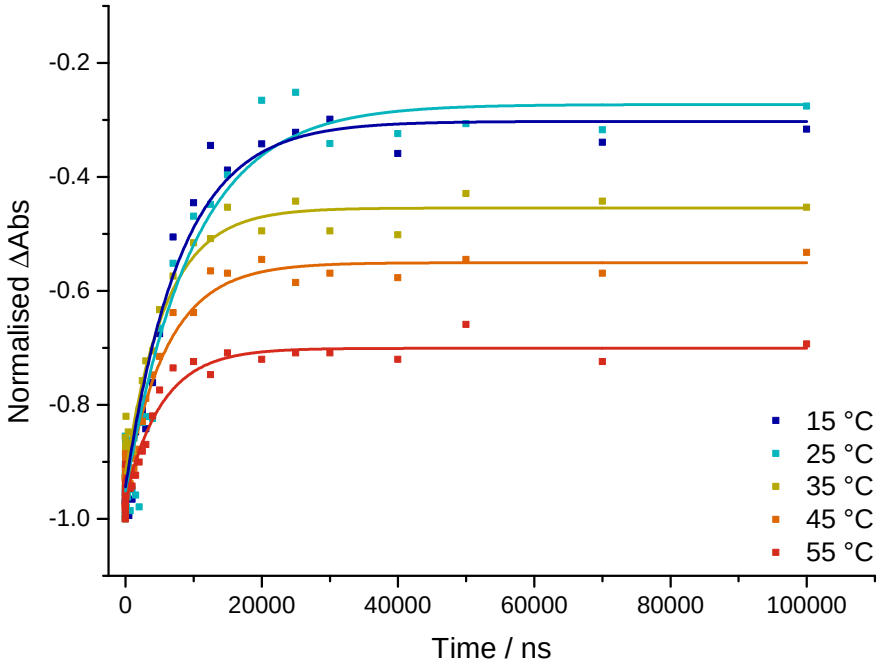

Figure 5.31: *Normalised kinetic traces at different temperatures for the reformation of the parent band at 2030 cm* $^{-1}$

It is much clearer that, in acetonitrile, in comparison to dichloromethane, the increase in temperature leads to an increased production of photoproduct and a decrease in the lifetime of formation of the photoproduct.

If we take a look at the proposed Jablonski diagram for this reaction, shown in Figure 5.32, the photoproduct is proposed to be made from the mixed ^{3}ILCT/MLCT state ('State II'). The variable temperature TRIR results suggest that for dichloromethane, the ^{3}ILCT/MLCT is not thermally accessible from State I, due to the lack of increase in photoproduct at elevated temperatures. Additionally there is little evidence for any decrease or increase in the excited state lifetimes. However, in acetonitrile, variable temperature TRIR results do suggest that the ^{3}ILCT/MLCT is thermally accessible from State I, due to increase in photoproduct production at elevated temperatures, alongside a decrease in the reformation of the parent. Furthermore, the lifetime of State I increases with temperature, indicating a separate process, i.e., a transfer from State I to the ^{3}ILCT/MLCT.

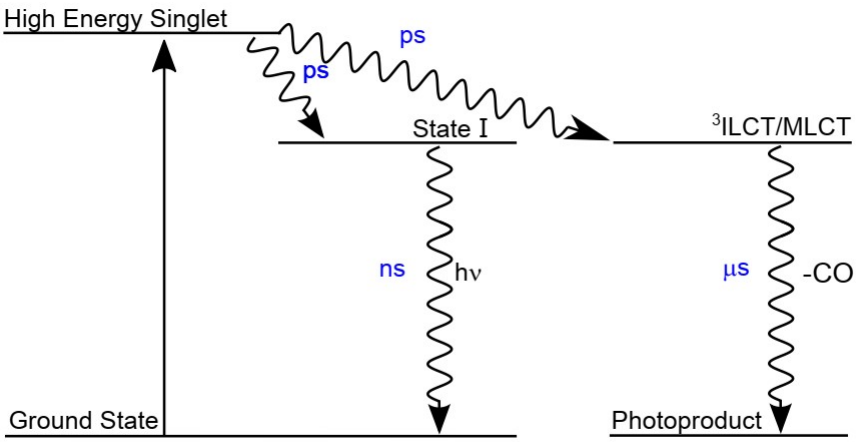

Figure 5.32: *Proposed Jablonski diagram for the photochemical and photophysical reactions of [Re(CO)$_4$(bpy)][PF$_6$] following excitation at 355 nm, reproduced from reference 212*

5.3.3 Preliminary Temperature Dependent Emission Studies

Preliminary emission measurements at varying temperatures were performed by Dr Katherine Reynolds at The University of Nottingham for the reaction of [Re(CO)$_4$][PF$_6$] in both dichloromethane and acetonitrile at 355 nm excitation. The results for dichloromethane are shown in Figure 5.33. This emission spectrum has been assigned in previous works,[121,212] with the strong vibronic character at 449 and 479 nm, along with the broader, structureless region at lower energy (*ca.* 507 nm) consistent with a mixed ^{3}ILCT/^{3}MLCT state. The emission clearly decreases as the temperature increases. There is little to no change in the shape of the emission spectra upon a change in temperature, implying that there is no increased production of any other state. This agrees with the temperature dependent TRIR results.

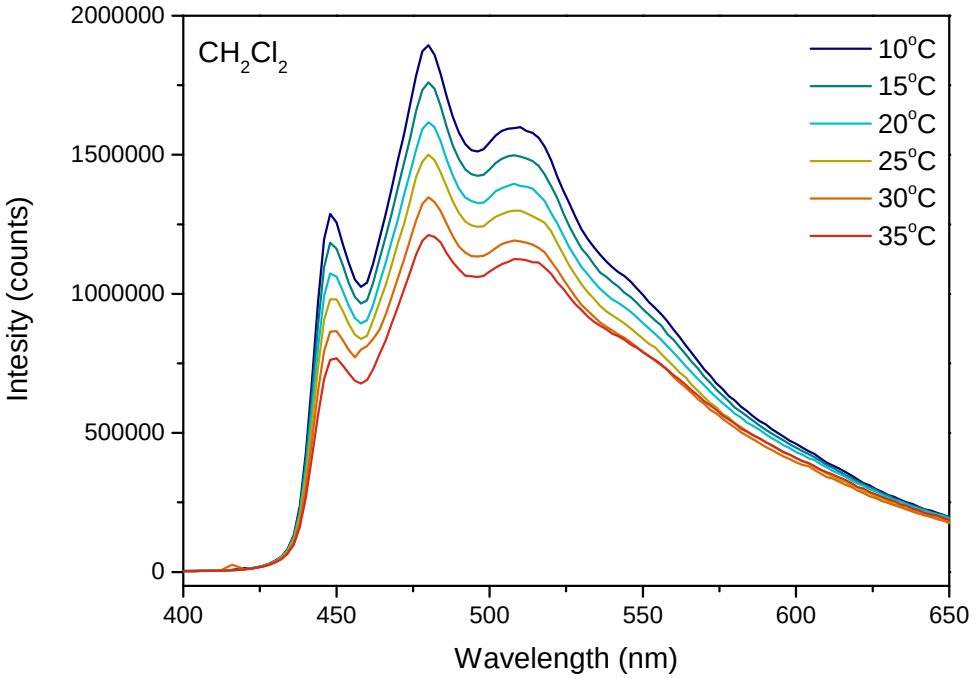

Figure 5.33: *The emission spectra of [Re(CO)$_4$(bpy)][PF$_6$] in dichloromethane at varying temperatures following 355 nm excitation*

The results in acetonitrile are shown in Figure 5.34. At lower temperatures, the emission is similar to the emission seen in dichloromethane and in previous works in acetonitrile, i.e., strong vibronic character at 449 and 479 nm, with a broader, structureless region at lower energy (*ca.* 507 nm) consistent with a mixed ^{3}ILCT/^{3}MLCT state. As the temperature increases, however, there appears to be change in the shape of the emission spectra. The spectra exhibit increasing ^{3}MLCT character, as shown by the broadening of the spectra and the centring of emission around 550 nm. The strong vibronic character at 449 and 479 nm associated with the ^{3}ILCT appears to weaken. This change would support observations of increased production of the photoproduct, as the photoproduct is produced from the MLCT state. The intensity of the emission also decreases as the temperature increases, as it did in dichloromethane.

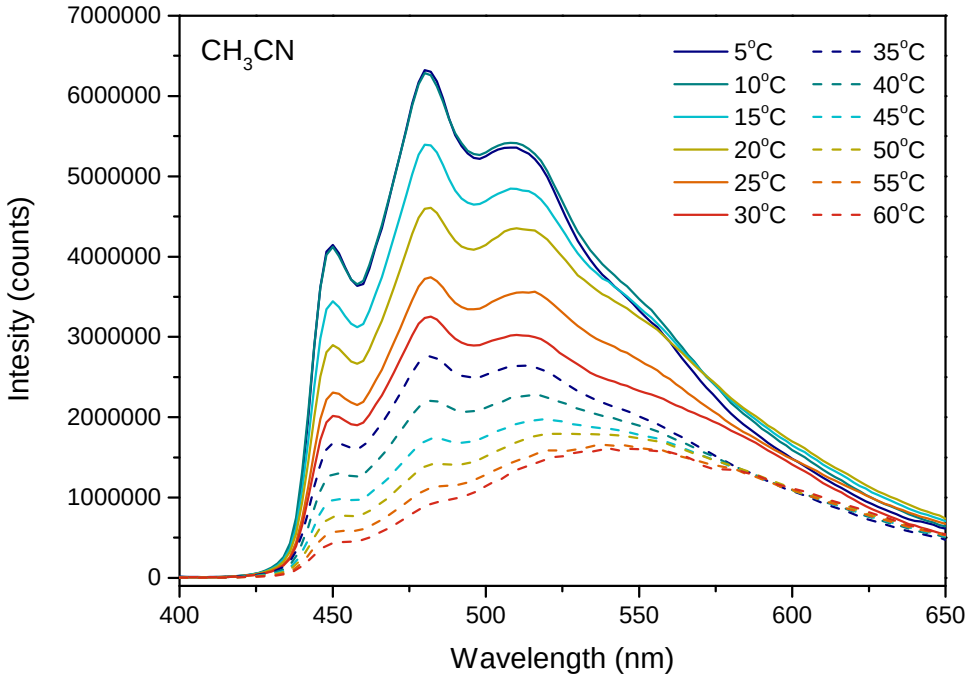

Figure 5.34: *The emission spectra of [Re(CO)$_4$(bpy)][PF$_6$] in acetonitrile at varying temperature following 355 nm excitation*

5.3.4 Density Functional Theory Results

To support and explain the experimental results, high level DFT calculations were performed by Mr Alexander Schwab and Dr Stephan Kupfer from Friedrich Schiller University, Jena. These sophisticated calculations have shown a complex interplay between states, and we have focussed validating our experimental results with their advanced calculations rather than attempting to elucidate the full reaction mechanism from their results.

Figure 5.36 shows the calculated vertical excitation energies of [Re(CO)$_4$(bpy)][PF$_6$] in dichloromethane. Calculation reveal two emissive states (T(ILCT$_1$) and T(ILCT$_2$)) and two MCLT states; T(MLCT$_1$) and T(MLCT$_2$), where T stands for triplet. Figure 5.37 shows the calculated vertical excitation energies of [Re(CO)$_4$(bpy)][PF$_6$] in acetonitrile. Again, there are two emissive states (T(ILCT$_1$) and T(ILCT$_2$)) and two MLCT states; T(MLCT$_1$) and T(MLCT$_2$). Both T(ILCT$_1$) and T(ILCT$_2$) are calculated to be emissive.

In both dichloromethane and acetonitrile, the T(ILCT$_1$) is calculated to have the same

geometry and electronic character, which is calculated to be ~3 % MLCT character, in excellent agreement with the work of Strouse *et al.*, who identified the lowest lying electronic state by using low temperature single crystal absorption to have 1–3 % MLCT character.[210] However, there are differences in the two calculated MLCT states between the two solvents, Figure 5.35. In dichloromethane, $MLCT_1$ shows a heavy tilt out of plane, where in $MLCT_2$ there is none. This is may indicate CO loss solely from the $MLCT_1$ state. In acetonitrile, $MLCT_1$ and $MLCT_2$ are quite different to those in dichloromethane. $MLCT_1$ shows a completely different kind of geometry, with elongation of the axial CO bond. $MLCT_2$ is much closer in geometry and electronic configuration to $MLCT_1$ in dichloromethane, with a strong out of plane tilt. This indicates that CO loss may occur from both $MLCT_1$ and $MLCT_2$ in acetonitrile. This would account for the apparent biexponential growth of the photoproduct peak seen in all acetonitrile experiments which was not observed for dichloromethane.

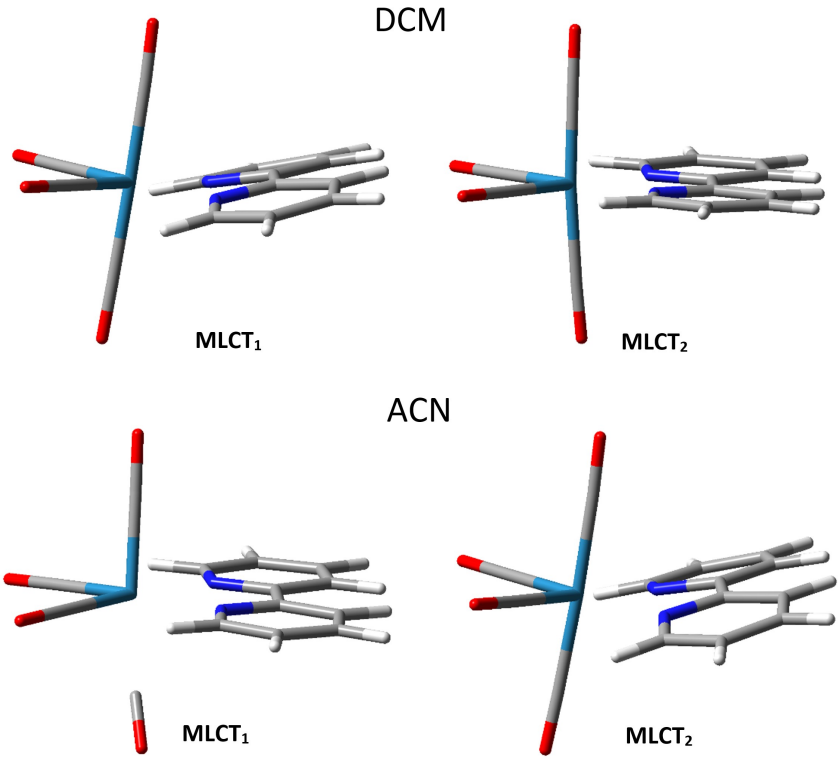

Figure 5.35: *Calculated geometries for $MLCT_1$ and $MLCT_2$ excited states in dichloromethane and acetonitrile*

In the ns-TRIR experiments, we found there was a difference in reactivity between the two solvents indicated by the nature of the decay rates. These vertical excitation energy diagrams demonstrate the complex interplay between states and also clearly highlight a difference between dichloromethane and acetonitrile; however, it is difficult to define the exact nature of the interplay between states due to their complexity. What we can ascertain, however, is that there is a difference in reactivity between acetonitrile and dichloromethane as observed in both experimental and computational results.

We could only directly observe two excited states in the TRIR experiments; one emissive state (State I), and a state that is proposed to lead to the CO loss photoproduct (State II). In both dichloromethane and acetonitrile, the energy of T($ILCT_2$) as seen in both 5.36 and Figure 5.37, is significantly high and therefore we might not expect its formation, which would correlate well with experimental results. Therefore, the so-called T($ILCT_1$), the emissive state and the lowest energy state in both solvents can be assigned to 'State I'. The computational results predict two further states; T($MLCT_1$) and T($MLCT_2$) in both solvents. Whilst we did not directly observe three excited states, the presence of a further state would certainly explain the difference between and also the complexity of the kinetics in the two solvents. Due to their geometric and electronic similarity, we tentatively assign T($MLCT_1$) in dichloromethane and T($MLCT_2$) in acetonitrile as 'State II'. In the ns-TRIR the decay of State II did not match the growth of the photoproduct, particularly in dichloromethane. These computational results however do confirm that the photoproduct is made from State II and the discrepancy we see in the experimental kinetics is probably due to overlapping excited state peaks distorting the apparent lifetime and the complexity of the interplay between states.

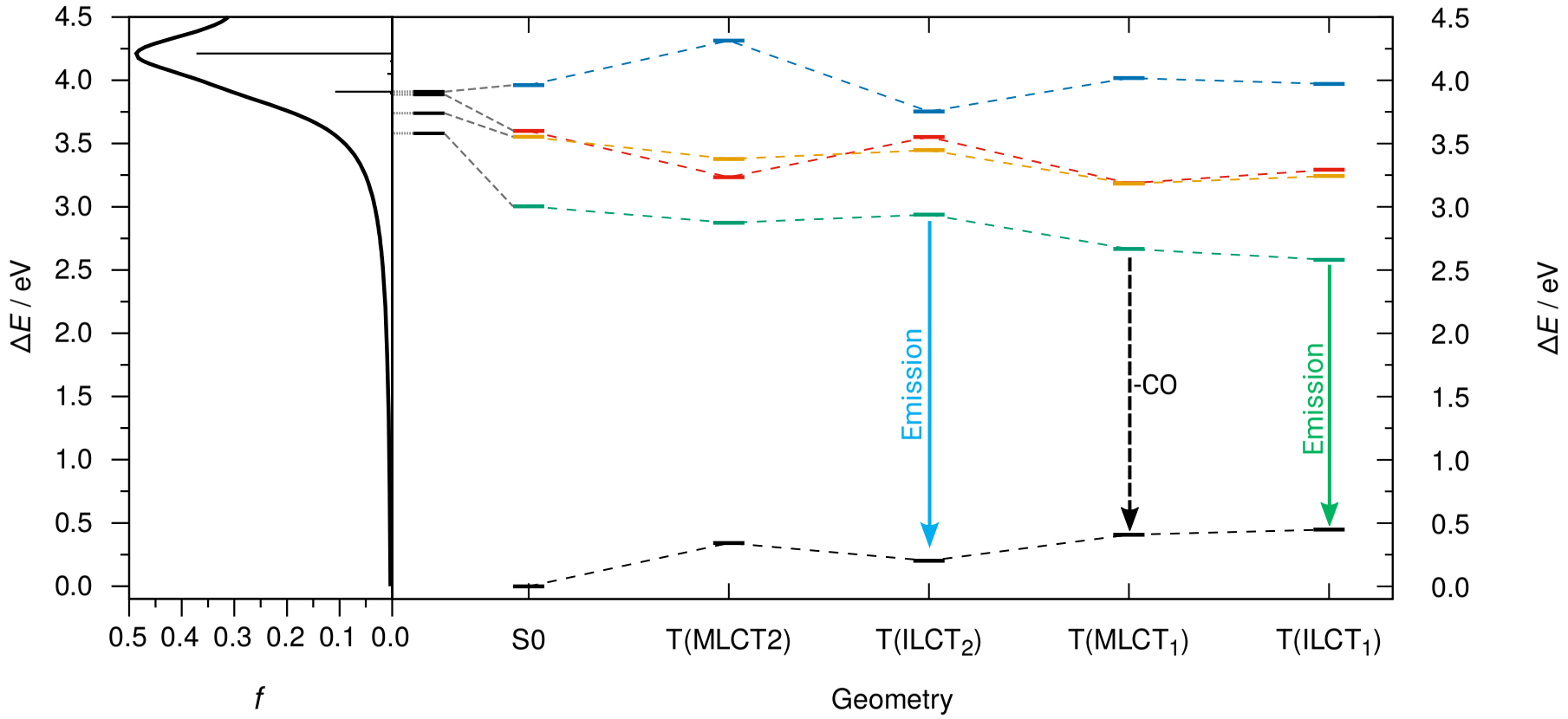

Figure 5.36: *Calculated vertical excitation energies for the excited states species following the photoexcitation of [Re(CO)$_4$(bpy)][PF$_6$] in dichloromethane, showing T(ILCT$_1$) (green), T(MLCT$_1$) (yellow), T(MLCT$_2$) (red) and T(ILCT$_2$) (blue)*

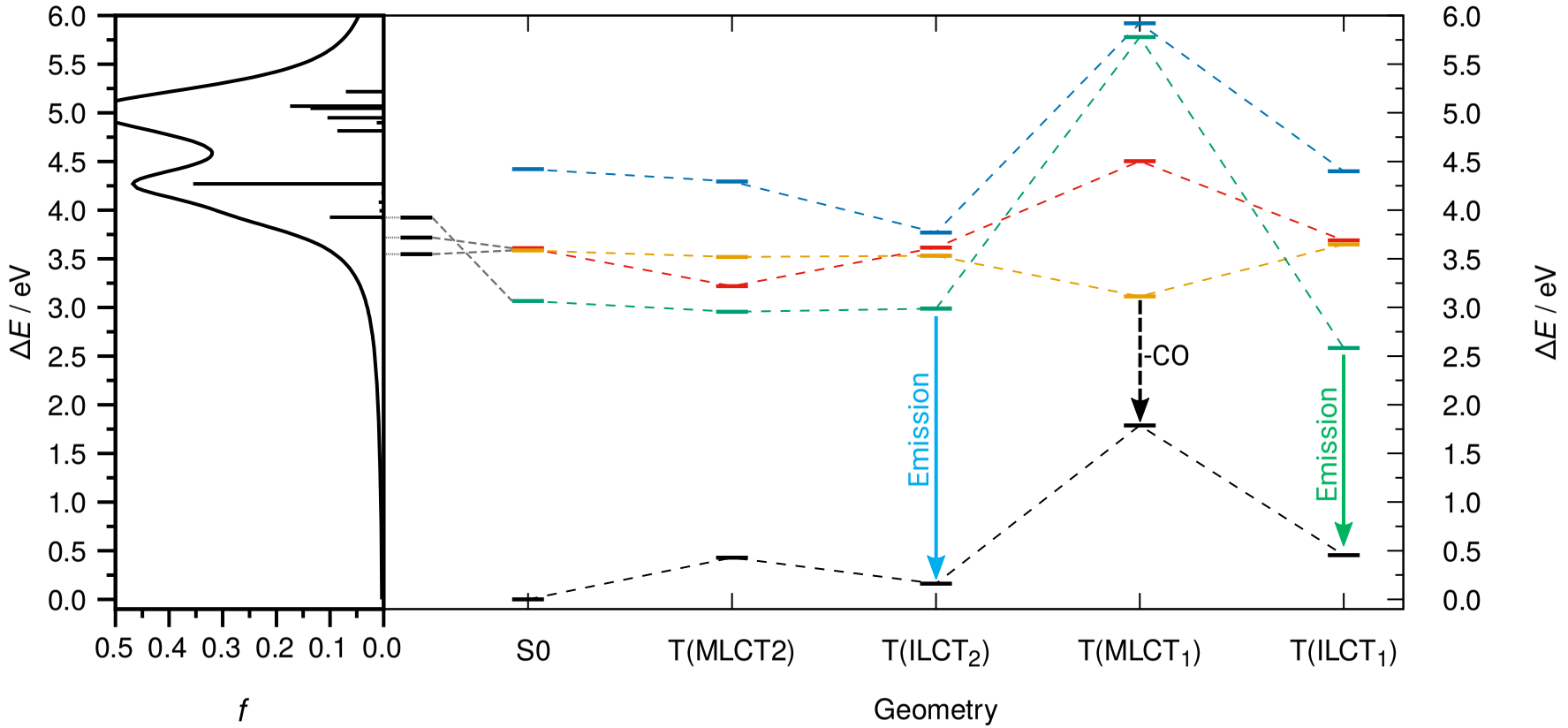

Figure 5.37: *Calculated vertical excitation energies for the excited states species following the photoexcitation of [Re(CO)$_4$(bpy)][PF$_6$] in acetonitrile, showing T(ILCT$_1$) (green), T(MLCT$_1$) (yellow), T(MLCT$_2$) (red) and T(ILCT$_2$) (blue)*

One clear difference between the diagrams is the crossover between T($ILCT_1$) and T($MLCT_1$) in acetonitrile that is not present in dichloromethane. This is shown more clearly in Figure 5.38 which show the Marcus parabola calculated for the reactions. In dichloromethane, the parabola show inverted Marcus character, whereas the parabola calculated for acetonitrile does not. This has interesting connotations and may explain the difference in reactivity seen in the variable temperature experiments in the different solvents. In the inverted Marcus region, where $\lambda < \Delta G^0$, one might imagine that a change in temperature might have relatively small effect on the large value for ΔG^0 and hence a small effect on the rate of reaction. This is reflected in the experimental results in the lack of trend in the lifetime of formation of the photoproduct or indeed in the decay or growth of any other species in dichloromethane. Indeed, according to the conventional electron transfer theory, temperature effect on the electron transfer rates in the true inverted region is expected to be quite insignificant due to the participation of nuclear tunnelling involving the high frequency vibrational modes.[224,225]

In the normal Marcus region, however, electron transfer should be highly temperature dependent.[225] The Marcus parabola in Figure 5.38 calculated for acetonitrile exhibit normal region character, and indeed we did find a dependence on temperature in our TRIR experimental results, with the rate of decay of State I and State II decreasing and increasing, respectively, with an increase in temperature.

We described in the Introduction that the crossing point of the parabola is a good estimation for the transition state for the reaction. As we can see from the Marcus parabola in Figure 5.38, in DCM there is no intersection between the parabola, and if we imagine extending the parabola, the crossing point might lie at a very high energy. This implies that the electron transfer reaction from $ILCT_1$ to $MLCT_1$ is energetically very unfavourable, with a very high activation barrier. Indeed, in the experimental results, we see no evidence for a transfer from $ILCT_1$ to $MLCT_1$. It was only at the very highest temperatures that we saw an increase in photoproduct production implying at only the highest temperatures there is enough energy to overcome this barrier. In contrast, there is

a crossing point in the parabola calculated for acetonitrile, which again can estimate the location of the transition state. Relative to dichloromethane, the transition state occurs at a much lower energy. This lower energy transition state implies that the transfer from $ILCT_1$ to MLCT1 is more favourable in acetonitrile. With increasing temperature, the transfer from $ILCT_1$ to $MLCT_1$ would become even more favourable. Indeed, we have seen this reflected in the experimental results.

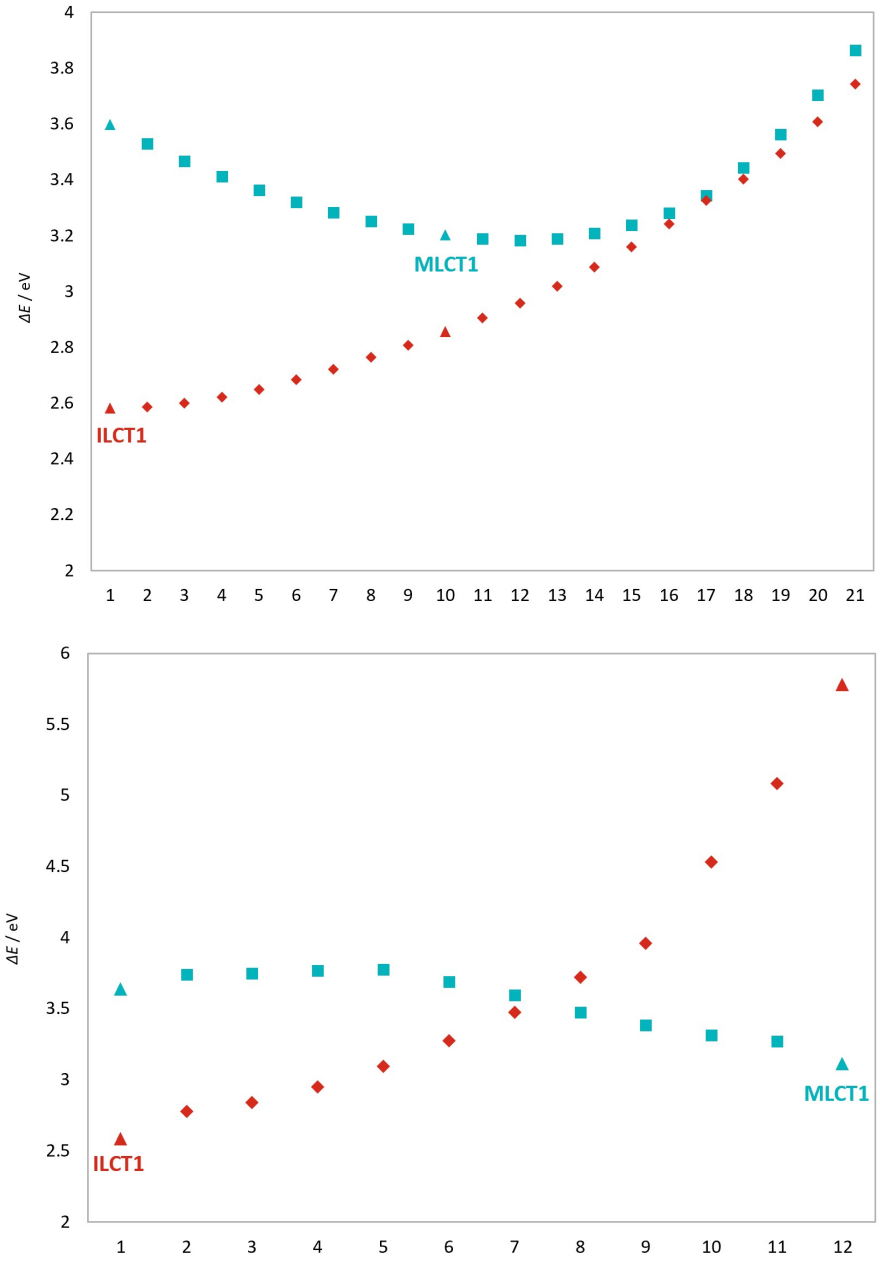

Figure 5.38: *Marcus parabolas for the electron transfer from $ILCT_1$ and $MLCT_1$ in dichloromethane (top) and acetonitrile (bottom)*

5.4 Conclusions and Future Work

The room temperature ns-TRIR of $[Re(CO)_4(bpy)][PF_6]$ at 355 nm excitation in both dichloromethane and acetonitrile has been repeated. Experimental results show the formation of two excited states; 'State I', a mixed ILCT/MLCT state and 'State II', assigned as a mixed MLCT/ILCT state with more MLCT character, and a final photoproduct $[Re(CO)_3(bpy)(X)][PF_6]$ (X = CH_2Cl_2 or CH_3CN), in accordance with previous works. Analysis of the single point kinetic data, however, has shown some differences in reactivity between the two solvents. These differences suggest that the interchange between states may be different in the two solvents.

To determine the effect of temperature on the reaction, the ns-TRIR of $[Re(CO)_4(bpy)][PF_6]$ in dichloromethane was conducted at 5 degree intervals from 5 to 35 °C. It was found that there was no increased formation of the photoproduct $[Re(CO)_3(bpy)(CH_2Cl_2)][PF_6]$ on an increase in temperature. Indeed, there was no dependence on temperature for any of the decay or growth lifetimes. There was some limited evidence for an increase in photoproduct production at 30 and 35 °C; however, the boiling point of dichloromethane limits us from increasing the temperature further to explore this trend. In future work, we can explore the variable temperature reactions in dichloroethane. This would enable us to probe the reaction in this solvent which is expected to behave in a similar fashion to dichloromethane; however, with the ability to probe the reaction at higher temperatures due to the increased boiling point of dichloroethane.

The ns-TRIR of $[Re(CO)_4(bpy)][PF_6]$ in acetonitrile was conducted at 10 degree intervals from 15 to 55 °C. In contrast to the same reaction in dichloromethane, there was a clear increase in formation of the photoproduct $[Re(CO)_3(bpy)(CH_3CN)][PF_6]$ with an increase in temperature. This was further supported by a decrease in the reformation of the parent complex. The lifetime of the decay of 'State I' increased from 130 to 326 ns with the increase in temperature from 15 to 55 °C, which is an interesting observation implying a competing long-lived process that becomes more favourable at higher temper-

atures. Both of these two observations together imply that there is a transfer from State I to the CO loss state. Future variable temperature experiments of the 266 nm excitation of $[Re(CO)_4(bpy)][PF_6]$ in dichloromethane and acetonitrile will help verify these observations. In previous work, it was found that at 266 nm excitation, only one excited state, State II, was formed, which then led to the photoproduct. If our theory is correct, a change in temperature should not result in an increase in photoproduct formation in acetonitrile at 266 nm excitation, as there is no pathway from State I to State II.

High level density functional theory calculations have been performed into the excited states of $[Re(CO)_4(bpy)][PF_6]$ and shown that indeed, there is a difference between then two solvents. The calculations show the possibility of three excited states, referred to as $^3(ILCT_1)$, $^3(MLCT_1)$ and $^3(MLCT_2)$. The $^3(ILCT_1)$ state is calculated to be the same in both solvents; however, the $^3(MLCT_1)$ states exhibit different geometry or electronic configuration in the different solvents. CO loss occurs from $^3(MLCT_1)$ in dichloromethane but in acetonitrile may occur from both $^3(MLCT_1)$ and $^3(MLCT_2)$. Calculations to determine the Marcus parabola have shown why there is a difference between the temperature dependence in dichloromethane and acetonitrile. In dichloromethane the Marcus parabola exhibit clear inverted character, which explains why there is no temperature dependence on any of the measured excited state rates. We postulate that the transition state is too high in energy for electron transfer from $^3(ILCT_1)$ to $^3(MLCT_1)$. Importantly, in acetonitrile, the Marcus parabola exhibit normal character, which can explain why the electron transfer rates are temperature dependent. Additionally, the transition state appears to be lower in energy; hence, we postulate that this is why there is a transfer from $^3(ILCT_1)$ to $^3(MLCT_1)$ only in acetonitrile.

These results have highlighted the important influence of solvent and temperature on the photophysical reactions of $[Re(CO)_4(bpy)][PF_6]$ and, indeed, of transition metal complexes. This has important implications for the development of all photophysical chemical reactions, including development of photovoltaic cells and catalysts for the photocatalytic reduction of CO_2.

Chapter 6

Experimental

6.1 Materials

Solvents for use in time-resolved measurements: PFMCH (Alfa Aesar, 94 %), *n*-heptane, *n*-hexane, cyclohexane and cyclopentane (Sigma Aldrich, ≥ 99 %) were distilled over CaH_2 for 3 days to remove any traces of water and stored under an Ar atmosphere. *n*-hexane-d_{14} and c-hexane-d_{12} (Sigma Aldrich, 99 atom % D) were dried over molecular sieves to remove traces of water. Acetonitrile (Sigma Aldrich, anhydrous, 99.8 %) and dichloromethane (Sigma Aldrich, anhydrous, ≥ 99.8 %) were used without further purification.

Reagents $[Rh(\mu\text{-}Cl)(CO)_2]_2$ (Fischer), KTp* (Fischer), 3,5-dimethyl pyrazole (Fluka), KBH_4 (Fischer), K_2CO_3 (Fischer), KOH (Merck), tetrabutylammonium bromide (Fischer), $AgBF_4$ (Alfa Aesar) and xenon (Aldrich, > 99.99 %) were used without further purification.

Solvents for general experimental use: hexane (Fischer), dichloromethane (Aldrich), toluene (Fischer), diethyl ether (Aldrich) and acetonitrile (Aldrich) were all used without further purification.

6.1.1 Synthesis of Bp*Rh(CO)$_2$

KBp*, was synthesised according to a modified literature procedure.[226] 3,5-dimethyl pyrazole was added to a solution of KBH_4 in toluene and refluxed for 3 hours. The mixture was added to toluene (5 mL) and washed with hexane (*ca.* 50 mL) to yield KBp* as a white crystalline product (0.52 g).

Bp*Rh(CO)$_2$ was synthesised according to a modified literature procedure.[110] [Rh(μ-Cl)(CO)$_2$]$_2$ was added to a stirred solution of KBp* in diethyl ether (100 mL). The mixture was stirred for 5 minutes. The mixture was filtered and the solvent removed under vacuum to leave a yellow solid. The solid was washed with hexane, filtered and the solvent removed under vacuum to leave a yellow solid. This was purified by vacuum sublimation (1×10^{-2} bar, 40 °C) to give Bp*Rh(CO)$_2$ as a pale yellow solid (21 mg). δH (400 MHz, $CDCl_3$) 5.76 (s, 2H, C4-H), 2.35 (s, 6H, C3-CH_3), 2.27 (s, 6H, C5-CH_3) ppm, m/z (ESI+ MS) 362 ($RhC_{12}H_{16}O_2N_4B$). υ_{max}/cm^{-1} (*n*-heptane): 2079 (s, υ(CO)), 2012 cm^{-1} (s, υ(CO)).

6.1.2 Synthesis of Tp*Rh(CO)$_2$

Tp*Rh(CO)$_2$ was synthesised according to a modified literature procedure.[110] [Rh(μ-Cl)(CO)$_2$]$_2$ was added to a stirred solution of KTp* in toluene at −45 °C. The mixture was stirred for 10 minutes, filtered, and then the solvent removed under vacuum to give a bright yellow solid. This was purified over a short alumina column (hexane) to give Tp*Rh(CO)$_2$ as a pale yellow solid (13 mg). δH (400 MHz, $CDCl_3$) 5.79 (s, 3H, C4-H), 2.39 (s, 9H, C3-CH_3), 2.34 (s, 9H, C5-CH_3) ppm, m/z (ESI+ MS) 457 ($RhC_{17}H_{22}O_2N_6B$), υ_{max}/cm^{-1} (*n*-heptane): 2054 (s, υ(CO)) , 1980 cm^{-1} (s, υ(CO)).

6.1.3 Synthesis of [Bpm*Rh(CO)$_2$][BF$_4$]

Bis(3,5-dimethylpyrazolyl)methane, Bpm*, was synthesised according to a modified literature procedure.[227] A mixture of 3,5-dimethyl pyrazole (1.61 g, 16.8 mmol), K_2CO_3 (2.32 g, 16.8 mmol), KOH (0.94 g, 16.8 mmol) and tetrabutylammonium bromide (TBAB)

(1.27 g, 0.85 mmol) in dichloromethane (25 mL) was heated under reflux for 36 hours. The mixture was then filtered, washed with hot dichloromethane (2 × 25 mL) and the organic solutions were combined. The solvent was removed, and the resulting solid was washed with water and purified by vacuum sublimation to give Bpm* as a white powder (0.35 g, 10.4 %). δH (400 MHz, $CDCl_3$) 6.05 (s, 2H), 5.78 (s, 2H), 2.41 (s, 6H), 2.25 (s, 6H) ppm, δC (400 MHz, $CDCl_3$) 148.2 (), 140.4 (), 106.4 (), 60.5 (), 13.4 (), 11.2 () ppm, m/z (ESI+ MS) 205 (M+H).

[Bpm*Rh$(CO)_2$][BF_4] was synthesised according to a modified literature procedure.[148] [Rh(μ-Cl)$(CO)_2]_2$ (0.19 g, 0.5mmol) was added to a solution of Bpm* (0.2 g, 1 mmol) in dry acetone and stirred for 15 minutes under argon. $AgBF_4$ (0.19 g, 1 mmol) was then added and the solution was stirred in the dark for 10 minutes. The solution was filtered through celite, and the solvent was removed. The solid was dissolved in dichloromethane, filtered, and the resulting solution reduced to *ca.* 1 mL under vacuum. Hexane (10 mL) was added to precipitate [Bpm*Rh$(CO)_2$][BF_4] as yellow crystals (0.36 g, 71.6 %). δH (400 MHz, acetone-d_6) 6.71 (s,), 6.32 (s,), 2.59 (s,), 2.49 (s,) ppm, δC (400 MHz, acetone-d_6) 182.7 (d,), 153.7 (d), 145.0 (s), 108.3 (s), 58.0 (s), 14.0 (s), 10.2 (s) ppm, m/z (ESI+ MS) 363 ($RhC_{13}H_{17}O_2N_4$), υ_{max}/cm^{-1} (dcm): 2110 (s, υ(CO)) , 2050 cm^{-1} (s, υ(CO)).

6.2 TRIR Sample Preparation

Samples for TRIR experiments were prepared with solvents dried over CaH_2 and stored under argon. All solutions were made up to 25 mL and prepared under an argon atmosphere using standard Schlenk line techniques. The concentrations were prepared so that UV/Vis and IR absorbances were below 1. The sample solution was degassed with three freeze–pump–thaw cycles. An infrared solution cell (Harrick Corp.) with CaF_2 windows (25 × 2 mm) was used with a path length which varied from 0.39–1 mm. A peristaltic pump was used to circulate the sample between the sample reservoir and the IR cell which was connected via teflon tubing in order to minimise degradation and overheating during the experiment.

Where xenon gas was dissolved in the sample, the sample was prepared via the method above and a pressure of 1.5 bar of Xe was introduced into the sample pot and the sample was shaken to encourage dissolution. The solution was held under a pressure of xenon gas during the experiment.

For variable temperature experiments, a variable temperature cell (Harrick Corp.) with CaF_2 windows (25 × 2 mm) was used with a path length that varied from 0.39–1mm. The cell was connected to a chiller which was set to the desired temperature. A peristaltic pump was again used to circulate the sample between the sample reservoir and the IR cell which was connected via teflon tubing. In order to make sure the temperature of the solution inside the cell was kept as constant as possible, the sample reservoir was also kept in the water bath of the chiller.

6.3 Ultrafast Experimental Techniques

6.3.1 Nottingham Ultrafast TRIR Apparatus

Picosecond and nanosecond TRIR was conducted using the Nottingham ultrafast setup.

A Ti:saphirre oscillator (MaiTai, SpectraPhysics) coupled with a regenerative amplifier

(Spitfire Pro, SpectraPhysics) were used to generate laser pulses of 800 nm (2.3 mJ, 1 kHz, 140 fs). This pulse is then separated into two separate beams. One beam was used to produce the pump pulse at 266 nm by harmonic generation (TimePlate Tripler, Minioptic Technology Inc.). The other beam was used to pump a TOPAS-C optical parametric amplifier (Light Conversion) to produce IR pulses (180 cm^{-1} FWHM, *ca.* 2 μJ at 2000 cm^{-1}). This pulse was further divided by a beam splitter, with one half directed to the sample for use as the probe beam and the other half directed to a single element MCT detector (Kolmar Technology) to act as a reference. In order to study excitation at a specific time delay, the pump beam can be delayed by up to 2 ns using an optical delay line.

For ns-TRIR, a q-switched Nd:YVO laser (1064 nm, 600 ps, Advanced Optical Technology) was used and its output was frequency quadrupled to produce a 266 nm pump pulse, or tripled to produce a 355 nm pump pulse. The pump and probe pulses were synchronised and the delay of the pump beam was set by a pulse generator (DG535, Stanford Research Systems), so that delays of 0.5 ns to 100 μs could be achieved.

For both ps- and ns-TRIR, change in absorbance was measured by taking the ratio between pump-on and pump-off IR intensity. Pump-off measurements were generated by use of an optical chopper (500 Hz) which blocks every second pump pulse. The cell was rastered in two dimensions, to counteract sample degradation and overheating.

6.3.2 Time-resolved X-ray Absorption Spectroscopy at the Advanced Photon Source

Rhenium L3-edge XAFS spectroscopic measurements were conducted at the Advanced Photon Source, Argonne National Laboratory (ANL), Argonne, IL, USA. Data were recorded using a Si(111) monochromator on the 11-ID-D X-ray beamline. APD detectors were used for fast detection in fluorescence mode on an open jet liquid sample system under an He atmosphere. Pump–probe measurements were collected using synchrotron radiation in 24-bunch mode giving 153 ns between photon bunches. Each data point is averaged over 10 seconds, and the final presented data is an average of 50 individual

scans for each 153 ns time slice, normalised to I_0 and smoothed using a moving average smoothing function. Liquid samples were prepared under standard Schlenk conditions, using dry, degassed solvents. Sample solutions were flowed through an open jet sample system with an aperture of *ca.* 200 μm at a flow rate of 0.5 mL/s.

6.4 Other Experimental Techniques

6.4.1 FTIR Spectroscopy

FTIR measurements were made using a Thermo Nicolet FTIR spectrometer fitted with a MCT detector. Spectra were recorded with a scan rate of 32 and a resolution of 2 cm^{-1}. An infrared solution cell (Harrick Corp.) with CaF_2 (2 × 25 mm) windows with a path length between 0.25 and 1 mm depending on the concentration of solution.

6.4.2 UV/Vis Spectroscopy

Absorption spectrum was taken using a Perkin Elmer Lambda 5 spectrometer in a quartz cuvette with 1 cm spacing or an infrared solution cell (Harrick Corp.) with CaF_2 windows (25 × 2 mm, Crystran) at a path length of 0.39–1 mm. An Hg-Arc lamp was used as the UV light source.

6.4.3 ^{1}H and ^{13}C NMR Spectroscopy

^{1}H NMR and ^{13}C NMR spectra were recorded at 400 MHz in chloroform-*d* or acetone-*d*6 at room temperature using the JEOL ex400 NMR spectrometer. Shifts in peaks due to changes in solvent were found in the literature.

6.4.4 Mass Spectroscopy

All mass spectra were obtained with the Mass Spectrometry Service at the University of Nottingham. Positive and negative ion electrospray mass spectra were recorded using an

automated Micromass LCT spectrometer using ElectroSpray Ionisation. Measurements were performed in methanol solutions.

6.5 Quantum Mechanical Calculations

All calculations were performed with Q-Chem quantum-chemical software package[228] with the M06 functional. All calculations were performed in the ground state and in vacuo. Geometry optimisation, frequency calculations and single point energy calculations were carried out. The basis set 6-311++G** was used for all atoms apart from transition metals and Xe. For the transition metals, the LANL08 basis set with effective core potential was used and for Xe, the Def2-TZVPD with effective core potential. All ECPs and basis sets are taken from the basis set exchange.[229]

Full bond dissociation calculation details are found in Appendix A.

Appendix A

Table 1: Calculated bond dissociation energies for complexes of the form Tpm'M(CO)$_2$(X), where Tpm' = Tpm or Tpm*, M = Cr, Mo or W and X = CH$_4$ or C$_7$H$_{16}$

Complex	BDE / kJmol^{-1}
TpmCr(CO)$_2$–CH$_4$	31.4
Tpm*Cr(CO)$_2$–CH$_4$	28.8
TpmCr(CO)$_2$–C$_7$H$_{16}$	38.2
Tpm*Cr(CO)$_2$–C$_7$H$_{16}$	34.7
TpmMo(CO)$_2$–CH$_4$	41.2
Tpm*Mo(CO)$_2$–CH$_4$	33.9
TpmMo(CO)$_2$–C$_7$H$_{16}$	50.7
Tpm*Mo(CO)$_2$–C$_7$H$_{16}$	49.7
TpmW(CO)$_2$–CH$_4$	48.9
Tpm*W(CO)$_2$–CH$_4$	47.9
TpmW(CO)$_2$–C$_7$H$_{16}$	61.2
Tpm*W(CO)$_2$–C$_7$H$_{16}$	55.9

Table 2: Calculated bond dissociation energies for complexes of the form Tp'M(CO)$_2$(X), where Tp' = Tp or Tp*, M = Mn or Re and X = CH_4 or C_7H_{16}

Complex	BDE / kJmol^{-1}
TpMn(CO)$_2$–CH_4	30.8
Tp*Mn(CO)$_2$–CH_4	20.1
TpMn(CO)$_2$–C_7H_{16}	37.0
Tp*Mn(CO)$_2$–C_7H_{16}	24.9
TpRe(CO)$_2$–CH_4	53.2
Tp*Re(CO)$_2$–CH_4	46.1
TpRe(CO)$_2$–C_7H_{16}	61.8
Tp*Re(CO)$_2$–C_7H_{16}	53.5

Table 3: Calculated bond dissociation energies for complexes of the form Bp'M(CO)(X), where Bp' = Bp or Bp*, M = Rh or Ir and X = CH_4 or C_7H_{16}

Complex	BDE / kJmol^{-1}
BpRh(CO)$_2$–CH_4	58.9
Bp*Rh(CO)$_2$–CH_4	54.0
BpRh(CO)$_2$–C_7H_{16}	64.9
Bp*Rh(CO)$_2$–C_7H_{16}	60.6
BpIr(CO)$_2$–CH_4	77.5
Bp*Ir(CO)$_2$–CH_4	71.1
BpIr(CO)$_2$–C_7H_{16}	86.4
Bp*Ir(CO)$_2$–C_7H_{16}	80.5

Table 4: Calculated single point energies for group V complexes $M(CO)_5X$ and $M(CO)_4(NO)X$ (M = V, Nb or Ta, X = CH_4 or C_7H_{16}) and the resulting bond dissociation energies

	Energy / E_h							Bond Dissociation Energy / $kJmol^{-1}$	
	E^{AB}_{AB}(AB)	E^{A}_{AB}(A)	E^{AB}_{AB}(A)	E^{A}_{A}(A)	E^{B}_{AB}(B)	E^{AB}_{AB}(B)	E^{B}_{B}(B)	Non-counterpoise Corrected	Counterpoise Corrected
$V(CO)_5$–CH_4	−678.37824	−637.87306	−637.87412	−637.87451	−40.48769	−40.48789	-40.48850	45.94	36.7
$V(CO)_5$–C_7H_{16}	−914.12436	−637.87417	−637.87580	−637.87451	−276.22954	−276.22990	−276.23062	54.21	45.3
$Nb(CO)_5$–CH_4	−663.34557	−622.84054	−622.84149	−622.84077	−40.48766	−40.48785	−40.48850	45.61	39.8
$Nb(CO)_5$–C_7H_{16}	−899.09163	−622.84052	−622.84199	−622.84077	−276.22948	−276.22984	−276.23062	56.81	48.3
$Ta(CO)_5$–CH_4	−664.82976	−624.32236	−624.32328	−624.32274	−40.48737	−40.48758	−40.48850	52.60	45.7
$Ta(CO)_5$–C_7H_{16}	−900.57629	−624.32236	−624.32384	−624.32274	−276.22915	−276.22953	−276.23062	65.06	55.3
$V(CO)_4(NO)$–(ax-CH_4)	−695.00787	−654.50691	−654.50782	−654.50714	−40.48776	−40.48797	−40.48850	34.63	29.2
$V(CO)_4(NO)$–(eq-CH_4)	−694.99582	−654.49360	−654.49466	−654.49397	−40.48768	−40.48787	−40.48850	38.19	31.7
$V(CO)_4(NO)$–(ax-C_7H_{16})	−930.75427	−654.50698	−654.50852	−654.50714	−276.22958	−276.22996	−287.23062	46.49	38.3
$V(CO)_4(NO)$–(eq-C_7H_{16})	−930.74205	−654.49383	−654.49561	−654.49397	−276.22944	−276.22982	−276.23062	49.31	40.2
$Nb(CO)_4(NO)$–(ax-CH_4)	−679.97494	−639.47284	−639.47371	−639.47297	−40.48778	−40.48796	−40.48850	37.60	32.6
$Nb(CO)_4(NO)$–(eq-CH_4)	−679.96322	−639.46074	−639.46167	−639.46092	−40.48780	−40.48798	−40.48850	38.54	33.3
$Nb(CO)_4(NO)$–(ax-C_7H_{16})	−915.72065	−639.47277	−639.47416	−639.47297	−276.22955	−276.22994	−276.23062	48.12	40.1
$Nb(CO)_4(NO)$–(eq-C_7H_{16})	−915.70866	−639.46077	−639.46232	−639.46092	−276.22952	−276.22991	−276.23062	48.25	39.9
$Ta(CO)_4(NO)$–(ax-CH_4)	−681.46236	−640.95798	−640.95889	−640.95823	−40.48754	−40.48774	−40.48850	44.21	38.1
$Ta(CO)_4(NO)$–(eq-CH_4)	−681.44951	−640.94449	−640.94543	−640.94481	−40.48752	−40.48770	−40.48850	45.95	39.6
$Ta(CO)_4(NO)$–(ax-C_7H_{16})	−917.20848	−640.95795	−640.95944	−640.95823	−276.22919	−276.22958	− 276.23062	56.59	46.6
$Ta(CO)_4(NO)$–(eq-C_7H_{16})	−917.19529	−640.94462	−640.94614	−640.94481	−276.22913	−276.22952	−276.23062	56.59	47.1

Table 5: Calculated single point energies for group VI complexes Tpm'M(CO)$_2$X and [Tpm'M(CO)(NO)X]$^+$ (Tpm' = Tpm or Tpm*, M = Cr, Mo or W and X = CH_4 or C_7H_{16}) and the resulting bond dissociation energies

	Energy / E_h							Bond Dissociation Energy / kJmol^{-1}	
	E_{AB}^{AB}(AB)	E_{AB}^{A}(A)	E_{AB}^{AB}(A)	E_{A}^{A}(A)	E_{AB}^{B}(B)	E_{AB}^{AB}(B)	E_{B}^{B}(B)	Non-counterpoise Corrected	Counterpoise Corrected
TpmCr(CO)$_2$–CH$_4$	−1068.61254	−1028.11046	−1028.11129	−1028.11100	−40.48743	−40.48773	−40.48850	38.51	31.4
TpmCr(CO)$_2$–C$_7$H$_{16}$	−1304.35827	−1028.11179	−1028.11328	−1028.11100	−276.22928	−276.22989	−276.23062	45.16	38.2
Tpm*Cr(CO)$_2$–CH$_4$	−1304.40810	−1263.90663	−1263.90731	−1263.90763	−40.48784	−40.48819	−40.48850	35.79	28.8
Tpm*Cr(CO)$_2$–C$_7$H$_{16}$	−1540.15338	−1263.90586	−1263.90708	−1263.90763	−276.22958	−276.23026	−276.23062	47.10	34.7
TpmMo(CO)$_2$–CH$_4$	−1049.85006	−1009.34469	−1009.34546	−1009.34486	−40.48706	−40.48730	−40.48850	48.10	41.2
TpmMo(CO)$_2$–C$_7$H$_{16}$	−1285.59693	−1009.34448	−1009.34595	−1009.34486	−276.22843	−276.22911	−276.23062	63.08	50.7
Tpm*Mo(CO)$_2$–CH$_4$	−1285.64587	−1245.14342	−1245.14400	−1245.14360	−40.48752	−40.48779	−40.48850	39.21	33.9
Tpm*Mo(CO)$_2$–C$_7$H$_{16}$	−1521.39491	−1245.14248	−1245.14361	−1245.14360	−276.22883	−276.22948	−276.23062	61.96	49.7
TpmW(CO)$_2$–CH$_4$	−1050.10398	−1009.59528	−1009.59631	−1009.59557	−40.48603	−40.48629	−40.48850	59.53	48.9
TpmW(CO)$_2$–C$_7$H$_{16}$	−1285.85080	−1009.59513	−1009.59693	−1009.59557	−276.22714	−276.22780	−276.23062	74.90	58.2
Tpm*W(CO)$_2$–CH$_4$	−1285.90354	−1245.39468	−1245.39560	−1245.39555	−40.48628	−40.48662	−40.48850	59.28	47.9
Tpm*W(CO)$_2$–C$_7$H$_{16}$	−1521.64960	−1245.39390	−1245.39535	−1245.39555	−276.22794	−276.22863	−276.23062	72.90	55.9
[TpmCr(CO)(NO)–CH$_4$]$^+$	−1085.05467	−1044.55179	−1044.55293	−1044.55221	−40.48727	−40.48753	−40.48850	40.97	33.0
[TpmCr(CO)(NO)–C$_7$H$_{16}$]$^+$	−1320.80240	−1044.55153	−1044.55348	−1044.55221	−276.22889	−276.22945	−276.23062	57.71	44.8
[Tpm*Cr(CO)(NO)–CH$_4$]$^+$	−1320.86250	−1280.36065	−1280.36162	−1280.36226	−40.48759	−40.48791	−40.48850	37.46	27.5
[Tpm*Cr(CO)(NO)–C$_7$H$_{16}$]$^+$	−1556.60993	−1280.36018	−1280.36181	−1280.36226	−276.22961	−276.23030	−276.23062	52.89	38.7
[TpmMo(CO)(NO)–CH$_4$]$^+$	−1066.29110	−1025.78172	−1025.78267	−1025.78203	−40.48575	−40.48602	−40.48850	62.03	50.8
[TpmMo(CO)(NO)–C$_7$H$_{16}$]$^+$	−1302.03837	−1025.78154	−1025.78332	−1025.78203	−276.22795	−276.22858	−276.23062	75.83	61.5
[Tpm*Mo(CO)(NO)–CH$_4$]$^+$	−1302.10138	−1261.59269	−1261.59360	−1261.59250	−40.48655	−40.48688	−40.48850	58.12	47.7
[Tpm*Mo(CO)(NO)–C$_7$H$_{16}$]$^+$	−1537.84794	−1261.59188	−1261.59336	−1261.59350	−276.22849	−276.22916	−276.23062	72.40	56.9
[TpmW(CO)(NO)–CH$_4$]$^+$	−1066.55044	−1026.04011	−1026.04135	−1026.04039	−40.48614	−40.48638	−40.48850	63.48	52.7
[TpmW(CO)(NO)–C$_7$H$_{16}$]$^+$	−1302.30121	−1026.03964	−1026.04184	−1026.04039	−276.22706	−276.22768	−276.23062	90.58	71.9
[Tpm*W(CO)(NO)–CH$_4$]$^+$	−1302.36566	−1261.85328	−1261.85447	−1261.85452	−40.48533	−40.48568	−40.48850	71.01	55.4
[Tpm*W(CO)(NO)–C$_7$H$_{16}$]$^+$	−1538.11256	−1261.85239	−1261.85423	−1261.85452	−276.22784	−276.22854	−276.23062	84.89	65.3

Table 6: Calculated single point energies for group VII complexes Tp'M(CO)$_2$X, [Tp'M(CO)(NO)X]$^+$ and [Tpm'M(CO)$_2$X]$^+$ (Tp' = Tp or Tp*, Tpm' = Tpm or Tpm*, M = Mn or Re and X = CH_4 or C_7H_{16}) and the resulting bond dissociation energies

	Energy / E_h							Bond Dissociation Energy / kJmol^{-1}	
	E_{AB}^{AB}(AB)	E_{AB}^{A}(A)	E_{AB}^{AB}(A)	E_{A}^{A}(A)	E_{AB}^{B}(B)	E_{AB}^{AB}(B)	E_{B}^{B}(B)	Non-counterpoise Corrected	Counterpoise Corrected
TpMn(CO)$_2$–CH$_4$	−1073.16426	−1032.66409	−1032.66400	−1032.66382	−40.48748	−40.48779	−40.48850	33.32	30.8
TpMn(CO)$_2$–C$_7$H$_{16}$	−1308.90963	−1032.66403	−1032.66455	−1032.66382	−276.22943	−276.23002	−276.23062	42.47	37.0
Tp*Mn(CO)$_2$–CH$_4$	−1308.94641	−1268.44760	−1268.44735	−1268.45015	−40.48787	−40.48823	−40.48850	28.72	20.1
Tp*Mn(CO)$_2$–C$_7$H$_{16}$	−1544.69227	−1268.44795	−1268.44929	−1268.45015	−276.23004	−276.23074	−276.23062	37.47	24.9
TpRe(CO)$_2$–CH$_4$	−1048.35857	−1007.84760	−1007.84844	−1007.84846	−40.48543	−40.48572	−40.48850	67.09	53.8
TpRe(CO)$_2$–C$_7$H$_{16}$	−1284.14081	−1007.84757	−1007.84897	−1008.84846	−276.22707	−276.22767	−276.23062	79.20	62.3
Tp*Re(CO)$_2$–CH$_4$	−1284.14617	−1243.63643	−1243.63717	−1243.63879	−40.48572	−40.48607	−40.48850	63.08	46.7
Tp*Re(CO)$_2$–C$_7$H$_{16}$	−1519.89190	−1243.63562	−1243.63685	−1243.63879	−276.22786	−276.22856	−276.23062	74.63	54.0
[TpMn(CO)(NO)–CH$_4$]$^+$	−1089.52992	−1049.02745	−1049.02709	−1049.02663	−40.48673	−40.48702	−40.48850	41.32	39.1
[TpMn(CO)(NO)–C$_7$H$_{16}$]$^+$	−1325.27833	−1049.02712	−1049.02759	−1049.02663	−276.22887	−276.22944	−276.23062	58.63	52.6
[Tp*Mn(CO)(NO)–CH$_4$]$^+$	−1325.32326	−1284.82384	−1284.82319	−1284.82594	−40.48744	−40.48778	−40.48850	31.45	24.0
[Tp*Mn(CO)(NO)–C$_7$H$_{16}$]$^+$	−1561.07067	−1284.82300	−1284.82304	−1284.82594	−276.22967	−276.23038	−276.23062	47.25	35.1
[TpRe(CO)(NO)–CH$_4$]$^+$	−1064.73832	−1024.22586	−1024.22689	−1024.22684	−40.48557	−40.48582	−40.48850	70.58	57.0
[TpRe(CO)(NO)–C$_7$H$_{16}$]$^+$	−1300.48853	−1024.22506	−1024.22695	−1024.22684	−276.22661	−276.22716	−276.23062	96.76	75.2
[Tp*Re(CO)(NO)–CH$_4$]$^+$	−1300.53722	−1260.02795	−1260.02889	−1260.03021	−40.48588	−40.48620	−40.48850	61.41	45.3
[Tp*Re(CO)(NO)–C$_7$H$_{16}$]$^+$	−1536.28636	−1260.02586	−1260.02749	−1260.03021	−276.22793	−276.22865	−276.23062	85.51	60.9
[TpmMn(CO)$_2$–CH$_4$]$^+$	−1086.06929	−1045.56426	−1045.56434	−1046.56499	−40.48688	−40.48719	−40.48850	47.64	40.5
[TpmMn(CO)$_2$–C$_7$H$_{16}$]$^+$	−1321.81669	−1045.56440	−1045.56519	−1045.56499	−276.22878	−276.22940	−276.23062	61.72	51.7
[Tpm*Mn(CO)$_2$–CH$_4$]$^+$	−1321.87427	−1281.37090	−1281.37086	−1281.37296	−40.48744	−40.48781	−40.48850	41.85	32.8
[Tpm*Mn(CO)$_2$–C$_7$H$_{16}$]$^+$	−1557.62105	−1281.370538	−1281.37101	−1281.37296	−276.22947	−276.23016	−276.23062	55.24	42.8
[TpmRe(CO)$_2$–CH$_4$]$^+$	−1061.25526	−1020.74006	−1020.74098	−1020.74091	−40.48440	−40.48469	−40.48850	80.85	64.7
[TpmRe(CO)$_2$–C$_7$H$_{16}$]$^+$	−1297.00363	−1020.73986	−1020.74150	−1020.74091	−276.22616	−276.22683	−276.23062	98.76	78.2
[Tpm*Re(CO)$_2$–CH$_4$]$^+$	−1297.06512	−1256.55131	−1256.55215	−1256.55294	−40.48500	−40.48535	−40.48850	75.63	59.1
[Tpm*Re(CO)$_2$–C$_7$H$_{16}$]$^+$	−1532.81240	−1256.55037	−1256.55171	−1256.55294	−276.22704	−276.22773	−276.23062	91.89	70.4

Table 7: Calculated single point energies for group IX complexes Bp'M(CO)X and $[Bpm'M(CO)X]^+$ (Bp' = Bp or Bp*, Bpm' = Bpm or Bpm*, M = Rh or Ir and X = CH_4 or C_7H_{16}) and the resulting bond dissociation energies

	Energy / E_h							Bond Dissociation Energy / $kJmol^{-1}$	
	E_{AB}^{AB}(AB)	E_{AB}^{A}(A)	E_{AB}^{AB}(A)	E_{A}^{A}(A)	E_{AB}^{B}(B)	E_{AB}^{AB}(B)	E_{B}^{B}(B)	Non-counterpoise Corrected	Counterpoise Corrected
BpRh(CO)–CH_4	−740.45410	−699.94183	−699.94249	−699.94224	−40.48631	−40.48656	−40.48850	68.17	58.9
BpRh(CO)–C_7H_{16}	−976.19911	−699.94176	−699.94286	−699.94224	−276.22689	−276.22731	−276.23062	79.97	64.9
Bp*Rh(CO)–CH_4	−897.64447	−857.13355	−857.13413	−857.13456	−40.48618	−40.48646	−40.48850	64.94	54.0
Bp*Rh(CO)–C_7H_{16}	−1133.38980	−857.13380	−857.13485	−857.13456	−276.22705	−276.22752	−276.23062	76.03	60.6
BpIr(CO)–CH_4	−735.64785	−695.12691	−695.12691	−695.12862	−40.48251	−40.48279	−40.48850	100.88	77.5
BpIr(CO)–C_7H_{16}	−971.39400	−695.12679	−695.12818	−695.12862	−276.22319	−276.22365	−276.23062	115.58	86.4
Bp*Ir(CO)–CH_4	−892.83841	−852.31935	−852.32020	−852.32168	−40.48261	−40.48291	−40.48850	95.68	71.1
Bp*Ir(CO)–C_7H_{16}	−1128.58484	−852.31948	−852.32083	−852.32168	−276.22348	−276.22399	−276.23062	109.96	80.5
$[BpmRh(CO)–CH_4]^+$	−753.41746	−712.89945	−712.90024	−712.89984	−40.48559	−40.48586	−40.48850	85.13	73.6
$[BpmRh(CO)–C_7H_{16}]^+$	−989.16447	−712.89941	−712.90061	−712.89984	−276.22581	−276.22625	−276.23062	103.03	85.0
$[Bpm*Rh(CO)–CH_4]^+$	−910.62168	−870.10613	−870.10682	−870.10688	−40.48567	−40.48596	−40.49950	78.45	66.5
$[Bpm*Rh(CO)–C_7H_{16}]^+$	−1146.36889	−870.10621	−870.10734	−870.10688	−276.22628	−276.22676	−276.23062	95.54	78.2
$[BpmIr(CO)–CH_4]^+$	−748.60713	−708.07831	−708.07924	−708.08005	−40.48182	−40.48210	−40.48850	123.41	98.1
$[BpmIr(CO)–C_7H_{16}]^+$	−984.35524	−708.07820	−708.07854	−708.08005	−276.22211	−276.22258	−276.23062	144.21	112.3
$[Bpm*Ir(CO)–CH_4]^+$	−905.81223	−865.28682	−865.28767	−865.28874	−40.48227	−40.48258	−40.48850	113.26	88.8
$[Bpm*Ir(CO)–C_7H_{16}]^+$	−1141.56057	−865.28671	−865.28805	−865.28874	−276.22275	−276.22326	−276.23062	134.18	103.4

Bibliography

[1] G. W. Coates and R. M. Waymouth, in *Compr. Organomet. Chem. II*, Elsevier, 1995, pp. 1193–1208.

[2] J. Magano and J. R. Dunetz, *Chem. Rev.*, 2011, **111**, 2177–2250.

[3] M. K. Nazeeruddin, A. Kay, I. Rodicio, R. Humphry-Baker, E. Müller, P. Liska, N. Vlachopoulos and M. Grätzel, *J. Am. Chem. Soc.*, 1993, **115**, 6382–6390.

[4] S. Linic, P. Christopher and D. B. Ingram, *Nat. Mater.*, 2011, **10**, 911.

[5] A. L. Pitts, A. Wriglesworth, X.-Z. Sun, J. A. Calladine, S. D. Zarić, M. W. George and M. B. Hall, *J. Am. Chem. Soc.*, 2014, **136**, 8614–8625.

[6] X. Z. Sun, D. C. Grills, S. M. Nikiforov, M. Poliakoff and M. W. George, *J. Am. Chem. Soc.*, 1997, **119**, 7521–7525.

[7] E. Whittle, D. A. Dows and G. C. Pimentel, *J. Chem. Phys.*, 1954, **22**, 1943.

[8] R. H. Hill and M. S. Wrighton, *Organometallics*, 1985, 413–415.

[9] E. D. Becker and G. C. Pimentel, *J. Chem. Phys.*, 1956, **25**, 224–228.

[10] R. B. Hitam, K. A. Mahmoud and A. J. Rest, *Coord. Chem. Rev.*, 1984, **55**, 1–29.

[11] T. Bally, *Reactive Intermediate Chemistry*, John Wiley & Sons, Ltd, 2004.

[12] J. A. Calladine, *Ph.D. thesis*, The University of Nottingham, 2010.

[13] R. G. W. Norrish and G. Porter, *Nature*, 1949, **164**, 658.

[14] R. G. Norrish and G. Porter, *Proc. R. Soc. London. Ser. A. Math. Phys. Sci.*, 1952, **210**, 439–460.

[15] G. Porter and F. J. Wright, *Discuss. Faraday Soc.*, 1953, **14**, 23–34.

[16] B. A. Thrush, *Photochem. Photobiol. Sci.*, 2003, **2**, 453–454.

[17] G. Porter and R. G. W. Norrish, *Proc. R. Soc. London. Ser. A. Math. Phys. Sci.*, 1950, **200**, 284–300.

[18] K. N. Tanner and R. L. King, *Nature*, 1958, **181**, 963–965.

[19] K. C. Herr and G. C. Pimentel, *Appl. Opt.*, 1965, **4**, 25–30.

[20] M. Poliakoff and E. Weitz, in *Adv. Organomet. Chem.*, Academic Press, 1986, vol. 25, pp. 277–316.

[21] G. C. Pimentel and K. C. Herr, *J. Chim. Phys.*, 1964, **61**, 1509–1516.

[22] A. S. Lefohn and G. C. Pimentel, *J. Chem. Phys.*, 1971, **55**, 1213–1217.

[23] L. Y. Tan, A. M. Winer and G. C. Pimentel, *J. Chem. Phys.*, 1972, **57**, 4028–4037.

[24] F. Siebert, W. MÄntele and W. Kreutz, *Biophys. Struct. Mech.*, 1980, **6**, 139–146.

[25] H. Hermann, F. W. Grevels, A. Henne and K. Schaffner, *J. Phys. Chem.*, 1982, **86**, 5151–5154.

[26] S. P. Church, F.-W. Grevels, H. Hermann and K. Schaffner, *Inorg. Chem.*, 1984, **23**, 3830–3833.

[27] S. P. Church, H. Hermann, F.-W. Grevels and K. Schaff, *J. Chem. Soc. Chem. Commun.*, 1984, **12**, 785–786.

[28] H. Hermann, F. W. Grevels, A. Henne and K. Schaffner, *J. Phys. Chem.*, 1982, **86**, 5151–5154.

[29] D. C. Grills, J. J. Turner and M. W. George, in *Compr. Coord. Chem. II*, Pergamon, Oxford, 2003, pp. 91–101.

[30] M. Towrie, D. C. Grills, J. Dyer, J. A. Weinstein, P. Matousek, R. Barton, P. D. Bailey, N. Subramaniam, W. M. Kwok, C. Ma, D. Phillips, A. W. Parker and M. W. George, *Appl. Spectrosc.*, 2003, **57**, 367–380.

[31] D. C. Grills and M. W. George, in *Handb. Vib. Spectrosc.*, Wiley Interscience, New York, 2006, pp. 677–692.

[32] A. E. Shilov and G. B. Shul'pin, *Activation and Catalytic Reactions of Saturated Hydrocarbons in the Presence of Metal Complexes*, Springer Netherlands, 1st edn., 2000.

[33] R. G. Bergman, *Nature*, 2007, **446**, 391–393.

[34] A. H. Janowicz and R. G. Bergman, *J. Am. Chem. Soc.*, 1982, **104**, 352–354.

[35] J. K. Hoyano and W. A. G. Graham, *J. Am. Chem. Soc.*, 1982, **104**, 3723–3725.

[36] C. Hall and R. N. Perutz, *Chem. Rev.*, 1996, **96**, 3125–3146.

[37] R. N. Perutz and J. J. Turner, *J. Am. Chem. Soc.*, 1975, **97**, 4791–4800.

[38] J. M. Kelly, H. Hermann and E. K. Von Gustorf, *J. Chem. Soc. Chem. Commun.*, 1973, 105–106.

[39] J. D. Simon and X. Xie, *J. Phys. Chem.*, 1986, **90**, 6751–6753.

[40] X. Xie and J. D. Simon, *J. Am. Chem. Soc.*, 1990, **112**, 1130–1136.

[41] G. I. Childs, D. C. Grills, X. Z. Sun and M. W. George, *Pure Appl. Chem.*, 2001, **73**, 443–447.

[42] G. I. Childs, C. S. Colley, J. Dyer, D. C. Grills, X. Z. Sun, J. X. Yang and M. W. George, *J. Chem. Soc. Dalt. Trans.*, 2000, **2**, 1901–1906.

[43] B. S. Creaven, M. W. George, A. G. Ginzburg, C. Hughes, J. M. Kelly, C. Long, I. M. McGrath and M. T. Pryce, *Organometallics*, 1993, **12**, 3127–3131.

[44] J. R. Wells, P. G. House and E. Weitz, *J. Phys. Chem.*, 1994, **98**, 8343–8351.

[45] C. E. Brown, Y. Ishikawa, P. A. Hackett and D. M. Rayner, *J. Am. Chem. Soc.*, 1990, **112**, 2530–2536.

[46] S. Geftakis and G. E. Ball, *J. Am. Chem. Soc.*, 1998, **120**, 9953–9954.

[47] J. A. Calladine, S. B. Duckett, M. W. George, S. L. Matthews, R. N. Perutz, O. Torres and K. Q. Vuong, *J. Am. Chem. Soc.*, 2011, **133**, 2303–2310.

[48] O. Torres, J. A. Calladine, S. B. Duckett, M. W. George and R. N. Perutz, *Chem. Sci.*, 2015, **6**, 418–424.

[49] R. D. Young, D. J. Lawes, A. F. Hill and G. E. Ball, *J. Am. Chem. Soc.*, 2012, **134**, 8294–8297.

[50] W. H. Bernskoetter, C. K. Schauer, K. I. Goldberg and M. Brookhart, *Science (80-.).*, 2009, **326**, 553 – 556.

[51] M. D. Walter, P. S. White, C. K. Schauer and M. Brookhart, *J. Am. Chem. Soc.*, 2013, **135**, 15933–15947.

[52] D. J. Lawes, S. Geftakis and G. E. Ball, *J. Am. Chem. Soc.*, 2005, **127**, 4134–4135.

[53] D. R. Evans, T. Drovetskaya, R. Bau, C. A. Reed and P. D. Boyd, *J. Am. Chem. Soc.*, 1997, **119**, 3633–3634.

[54] I. Castro-Rodriguez, H. Nakai, P. Gantzel, L. N. Zakharov, A. L. Rheingold and K. Meyer, *J. Am. Chem. Soc.*, 2003, **125**, 15734–15735.

[55] S. D. Pike, A. L. Thompson, A. G. Algarra, D. C. Apperley, S. A. Macgregor and A. S. Weller, *Science (80-.).*, 2012, **337**, 1648–1651.

[56] A. J. Martínez-Martínez, B. E. Tegner, A. I. McKay, A. J. Bukvic, N. H. Rees, G. J. Tizzard, S. J. Coles, M. R. Warren, S. A. Macgregor and A. S. Weller, *J. Am. Chem. Soc.*, 2018, **140**, 14958–14970.

[57] S. A. Bartlett, N. A. Besley, A. J. Dent, S. Diaz-Moreno, J. Evans, M. L. Hamilton, M. W. D. Hanson-Heine, R. Horvath, V. Manici, X.-Z. Sun, M. Towrie, L. Wu, X. Zhang and M. W. George, *J. Am. Chem. Soc.*, 2019, **141**, 11471–11480.

[58] J. J. Turner, J. K. Burdett, R. N. Perutz and M. Poliakoff, *Pure Appl. Chem.*, 1977, **49**, 271–285.

[59] M. B. Simpson, M. Poliakoff, J. J. Turner, W. B. Maier and J. G. McLaughlin, *J. Chem. Soc. Chem. Commun.*, 1983, 1355–1357.

[60] R. N. Perutz and J. J. Turner, *J. Am. Chem. Soc.*, 1975, **97**, 4800–4804.

[61] J. K. Burdett, M. A. Graham, R. N. Perutz, M. Poliakoff, J. J. Turner, R. F. Turner and A. J. Rest, *J. Am. Chem. Soc.*, 1975, **97**, 4805–4808.

[62] M. Poliakoff and J. J. Turner, *J. Chem. Soc. Dalt. Trans.*, 1974, 2276–2285.

[63] M. Brookhart, W. Chandler, R. J. Kessler, Y. Liu, N. J. Pienta, C. S. Chris, R. N. Perutz and J. A. Timney, *J. Am. Chem. Soc.*, 1992, **114**, 3802–3815.

[64] R. J. Mawby, R. N. Perutz and M. K. Whittlesey, *Organometallics*, 1995, **14**, 3268–3274.

[65] M. K. Whittlesey, R. N. Perutz, I. G. Virrels and M. W. George, *Organometallics*, 1997, **16**, 268–274.

[66] D. C. Grills, X. Z. Sun, G. I. Childs and M. W. George, *J. Phys. Chem. A*, 2000, **104**, 4300–4307.

[67] D. C. Grills, G. I. Childs and M. W. George, *Chem. Commun.*, 2000, **3**, 1841–1842.

[68] O. S. Jina, X. Z. Sun and M. W. George, *Dalt. Trans.*, 2003, **2**, 1773–1778.

[69] X.-Z. Sun, M. W. George, S. G. Kazarian, S. M. Nikiforov and M. Poliakoff, *J. Am. Chem. Soc.*, 1996, **118**, 10525–10532.

[70] D. C. Grills and M. W. George, *Advances in Inorganic Chemistry*, Academic Press, 2001, vol. 52, pp. 113–150.

[71] J. B. Asbury, H. N. Ghosh, J. S. Yeston, R. G. Bergman and T. Lian, *Organometallics*, 1998, **17**, 3417–3419.

[72] G. E. Ball, T. A. Darwish, S. Geftakis, M. W. George, D. J. Lawes, P. Portius and J. P. Rourke, *Proc. Natl. Acad. Sci. U. S. A.*, 2005, **102**, 1853–1858.

[73] S. Seidel and K. Seppelt, *Science (80-.).*, 2000, **290**, 117–118.

[74] *Org. React.*, ed. F. Ruff and I. G. B. T. S. i. O. C. Csizmadia, Elsevier, 1994, vol. 50, pp. 131–160.

[75] J. M. Morse, G. H. Parker and T. J. Burkey, *Organometallics*, 1989, **8**, 2471–2474.

[76] C. J. Breheny, J. M. Kelly, C. Long, S. O'Keeffe, M. T. Pryce, G. Russell and M. M. Walsh, *Organometallics*, 1998, **17**, 3690–3695.

[77] S. Trofimenko, *Scorpionates: The Coordination Chemistry Of Polypyrazolylborate Ligands*, World Scientific Publishing Company, 1999.

[78] A. Bérces, *Inorg. Chem.*, 1997, **36**, 4831–4837.

[79] J. E. Sheats, R. S. Czernuszewicz, G. C. Dismukes, A. L. Rheingold, V. Petrouleas, J. Stubbe, W. H. Armstrong, R. H. Beer and S. J. Lippard, *J. Am. Chem. Soc.*, 1987, **109**, 1435–1444.

[80] L. L. Blosch, A. S. Gamble and J. M. Boncella, *J. Mol. Catal.*, 1992, **76**, 229–237.

[81] S. Scheuer, J. Fischer and J. Kress, *Organometallics*, 1995, **14**, 2627–2629.

[82] S. Trofimenko, *J. Chem. Educ.*, 2005, **82**, 1715.

[83] D. M. Tellers, S. J. Skoog and R. G. Bergman, *Organometallics*, 2000, **19**, 2428–2432.

[84] S. E. Bromberg, H. Yang, M. C. Asplund, T. Lian, B. K. McNamara, K. T. Kotz, J. S. Yeston, M. Wilkens, H. Frei, R. G. Bergman and C. B. Harris, *Science (80-.).*, 1997, **278**, 260–263.

[85] C. E. Webster and M. B. Hall, *Inorganica Chim. Acta*, 2002, **330**, 268–282.

[86] C. K. Ghosh and W. A. G. Graham, *J. Am. Chem. Soc.*, 1987, **109**, 4726–4727.

[87] A. A. Purwoko, D. P. Drolet and A. J. Lees, *J. Organomet. Chem.*, 1995, **504**, 107–113.

[88] P. E. Bloyce, J. Mascetti and A. J. Rest, *J. Organomet. Chem.*, 1993, **444**, 223–233.

[89] T. Lian, S. E. Bromberg, H. Yang, G. Proulx, R. G. Bergman and C. B. Harris, *J. Am. Chem. Soc.*, 1996, **118**, 3769–3770.

[90] M. C. Asplund, P. T. Snee, J. S. Yeston, M. J. Wilkens, C. K. Payne, H. Yang, K. T. Kotz, H. Frei, R. G. Bergman and C. B. Harris, *J. Am. Chem. Soc.*, 2002, **124**, 10605–10612.

[91] A. J. Blake, M. W. George, M. B. Hall, J. McMaster, P. Portius, X. Z. Sun, M. Towrie, C. E. Webster, C. Wilson and S. D. Zarić, *Organometallics*, 2008, **27**, 189–201.

[92] N. Kitajima and W. B. Tolman, *Prog. Inorg. Chem.*, 1995, 419–531.

[93] R. Krentz, *Ph.D. thesis*, The University of Alberta, 1989.

[94] E. Clot, O. Eisenstein and W. D. Jones, *Proc. Natl. Acad. Sci.*, 2007, **104**, 6939–6944.

[95] D. Balcells, E. Clot and O. Eisenstein, *Chem. Rev.*, 2010, **110**, 749–823.

[96] S. Zarić and M. B. Hall, *J. Phys. Chem. A*, 1998, **102**, 1963–1964.

[97] J. S. Yeston and R. G. Bergman, *Organometallics*, 2000, **19**, 2947–2949.

[98] J. S. Yeston, B. K. McNamara, R. G. Bergman and C. B. Moore, *Organometallics*, 2000, **19**, 3442–3446.

[99] C. Tamborski, C. E. Snijder and J. B. Christian, Chem. Abstr, 1984, p. 152079z.

[100] E. De Wolf, G. Van Koten and B. J. Deelman, *Chem. Soc. Rev.*, 1999, **28**, 37–41.

[101] R. K. Kobos, J. W. Eveleigh and R. Arentzen, *Trends Biotechnol.*, 1989, **7**, 101–105.

[102] D.-W. Zhu, *Synthesis (Stuttg).*, 1993, **1993**, 953–954.

[103] A. M. A. Dias, R. P. Bonifácio, I. M. Marrucho, A. A. H. Pádua and M. F. Costa Gomes, *Phys. Chem. Chem. Phys.*, 2003, **5**, 543–549.

[104] U. Kaisers, K. P. Kelly and T. Busch, *BJA Br. J. Anaesth.*, 2003, **91**, 143–151.

[105] B. Rábay, T. Braun and J. P. Falkenhagen, *Dalt. Trans.*, 2013, **42**, 8058–8065.

[106] B. M. Ahmed and G. Mezei, *RSC Adv.*, 2015, **5**, 24081–24093.

[107] B. M. Ahmed, H. Zhang, Y. Mo and G. Mezei, *J. Org. Chem.*, 2016, **81**, 1718–1722.

[108] Y. Mo, B. M. Ahmed, L. Guan, J. Karty and G. Mezei, *Org. Lett.*, 2014, **16**, 4680–4683.

[109] R. P. Hughes and H. A. Trujillo, *Organometallics*, 1996, **15**, 286–294.

[110] E. Del Ministro, O. Renn, H. Rüegger, L. M. Venanzi, U. Burckhardt and V. Gramlich, *Inorganica Chim. Acta*, 1995, **240**, 631–639.

[111] H. Yang, M. C. Asplund, K. T. Kotz, M. J. Wilkens, H. Frei and C. B. Harris, *J. Am. Chem. Soc.*, 1998, **120**, 10154–10165.

[112] R. Perutz, O. Torres and A. Vlček, in *Compr. Inorg. Chem. II*, 2013, pp. 229–253.

[113] J. Guan, A. Wriglesworth, X. Z. Sun, E. N. Brothers, S. D. Zarić, M. E. Evans, W. D. Jones, M. Towrie, M. B. Hall and M. W. George, *J. Am. Chem. Soc.*, 2018, **140**, 1842–1854.

[114] T. Murphy, *Ph.D. thesis*, The University of Nottingham, 2015.

[115] B. Procacci, Y. Jiao, M. E. Evans, W. D. Jones, R. N. Perutz and A. C. Whitwood, *J. Am. Chem. Soc.*, 2015, **137**, 1258–1272.

[116] A. Wriglesworth, *Ph.D. thesis*, The University of Nottingham, 2014.

[117] O. S. Mills and J. P. Nice, *J. Organomet. Chem.*, 1967, **10**, 337–342.

[118] S. Trofimenko, *Chem. Rev.*, 1972, **72**, 497–509.

[119] G. Banditelli, A. L. Bandini, F. Bonati and G. Minghetti, *J. Organomet. Chem.*, 1981, **218**, 229–239.

[120] J. M. Kelly, C. Long and R. Bonneau, *J. Phys. Chem.*, 1983, **87**, 3344–3349.

[121] X. Wu, *Ph.D. thesis*, The University of Nottingham, 2019.

[122] A. A. Bengali, R. H. Schultz, C. B. Moore and R. G. Bergman, *J. Am. Chem. Soc.*, 1994, **116**, 9585–9589.

[123] A. K. Chandra and T. Uchimaru, *J. Phys. Chem. A*, 2000, **104**, 9244–9249.

[124] M. Born and R. Oppenheimer, *Ann. Phys.*, 1927, **389**, 457–484.

[125] V. Fock, *Zeitschrift für Phys.*, 1930, **61**, 126–148.

[126] P. Hohenberg and W. Kohn, *Phys. Rev.*, 1964, **136**, B864–B871.

[127] W. Kohn and L. J. Sham, *Phys. Rev.*, 1965, **140**, A1133–A1138.

[128] C. J. Cramer, *Essentials of Computational Chemistry: Theories and Models*, John Wiley & Sons, Ltd, 2nd edn., 2004.

[129] E. G. Lewars, in *E. G. Lewars*, ed. E. G. Lewars, Springer Netherlands, Dordrecht, 2011, pp. 445–519.

[130] Y. Zhao and D. G. Truhlar, *Theor. Chem. Accounts*, 2008, **120**, 215–241.

[131] C. Flener-Lovitt, D. E. Woon, T. H. Dunning and G. S. Girolami, *J. Phys. Chem. A*, 2010, **114**, 1843–1851.

[132] D. Feller and E. R. Davidson, in *Rev. Comput. Chem.*, 1990, pp. 1–43.

[133] F. Jensen, *Introduction to Computational Chemistry*, John Wiley & Sons, Ltd, 2nd edn., 2007, p. 225.227.

[134] E. Welch, *Ph.D. thesis*, Texas State University, 2019.

[135] E. A. Cobar, R. Z. Khaliullin, R. G. Bergman and M. Head-Gordon, *Proc. Natl. Acad. Sci. U. S. A.*, 2007, **104**, 6963–6968.

[136] B. Chan and G. E. Ball, *J. Chem. Theory Comput.*, 2013, **9**, 2199–2208.

[137] Q. Lu, F. Neese and G. Bistoni, *Phys. Chem. Chem. Phys.*, 2019, **21**, 11569–11577.

[138] V. Elwell, *Computational Studies Of Organometallic Alkane and Noble Gas Complexes*, The university of nottingham technical report, 2017.

[139] A. W. Ehlers, G. Frenking and E. J. Baerends, *Organometallics*, 1997, **16**, 4896–4902.

[140] R. L. Dekock, *Inorg. Chem.*, 1971, **10**, 1205–1211.

[141] Q. Z. Shi, T. G. Richmond, W. C. Trogler and F. Basolo, *J. Am. Chem. Soc.*, 1984, **106**, 471–76.

[142] F. Calderazzo and G. Pampaloni, *J. Organomet. Chem.*, 1986, **303**, 111–120.

[143] H. M. Yau, A. I. McKay, H. Hesse, R. Xu, M. He, C. E. Holt and G. E. Ball, *J. Am. Chem. Soc.*, 2016, **138**, 281–288.

[144] R. Z. Khaliullin, E. A. Cobar, R. C. Lochan, A. T. Bell and M. Head-Gordon, *J. Phys. Chem. A*, 2007, **111**, 8753–8765.

[145] M. Thenraj and A. G. Samuelson, *J. Comput. Chem.*, 2015, **36**, 1818–1830.

[146] E. Teuma, M. Loy, C. Le Berre, M. Etienne, J. C. Daran and P. Kalck, *Organometallics*, 2003, **22**, 5261–5267.

[147] S. Burling, L. D. Field, B. A. Messerle and P. Turner, *Organometallics*, 2004, **23**, 1714–1721.

[148] S. L. Dabb, J. H. Ho, R. Hodgson, B. A. Messerle and J. Wagler, *Dalt. Trans.*, 2009, 634–642.

[149] L. D. Field, B. A. Messerle, M. Rehr, L. P. Soler and T. W. Hambley, *Organometallics*, 2003, **22**, 2387–2395.

[150] G. S. McGrady, P. Sirsch, N. P. Chatterton, A. Ostermann, C. Gatti, S. Altmannshofer, V. Herz, G. Eickerling and W. Scherer, *Inorg. Chem.*, 2009, **48**, 1588–1598.

[151] R. H. Crabtree, *Angew. Chemie Int. Ed. English*, 1993, **32**, 789–805.

[152] J. Y. Corey, *Chem. Rev.*, 2011, **111**, 863–1071.

[153] Z. Lin, *Chem. Soc. Rev.*, 2002, **31**, 239–245.

[154] J. K. Hoyano, M. Elder and W. A. G. Graham, *J. Am. Chem. Soc.*, 1969, **91**, 4568–4569.

[155] U. Schubert, in *Adv. Organomet. Chem.*, 1990, vol. 30, pp. 151–187.

[156] U. Schubert, G. Scholz, J. Müller, K. Ackermann, B. Wörle and R. Stansfield, *J. Organomet. Chem.*, 1986, **306**, 303–326.

[157] J. L. Speier, in *Catal. Org. Synth.*, ed. F. G. A. Stone and R. B. T. A. i. O. C. West, Academic Press, 1979, vol. 17, pp. 407–447.

[158] J. Yang, P. S. White, C. K. Schauer and M. Brookhart, *Angew. Chemie*, 2008, **120**, 4209–4211.

[159] R. H. Hill and M. S. Wrighton, *Organometallics*, 1987, **6**, 632–638.

[160] C. R. Kemnitz, E. S. Ball and R. J. McMahon, *Organometallics*, 2012, **31**, 70–84.

[161] Z. F. Zhang and M. D. Su, *RSC Adv.*, 2018, **8**, 10987–10998.

[162] S. J. La Placa and J. A. Ibers, *Inorg. Chem.*, 1965, **4**, 778–783.

[163] D. M. Roe, P. M. Bailey, K. Moseley and P. M. Maitlis, *J. Chem. Soc. Chem. Commun.*, 1972, 1273–1274.

[164] R. H. Crabtree and D. G. Hamilton, in *Adv. Organomet. Chem.*, 1988, vol. 28, pp. 299–337.

[165] G. J. Kubas, in *Met. Dihydrogen σ-Bond Complexes*, 2002, pp. 365–415.

[166] A. Dedieu and A. Strich, *Inorg. Chem.*, 1979, **18**, 2940–2943.

[167] J.-Y. Saillard and R. Hoffman, *J. Am. Chem. Soc.*, 1984, **106**, 2006–2026.

[168] H. B. Bürgi and J. D. Dunitz, *Acc. Chem. Res.*, 1983, **16**, 153–161.

[169] U. Schubert, K. Ackermann, G. Kraft and B. Worle, *Zeitschrift für Naturforsch. B*, 1983, **38**, 1488–1492.

[170] U. Schubert, G. Scholz, J. Müller, K. Ackermann, B. Wörle and R. F. D. Stansfield, *J. Organomet. Chem.*, 1986, **306**, 303–326.

[171] R. H. Crabtree, E. M. Holt, M. Lavin and S. M. Morehouse, *Inorg. Chem.*, 1985, **24**, 1986–1992.

[172] J. Song and M. B. Hall, *Organometallics*, 1993, **12**, 3118–3126.

[173] S. A. Macgregor, O. Eisenstein, M. K. Whittlesey and R. N. Perutz, *J. Chem. Soc. Dalt. Trans.*, 1998, 291–300.

[174] C. J. Milne and M. Chergui, *Spectrosc. Eur.*, 2012, **24**, 17–21.

[175] M. Newville, *Rev. Mineral. Geochemistry*, 2014, **78**, 33–74.

[176] L. R. Sharpe, *Chem. Rev.*, 1990, **90**, 705–722.

[177] M. Fracchia, P. Ghigna, A. Vertova, S. Rondinini and A. Minguzzi, *Surfaces*, 2018, **1**, 138–150.

[178] A. Oguz Er, J. Chen and P. M. Rentzepis, *J. Appl. Phys.*, 2012, **112**, 031101.

[179] C. Bressler, R. Abela and M. Chergui, *Zeitschrift fur Krist.*, 2008, **223**, 307–321.

[180] P. Beaud, S. L. Johnson, A. Streun, R. Abela, D. Abramsohn, D. Grolimund, F. Krasniqi, T. Schmidt, V. Schlott and G. Ingold, *Phys. Rev. Lett.*, 2007, **99**, 1–4.

[181] K. Zhang, M.-F. Lin, E. S. Ryland, M. A. Verkamp, K. Benke, F. M. F. de Groot, G. S. Girolami and J. Vura-Weis, *J. Phys. Chem. Lett.*, 2016, **7**, 3383–3387.

[182] Y. Pertot, C. Schmidt, M. Matthews, A. Chauvet, M. Huppert, V. Svoboda, A. von Conta, A. Tehlar, D. Baykusheva, J.-P. Wolf and H. J. Wörner, *Science (80-.).*, 2017, **355**, 264–267.

[183] E. S. Ryland, M.-F. Lin, M. A. Verkamp, K. Zhang, K. Benke, M. Carlson and J. Vura-Weis, *J. Am. Chem. Soc.*, 2018, **140**, 4691–4696.

[184] K. Zhang, R. Ash, G. S. Girolami and J. Vura-Weis, *J. Am. Chem. Soc.*, 2019, **141**, 17180–17188.

[185] C. Bressler, C. Milne, V. Pham, A. ElNahhas, R. M. van der Veen, W. Gawelda, S. Johnson, P. Beaud, D. Grolimund, M. Kaiser, C. N. Borca, G. Ingold, R. Abela and M. Chergui, *Science (80-.).*, 2009, **323**, 489–492.

[186] W. Gawelda, V. T. Pham, R. M. Van Der Veen, D. Grolimund, R. Abela, M. Chergui and C. Bressler, *J. Chem. Phys.*, 2009, **130**, 124520.

[187] R. M. Van Der Veen, C. J. Milne, A. E. Nahhas, F. A. Lima, V. T. Pham, J. Best, J. A. Weinstein, C. N. Borca, R. Abela, C. Bressler and M. Chergui, *Angew. Chemie - Int. Ed.*, 2009, **48**, 2711–2714.

[188] B. S. Creaven, A. J. Dixon, J. M. Kelly, C. Long and M. Poliakoff, *Organometallics*, 1987, **6**, 2600–2605.

[189] B. S. Creaven, *Ph.D. thesis*, 1989.

[190] G. A. Crosby, *Acc. Chem. Res.*, 1975, **8**, 231–238.

[191] O. S. Wenger, *Coord. Chem. Rev.*, 2009, **253**, 1439–1457.

[192] A. Kumar, S. S. Sun and A. J. Lees, *Top. Organomet. Chem.*, 2010, **29**, 37–71.

[193] V.-W. Yam, B. Li, Y. Yang, B.-K. Chu, K.-C. Wong and K.-K. Cheung, *Eur. J. Inorg. Chem.*, 2003, **2003**, 4035–4042.

[194] F. Li, M. Zhang, G. Cheng, J. Feng, Y. Zhao, Y. Ma, S. Liu and J. Shen, *Appl. Phys. Lett.*, 2003, **84**, 148–150.

[195] G. M. Hasselmann and G. J. Meyer, *Zeitschrift für Phys. Chemie*, 1999, **212**, 39–44.

[196] J. Hawecker, J.-M. Lehn and R. Ziessel, *Helv. Chim. Acta*, 1986, **69**, 1990–2012.

[197] H. Hori, F. P. A. Johnson, K. Koike, O. Ishitani and T. Ibusuki, *J. Photochem. Photobiol. A Chem.*, 1996, **96**, 171–174.

[198] H. Hori, J. Ishihara, K. Koike, K. Takeuchi, T. Ibusuki and O. Ishitani, *J. Photochem. Photobiol. A Chem.*, 1999, **120**, 119–124.

[199] L. Sacksteder, A. P. Zipp, E. A. Brown, J. Streich, J. N. Demás and B. A. DeGraff, *Inorg. Chem.*, 1990, **29**, 4335–4340.

[200] K. Koike, N. Okoshi, H. Hori, K. Takeuchi, O. Ishitani, H. Tsubaki, I. P. Clark, M. W. George, F. P. Johnson and J. J. Turner, *J. Am. Chem. Soc.*, 2002, **124**, 11448–11455.

[201] A. Vlček, *Top. Organomet. Chem.*, 2010, **29**, 73–114.

[202] R. Kirgan, M. Simpson, C. Moore, J. Day, L. Bui, C. Tanner and D. P. Rillema, *Inorg. Chem.*, 2007, **46**, 6464–6472.

[203] R. J. Shaver, P. D. Rillema and C. Woods, *J. Chem. Soc. Chem. Commun.*, 1990, 179–180.

[204] R. J. Shaver and P. D. Rillema, *Inorg. Chem.*, 1992, **31**, 4101–4107.

[205] S. Bernhard, K. M. Omberg, G. F. Strouse and J. R. Schoonover, *Inorg. Chem.*, 2000, **39**, 3107–3110.

[206] J. J. Turner, M. W. George, F. P. A. Johnson and J. R. Westwell, *Coord. Chem. Rev.*, 1993, **125**, 101–114.

[207] J. R. Schoonover, G. F. Strouse, R. B. Dyer, W. D. Bates, P. Chen and T. J. Meyer, *Inorg. Chem.*, 1996, **35**, 273–274.

[208] D. J. Stufkens, *Spectr.*, 1996, **9**, 2–7.

[209] B. D. Rossenaar, M. W. George, F. P. A. Johnson, D. J. Stufkens, J. J. Turner and A. Vlcek, *J. Am. Chem. Soc.*, 1995, **117**, 11582–11583.

[210] G. F. Strouse, H. U. Guedel, V. Bertolasi and V. Ferretti, *Inorg. Chem.*, 1995, **34**, 5578–5587.

[211] G. F. Strouse and H. U. Güdel, *Inorganica Chim. Acta*, 1995, **240**, 453–464.

[212] K. E. A. Reynolds, *Ph.D. thesis*, The University of Nottingham, 2019.

[213] R. A. Marcus and N. Sutin, *BBA Rev. Bioenerg.*, 1985, **811**, 265–322.

[214] T. P. Silverstein, *J. Chem. Educ.*, 2012, **89**, 1159–1167.

[215] E. Anslyn and D. Dougherty, *Modern Physical Organic Chemistry*, 2004, vol. 168.

[216] B. Zhuang and Z. G. Wang, *J. Chem. Phys.*, 2015, **143**, 224502.

[217] R. A. Marcus, *Rudolph A. Marcus - Nobel Lecture*, 1992, https://www.nobelprize.org/prizes/chemistry/1992/marcus/lecture/.

[218] P. F. Barbara, T. J. Meyer and M. A. Ratner, *J. Phys. Chem.*, 1996, **100**, 13148–13168.

[219] J. R. Miller, *J. Am. Chem. Soc.*, 1984, **106**, 3047–3049.

[220] G. L. Closs and J. R. Miller, *Science (80-.).*, 1988, **240**, 440–447.

[221] M. Kuss-Petermann and O. S. Wenger, *Phys. Chem. Chem. Phys.*, 2016, **18**, 18657–18664.

[222] H. Oberhofer and J. Blumberger, *J. Chem. Phys.*, 2009, **131**, 064101.

[223] M. L. Tan, E. A. Dolan and T. Ichiye, *J. Phys. Chem. B*, 2004, **108**, 20435–20441.

[224] J. Kroon, H. Oevering, J. W. Verhoeven, J. M. Warman, A. M. Oliver and M. N. Paddon-Row, *J. Phys. Chem.*, 1993, **97**, 5065–5069.

[225] M. Kumbhakar, S. Nath, T. Mukherjee and H. Pal, *J. Photochem. Photobiol. A Chem.*, 2006, **182**, 7–16.

[226] S. Trofimenko, *J. Am. Chem. Soc.*, 1967, **89**, 6288–6294.

[227] A. Boni, G. Pampaloni, R. Peloso, D. Belletti, C. Graiff and A. Tiripicchio, *J. Organomet. Chem.*, 2006, **691**, 5602–5609.

[228] Y. Shao, Z. Gan, E. Epifanovsky, A. T. B. Gilbert, M. Wormit, J. Kussmann, A. W. Lange, A. Behn, J. Deng, X. Feng, D. Ghosh, M. Goldey, P. R. Horn, L. D. Jacobson, I. Kaliman, R. Z. Khaliullin, T. Kuś, A. Landau, J. Liu, E. I. Proynov,

Y. M. Rhee, R. M. Richard, M. A. Rohrdanz, R. P. Steele, E. J. Sundstrom, H. L. Woodcock, P. M. Zimmerman, D. Zuev, B. Albrecht, E. Alguire, B. Austin, G. J. O. Beran, Y. A. Bernard, E. Berquist, K. Brandhorst, K. B. Bravaya, S. T. Brown, D. Casanova, C.-M. Chang, Y. Chen, S. H. Chien, K. D. Closser, D. L. Crittenden, M. Diedenhofen, R. A. DiStasio, H. Do, A. D. Dutoi, R. G. Edgar, S. Fatehi, L. Fusti-Molnar, A. Ghysels, A. Golubeva-Zadorozhnaya, J. Gomes, M. W. D. Hanson-Heine, P. H. P. Harbach, A. W. Hauser, E. G. Hohenstein, Z. C. Holden, T.-C. Jagau, H. Ji, B. Kaduk, K. Khistyaev, J. Kim, J. Kim, R. A. King, P. Klunzinger, D. Kosenkov, T. Kowalczyk, C. M. Krauter, K. U. Lao, A. D. Laurent, K. V. Lawler, S. V. Levchenko, C. Y. Lin, F. Liu, E. Livshits, R. C. Lochan, A. Luenser, P. Manohar, S. F. Manzer, S.-P. Mao, N. Mardirossian, A. V. Marenich, S. A. Maurer, N. J. Mayhall, E. Neuscamman, C. M. Oana, R. Olivares-Amaya, D. P. O'Neill, J. A. Parkhill, T. M. Perrine, R. Peverati, A. Prociuk, D. R. Rehn, E. Rosta, N. J. Russ, S. M. Sharada, S. Sharma, D. W. Small, A. Sodt, T. Stein, D. Stück, Y.-C. Su, A. J. W. Thom, T. Tsuchimochi, V. Vanovschi, L. Vogt, O. Vydrov, T. Wang, M. A. Watson, J. Wenzel, A. White, C. F. Williams, J. Yang, S. Yeganeh, S. R. Yost, Z.-Q. You, I. Y. Zhang, X. Zhang, Y. Zhao, B. R. Brooks, G. K. L. Chan, D. M. Chipman, C. J. Cramer, W. A. Goddard, M. S. Gordon, W. J. Hehre, A. Klamt, H. F. Schaefer, M. W. Schmidt, C. D. Sherrill, D. G. Truhlar, A. Warshel, X. Xu, A. Aspuru-Guzik, R. Baer, A. T. Bell, N. A. Besley, J.-D. Chai, A. Dreuw, B. D. Dunietz, T. R. Furlani, S. R. Gwaltney, C.-P. Hsu, Y. Jung, J. Kong, D. S. Lambrecht, W. Liang, C. Ochsenfeld, V. A. Rassolov, L. V. Slipchenko, J. E. Subotnik, T. Van Voorhis, J. M. Herbert, A. I. Krylov, P. M. W. Gill and M. Head-Gordon, *Mol. Phys.*, 2015, **113**, 184–215.

[229] B. P. Pritchard, D. Altarawy, B. Didier, T. D. Gibson and T. L. Windus, *J. Chem. Inf. Model.*, 2019, **59**, 4814–4820.